



Floyd, Cameron James (2019) *Characterisation of terrestrial weathering products in ordinary and CM carbonaceous chondrites*. MSc(R) thesis.

<https://theses.gla.ac.uk/77898/>

Copyright and moral rights for this work are retained by the author

A copy can be downloaded for personal non-commercial research or study, without prior permission or charge

This work cannot be reproduced or quoted extensively from without first obtaining permission in writing from the author

The content must not be changed in any way or sold commercially in any format or medium without the formal permission of the author

When referring to this work, full bibliographic details including the author, title, awarding institution and date of the thesis must be given

# **Characterisation of terrestrial weathering products in ordinary and CM carbonaceous chondrites.**

Cameron James Floyd  
BSc (Hons)

Thesis presented for the degree of Master of Science in Earth Science

**University of Glasgow**

**College of Science and Engineering  
School of Geographical and Earth Sciences**

**September 2019**



# Abstract

Research investigating the terrestrial weathering experienced by ordinary and CM chondrites at high spatial resolution is sparse, with most published work using either bulk mineralogical or chemical analysis techniques. With asteroid sample return missions, Hayabusa 2 and OSIRIS-REx expected to return samples in near future, understanding the effects of terrestrial contamination and weathering in fine detail is of paramount importance.

The research presented here sets out to investigate terrestrial weathering by analysing the alteration products found around Fe,Ni metal grains by coupled chemical and mineralogical analysis for the first time. Analysis is conducted using a suite of high spatial resolution imaging and spectroscopic techniques including EDS spectroscopy and Raman spectroscopy, an approach with very limited previous use in this field.

Initially characterisation of the effects of terrestrial weathering on ordinary chondrites, which should have only experienced significant aqueous alteration in the terrestrial environment, is conducted. The effects of weathering in three climates (the Antarctic, Sahara and Western Australia) are investigated to compare the intensity of alteration between typical find environments. The results of ordinary chondrite analysis reveal Cl-bearing akaganeite is the first terrestrial alteration product to form, followed by goethite and a poorly crystallised hydrated iron III oxide or oxyhydroxide. Analysis also reveals that terrestrial weathering was least intense in cold desert environments (Antarctica) and most intense in semi-arid environments (Western Australia).

Having characterised the terrestrial weathering products which form around Fe,Ni metal the effects of terrestrial weathering on CM chondrites, which have experienced significant aqueous alteration both terrestrially and on their parent bodies, is investigated. Analysis of the weathering products in CM chondrites revealed the terrestrial alteration products akaganeite and goethite eroding/replacing parent body alteration products tochilinite and magnetite.

The work presented here highlights the need for high resolution, chemical and mineralogical analysis of the alteration products found in ordinary and CM chondrites in order to prevent misinterpretation of terrestrially derived alteration products as evidence of parent body alteration.

# Table of Contents

<b>Abstract</b>	<b>3</b>
<b>Table of Contents</b>	<b>4</b>
<b>List of Tables</b>	<b>6</b>
<b>List of Figures</b>	<b>8</b>
<b>List of Equations</b>	<b>15</b>
<b>Acknowledgements</b>	<b>16</b>
<b>Declaration</b>	<b>17</b>
<b>Chapter 1 Introduction</b>	<b>18</b>
1.1 An Introduction to Meteorites	18
1.2 Ordinary Chondrites	19
1.2.1 Origin and Formation	19
1.2.2 Classification	21
1.2.3 Composition	22
1.3 Carbonaceous Chondrites	23
1.3.1 Origin and Formation	24
1.3.2 Composition and Classification	24
1.4 Age	27
1.4.1 Formation Age	27
1.4.2 Cosmogenic Age	27
1.4.3 Terrestrial Age	27
1.5 Sources of meteorites on Earth	30
1.5.1 Find or Fall	31
1.6 Previous Work on Weathering	31
1.6.1 Classification	31
1.6.2 Oxidation	33
1.6.3 The Importance of Akaganeite	34
1.6.4 Museum Weathering	35
1.7 Aims of This Project	36
<b>Chapter 2 Sample Selection, Preparation and Analysis Techniques</b>	<b>39</b>
2.1 Sample Selection	39
2.1.1 Ordinary Chondrites	39
2.1.2 Carbonaceous Chondrites	40
2.2 Sample Preparation	40
2.2.1 Resin Blocks	40
2.2.2 Polishing	41
2.3 Experimental Analysis	41
2.3.1 Optical Microscopy	41
2.3.2 Scanning Electron Microscopy Imaging	42
2.3.3 Quantitative Analysis	42
2.3.3.1 Detection Limits	43
2.3.4 Raman Spectroscopy	43
2.3.4.1 Point Analysis	44
2.3.4.2 Principle Component Mapping	45
2.3.4.3 Raman Spectrum Identification	45
<b>Chapter 3 Ordinary Chondrites</b>	<b>49</b>
3.1 Antarctic Ordinary Chondrites	49
3.1.1 Environment	49
3.1.2 Fe,Ni Metal	50

3.1.3	Alteration Products	50
3.1.3.1	DOM 14010	50
3.1.3.2	ALHA 77180	59
3.1.4	Summary of Antarctic Ordinary Chondrite Alteration	63
3.2	Australian Ordinary Chondrites	64
3.2.1	Environment	64
3.2.2	Fe,Ni Metal	64
3.2.3	Alteration Products	65
3.2.3.1	Forrest 016	65
3.2.3.2	Forrest 028	71
3.2.3.3	Gunnadorah 004	77
3.2.4	Summary of Australian Ordinary Chondrites	80
3.3	Saharan Ordinary Chondrites	82
3.3.1	Environment	82
3.3.2	Fe,Ni Metal	82
3.3.3	Alteration Products	82
3.3.3.1	Daraj 014	83
3.3.3.2	Acfer 019	89
3.3.4	Summary of Saharan Ordinary Chondrite Alteration	93
3.4	Summary of Ordinary Chondrite Characterisation	93
3.5	Discussion	96
3.5.1	Antarctica	96
3.5.2	Sahara and Western Australia	97
3.6	Conclusions	98
<b>Chapter 4</b>	<b>Carbonaceous Chondrites</b>	<b>100</b>
4.1	Antarctic CM Chondrites	100
4.1.1	Environment	101
4.1.2	Fe,Ni Metal	101
4.1.3	Alteration products	101
4.1.3.1	LEW 85311	102
4.1.3.2	LAP 02239	113
4.1.4	Summary of Antarctic Carbonaceous Alteration	119
4.2	Saharan CM Chondrites	121
4.2.1	Environment	121
4.2.2	Metal Content	121
4.2.3	Alteration Products	121
4.2.3.1	Jbilet Winselwan	122
4.2.4	Summary of Saharan Carbonaceous Alteration	133
4.3	Summary of Analysis	133
4.4	Discussion	134
4.5	Conclusion	137
<b>Chapter 5</b>	<b>Summary</b>	<b>139</b>
5.1	Summary of Analytical Techniques	139
5.2	Summary of Alteration Products	140
5.2.1	Ordinary Chondrites	140
5.2.2	Carbonaceous Chondrites	141
5.3	Environmental Differences	145
5.4	Future Work	146
5.5	Conclusion	147
<b>Appendix</b>		<b>149</b>

## List of Tables

### Chapter 1

Table 1.1	<i>Average results of typical chemical analysis conducted on Antarctic H and L chondrites, taken from Jarosewich, (1990). Fe<sub>(m)</sub> is Fe-Metal. The oxidation of Fe<sub>(m)</sub> can produce the oxidation product Fe<sub>2</sub>O<sub>3</sub>. In this table all Fe<sub>2</sub>O<sub>3</sub> was converted to Fe<sub>(m)</sub> and normalised to 100% before the composition was calculated. FeO was calculated by subtracting Fe<sub>(m)</sub> and FeS from Fe<sub>(total)</sub>.</i>	23
Table 1.2	<i>Average results of chemical analysis conducted on CM2 chondrite falls, taken from Jarosewich, (1990). Fe<sub>(m)</sub> is Fe-Metal. The oxidation of Fe<sub>(m)</sub> can produce the oxidation product Fe<sub>2</sub>O<sub>3</sub>. In this table all Fe<sub>2</sub>O<sub>3</sub> was converted to Fe<sub>(m)</sub> and normalised to 100% before the composition was calculated. FeO was calculated by subtracting Fe<sub>(m)</sub> and FeS from Fe<sub>(total)</sub>.</i>	26
Table 1.3	<i>Weathering scale developed for polished sections based on the amount of oxidation (Wlotzka, 1993).</i>	32
Table 1.4	<i>The Fe-rich oxidation products which have been reported in the literature to form ‘metallic rust’ found around the Fe,Ni metal grains within ordinary chondrites (modified from Velbel, (2014)).</i>	33

### Chapter 2

Table 2.1	<i>Details of the ordinary chondrites selected and used. They are grouped according to their terrestrial environment. Those with no weathering classification listed have no recorded weathering classification on the Meteoritical Society Database (The Meteoritical Society, 2017). NASA (National Aeronautics and Space Administration), UoG (University of Glasgow).</i>	39
Table 2.2	<i>The CM carbonaceous chondrites selected and used for this research. Two samples of the Jbilet Winselwan CM chondrite are investigated. UoG (University of Glasgow), NHM (Natural History Museum).</i>	40
Table 2.3	<i>The standards used during quantitative analysis of samples</i>	42

## Chapter 3

Table 3.1	<i>ImageJ calculated, percentage of kamacite, taenite and troilite in each of the Antarctic samples calculated from reflected light microscopy images. Troilite is included despite being as sulphide as it could not be distinguished from Fe,Ni metal in ImageJ.</i>	50
Table 3.2	<i>Results of EDS analysis in metal 4 with positions numbers corresponding to those shown in figure 3.7. Values shown in wt.%. MDL = Minimum Detection Limit.</i>	55
Table 3.3	<i>ImageJ calculated, percentage of kamacite, taenite and troilite in each of the Antarctic samples calculated from reflected light microscopy. Troilite is included despite being as sulphide as it could not be distinguished from Fe,Ni metal in ImageJ.</i>	64
Table 3.4	<i>Results of EDS analysis in grain 9 with position numbers corresponding to those shown in figure 3.19. Values shown in wt.%. MDL = Minimum Detection Limit.</i>	68
Table 3.5	<i>Results of EDS analysis in metal 11 with positions numbers corresponding to those shown in figure 3.27. Values shown in wt.%. MDL = Minimum Detection Limit.</i>	75
Table 3.6	<i>ImageJ calculated, percentage of kamacite, taenite and troilite in each of the Antarctic samples calculated from reflected light microscopy images. Troilite is included despite being as sulphide as it could not be distinguished from Fe,Ni metal in ImageJ.</i>	82
Table 3.7	<i>Results of EDS analysis in metal 16 with positions numbers corresponding to those shown in figure 3.34. Values shown in wt.%. MDL = Minimum Detection Limit.</i>	86
Table 3.8	Table showing the decreasing steel corrosion rate with increasing distance inland from the nearest Antarctic coastline. Also shown are the approximate locations of the Antarctic samples analysed in this research. Edited from Morcillo et al., (2004) with data from Hughes et al., (1996).	99

## Chapter 4

Table 4.1	<i>ImageJ calculated, percentage volume of kamacite, taenite and troilite in each of the Antarctic samples calculated from reflected light microscopy images. Troilite is included despite being a sulphide as it could not be distinguished from Fe,Ni metal in ImageJ.</i>	101
Table 4.2	<i>Results of quantitative analysis around the large kamacite grain and as labelled in figure 4.7. Values shown are in wt. %. MDL= Minimum detection limit.</i>	108
Table 4.3	<i>ImageJ calculated, percentage volume of kamacite, taenite and troilite in each of the Saharan samples calculated from reflected light microscopy images. Troilite is included despite being a sulphide as it could not be distinguished from Fe,Ni metal in ImageJ.</i>	121

Table 4.4	<i>Results of quantitative analysis around Metal 24 and as labelled in figure 4.21. Values shown are in weight %. MDL = Minimum Detection Limit.</i>	128
-----------	------------------------------------------------------------------------------------------------------------------------------------------------------	-----

## List of Figures

### Chapter 1

- Figure 1.1 *The meteorite classification system. Many sub-groups exist beyond this. Those highlighted in green will be the focus of this research. \*denotes differentiated meteorites, \*\*denotes undifferentiated meteorites.* 19
- Figure 1.2 *Schematic illustration of the Grand tack model taken from Walsh et al., (2012). Large black circle is Jupiter and small black circle is Saturn. It demonstrates the migration of the giant planets inwards initially and then outwards causing scattering among the two parent populations and the mixing of these in the main asteroid belt.* 20
- Figure 1.3 *Images illustrating the changes observed with increasing thermal alteration in ordinary chondrites. A) Image taken in plane polarised light (PPL) of H4 ordinary chondrite Beaver Creek (BM 73646) taken at 5x magnification. Well defined chondrules can be seen throughout as can some matrix material. B) PPL image of H5 ordinary chondrite Allegan (BM 1920, 281) taken at 4x magnification. Chondrules are becoming less distinct and grain size is increasing. C) Image taken in PPL of H6 ordinary chondrite Kernouye (BM 43400) taken at 4x magnification. No chondrules are visible and there is a large grain size. D) Image taken in reflected light (RL) of H6 ordinary chondrite Kernouye (BM 43400) at 5x magnification demonstrating the presence and distribution of metal grains (white) in an H-chondrite.* 22
- Figure 1.4 *Terrestrial age distribution of meteorites from hot desert environments and Western Australia (Jull, 2011).* 29
- Figure 1.5 *Terrestrial age distribution from cold desert environments (Antarctica): Yamato site (slanted bars), Allan Hills (black bars) and Elephant Moraine (white bars) (Jull, 2001).* 29
- Figure 1.6 *A) Meteorite found in Antarctica in 2004. The dark colour is easily distinguished from the white Antarctic surface (Geiger, 2018). B) Meteorite found in Western Sahara in 2013. The dark colour of the meteorite stands out against the pale brown sandy soil (“Website 1.2”).* 30
- Figure 1.7 *A diagram showing the pathways and inter-relatedness of Iron-oxides and their hydrates. (from Buddhue, (1957)).* 35
- Figure 1.8 *Flow diagram showing how conventional meteorite collection compares to the sample return missions. The red box highlights the area of research for this project and the yellow box where this project may develop further insight.* 37

## Chapter 2

- Figure 2.1 Edited Raman spectrum from Neff et al., (2006) illustrating a spectrum of akaganeite which helped establish the typical peak positions. 46
- Figure 2.2 Edited Raman spectrum from the Ruff database illustrating a spectrum of goethite which helped establish the typical peak positions 47
- Figure 2.3 Raman spectrum from Neff et al., (2006) illustrating a spectrum of hydrated iron III oxide or oxyhydroxide which helped establish the typical peak positions. 47
- Figure 2.4 Edited Raman spectrum from the Ruff database illustrating a spectrum of tochilinite which helped establish the typical peak positions. 48
- Figure 2.5 Edited Raman spectrum from Bellot-Guelet et al. (2009) illustrating a spectrum of magnetite which helped establish the typical peak positions. 48

## Chapter 3

- Figure 3.1 Backscattered electron image (BSE) of Metal 1, Fe,Ni metal grain (white) within DOM 14010. The red dashed line indicates the boundary between the ordered and disordered material. They can be easily distinguished by the presence of fractures and by lamination thickness. 51
- Figure 3.2 BSE image of metal 2, Fe,Ni metal grain (white) within in DOM 14010. The highlighted area (red) indicates an area of ordered material which is very heavily fractured. The remaining material is disordered. 51
- Figure 3.3 BSE image of metal 3, Fe,Ni metal grain (white) demonstrating a subtle colour difference (blue line indicates boundary). The alteration material around this metal grain does not have a distinct ordered/disordered texture. 52
- Figure 3.4 BSE image of metal 4, Fe,Ni metal grain (white) showing subtle variation in colour (blue line indicates boundary). There is a large irregularly shaped alteration rim surrounding this metal grain with only a small pocket of ordered material (highlighted area). 52
- Figure 3.5 EDS maps of Metal 1 (A) and Metal 4 (B). EDS maps for Cl (left). EDS map for Cl overlain on a BSE image (right). Images demonstrate that the Cl-rich material is confined to the disordered material away from the metal grain boundary. 54

Figure 3.6	<i>Graphs illustrating the relationship between Fe<sub>2</sub>O<sub>3</sub> (wt.%) and the key elements investigated in metal 1 (a taenite metal grain). Data taken from Appendix: ‘Quantitative analysis of metal 1’ and values given in wt.%. Labels correspond to position numbers in data table.</i>	
	<i>A) Graph of Fe<sub>2</sub>O<sub>3</sub> - NiO. B) Graph of Fe<sub>e</sub>O<sub>3</sub> - S, C) Graph of Fe<sub>2</sub>O<sub>3</sub> - Cl.</i>	55
Figure 3.7	<i>EDS map of Cl overlain on a BSE image of metal 4. Labelled are the points of analysis shown in Table 3.2</i>	56
Figure 3.8	<i>Graphs illustrating the relationships between Fe<sub>2</sub>O<sub>3</sub> (wt.%) and the key elements investigated in metal 4 (a mixed kamacite, taenite metal grain). Data taken from table 3.2 and values given in wt.%. Labels correspond to position numbers in Figure 3.7 and Table 3.2.</i>	
	<i>A) Graph of Fe<sub>2</sub>O<sub>3</sub> - NiO. B) Graph of Fe<sub>e</sub>O<sub>3</sub> - S, C) Graph of Fe<sub>e</sub>O<sub>3</sub> - Cl.</i>	57
Figure 3.9	<i>EDS maps and accompanying Raman spectra for selected locations in metals 1 and 4. Spectrum A) Akaganeite, B) Inconclusive, C) Inconclusive, D) Akaganeite, E) Akaganeite.</i>	58
Figure 3.10	<i>BSE image of metal 5, Fe,Ni metal grain (white) with a large lobe of alteration products. The alteration material appears to have shared characteristics of the ordered and disordered material with crosscutting fractures and coarse, chaotic laminations.</i>	59
Figure 3.11	<i>BSE image of metal 6, Fe,Ni metal grain (white) with a zone of mixing between two materials. Most of the material is disordered with a small region of ordered material highlighted.</i>	60
Figure 3.12	<i>BSE image of Metal 7, Fe,Ni metal grain (white) surrounded by an alteration rim of uniform thickness consisting of fractured and disordered material.</i>	60
Figure 3.13	<i>EDS maps of metal 5 (A), metal 6 (B) and metal 7 (C). EDS maps for Cl (left). EDS maps for Cl overlain on BSE images (right). Maps show consistently low Cl concentrations throughout all the alteration rims with only a slight increase seen in metal 6 (B), within the thin band of ordered material.</i>	62
Figure 3.14	<i>EDS maps and accompanying Raman spectra for selected locations in metals 5 and 6. Spectrum A) Inconclusive, B) Goethite, C) Akaganeite, D) Inconclusive.</i>	63
Figure 3.15	<i>BSE image of Forrest 016 showing the high proportion of Fe-rich minerals (white) and alteration products (grey) within the sample. Alteration products are found in veins and replacing entire metal gains. The highlighted regions are examples of complete metal grain replacement.</i>	65
Figure 3.16	<i>BSE image of metal 8, a rare Fe,Ni metal grain (white) with an irregular and fractured alteration rim. This is the only Fe,Ni metal grain with an alteration rim observed in this sample.</i>	66
Figure 3.17	<i>BSE image of grain 9, a troilite grain (white) surrounded by an alteration rim and occluded veins. The material in the alteration rim and veins does not have any of the textural differences seen in the Antarctic samples.</i>	66

- Figure 3.18 EDS maps of Cl overlain on BSE images for; Metal 8 (A) and, Grain 9 (B). Maps show negligible increase in Cl between metal, alteration rim and surrounding material. 67
- Figure 3.19 EDS map of Cl overlain on BSE image of grain 9. Labelled are the points of analysis shown in Table 3.4 68
- Figure 3.20 Graphs illustrating the relationships between  $Fe_2O_3$  (wt.%) and the key elements investigated in grain 9 (a troilite). Data taken from Table 3.4 and values given in wt.%. Labels correspond to position numbers in Figure 3.19 and Table 3.4 A) Graph of  $Fe_2O_3$  - NiO, B) Graph of  $Fe_2O_3$  - S. 69
- Figure 3.21 EDS maps and accompanying Raman spectra for selected points in metals 8 and 9. Spectrum A) Hydrated iron III oxide or oxyhydroxide, B) Goethite, C) Goethite, D) Goethite. 70
- Figure 3.22 BSE image of metal 10, an Fe,Ni metal grain (white) with a lobe of alteration. This alteration rim has chaotic laminations and fractures throughout and does not show any changes in material colour. 71
- Figure 3.23 BSE image of metal 11, an Fe,Ni metal grain (white) with a significant alteration rim demonstrating two bands of material (pale and dark grey).The boundary between the bands is highlighted. 72
- Figure 3.24 BSE image of metal 12, an Fe,Ni metal grain (white) with a large alteration rim demonstrating alternating bands of material with different greyscales (and thus atomic numbers) throughout the alteration rim. 72
- Figure 3.25 BSE image of metal 13, an Fe,Ni metal grain completely surrounded by a significant alteration rim and demonstrating bands of material running through the alteration rim. 73
- Figure 3.26 EDS maps of metal 10 (A), metal 11 (B) and metal 12 (C). EDS maps for Cl (left). EDS maps for Cl overlain on BSE images (right). Figures B and C demonstrate the Cl enrichment confined to the darker coloured material. 74
- Figure 3.27 EDS map of Cl overlain on a BSE image of metal 11. Labelled are the points of analysis shown in Table 3.5. 75
- Figure 3.28 EDS maps and accompanying Raman spectra for selected points within metals 11 and 12. Spectrum A) Hydrated iron III oxide or oxyhydroxide, B) Akaganeite, C) Goethite, D) Akaganeite. 76
- Figure 3.29 BSE image of Gunnadorah 004 showing no metal grains but significant amounts of alteration material (grey). The alteration material is replacing most of the original metal grains and occluding fractures throughout the sample. 77
- Figure 3.30 BSE image of grain 14, troilite grain (white), one of only a handful of Fe-rich grains present within Gunnadorah 004. It shows a heavily fractured nature and is surrounded by veins of alteration product. 78
- Figure 3.31 EDS maps of Gunnadorah 004. EDS map of Cl (left). EDS map of Cl overlain on a BSE image (right). Highlighted are areas appearing to

be slightly Cl enriched but still have a negligible measured concentration.

79

Figure 3.32 EDS maps and accompanying Raman spectra for selected areas within Gunnadorah 004 and metal 14. Spectrum A) Goethite, B) Goethite, C) Goethite, D) Hydrated iron III oxide or oxyhydroxide.

80

Figure 3.33 BSE image of metal 15, an Fe,Ni metal grain (white) with alteration rim demonstrating greyscale bands, like those seen in the Western Australian samples.

83

Figure 3.34 BSE image of metal 16, an Fe,Ni metal grain (white) made up of two materials (boundary highlighted). The alteration rim around this grain does not exhibit colour banding.

83

Figure 3.35 BSE image of metal 17, an Fe,Ni metal grain surrounded by a very large alteration rim demonstrating bands of material forming almost concentric rings within the alteration rim.

84

Figure 3.36 EDS maps of metal 15 (A), metal 16 (B) and metal 17 (C). EDS maps of Cl (left). EDS maps of Cl overlain on BSE images (right). With A and B Cl enrichment is concentrated closest to the metal grain. Within A and C, Cl enrichment is broadly confined to zones or darker coloured alteration material.

85

Figure 3.37 Graphs illustrating the relationships between  $\text{Fe}_2\text{O}_3$  (wt.%) and the key elements investigated in metal 15 (a kamacite grain). Data taken from Appendix: ‘Quantitative analysis of metal 15’ and values given in wt.%. Arrows indicate increasing distance from the metal grain boundary A) Graph of  $\text{Fe}_2\text{O}_3$  - NiO, B) Graph of  $\text{Fe}_e\text{O}_3$  - S, C) Graph of  $\text{Fe}_e\text{O}_3$  - Cl.

86

Figure 3.38 EDS map of Cl overlain on a BSE image of metal 16. Labelled are the points of analysis shown in Table 3.7

87

Figure 3.39 EDS maps with accompanying Raman spectra for selected areas. Spectrum A) Hydrated iron III oxide or oxyhydroxide, B) Akaganeite, C) Akaganeite, D) Akaganeite, E) Goethite.

88

Figure 3.40 BSE image of metal 18, a group of Fe,Ni metal grains (white) with alteration material between. Previously, this may have been one large metal grain however, alteration has now replaced much of the original gain.

89

Figure 3.41 BSE image of metal 19, an Fe,Ni metal grain (white) with extensive alteration rim demonstrating colour banding. The highlighted region is an area of complete metal grain replacement.

90

Figure 3.42 BSE image of metal 20, an Fe,Ni metal grain (white) with extensive alteration rim demonstrating more subtle colour banding. The highlighted area shows another entirely replaced metal grain.

90

Figure 3.43 EDS maps of metal 19 (A) and metal 20 (B). EDS maps of Cl (left). EDS maps of Cl overlain on BSE images (right).

91

Figure 3.44 EDS maps with accompanying Raman spectra for selected areas in metals 19 and 20. Spectrum A) Hydrated iron III oxide or

- Figure 3.45 Graphs showing how Cl (wt.%) changes between environments within the alteration rims of Fe,Ni metal. 95
- Figure 3.46 Graphs showing how S (wt.%) changes between environments within the alteration rims of Fe,Ni metal 95
- Figure 3.47 Graph showing how oxidation increases with terrestrial age in different environments. It shows that Australia has the fastest rate of oxidation when compared to the Sahara and Antarctica. Edited from Bland. (2006). 98
- Figure 3.48 Flow diagram of the processes effecting Fe,Ni metal within ordinary chondrites when they fall and the resulting alteration products. 99

## Chapter 4

- Figure 4.1 Backscattered electron (BSE) image of Fe,Ni metal grain (white) typical of the smaller-type Fe,Ni metal grains in LEW 85311. The surrounding alteration rim is thin and almost featureless. 103
- Figure 4.2 BSE image of metal 22, Fe,Ni metal grain. This is the large Fe,Ni metal grain (white) in LEW 85311 and it demonstrates the thick alteration rim. 103
- Figure 4.3 BSE image of metal 22, magnified view of a section around the large Fe,Ni metal (white) and the alteration rim. Annotations show the three different textures observed. T1) finely laminated, heavily fractured ‘ordered’ material. T2) coarse, chaotic laminations with some fractures ‘disordered’ material. T3) extremely disordered material surrounded by a thin, fine grain rind of material (R). 104
- Figure 4.4 BSE image of Metal 22, a magnified view of a section around the large Fe,Ni metal grain (white) and the alteration rim surrounding it. Textures T1, T2 and T3 (including rind) are labelled. 104
- Figure 4.5 EDS map of metal 21. EDS map for S (left). EDS map for S overlain on a BSE image (right). Image demonstrates the S rich alteration rim surrounding the kamacite. 106
- Figure 4.6 Metal 22, showing S and Cl EDS maps overlain on BSE images. A) EDS maps of the entire large kamacite grain as shown in figure 4.2. B) EDS map of the magnified region shown in figure 4.3. C) EDS map of the magnified region shown in figure 4.4. 107
- Figure 4.7 Metal 22, EDS maps of Cl and S overlain on a BSE image of magnified alteration rim around the large kamacite grain. Labelled are the points of quantitative analysis, listed in table 4.2. 108
- Figure 4.8 Graphs illustrating the relationships between  $\text{Fe}_2\text{O}_3$  (wt.%) and the key elements investigated in metal 22. Data taken from table 4.2 and values given in wt.%. Labels correspond to position numbers in

- table 4.2. A) Graph of  $Fe_2O_3$  - NiO, B) Graph of  $Fe_eO_3$  - S, C) Graph of  $Fe_eO_3$  - Cl. 109
- Figure 4.9 EDS maps of Cl and S in metal 21 overlain on BSE images and accompanying Raman spectra. Spectrum A) Tochilinite, B) Tochilinite. 110
- Figure 4.10 EDS maps of Cl and S in metal 22 overlain on BSE images and accompanying Raman spectra. The yellow highlighted region represents the region in which Principle Component Mapping was undertaken. Spectrum A) Inconclusive, B) Goethite, C) Akaganeite, D) Tochilinite, E) Goethite, F) Tochilinite. 112
- Figure 4.11 Reflected light image of kamacite grain (metal 22) and the alteration rim with the results of a Principle Component Map (PCM) from the yellow highlighted region in figure 4.9 overlain. A = akaganeite. T = tochilinite. 113
- Figure 4.12 BSE image of metal 23 in LAP 02239. A) Overview of both Fe,Ni metal grains (white) and the conjoined alteration rims, B) Magnified image of the smaller metal grain (white) showing the two textures observed, C) Magnified image of the larger metal grain (white) showing the two textures observed. Textures T1 and T3 mimic those found in LEW 85311. 114
- Figure 4.13 EDS maps of the alteration rim surrounding the smaller kamacite grain. A) EDS maps of Cl and S overlain on a BSE image of the area. B) EDS map of Cl. C) EDS map of S. 116
- Figure 4.14 EDS maps of the alteration rim surrounding the larger kamacite grain. A) EDS maps of Cl and S overlain on a BSE image of the area. B) EDS map of Cl. C) EDS map of S. 117
- Figure 4.15 EDS maps of metal 23 overlain on BSE images and accompanying Raman spectra for selected areas (Highlighted). Spectrum A) Akaganeite, B) Inconclusive but potentially tochilinite, C) Akaganeite, D) Akaganeite, E) Akaganeite (weak spectrum) 119
- Figure 4.16 BSE image of metal 24, an Fe,Ni metal grain (white). The alteration rim in this sample displays a pitted region and a non-pitted region. The boundary between these textures is highlighted. 122
- Figure 4.17 BSE image of metal 25, an Fe,Ni metal grain (white). The alteration rim also appears pitted with the exception of a region of darker coloured material along the top edge. 123
- Figure 4.18 BSE image of metal 26, an Fe,Ni metal grain (white). The alteration rim demonstrates a pitted texture in the inner region and a non-pitted texture in the outer region. 123
- Figure 4.19 EDS maps of metal 24, showing A) EDS maps of S and Cl overlain on a BSE image. B) EDS map of Cl. C) EDS map of S. These maps show the slight elevation in the Cl concentration within the inner, pitted region of the alteration rim and the S-rich region within the outer, non-pitted area of the alteration rim. 125

- Figure 4.20 EDS maps of metal 25, showing A) EDS maps of S and Cl overlain on a BSE image. B) EDS map of Cl. C) EDS map of S. These maps show the enrichment in Cl within the dark region of material along the top edge of the alteration rim and the elevated S concentration around the very edge of the alteration rim. 126
- Figure 4.21 EDS maps of metal 26, showing A) EDS maps of S and Cl overlain on a BSE image. B) EDS map of Cl. C) EDS map of S. These maps show a slight increase in Cl within the bulk of the alteration rim and the patchy areas of elevated S around the periphery of the alteration rim. 127
- Figure 4.22 EDS maps of Cl and S overlain on BSE image of metal 24. Labelled are the points of quantitative analysis, shown in table 4.4 128
- Figure 4.23 Graphs illustrating the relationships between  $\text{Fe}_2\text{O}_3$  (wt.%) and the key elements investigated in metal 24. Data taken from Table 4.4. and values given in wt.%. Labels represent position numbers stated in table 4.4 A) Graph of  $\text{Fe}_2\text{O}_3$  - NiO. B) Graph of  $\text{Fe}_2\text{O}_3$  - S. Position numbers correspond to Figure 4.22 and Table 4.4. C) Graph of  $\text{Fe}_2\text{O}_3$  - Cl. 129
- Figure 4.24 EDS maps of metal 24 overlain on BSE image and accompanying Raman spectra for selected locations (highlighted). Spectrum A) Magnetite, B) Inconclusive, C) Magnetite. 131
- Figure 4.25 EDS maps of metal 25 overlain on a BSE image and accompanying Raman spectra for selected locations (highlighted). Spectrum A) Akaganeite, B Magnetite, C) Magnetite. 132
- Figure 4.26 Flow diagram showing the proposed alteration pathways of Fe,Ni metal both terrestrially and pre-terrestrially. 138

## Chapter 5

- Figure 5.1 BSE image taken from Brearley (2006), showing a corrosion rim interpreted as being composed of parent body, tochilinite/cronstedtite alteration products and which following this research may have been misinterpreted. 143
- Figure 5.2 Flow diagram summarising the alteration experienced around Fe,Ni metals in carbonaceous and ordinary chondrites. The blue arrow indicates what is proposed to occur should CM chondrites survive long enough for the reaction to go to completion. 144

## List of Equations

Equation 1. Minimum Detection Limits (Potts, 1992)

43

# Acknowledgements

There are many people I would like to thank for their help, support and guidance throughout this work.

Firstly, I must thank my supervisor Prof. Martin Lee whose guidance and encouragement were second to none throughout this project and I could not have asked for a better supervisor. This project would not have been possible without him.

I would also like to thank the other post-graduate researchers in Room 414A of the Gregory Building and the schools' technicians whose insights, support and general tomfoolery throughout the year were greatly appreciated; Sammy Griffin, Rory Porteous, Aine O'Brien, Octria Adi Prasojo, Tara McElhinney, Chris Holdsworth, Kelly James, Ellen MacDonald and Peter Chung. I should also like to thank my close friends outside of university particularly; Maia Stables, John Rothwell, George Elderfield, Jonathan Bell and Catriona McBride, who have managed to keep me suitably distracted over the weekends.

Finally, I must thank my parents, who over the last five years at the University of Glasgow have supported and encouraged me, answering phone calls at all hours of the day and night to hear my rants and raves.

## **Author's Declaration**

The work in this thesis summarises the findings from one year of independent research carried out at the University of Glasgow. This work was supervised by Professor Martin Lee and Dr. Lydia Hallis.

Cameron Floyd - 2019

# Chapter 1 Introduction

## 1.1 An Introduction to Meteorites

Meteorites are fragments of extra-terrestrial material which have broken off from asteroids, the Moon, Mars or other planetary bodies and eventually fall to Earth. These pieces of asteroids provide some of the best and most readily available insights into the composition of the early solar system. Consequently, these materials have been subject to a great deal of scientific investigation. However, there is a lack of information regarding the evolution and development of terrestrial weathering products within meteorites, particularly on the micron-scale. This knowledge gap is what this research sets out to change.

Meteorites can be divided according to their composition and then classified into an array of groups and sub-groups. The three primary compositional groups as set out in Figure 1.1 are: Irons, Stony Irons and Stony meteorites. Stony meteorites represent the majority of meteorites on Earth today, accounting for ~88.4 % of all meteorites collected (The Meteoritical Society, 2017). Chondrites are a sub-group of the Stony meteorite group, and account for ~84.3 % of all samples (The Meteoritical Society, 2017). The chondrites are then divided into 5 sub-groups, two of which, the ordinary chondrites (OC's) and carbonaceous chondrites (CC's), are the focus of this research.

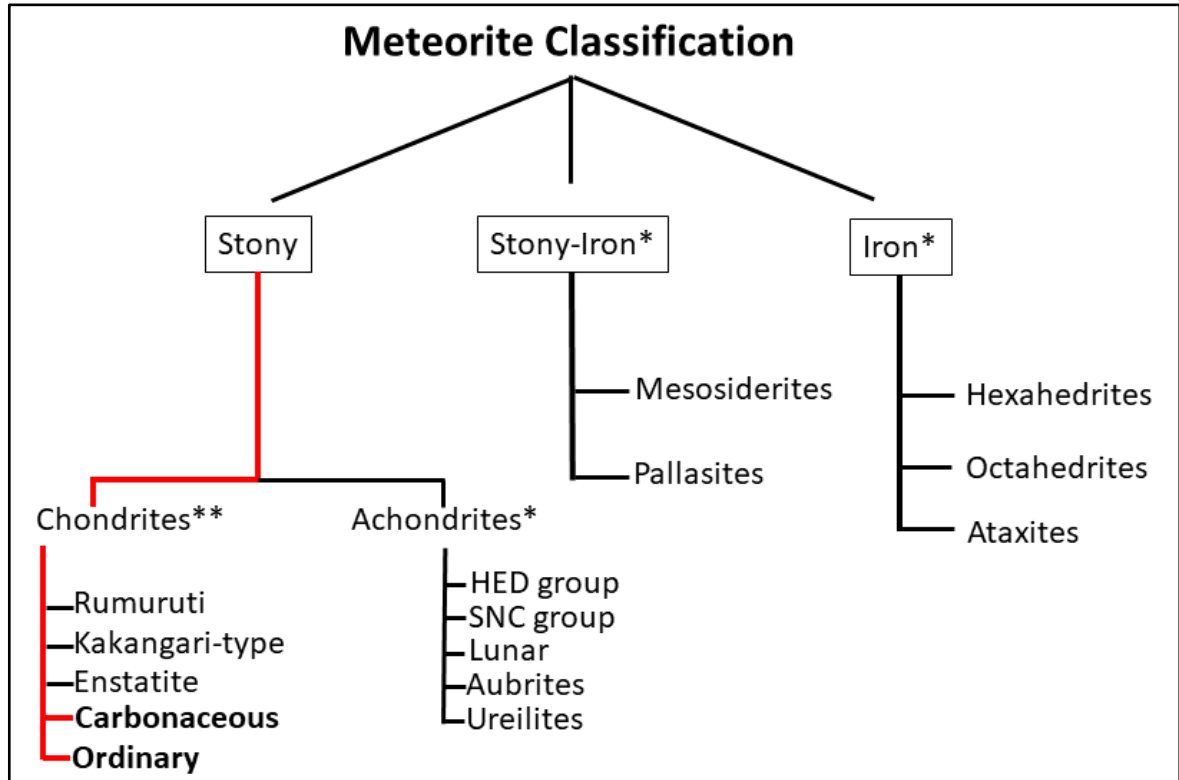


**Figure 1.1** Simplified chart of the meteorite classification system (many sub-groups exist beyond this). Those highlighted in red will be the focus of this research. \*denotes differentiated meteorites, \*\*denotes undifferentiated meteorites.

## 1.2 Ordinary Chondrites

Ordinary chondrites make up the largest proportion of all meteorites collected (~76 %) (The Meteoritical Society, 2017). This class of meteorite is characterised by their spherical inclusions called chondrules from which they derive their name.

### 1.2.1 Origin and Formation

Ordinary chondrites are thought to originate from Stony (S-Type) asteroids, forming *in situ* within the main asteroid belt between Jupiter and Mars (Anders, 1964; Van Schmus, 1969a; Chapman, 1996; Lauretta and Killgore, 2005; Nakamura et al., 2011; Alexander et al., 2012). Asteroids found within the main asteroid belt are composed of early solar material and condensates, which are thought to have been collected together by the migration of the giant planets Jupiter and Saturn in what has become known as the Grand Tack. It is thought that initially there were two separate populations of asteroids, one inside the

orbits of the giant planets (volatile-poor and dry, S-type asteroids) and one lying beyond the orbit of the giant planets (more primitive and water-rich, C-type asteroids, which will be discussed in section 1.3) (Walsh et al., 2012). The Grand Tack model suggests how these populations mixed and formed what is seen today as the main asteroid belt. The model suggests that initially Jupiter migrated inwards scattering some of the inner disk of S-type material into more distant orbits. The ‘Tack’ then sees the outward migration of Jupiter and Saturn. During the outward migration the giant planets first encounter the just scattered S-type material which is subsequently scattered back into a stable orbit within the asteroid belt. With continued outward migration the giants encounter C-type material from the outer disk which is then also scattered inwards onto stable orbits in the asteroid belt. The result is an asteroid belt composed of material from both parent populations but, with the inner region dominated by S-type material and outer region dominated by C-type material (figure 1.2) (Walsh et al., 2012).

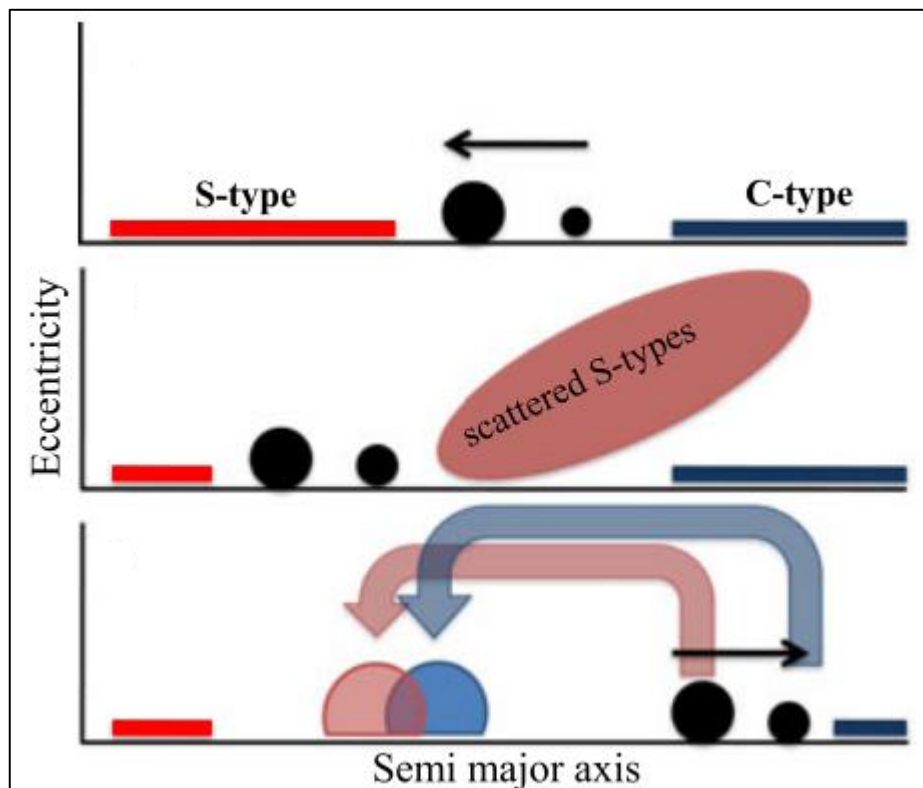


**Figure 1.2** Schematic illustration of the Grand Tack model taken from Walsh et al., (2012). Large black circle is Jupiter and small black circle is Saturn. It demonstrates the migration of the giant planets inwards initially and then outwards causing scattering among the two parent populations and the mixing of these populations in the main asteroid belt.

Ordinary chondrites from S-type material within the inner region of the main asteroid belt originate from two specific zones; the 1:3 Kirkwood gap and the v<sub>6</sub> resonance (Britt et al., 2014). These two zones are calculated to be the most advantageous for producing Earth-crossing orbits and this is likely why ordinary chondrites dominate the meteoritic material found on Earth today (Gaffey and Gilbert, 1998; Britt et al., 2014).

During the time within their parent bodies ordinary chondrites have been subjected to thermal metamorphism, a result of decaying short-lived radionuclides such as <sup>26</sup>Al (Krot et al., 2006). The extent of thermal metamorphism varies between parent bodies and over time produces different classifications of ordinary chondrite (Miyamoto et al., 1981). Importantly for this project ordinary chondrites are not thought to have experienced significant aqueous alteration whilst part of their parent bodies and therefore any alteration which is observed should be entirely a result of the terrestrial environment.

### 1.2.2 Classification

Ordinary chondrites are classified as either H, L or LL according to their metal content. H-type ordinary chondrites have the highest metal content ~10 vol.%, L-type ordinary chondrites have a low metal content ~5 vol.% and LL-type ordinary chondrites have both a low total iron and a low metal content ~2 vol.% (Lauretta and Killgore, 2005).

Once classified compositionally as H, L or LL, ordinary chondrites are assigned a petrological classification between 3 and 6 according to the amount of thermal metamorphism they have experienced. The amount of thermal metamorphism experienced is assessed using microscopy and relies on the extent of grain growth and recrystallisation (Figure 1.3). Classification as group 3 indicates the most primitive meteorites with little to no thermal alteration. In petrological group 3 well defined chondrules sit within a fine-grained, black matrix. Moving through groups 4 - 6 each successive group represents an increase in thermal alteration. Group 6 ordinary chondrites are the most metamorphosed and have experienced extensive recrystallisation. Samples of type 6 typically have no chondrules or original matrix remaining (Lauretta and Killgore, 2005). Groups

1 and 2 represent increasing hydrous alteration. This is not observed in ordinary chondrites as they lack heavily hydrated end members (Weisberg et al., 2006).

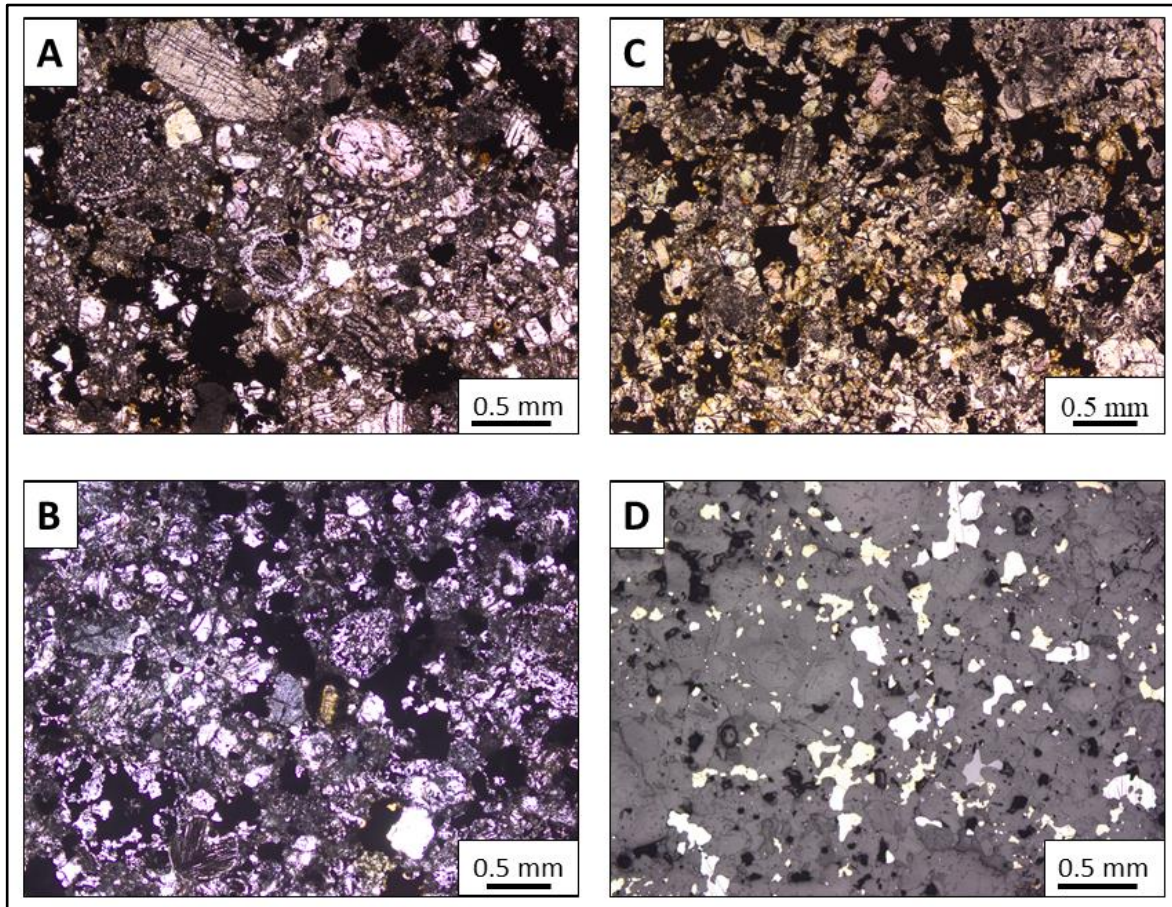


**Figure 1.3.** Images illustrating the changes observed with increasing thermal alteration in ordinary chondrites. A) Image taken in plane polarised light (PPL) of H4 ordinary chondrite Beaver Creek (BM 73646) taken at 5x magnification. Well defined chondrules can be seen throughout as can some matrix material. B) PPL image of H5 ordinary chondrite Allegan (BM 1920, 281) taken at 4x magnification. Chondrules are becoming less distinct and grain size is increasing. C) Image taken in PPL of H6 ordinary chondrite Kernouye (BM 43400) taken at 4x magnification. No chondrules are visible and there is a large grain size. D) Image taken in reflected light (RL) of H6 ordinary chondrite Kernouye (BM 43400) at 5x magnification demonstrating the presence and distribution of metal grains (white) in an H-chondrite.

### 1.2.3 Composition

The most abundant minerals within ordinary chondrites are silicates, specifically olivine and low Ca-pyroxene which together make up around 70-80 % of ordinary chondrites (Van Schmus, 1969b; Norton and Chitwood, 2008; Vernazza et al., 2015). The remainder is made up of metals and matrix material. Table 1.1 shows the average chemical analysis of Antarctic H and L chondrites (Jarosewich, 1990). The abundance of metal depends on the class of ordinary chondrite (H, L or LL). There are three Fe-rich minerals within ordinary chondrites, two metal alloys: kamacite (4-7 wt.% Ni) and taenite (> 20 wt.% Ni) (Van Schmus, 1969b;

Buchwald and Clarke, 1989) and troilite (FeS) an Fe-sulphide which is present in lower abundances. The Fe,Ni metals are thought to have formed from molten or semi-molten droplets of material during heating events within the early solar nebula (Shu et al., 2001; Weisberg et al., 2006).

**Table 1.1** Average results of typical chemical analysis conducted on Antarctic H and L chondrites, taken from Jarosewich, (1990).  $Fe_{(m)}$  is Fe-Metal. The oxidation of  $Fe_{(m)}$  can produce the oxidation product  $Fe_2O_3$ . In this table all  $Fe_2O_3$  was converted to  $Fe_{(m)}$  and normalised to 100% before the composition was calculated.  $FeO$  was calculated by subtracting  $Fe_{(m)}$  and FeS from  $Fe_{(total)}$ .

	H-Chondrite (wt. %)	L-Chondrite (wt. %)
$SiO_2$	36.90	39.64
$TiO_2$	0.12	0.13
$Al_2O_3$	2.20	2.29
$CrO_3$	0.49	0.54
$FeO$	10.86	15.88
$MnO$	0.31	0.31
$MgO$	23.19	24.72
$CaO$	1.75	1.85
$Na_2O$	0.88	0.88
$K_2O$	0.1	0.10
$P_2O_5$	0.25	0.22
$H_2O+$	1.09	0.51
$H_2O-$	0.41	0.27
$Fe_{(m)}$	14.35	5.59
Ni	1.75	1.20
Co	0.08	0.06
FeS	4.90	5.29
C	0.16	0.12
Total	99.77	99.59
$Fe_{(total)}$	25.63	21.30

### 1.3 Carbonaceous Chondrites

Carbonaceous chondrites are a very diverse group of chondrites making up ~3.5 % of all meteorite samples on Earth (Lauretta and Killgore, 2005; The Meteoritical Society, 2017). Despite the limited number of samples, they are of significant scientific interest with diverse compositions and two upcoming sample return missions from asteroids believed to be of carbonaceous affinity (Website 1.1; Okada et al., 2017). These missions, the United States of America's National Aeronautics and Space Administration (NASA) OSIRIS-Rex mission, which will travel to and collect samples from Bennu (asteroid 101955), and Japan's Japan Aerospace Exploration Agency (JAXA) Hayabusa 2 mission to asteroid (162173)

Ryugu (1999 JU3) (Watanabe et al., 2017; Lauretta et al., 2017). These missions are due to return samples to Earth in 2023 and 2020, respectively (Tachibana et al., 2014; Lauretta et al., 2017).

### 1.3.1 Origin and Formation

Carbonaceous chondrites originate from water-rich C-type asteroids (Vernazza et al., 2015). These asteroids are believed to have formed either between the giant planets or in the trans-Neptunian region during early planetary formation in the young solar nebular (Alexander et al., 2012; Watanabe et al., 2019). Following scattering during the Grand Tack (discussed in section 1.2.1), C-type material was projected from its original outer solar system region of formation in to stable orbits in the outer part of the main asteroid belt alongside scattered S-type material. In the outer regions of the main asteroid belt C-type material occasionally falls into Earth crossing orbits and thus eventually impacts Earth (Walsh et al., 2012). This class of chondrites although small is scientifically very valuable due to the presence of water-bearing phases and evidence of aqueous alteration which they experienced whilst on their parent bodies (Bunch and Chang, 1980; Browning and Bourcier, 1996; Palmer and Lauretta, 2011).

### 1.3.2 Composition and Classification

Carbonaceous chondrites can be divided into 8 groups: CI (Ivuna-like), CM (Mighei-like), CO (Ornans-like), CV (Vigarano-like), CR (Renazzo-like), CH (ALH85085-like), CB (Bencubbin-like) and CK (Karoonda-like). This research will be investigating CM carbonaceous chondrites, so only they will be discussed in further detail.

The CM chondrites fall into petrological groups: 2 and 3 (having hydrated end members) and are distinguished by small chondrules which make up around 30 vol. %, refractory inclusions ~0.3 mm in size and an abundant fine-grained matrix ~70 vol. % (Lauretta and Killgore, 2005; Krot et al., 2007; The Meteoritical Society, 2017). CM chondrites have a very primitive bulk composition and were not subjected to high temperatures. They contain little metal of any kind and are instead dominated by hydrous silicate minerals (giving them an indigenous water content of 9 % by weight), anhydrous silicate minerals, organic compounds and a

relatively high noble gas concentration (Bunch and Chang, 1980; Lauretta and Killgore, 2005; Rubin et al., 2007; Scott and Krot, 2013). Table 1.2 displays the results of chemical analysis of a CM chondrite. Palmer and Lauretta (2011) suggest that the distribution and associations of these hydrated phases could provide key insights into water in the early solar system.

The presence of indigenous fluids within CM parent bodies is believed to lead to major pre-terrestrial, aqueous alteration. Significantly this causes the conversion of Fe,Ni metal (kamacite) into tochilinite by the action of S-bearing fluids (Mackinnon and Zolensky, 1984; Palmer and Lauretta, 2011). Tochilinite is characteristic of CM chondrites and is widely discussed in the literature as evidence of parent body alteration (Palmer and Lauretta, 2011). Rubin et al. (2007) and Howard et al. (2015) describe two separate alteration scales of carbonaceous alteration, both of which are used in the literature. Rubin et al. (2007) proposed a downward scale ranging from 2.6 representing moderately altered material to 2.00 representing the heavily altered material, material between 2.60 and 3.00 is hypothetical and has never been observed. Howard et al. (2015) developed a scale between 3.00 and 1.00 with type 3.00 having the lowest phyllosilicate fraction (<0.05) to type 1.00 having the highest phyllosilicate fraction (>0.95).

**Table 1.2** Average results of chemical analysis conducted on CM2 chondrite falls, taken from Jarosewich, (1990). Fe<sub>(m)</sub> is Fe-Metal. The oxidation of Fe<sub>(m)</sub> can produce the oxidation product Fe<sub>2</sub>O<sub>3</sub>. In this table all Fe<sub>2</sub>O<sub>3</sub> was converted to Fe<sub>(m)</sub> and normalised to 100% before the composition was calculated. FeO was calculated by subtracting Fe<sub>(m)</sub> and FeS from Fe<sub>(total)</sub>.

CM2 Chondrite (wt. %)	
SiO <sub>2</sub>	28.97
TiO <sub>2</sub>	0.13
Al <sub>2</sub> O <sub>3</sub>	2.17
Cr <sub>2</sub> O <sub>3</sub>	0.43
FeO	22.14
MnO	0.25
MgO	19.88
CaO	1.89
Na <sub>2</sub> O	0.43
K <sub>2</sub> O	0.06
P <sub>2</sub> O <sub>5</sub>	0.24
H <sub>2</sub> O+	8.73
H <sub>2</sub> O-	1.67
Fe <sub>(m)</sub>	0.14
Ni	0.00
Co	0.00
FeS	6.76
C	1.82
NiO	1.71
CoO	0.08
SO <sub>3</sub>	1.59
CO <sub>2</sub>	0.78
Total	99.82
Fe <sub>(total)</sub>	21.64

## **1.4 Age of Meteorites**

### **1.4.1 Formation Age**

Meteorites found on Earth have extremely ancient formation ages. These ages have been calculated using  $^{207}\text{Pb}/^{206}\text{Pb}$  radio-isotope dating and the most recent age calculated is  $\sim 4.568 \times 10^9$  years (Bouvier and Wadhwa, 2010). Bouvier and Wadhwa's age was calculated from a calcium-aluminium-rich inclusion from Northwest Africa 2364, a CV3-group chondritic meteorite. Comparing this calculated age to that calculated for the age of the solar system suggests that meteorites represent some of the oldest solid material to have formed in the solar system, forming in the first few million years after its creation. Asteroids and meteorites therefore provide vital insights into the processes occurring at this time.

### **1.4.2 Cosmogenic Age**

Cosmogenic exposure age (CRE) is the length of space exposure a meteorite has, having broken off into approximately meter-sized pieces, or smaller, from its parent body (Eugster, 2003). CRE age is most commonly determined using the concentration and production rate of stable noble gas isotopes:  $^3\text{He}$ ,  $^{21}\text{Ne}$ ,  $^{38}\text{Ar}$ ,  $^{83}\text{Kr}$  and  $^{126}\text{Xe}$  (Eugster, 2003). Analysis shows H-chondrites typically have CRE ages of 7 Ma but data also suggests clusters (representing significant asteroid fragmentation events) at 24 and 33 Ma (Eugster, 2003). L-chondrites have a wider spread of CRE ages, with clusters at 6, 15, 27 and 39 Ma and carbonaceous CM chondrites were found to have the youngest CRE ages with the majority between 0.05 and 2 Ma (Eugster, 2003).

### **1.4.3 Terrestrial Age**

In addition to calculating the formation age of meteorites, it is also important to try and determine their terrestrial age as Earth residency time can help our understanding of the impacts of the terrestrial environment on samples.

Cosmic-ray-produced radionuclides are used to determine the terrestrial ages of meteoritic material (Jull, 2001). In space meteorites are bombarded by cosmic rays which produce an accumulation of stable and unstable cosmogenic

nuclides with varying half-lives. After falling to Earth meteorites becomes shielded from these cosmogenic rays and the production and accumulation of nuclides stops. The terrestrial age can then be calculated using the concentration of these decayed cosmogenic radio-nuclides (Nishiizumi et al., 1989). It was not until the advent of accelerator mass spectroscopy (AMS) that this technique began to become more useful, as samples could be far smaller and the counting process was much quicker (Jull, 2001). Radio-nuclides which are of interest for terrestrial aging include  $^{39}\text{Ar}$ ,  $^{14}\text{C}$ ,  $^{41}\text{Ca}$ ,  $^{59}\text{Ni}$ ,  $^{81}\text{Kr}$ ,  $^{36}\text{Cl}$ ,  $^{26}\text{Al}$ ,  $^{60}\text{Fe}$ ,  $^{10}\text{Be}$  and  $^{53}\text{Mn}$  (Jull, 2001). Research using  $^{14}\text{C}$  and  $^{36}\text{Cl}$  has shown that the terrestrial ages of most hot desert meteorites is less than 50ky (figure 1.4) (Jull, 2001). Comparatively, samples found in Antarctica (a cold desert environment) have much longer terrestrial ages (Figure 1.5). Scherer et al. (1997) described an Antarctic H-chondrite (ALHA 88019) with a terrestrial age of  $2 \pm 0.4$  Ma. The stark difference in terrestrial age between these two environments illustrates the influence terrestrial environment can have on meteorite survivability.

During early work on meteorites it was thought that the degree of terrestrial alteration could be used as a comprehensive indicator for terrestrial age (Jull, 2001). However, work by Buchwald (1975) and Buchwald & Clarke (1989), demonstrated that meteorite class/composition, Cl availability and the environment of landing have a far greater influence on the degree of alteration and sample survivability. This is highlighted by the differences in ages observed between environments, as shown by Jull (2001) in Figures 1.4 and 1.5. In this case the lower terrestrial ages observed in desert samples suggests faster destruction and thus greater weathering of samples in this environment. The level of alteration a meteorite has experienced is therefore not a proxy for terrestrial age.

Most terrestrial age studies have used ordinary chondrites. This is not only because ordinary chondrites are more common, but also because carbonaceous chondrites don't typically survive over long timescales and are quickly destroyed. This is a result of their fragile composition, a consequence of a fine-grained matrix which increases the available surface area for reaction, their enrichment in volatile elements and abundant organic compounds (Bland et al., 2006).

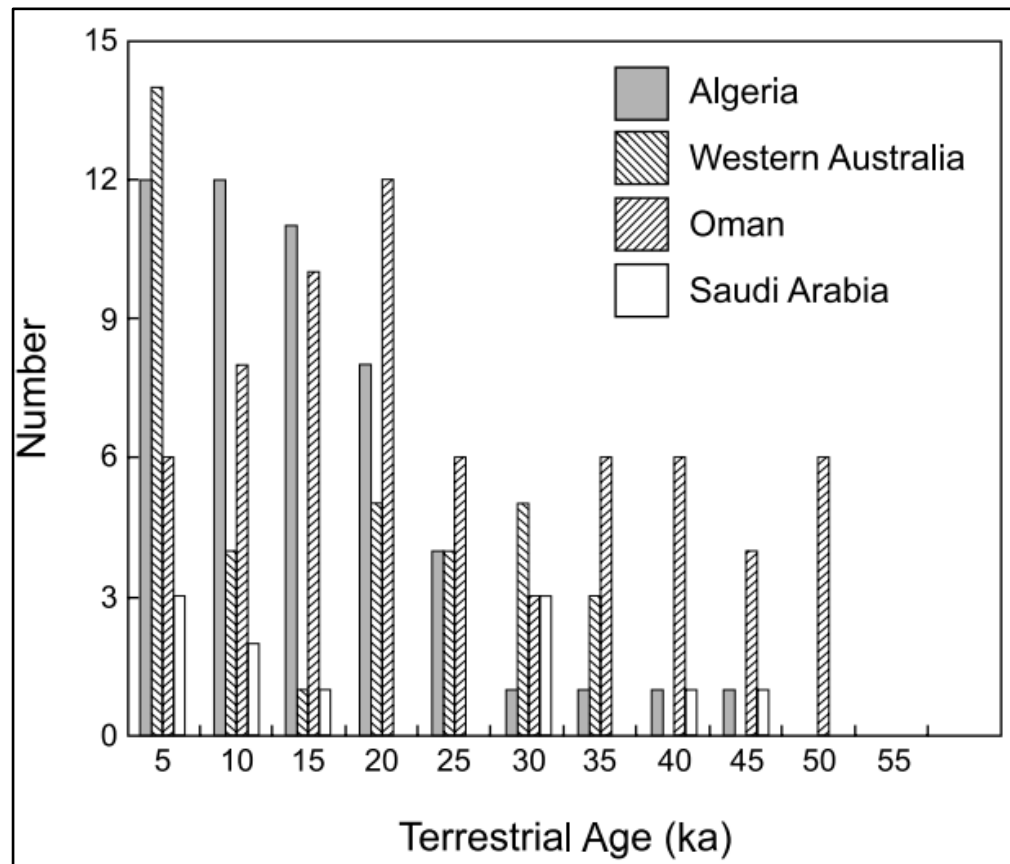


**Figure 1.4** Terrestrial age distribution of meteorites from hot desert environments and Western Australia (Jull, 2011).

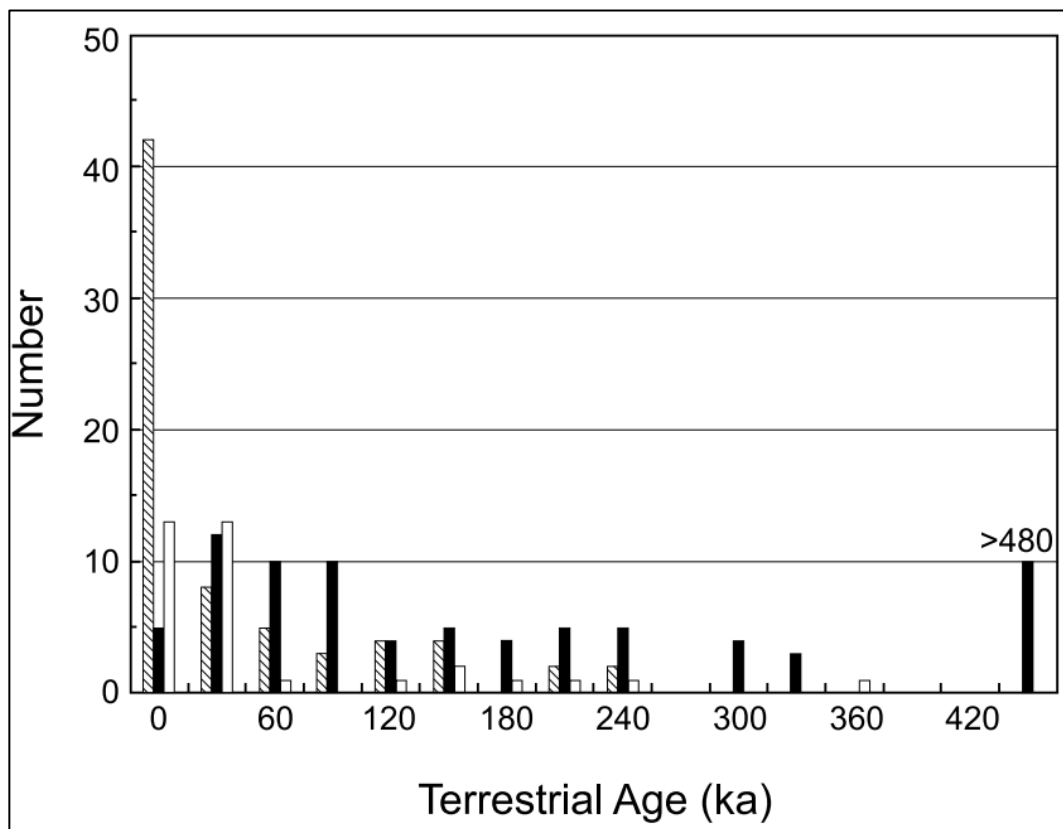


**Figure 1.5** Terrestrial age distribution from cold desert environments (Antarctica): Yamato site (slanted bars), Allan Hills (black bars) and Elephant Moraine (white bars) (Jull, 2001).

## 1.5 Sources of Meteorites on Earth

Most of the meteorites found on Earth today have been collected from desert environments where their dark (often black) colour is easily distinguished from the bleak, white/brown surrounding landscape (Figure 1.6).

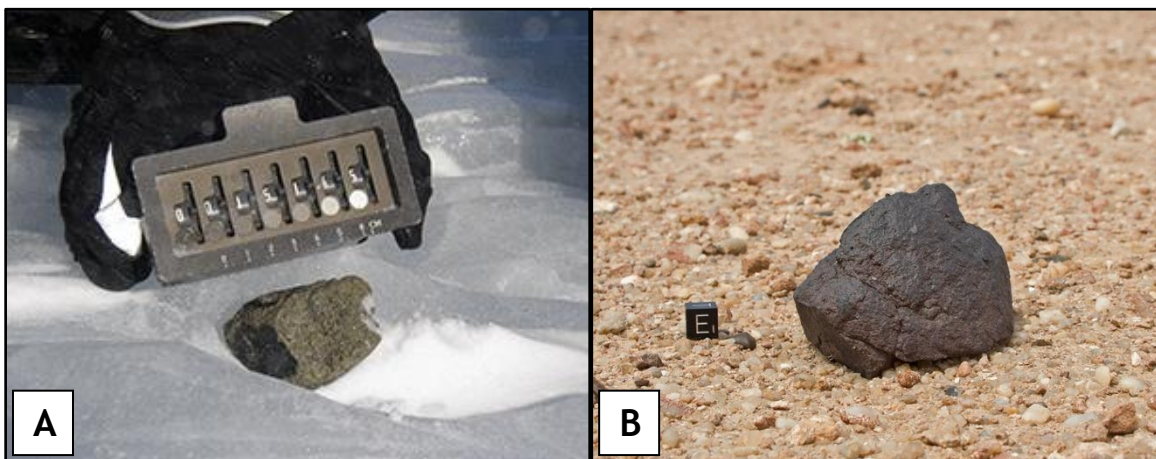


**Figure 1.6** A) Meteorite found in Antarctica in 2004. The dark colour is easily distinguished from the white Antarctic surface (Geiger, 2018). B) Meteorite found in Western Sahara in 2013. The dark colour of the meteorite stands out against the pale brown sandy soil (Website 1.2).

Antarctica, a cold desert, has proved to be the best environment for meteorite discovery and collection. To date 43,482 meteorites have been recovered from the Antarctic continent, representing 63.70 % of the total meteorites found on Earth (The Meteoritical Society, 2017). The reasons behind Antarctica's success as a source of meteorites are numerous. Firstly, falls on the ice fields can be transported over time, either within or on top of the ice, to ablation zones typically near mountainous regions. Here they can become concentrated by the melting ice. Secondly, Antarctica's typically white backdrop and complete lack of vegetation makes spotting meteorites far easier than in other regions. Finally, the cold, dry climate on the Antarctic continent slows the breakdown of material, preserving samples for long periods of time (Bischoff, 2001; Jull, 2001).

Hot desert environments such as the Sahara and the Arabian Peninsula, and semi-arid environments such as Australia, have also proven to be good sources of meteoritic material. These regions have a lower yield than Antarctica accounting for ~25 % of collected meteorites (Gattacceca et al., 2011). However, the higher temperatures in these environments mean meteorite breakdown is faster and samples don't survive for as long as in cold deserts (Jull, 2001). The shifting sands

of hot deserts can also result in sample burial and the lack of a transport mechanism to concentrate samples means that samples are often geographically widespread.

### 1.5.1 Find or fall

Meteorites are also categorised as ‘finds’ or ‘falls’. ‘Fall’ meteorites are those which are seen falling to Earth and then collected. Consequently, they have very short terrestrial exposure time and therefore little opportunity to be contaminated by the terrestrial environment (French et al., 2010). Unfortunately, meteorite falls are exceptionally rare. To be observed falls typically need to be in close proximity to a built-up area where there is the greatest chance they will be seen. It is for this reason that no falls exist from Antarctica (The Meteoritical Society, 2017).

Most meteorites are collected as ‘finds’ and therefore are not seen falling to Earth. They are found some time after and have an unknown terrestrial age until it is determined using the methods discussed in section 1.4.2. Find meteorites make up the majority of all meteorites collected and thus, the majority of meteorites collected have been exposed to terrestrial conditions for a period of time. Understanding the effects of these terrestrial conditions on meteorite samples and how this varies with environment is therefore of the greatest importance. This is especially true for fragile and scientifically important CM carbonaceous chondrites especially with the upcoming samples return missions.

## 1.6 Previous Work on Weathering

### 1.6.1 Classification

There has been limited previous work examining the effects of the terrestrial environment on meteorites through processes termed weathering and the alterations this causes. Most work to date has focused on classifying the extent of terrestrial weathering. This has led to the development of two classification systems. The first, and most established, is that used by the Meteorite Working

Group at the NASA Johnson Space Centre in Houston. It involves a simplistic visual inspection at hand specimen scale and subsequent classification as either A, B or C. Each of these categories corresponds to varying levels of rusting which can be observed on the samples surface: A- indicates minor rusting, B- indicates moderate rusting and C- indicates severe rusting (Wlotzka, 1993). Evaporite minerals have been observed on approximately 5 % of all Antarctic meteorites (Losiak and Velbel, 2011). To provide reference to this in the weathering classification Velbel (1988) added an “e”, which follows the weathering category and indicates if evaporite minerals are present and visible to the unaided eye.

The second classification method was initially proposed by Jull et al., (1991) and was adapted by Wlotzka, (1993) and Al-Kathiri et al., (2005). This scale defines the weathering effects observed in polished thin sections using microscopy (Wlotzka, 1993; Bland et al., 2006). The scale ranges from W0 to W6 with the grading determined by the levels of oxidation experienced (see table 1.3).

**Table 1.3** Weathering scale developed for polished sections based on the amount of oxidation (Wlotzka, 1993).

Weathering Grade	Description
<b>W0</b>	No visible oxidation of metal or sulphide
<b>W1</b>	Minor oxide rims around metal and troilite; minor oxide veins
<b>W2</b>	Moderate oxidation of metal, about 20-60 % being affected
<b>W3</b>	Heavy oxidation of metal and troilite, about 60-95 % being replaced
<b>W4</b>	Complete (>95 %) oxidation of metal and troilite, but no alteration of silicates
<b>W5</b>	Beginning alteration of mafic silicates, mainly along cracks
<b>W6</b>	Massive replacement of silicates by clay minerals and oxides

Research focusing on aspects of terrestrial weathering and alteration not relating to classification has been sparse. This is especially true with regards to the precise characterisation of weathering products and understanding of their development. Given the highly metallic nature of ordinary chondrites it is perhaps unsurprising that their Fe-rich phases (Fe,Ni and FeS) are the first to show the effects of terrestrial alteration. Fe,Ni metals are the focus of this research and these metals are altered via oxidation to produce Fe-oxide alteration products around metal grains (Velbel and Gooding, 1990; Bland et al., 2006). Gooding,

(1986) termed this form of weathering in meteorites as ‘metallic rusting’. There has been some limited work examining the products of terrestrial weathering around Fe,Ni metals in ordinary chondrites conducted by Buchwald and Clarke (1989) and Bland et al., (2006). However, there has been almost no literature examining the impacts and products of terrestrial weathering around Fe,Ni metal in CM chondrites (Bland et al., 2006).

### 1.6.2 Oxidation

Oxidation in ordinary chondrites involves reaction of the Fe-rich minerals present (kamacite, taenite and troilite) with the terrestrial atmosphere and liquid water to produce Fe-oxides. Oxidation products form initially around kamacite as it is the most susceptible to alteration, this is followed by taenite and finally troilite which is the least susceptible of the Fe-rich minerals to oxidation (Gooding, 1986). Following the alteration of the Fe-rich minerals the silicates begin to alter (Wlotzka, 1993). This project will be investigating the oxidation of the Fe,Ni metals so only they will be discussed further.

The oxidation Fe,Ni metal produces an array of oxides, hydroxides and oxyhydroxides. These have been identified in previous work and are outlined in Table 1.4 which summarises the main oxidation products which are reported in the literature as meteoritical ‘metallic rust’ (Velbel, 2014). Figure 1.7 also demonstrates the inter-relatedness of some of these products and how they can transform into each other.

**Table 1.4** The Fe-rich oxidation products which have been reported in the literature to form ‘metallic rust’ found around the Fe,Ni metal grains within ordinary chondrites (modified from Velbel, (2014)).

Mineral Name	Formula	References
Goethite	$\alpha\text{-Fe}^{3+}\text{OOH}$	Gooding, 1982; Buchwald and Clarke, 1989; Bland et al., 1996
Lepidocrocite	$\gamma\text{-Fe}^{3+}\text{OOH}$	Velbel et al., 1991; Bland et al., 1996
Akaganeite	$\beta\text{-Fe}^{3+}\text{O(OH, Cl)}$	Buchwald and Clarke, 1989; Bland et al., 1996
Magnetite	$\text{Fe}^{3+}_2\text{Fe}^{2+}\text{OH}_4$	Bland et al., 1996, 2006
Maghemite	$\gamma\text{-Fe}^{3+}_2\text{O}_3$	Bland et al., 1996

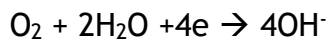
Buchwald and Clarke (1989) found that the corrosion of Fe,Ni metal in ordinary chondrites initially involves the production of the Cl-bearing mineral akaganeite via an electrochemical reaction. The Cl required for forming this mineral is believed to be carried inland as an aerosol or gas from sea spray and

volcanic exhalations (Buchwald and Clarke, 1989). This reaction takes place around kamacite and taenite grains with fractures through the meteorite facilitating the transportation of O<sub>2</sub> and electrolytes to the metal grain surface where they produce a chemical potential (Buchwald and Clarke, 1989). Buchwald and Clarke, (1989) described the complete initial reaction to produce akaganeite using conventional half reactions:

Metal (Fe<sup>0</sup>) is oxidised at the anode (surface where Fe<sup>0</sup> goes into solution):

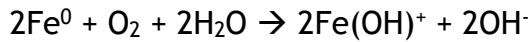


O<sub>2</sub> reduced at the cathode (site of akaganeite precipitation):

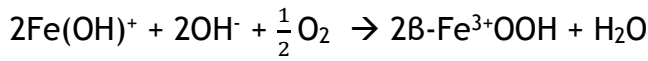


(alternatively) H is reduced at the cathode: 2H<sup>+</sup> + 2e → H<sub>2</sub>

Combining the first two equations:



This follows under oxidising conditions by the formation of akaganeite:



In the Antarctic environment there is almost no liquid water and so it is suggested that these reactions can take place without it. However, due to the low coefficients of diffusion in ice and oxides this reaction must take place over a much longer time period (Buchwald and Clarke, 1989).

With the exception of the work conducted by Buchwald and Clarke (1989), who have come closest to a detailed characterisation and analysis of the terrestrial alteration products, most of the existing literature has focused on broader scale analysis. This includes determining the total extent of oxidation products in a sample using Mossbauer spectroscopy (a whole rock technique) and comparing this to the terrestrial age and find environment of samples (Burns et al., 1995; Bland, 2006).

### 1.6.3 The Importance of Akaganeite

Akaganeite is described by Buchwald and Clarke (1989) as being key to the development of oxidation products around Fe,Ni meteoritic metals. Akaganeite's importance derives from its  $\text{Cl}^-$  bearing nature and small crystal size (which improves the minerals water absorption ability). The Cl is present within akageneite's tunnel sites and maintains a charge balance at the reaction surface and serves to de-passivate Fe and initiate corrosion, whilst the increase in water capacity allows for a reservoir of corrosion promoting fluid to build up at the reaction surface and promote further corrosion (Buchwald and Clarke, 1989).

The  $\text{Cl}^-$  found in the akaganéite is thought to derive from the terrestrial environment. It is currently thought that it is carried across the land as an aerosol or gas from sea spray and volcanic exhalations where it is then incorporated into the snow, ice or sand (Buchwald and Clarke, 1989).

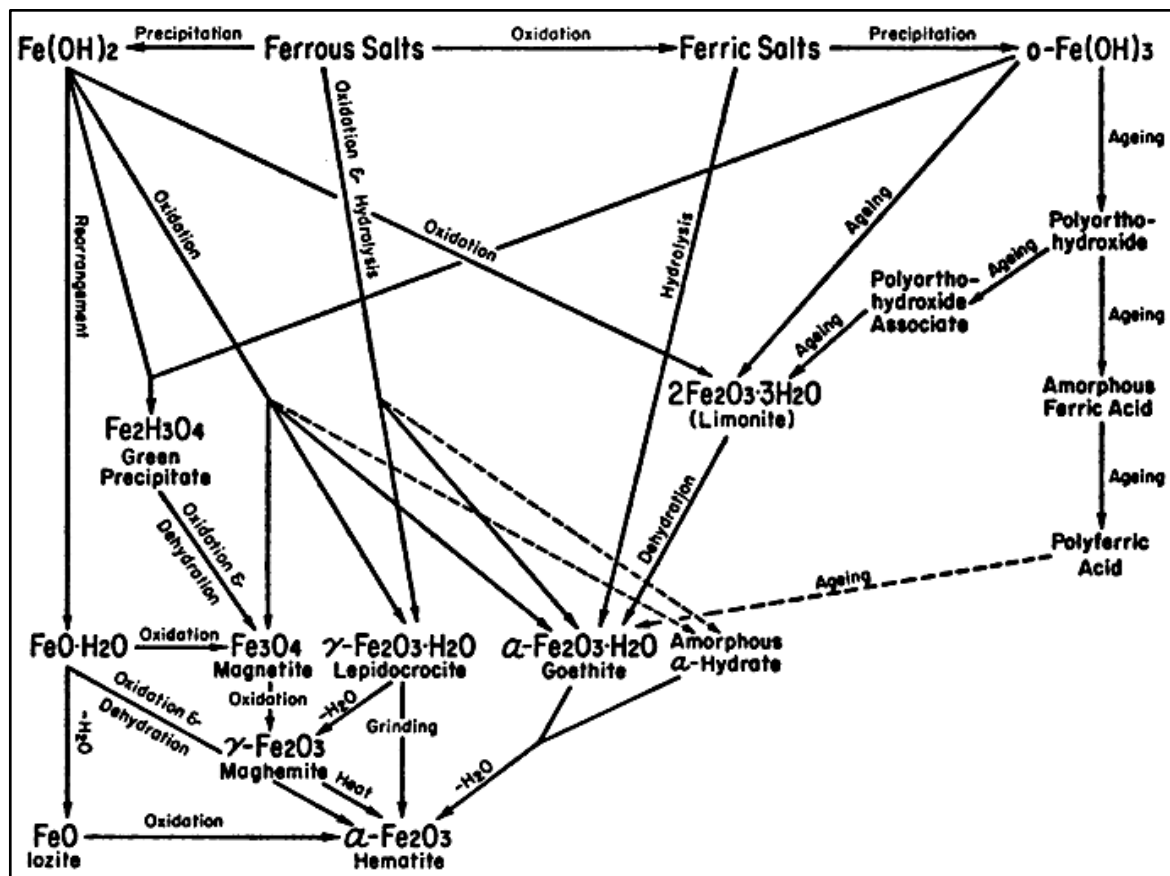


**Figure 1.7** A diagram showing the pathways and inter-relatedness of iron-oxides and their hydrates. (from Buddhue, 1957).

### 1.6.4 Museum Weathering

In addition to all the weathering mechanisms mentioned previously, museum weathering is also discussed, albeit very briefly, in the literature.

Museum weathering is the process whereby collected samples continue to develop alteration products after curation (Buchwald and Clarke, 1989; Velbel, 2014). Buchwald and Clarke (1989) suggest that akaganeite is, once again key. They suggest it resides in and across the interfaces of uncorroded metals and Fe-oxides. When stored in a museum, moisture from the natural humidity of the storage environment slowly reinitiates active corrosion which continues unmonitored. They go on to suggest flushing the Cl<sup>-</sup> from the reaction surface and storage in a low oxygen, low humidity environment could be a measure used to protect against this. By improving our understanding of the terrestrial alteration product development, we could also simultaneously improve our understanding of this ‘museum weathering’ and how it progresses in samples.

## 1.7 Aims of This Project

This project aims to characterise the terrestrial alteration products of Fe,Ni metal in ordinary and carbonaceous chondrites, utilising high resolution chemical and mineralogical analysis techniques for the first time. To date, the techniques used to investigate terrestrial alteration have typically been used separately. Mineralogy has been investigated by bulk Mossbauser spectroscopy but with no chemical analysis (Bland et al., 1998). Similarly, SEM analysis has been used to investigate chemistry and petrography but without mineralogical analysis (Lee and Bland, 2004). A study of the chemistry and mineralogy of terrestrial weathering and alteration has never been undertaken and consequently there is a lack of understanding regarding alteration product development. This project aims to collect mineralogical, chemical and petrographical data at a high spatial resolution to develop a complete understanding of the terrestrial weathering occurring around Fe,Ni metals.

Ordinary chondrites from three climatic regions and whose alteration should be solely terrestrial will be analysed initially. This will build a detailed understanding of the alteration products which develop in the terrestrial environment and how they vary between three different terrestrial climates. These findings will then be applied to CM chondrites from two climatic regions, and that should have alteration products which are both terrestrial and pre-terrestrial in origin. This will allow investigation into the not previously studied interaction between terrestrial weathering products and the existing parent body

alteration products (typically seen as tochilinite). This work will also help develop a better understanding of how and why weathering continues once samples are curated, a vital area of meteorite weathering highlighted by Lee and Bland (2004) and which has been severely neglected in the literature.

Understanding the effects of terrestrial alteration on parent body alteration both, pre- and post-curation is crucial for the accurate interpretation of the samples being returned by the OSIRIS-Rex and Hayabusa 2 sample return missions. Without the ability to accurately distinguish between what is parent-body alteration and what is terrestrial alteration these missions could be of little scientific value. Figure 1.8 illustrates the paths of conventionally collected meteorites and those collected via sample return missions and the areas which will be the primary and secondary focus for this research (red box and yellow box respectively).

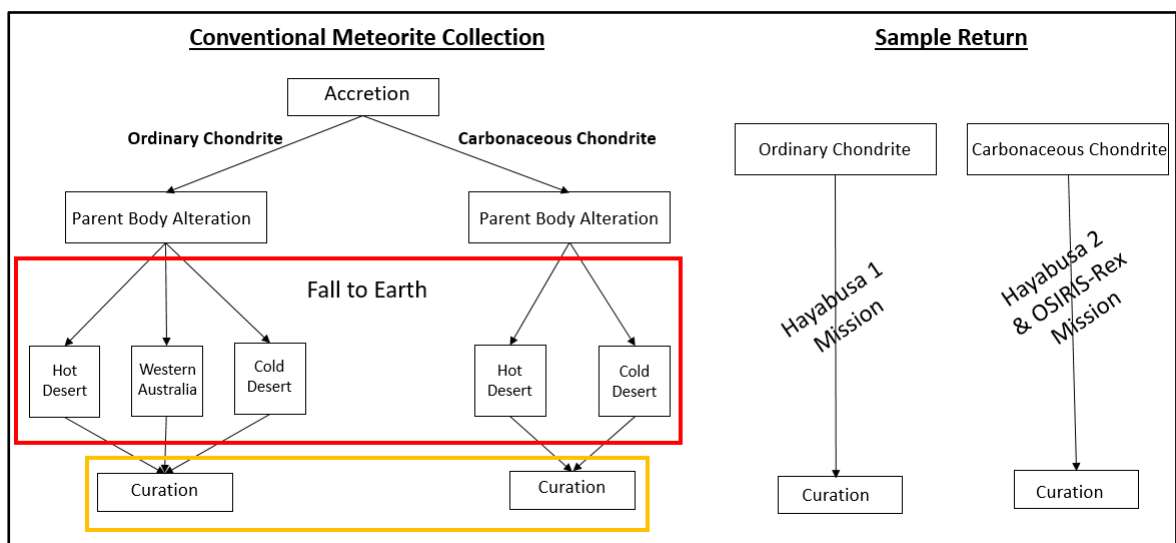


**Figure 1.8** Flow diagram showing how conventional meteorite collection compares to the sample return missions. The red box highlights the area of research for this project and the yellow box where this project may develop further insight.

This research hopes to fill the knowledge gap by addressing 3 aims:

1. In chapter 3: I will precisely characterise the micro-scale mineralogy and chemistry of terrestrial alteration products found in ordinary chondrites and explore how they differ between hot, semi-arid and cold desert climates.
2. In chapter 4: I will investigate the terrestrial alteration products found in CM carbonaceous chondrites, exploring how they differ between

hot and cold deserts and how the development of this terrestrial material effects pre-terrestrial alteration products and visa versa.

3. In chapter 5: I will present the conclusions of this research and suggest areas where further research could be conducted.

Almost all meteorites studied have been subjected to terrestrial weathering at some stage and understanding the processes involved in the development of these weathering products is of paramount importance. This study will demonstrate the importance of understanding terrestrial weathering for future curation and upcoming sample return missions. It will also highlight the unique relationship between climate and terrestrial weathering, revealing new and exciting directions for study linking meteorite weathering and climate studies.

# Chapter 2 Sample Selection, Preparation and Analysis Techniques

## 2.1 Sample Selection

The ordinary and carbonaceous chondrites for this research were selected to represent a broad variety of terrestrial landing environments. Samples were sourced from those already held by the University of Glasgow (with Prof. M. Lee), NASA (USA) and the Natural History Museum (London).

### 2.1.1 Ordinary Chondrites

Seven ordinary chondrites were selected and analysed (Table 2.1). Three terrestrial landing environments; cold desert (Antarctica), hot desert (Saharan) and semi-arid (Australian) were investigated within the ordinary chondrite class.

**Table 2.1** Details of the ordinary chondrites selected and used. They are grouped according to their terrestrial environment. Those with no weathering classification listed have no recorded weathering classification on the Meteoritical Society Database (The Meteoritical Society, 2017). NASA (National Aeronautics and Space Administration), UoG (University of Glasgow).

Sample Name	Petrological Group	Weathering Category	Chip or Thin/Thick Section	Climatic Environment	Sample Source
Dominion Range (DOM) 14010 Allan Hills (ALHA) A77180	L5	B	Chip/Thick Section	Antarctic	NASA
	L6	C	Thick Section	Antarctic	UoG
Forrest 016	H5-6	B/C	Thin Section	Australian	UoG
Forrest 028	L7	C	Thin Section	Australian	UoG
Gunnadorah 004	H5	W2	Thin Section	Australian	UoG
Acfer 019	L6	N/A	Thin Section	Saharan	UoG
Daraj 014	L6	N/A	Thin Section	Saharan	UoG

## 2.1.2 Carbonaceous Chondrites

Three CM carbonaceous chondrites were selected and analysed for comparison to the ordinary chondrites (Table 2.2). CM chondrites were investigated from two terrestrial landing environments; cold desert (Antarctica) and hot desert (Saharan).

**Table 2.2** The CM carbonaceous chondrites selected and used for this research. Two samples of the Jbilet Winselwan CM chondrite are investigated. UoG (University of Glasgow), NHM (Natural History Museum).

Sample Name	Petrological Group	Weathering Category	Chip or Thin Section	Climatic Environment	Source
LaPaz Icefield (lap) 02239	CM2	B	Thick Section	Antarctic	UoG
Lewis cliff (LEW) 85311	CM2	Be	Thick Section	Antarctic	UoG
Jbilet Winselwan (Sections: P19398 and P19399))	CM2	W1	Thick Section	Saharan	NHM

## 2.2 Sample Preparation

### 2.2.1 Resin Blocks

Samples in the form of chips (DOM 14010) were prepared and made into thick sections prior to analysis. To produce sections, chips were cut in to thin slices using a Struers Accutom sample cutter. Ethanol was used as a lubricating fluid during this process to avoid possible contamination and dissolution resulting from the use water. Once cut, the samples were impregnated using Buehler EpoHeat CLR Epoxy Resin and hardener (ratio of 100:21 parts by weight). This resin was cured in a Vacucell 22 vacuum oven, at 60°C for a period of 2 hours after which they were removed and allowed to finish curing at room temperature for 24 hours.

Following impregnation samples were mounted in resin. Struers EpoFix Resin and Hardener was used for sample mounting and was mixed at a weight ratio of 25:3 (resin:hardner). The resin mix was poured over the sample in 30 mm resin moulds which were pre-coated with Buehler Release Agent. The moulds were allowed to cure for 24 hours before removal.

## **2.2.2 Polishing**

Before sections could be polished the samples first needed grinding to remove the surface epoxy layer. This was conducted using grit paper on a Buehler Beta Grinder-Polisher with ethanol used as the lubricant. As samples were brought closer to the surface the coarseness of the grit paper was reduced incrementally from 180 p (average particle diameter 82 µm) to 4000 p (average particle size 6 µm) (Website 2.1).

Following grinding the sample was polished using a Kemet 300 series polisher, a 1 µm polishing pad and 1 µm AlO polishing solution. Samples were polished by hand for two minutes at a pad rotation speed of 115 rpm. Following polishing the samples were wiped clean with ethanol and stored in clean, dry sample boxes awaiting analysis.

## **2.3 Experimental Analysis**

Experimental analysis was carried out on these samples using a variety of techniques as outlined below. All analysis was carried out at the University of Glasgow, School of Geographical and Earth Sciences (GES). All Scanning Electron Microscopy (SEM), quantitative analysis and Raman spectroscopy were carried out at the Imaging Spectroscopy and Analysis Centre (ISAAC) within GES.

### **2.3.1 Optical Microscopy**

Optical microscopy was the first analysis carried out on samples. It was used to guide further analysis by locating metal grains and giving an indication as to the size and presence of alteration rims. Optical microscopy in transmitted and reflected light at magnifications of x5, x10, x20 and x40 was carried out using an Olympus BX41 microscope with attached Olympus DP25 5-megapixel camera. Cell^B software was used for image processing.

### **2.3.2 Scanning Electron Microscopy Imaging**

Two different SEMs were used: 1) Zeiss Sigma Variable Pressure Analytical SEM equipped with Oxford Instruments AZTEC system (version 3.3), 2) FEI Quanta SEM equipped with EDAX Genesis microanalysis system (version 6.5.3). Samples analysed using the Zeiss Sigma SEM were carbon coated to a thickness of 10 nm

using an Agar Scientific automatic carbon coater. The imaging conducted was angle selective backscattered electron imaging (AsB) at a resolution of 2048 x 1536, a working distance of 8.5 mm, an aperture size of 30 µm, an accelerating voltage of 20 keV and a beam current on 1-3 nA.

### 2.3.3 Chemical Analysis

Energy-dispersive X-ray Spectroscopy (EDS) mapping was carried out at a resolution of 1024 x 768, with acquisition times ranging from 20 minutes to 2 hours. Again, a working distance of 8.5 mm was used throughout with an aperture size of 30 µm, an accelerating voltage of 20keV and a beam current of 1-3 nA.

Quantitative analysis was carried out using the Zeiss Sigma SEM equipped with Oxford Instruments INCA analysis software (version 5.05). Throughout the analysis the count time used for the samples and the standards was 60 seconds and throughout the analysis the beam current was monitored (via the Faraday cup and Co standard). The standards used to quantify each element were sourced from P&H Developments Ltd. and are outlined in Table 2.3. The pre-calibration values for the standards are provided in the appendix. Where quantitative data is graphed the scales used for each element will be the same to aid comparison.

**Table 2.3** The standards used during quantitative analysis of samples.

Element	Standard	Formula	Wt.% Element in Standard
O	Hematite	Fe <sub>2</sub> O <sub>3</sub>	30.06
Mg	Periclase	MgO	60.03
Al	Corundum	Al <sub>2</sub> O <sub>3</sub>	52.92
Si	Diopside	MgCaSi <sub>2</sub> O <sub>6</sub>	25.88
P	Apatite	Ca <sub>5</sub> (PO <sub>4</sub> ) <sub>3</sub> (F,Cl,OH)	17.80
S	Pyrite	FeS <sub>2</sub>	53.45
Cl	Tugtupite	Na <sub>4</sub> (AlBeSi <sub>4</sub> O <sub>12</sub> )Cl	7.58
Ca	Diopside	MgCaSi <sub>2</sub> O <sub>6</sub>	18.38
Cr	Chromite	(Fe,Mg)Cr <sub>2</sub> O <sub>4</sub>	68.42
Mn	Rhodonite	(Mn <sup>2+</sup> ,Fe <sup>2+</sup> ,Mg,Ca)SiO <sub>3</sub>	32.93
Fe	Hematite	Fe <sub>2</sub> O <sub>3</sub>	69.94
Ni	Nickel Metal	Ni	100.00

### 2.3.3.1 Detection Limits

Minimum detection limits (MDL's) were calculated to show the minimum quantity (wt.%) of an element that can be distinguished/detected by quantitative analysis. This is taken as the uncertainty of these measurements. Calculations were conducted by extracting data from the INCA software and applying this to the MDL equation in Potts (1992) (see Equation 1). As each MDL varies between elements and between analysis dates, where quantitative analysis data is used the MDL will be quoted with it.

$$\text{MDL} = \frac{3\sqrt{Nb * Cstd}}{Nnp}$$

**Equation 1.** Minimum Detection Limits (Potts, 1992)

MDL - Minimum detection limits

Nb - Background counts (counts)

Cstd - Concentration in standard (wt. % or ppm)

Nnp - Net peak counts (counts)

### 2.3.4 Raman Spectroscopy

Raman spectroscopy was carried out at the ISAAC and used a Renishaw InVia Raman microscope. Raman analysis is a vibrational spectroscopic technique which utilises a laser light source to irradiate and excite a sample. The incident light is then scattered by the molecules in the sample. Most of this light is scattered at the same frequency as before this interaction. However, some interacts with the vibrating molecules and changes frequency: this is Raman scattering (Website 2.2). This Raman scattered light is then dispersed by a diffraction grating and is detected on a charge coupled device (CCD). This information is then presented in graphical form. As materials produce slightly different frequencies of reflected light this technique makes it possible to identify polymorphs and changes in the crystal structure. This is of great help when examining Fe-oxides and is used extensively in this research to identify Fe-oxide alteration products.

During this research Raman spectroscopy was used in two ways: Point Analysis and Principle Component Mapping (PCM). All Raman analysis was carried out using a Renishaw InVia Raman microscope attached to a RL514C100, 514 nm laser source (max power 45 W) and 2400 mm grating. The laser had a spot size of 1 µm. Wire 4.4 software was used to process the collected data and produce spectra.

#### 2.3.4.1 Point Analysis

Point analysis was conducted on precise, single spots within the alteration rims of metal grains. These spots were selected and aligned using the reflected light Raman microscope at x100 magnification. During point analysis the laser power was set to 0.1 % and exposure time to 3 seconds. Each analysis comprised 3 accumulations (which sum to make up one spectrum) and 25 acquisitions (repeats). Each point of analysis was therefore exposed to the laser source a total of 75 times and produced 25 spectra per point.

The resulting 25 spectra were processed and analysed using Renishaw's Wire 4.4 software. Processing firstly involved a Cosmic Ray Analysis Test and, if present, removal using Wire's in-built 'Cosmic Ray Removal' tool. This was done to reduce error in the spectra. Whilst the occurrence of cosmic-rays is random, during this research cosmic ray spikes appeared more likely to occur in spectra when there was a disturbance to the laser during analysis (for example, laboratory door closing).

Once free of cosmic rays the 25 spectra were normalised to an upper limit of 100 and then averaged using the 'Average Collected Data' function in Wire 4.4 to produce one high quality spectrum. Data was normalised to show the intensity of peaks as a percentage relative to the largest peak detected. This method was used in favour of single exposure methods due to sample fragility. Samples, especially CM meteorites, were incredibly delicate and experienced burning at laser powers above 1 %. Laser powers below 1 %, even with long exposure times (80 seconds), produced weak spectra which were difficult to interpret. This averaging method was therefore applied and consistently produced high-quality spectra.

#### **2.3.4.2 Principle Component Mapping**

Principle Component Mapping (PCM) was conducted on some larger alteration rims. In these instances, the ‘map area’ feature in Wire 4.4 was used to sample hundreds of points (> 450 points) across an area to show how composition changes on a larger scale. Due to the time taken by area sampling and software limitations (multiple acquisitions were not possible) the measurement parameters had to be altered from those used in point analysis. A single exposure method had to be employed with a laser power of 0.5 % for 5 seconds with 1 acquisition. This produced weaker spectra and only weathering products with significantly different spectra (such as akaganeite and tochilinite) could be distinguished.

Once the area map was completed sample spectra for the minerals being mapped were loaded into Wire 4.4. These sample spectra were collected prior to mapping using point analysis in the alteration rim. The Wire software then produced colour maps of the area with the brightest colours indicating the greatest match to a sample spectrum. Whilst this produced good maps showing the general distribution of different alteration products, the weak spectra lead to poorly constrained boundaries between minerals.

#### **2.3.4.3 Raman Spectrum Identification**

Materials analysed using Raman spectroscopy were identified by the presence and positions of peaks at specific Wave Numbers/Raman Shifts ( $\text{cm}^{-1}$ ). These spectra were identified using the ‘Library Search’ function within the Wire 4.4 software, the Rruff database and comparisons with the wider literature. The five major minerals identified during this research and the characteristics of the spectra which were used to identify them are listed below.

##### Akaganeite:

Akaganeite ( $\text{Fe}^{3+}(\text{O},\text{OH},\text{Cl})$ ) is not listed in the Rruff database or within the Wire software. Consequently, to confirm the presence of akaganeite, spectra were searched from the literature to establish typical spectrum shapes and peak positions. The typical peak positions for akaganeite were established to be; ~310, ~390, ~540, ~610 and ~720 (Figure 2.1) (Neff et al., 2006; Colombar et al., 2008a;

Bellot-Gurlet et al., 2009; Cambier et al., 2014; Li and Hihara, 2015; Mohammed et al., 2018). Akaganeite is composed of 79.70 %  $\text{Fe}_2\text{O}_3$ , 3.92 % NiO, 11.48 %  $\text{H}_2\text{O}$ , 6.05 % Cl (Website 2.3).

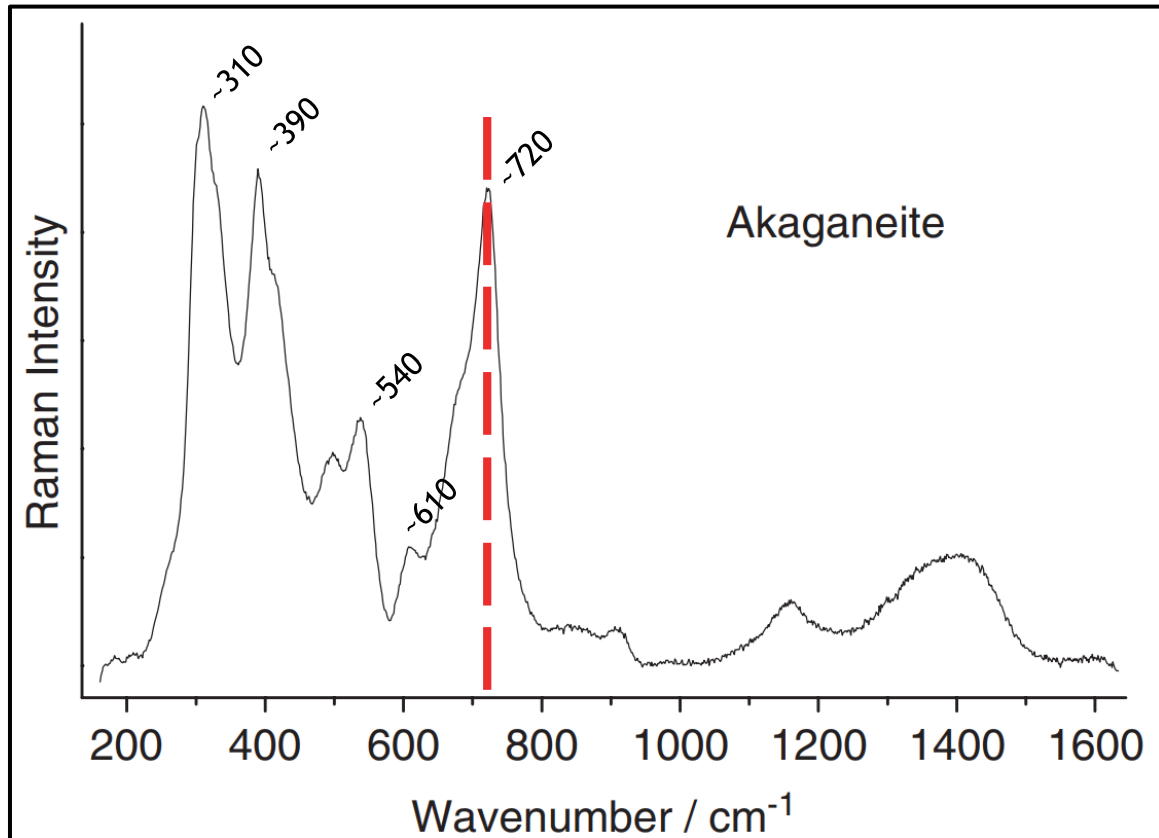


**Figure 2.1** Edited Raman spectrum from Neff et al., (2006) illustrating a spectrum of akaganeite which helped establish the typical peak positions.

#### Goethite:

Goethite ( $\text{FeO(OH)}$ ) is listed in the Rruff database and the Wire software's library. These spectra were compared with spectra from the literature to establish the typical peak positions for goethite. These positions are; ~240, ~300, ~390, ~485, ~550 and ~685 (Figure 2.2) (Goethite R120086 - RRUFF Database: Raman, X-ray, Infrared, and Chemistry; Neff et al., 2006; Colomban et al., 2008b; Bellot-Gurlet et al., 2009; Chicot et al., 2011; Cambier et al., 2014; Li and Hihara, 2015; Mohammed et al., 2018). Goethite is composed of 89.86 %  $\text{Fe}_2\text{O}_3$  and 10.14 %  $\text{H}_2\text{O}$  (Website 2.4).

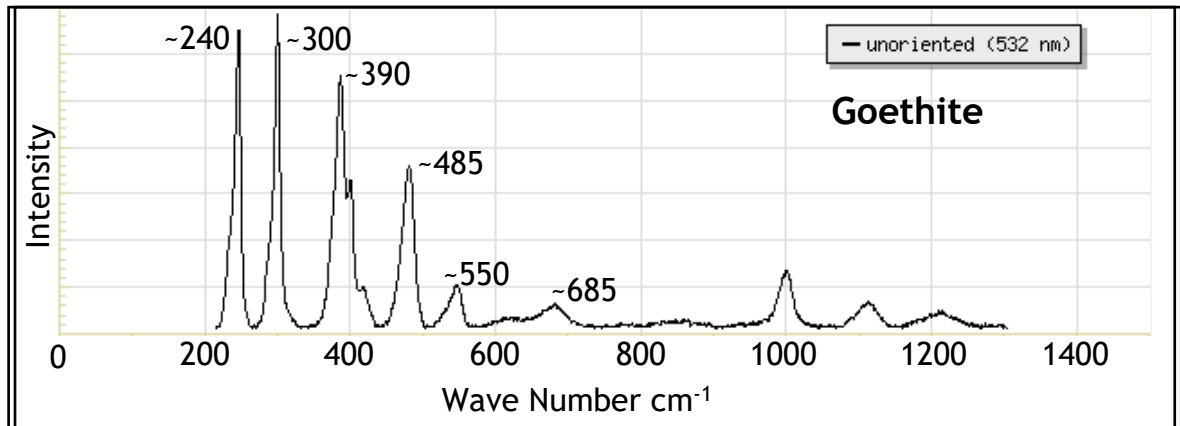


**Figure 2.2** Edited Raman spectrum from the Rruff database illustrating a spectrum of goethite which helped establish the typical peak positions.

#### Hydrated Iron III Oxide or Oxyhydroxide:

Hydrated iron III oxide or oxyhydroxide is a generic term for maghemite, ferrihydrite and feroxyhite and is used because of the close similarities between the spectra and difficulties in accurately distinguishing between them (Bellot-Gurlet et al., 2009). There are very limited examples of Raman spectra for Hydrated iron III oxide or oxyhydroxide within the literature and no sample spectra was available on the Rruff database. Using those published in the literature the typical peak positions were established to be ~380 cm<sup>-1</sup>, ~510 cm<sup>-1</sup> and ~700 cm<sup>-1</sup> (Figure 2.3) (Neff et al., 2006; Bellot-Gurlet et al., 2009).

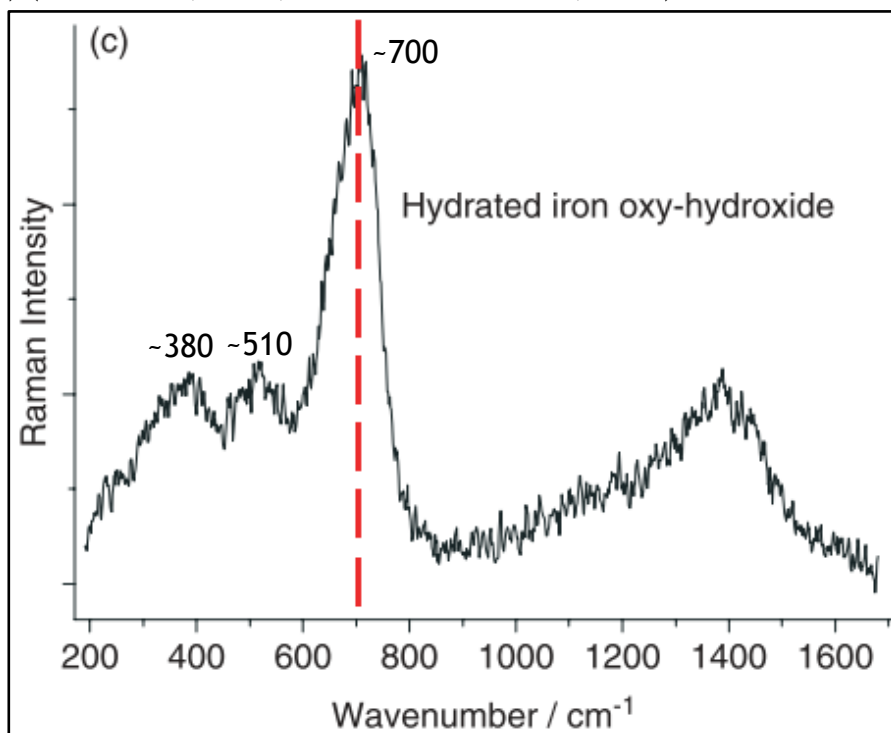


**Figure 2.3** Raman spectrum from Neff et al., (2006) illustrating a spectrum of hydrated iron III oxide or oxyhydroxide which helped establish the typical peak positions.

### Tochilinite:

Tochilinite ( $\text{FeS}(\text{Mg}, \text{Fe}^{2+})(\text{OH})_2$ ) is also listed in the Rruff database but not in the Wire software library. There are limited examples of tochilinite Raman spectra in the literature but from these the typical peak positions were established to be: ~250, ~300 and ~350 (Figure 2.4) (Tochilinite - RRUFF Database: Raman, X-ray, Infrared, and Chemistry; Vacher et al., 2017). Tochilinite is composed of 12.77 % Mg, 51.56 % Fe, 0.22 % H, 31.91 % S and 3.54 % O (Website 2.5).

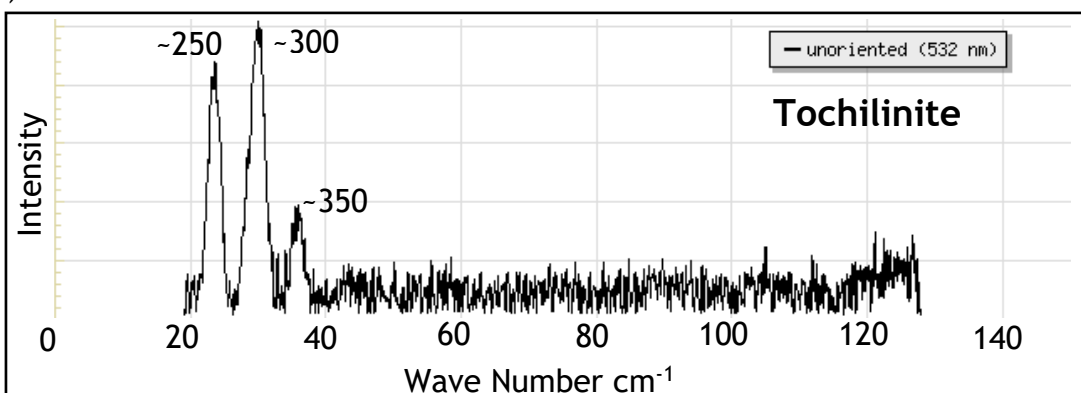


**Figure 2.4** Edited Raman spectrum from the Rruff database illustrating a spectrum of tochilinite which helped establish the typical peak positions.

### Magnetite:

Magnetite ( $\text{Fe}^{3+}_2\text{Fe}^{2+}\text{O}_4$ ) is listed in the Rruff database and mentioned in the literature. From these sources typical peak positions at  $\sim 310 \text{ cm}^{-1}$ ,  $\sim 540 \text{ cm}^{-1}$  and  $\sim 670 \text{ cm}^{-1}$  (Figure 2.5) (“Magnetite R061111 - RRUFF Database: Raman, X-ray, Infrared, and Chemistry”; Bellot-Gurlet et al., 2009). Magnetite is composed of 31.03 %  $\text{FeO}$  and 68.97 %  $\text{Fe}_2\text{O}_3$  (Website 2.6).

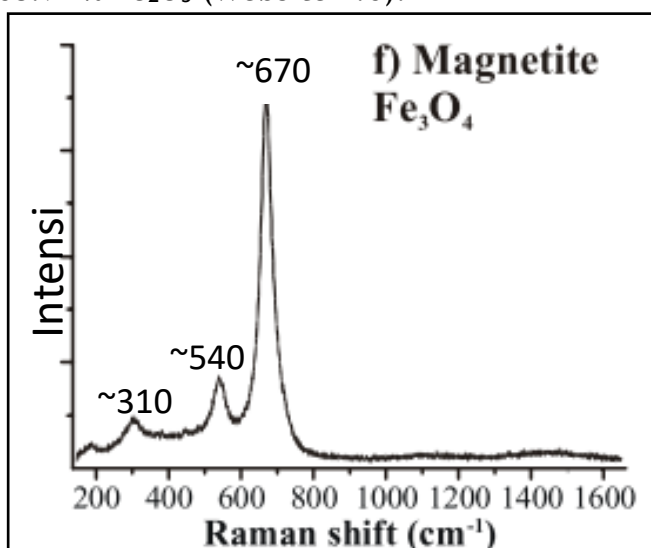


**Figure 2.5** Edited Raman spectrum from Bellot-Guelet et al. (2009) illustrating a spectrum of magnetite which helped establish the typical peak positions.

# **Chapter 3 Ordinary Chondrites**

As discussed in chapter one, ordinary chondrites are thought to have experienced no significant low temperature, aqueous alteration whilst part of their parent bodies. Therefore, any alteration which is observed should be a result of terrestrial weathering processes. In this chapter I will be investigating and characterising the terrestrial alteration products associated with Fe,Ni metal and sulphide grains in ordinary chondrites. I will, for the first time, use a combined array of chemical and mineralogical investigative techniques for this characterisation to enable accurate, micron-scale examination of Fe,Ni metal alteration products. I will also explore how these alteration products vary between three different terrestrial environments: the Antarctic, Western Australia and Sahara. All three environments are major sources of meteorites on Earth.

## **3.1 Antarctic Ordinary Chondrites**

### **3.1.1 Environment**

Antarctica is a cold, desert environment which rarely experiences temperatures above 0°C. The Dominion Range (from which DOM 14010 was collected) is a mountain range forming part of the Queen Maud Mountains. It experiences summer maximum average temperatures of -16°C and winter maximum average temperatures of -40°C (“Website 3.1”). The Dominion Range also experiences minimal precipitation with an average of 2 mm annually (“Website 3.1”). The Allan Hills (from which AHLA 77180 was collected) is another mountain range to the North of the Dominion Range forming part of the Trans-Antarctic mountain range. The Allan Hills experience summer maximum average temperatures of -12°C and winter maximum average temperatures of -39°C (“Website 3.2”). Average annual precipitation in this region is significantly higher than in the Dominion Range at 24 mm (“Website 3.2”).

### 3.1.2 Fe,Ni Metal

Both of the Antarctic ordinary chondrites analysed here had abundant Fe,Ni metal (Table 3.1). The majority of Fe,Ni metal in these samples was kamacite, with minor amounts of taenite also present.

**Table 3.1** ImageJ calculated, percentage of kamacite, taenite and troilite in each of the Antarctic samples calculated from reflected light microscopy images. Troilite is included despite being as sulphide as it could not be distinguished from Fe,Ni metal in ImageJ.

Sample	Abundance (volume %)
DOM 14010	6.05
ALHA 77180	3.75

### 3.1.3 Alteration Products

Initial reflected light microscopy reveals significant ‘halos’ of alteration around the majority of the Fe,Ni metals within the Antarctic samples. In most cases these alteration halos surrounded the metal grains with thicknesses ranging from 5-100+ µm. Intricate internal structures were also visible in reflected light in some of the alteration halos.

#### 3.1.3.1 DOM 14010

DOM 14010 is an L5 chondrite with a weathering category of B- moderately rusty. Initial AsB imaging revealed two distinctive textures within the alteration rims surrounding the Fe,Ni metal grains, an ordered texture and a disordered texture (Figures 3.1, 3.2, 3.3, 3.4). The ordered texture is characterised by very fine laminations and many cross-cutting fractures. The disordered texture is the dominant texture throughout the samples and is characterised by much coarser and more chaotic laminations and fewer fractures. There does not appear to be any correlation between the texture observed and proximity to the metal grain. In addition to the changes seen within the alteration rims, figures 3.3 and 3.4 also

demonstrate two subtly different greyscales, one brighter and one duller within the Fe,Ni metal grains.

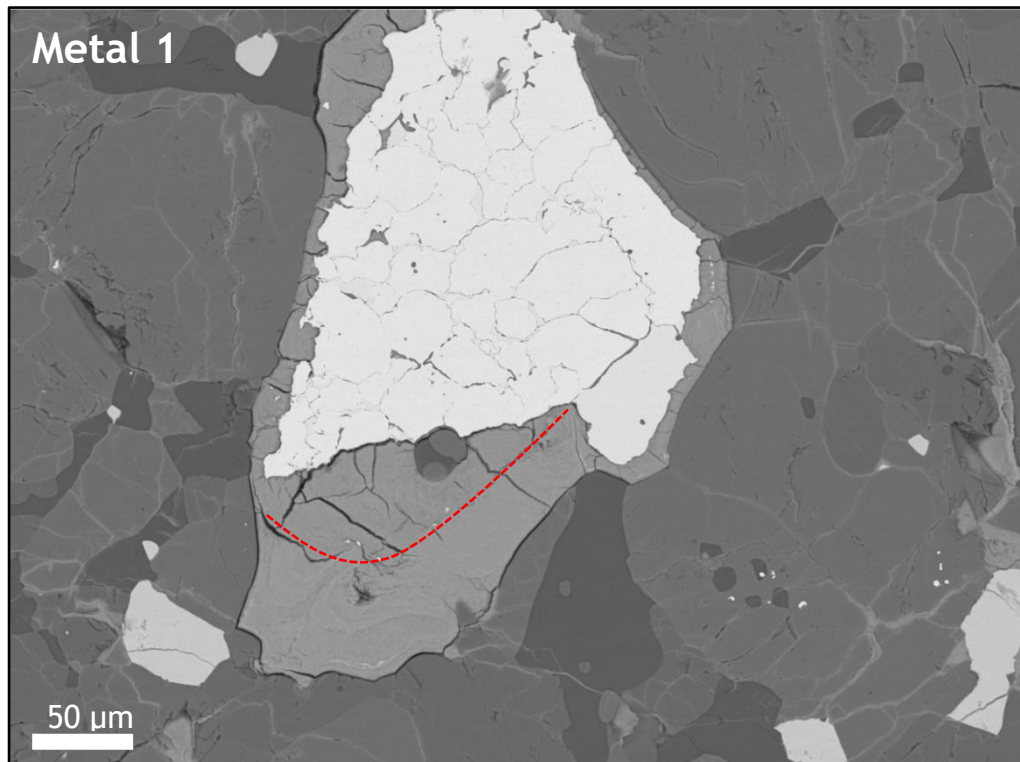


**Figure 3.1** Backscattered electron image (BSE) of Metal 1, Fe,Ni metal grain (white) within DOM 14010. The red dashed line indicates the boundary between the ordered and disordered material. They can be easily distinguished by the presence of fractures and by lamination thickness.

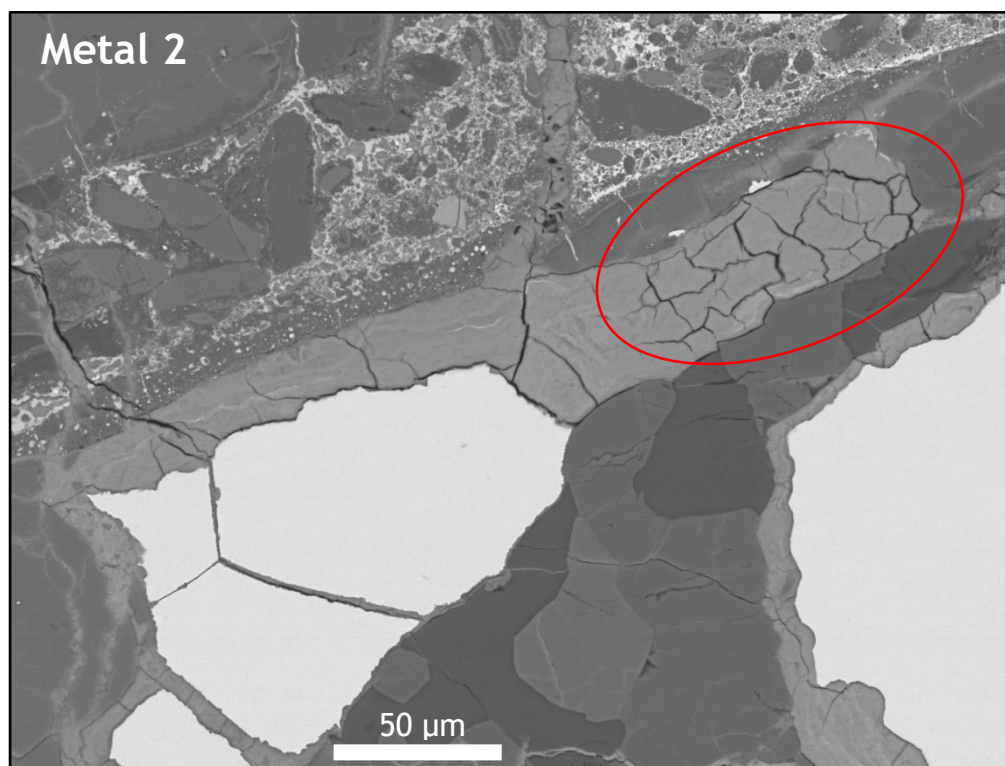


**Figure 3.2** BSE image of metal 2, Fe,Ni metal grain (white) within in DOM 14010. The highlighted area (red) indicates an area of ordered material which is very heavily fractured and is finely laminated. The remaining material is disordered.

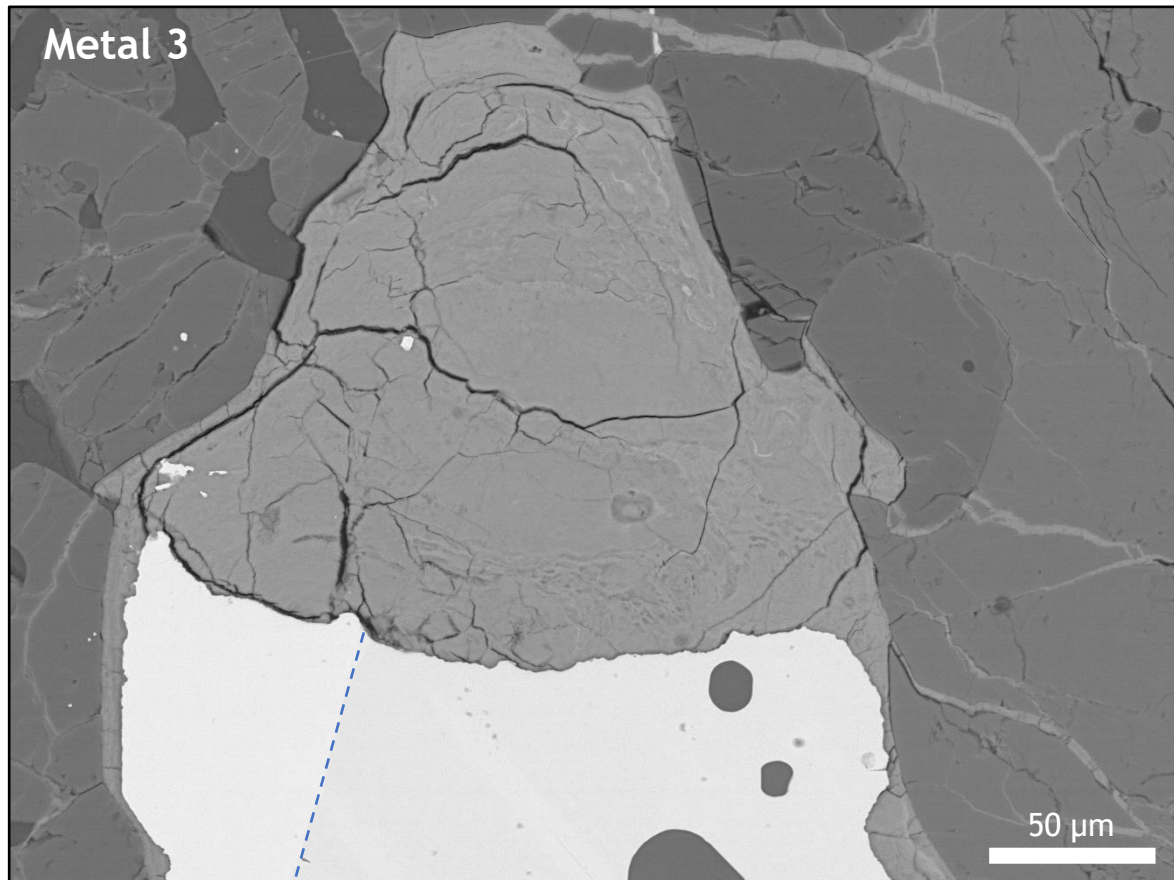


**Figure 3.3** BSE image of metal 3, Fe,Ni metal grain (white) demonstrating a subtle colour difference (dashed line indicates boundary). The alteration material around this metal grain does not have a distinct ordered/disordered texture.

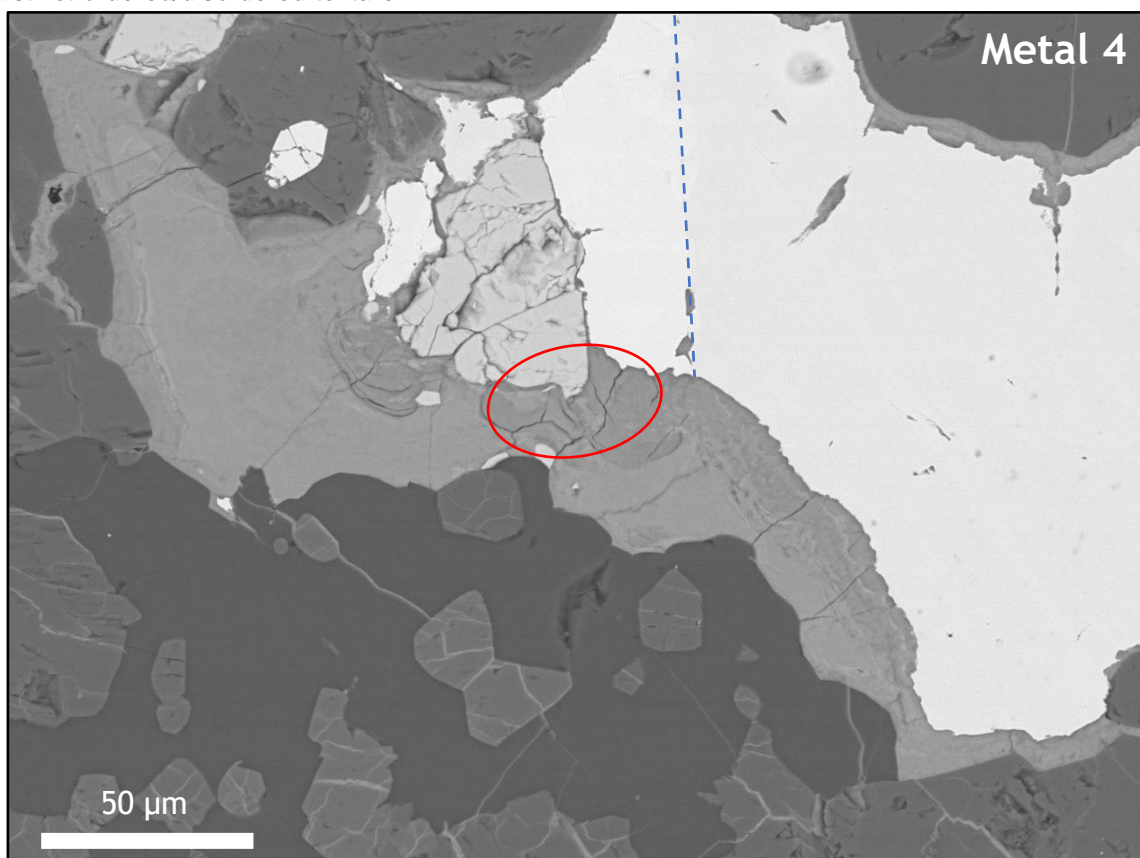


**Figure 3.4** BSE image of metal 4, Fe,Ni metal grain (white) showing subtle variation in colour (dashed line indicates boundary). There is a large irregularly shaped alteration rim surrounding this metal grain with only a small pocket of ordered material (highlighted area).

### Chemical Composition:

EDS mapping and analysis was conducted to determine which of the Fe,Ni alloys (kamacite or taenite) were present, and investigate the composition of the alteration rims.

Qualitative analysis of metal grains 1, 2, 3 and 4 revealed the subtle changes in metal colour (lighter or darker) which were observed in AsB imaging were the result of different Fe,Ni alloys. Metal grains appearing brighter during AsB imaging were taenite grains and metals which were slightly darker were kamacite. This difference in observed colour during AsB imaging is the result of taenite's higher Ni concentration and the effect this has on the electron beam (more opaque material). Metal 1 was shown to be a taenite grain and metal 2 a kamacite grain. Metals 3 and 4 were mixed grains and composed of both kamacite and taenite.

Buchwald and Clarke (1989) found that Cl was of paramount importance for the development of the primary alteration product akaganeite in meteorites. Buchwald and Clarke (1989) describe akaganeite as having an important role in facilitating the initial corrosion of metal. As a result of akageneite's importance and Cl-bearing nature metals 1 and 4 were also mapped for Cl.

EDS maps of metals 1 and 4 showed that both had significant areas of Cl enrichment within their alteration rims (Figure 3.5). Figure 3.5A shows metal 1 has a band of Cl-rich material running through the middle of the alteration rim. Figure 3.5B, the EDS map for Cl in metal 4, shows a Cl-rich band of material towards the edge of the alteration rim. Within metal 4, the Cl-rich regions has a concentration of up to 3.52 wt.% Cl (Table 3.2) and the non-Cl rich region has a concentration of 0.13 wt.% Cl (Table 3.2).

Also revealed from analysis of metals 1 and 4 is the difference in Ni content measured in the alteration products surrounding kamacite and taenite and how this alters through the alteration rim. Figure 3.6A shows the relationship between  $\text{Fe}_2\text{O}_3$  and NiO in metal 1 (taenite). The scatter plot illustrates an almost proportional relationship between the two components with NiO decreasing with increasing  $\text{Fe}_2\text{O}_3$ .  $\text{Fe}_2\text{O}_3$  increases away from the metal grain therefore NiO

decreases away from the metal grain, positions numbers 1-12 therefore represent areas furthest from the reaction front whereas position numbers 13 and 15 are far closer. Also illustrated is the very high NiO content within alteration material adjacent to taenite. Figure 3.8A shows  $\text{Fe}_2\text{O}_3$  and NiO in metal 4, a mixed taenite, kamacite metal grain. Used alongside figure 3.7 and table 3.2 it shows two distinct clusters of material. Material richest in NiO is found adjacent to taenite (position numbers 5 and 9) and material not rich in NiO is found either adjacent to kamacite or further from the metal grain boundary. Figures 3.6B and 3.8B illustrate the relationship between  $\text{Fe}_2\text{O}_3$  and S and demonstrates a similar, albeit weaker relationship compared when compared to Ni. The highest S detected in the regions with the highest Ni concentrations. Figures 3.6C and 3.8C show the  $\text{Fe}_2\text{O}_3$  - Cl relationship. In both cases there is only a weak positive correlation with Cl generally increasing with increasing  $\text{Fe}_2\text{O}_3$  and away from the metal grain. A wide array of Cl concentrations are detected.

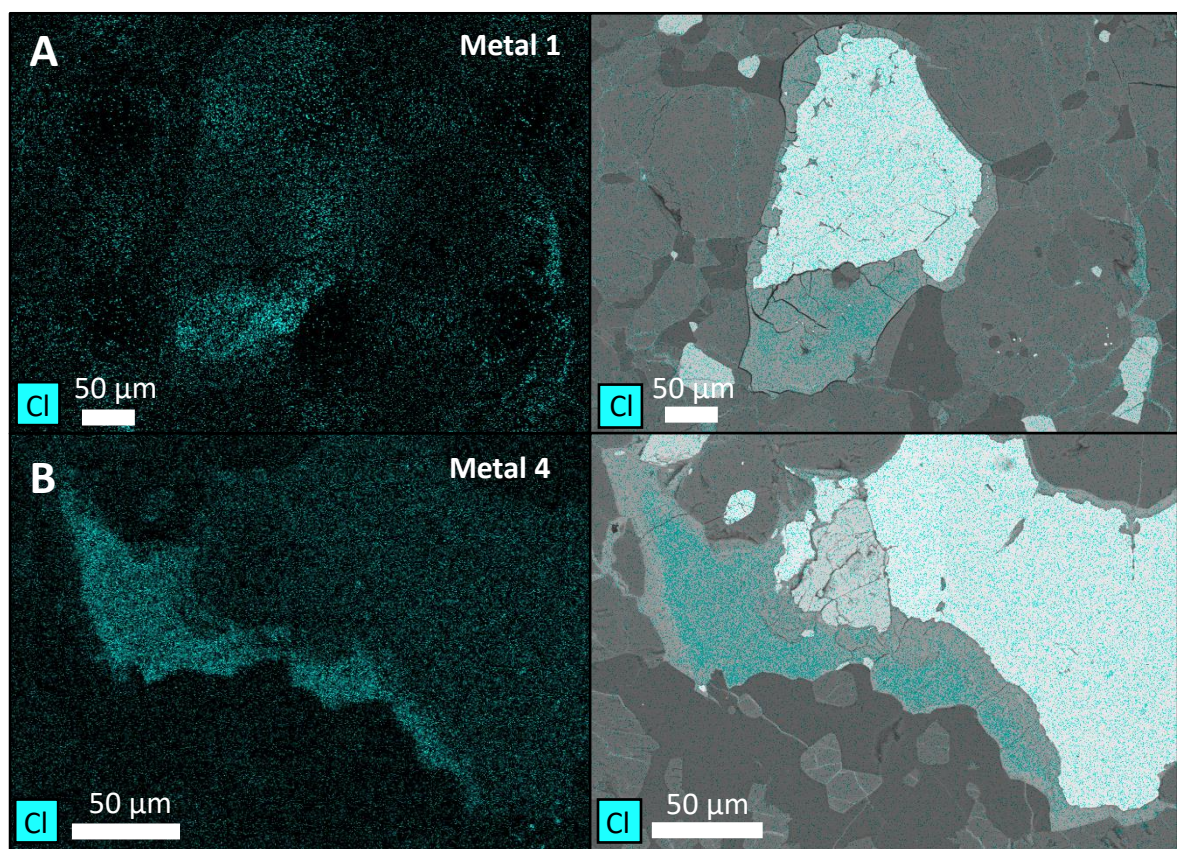


**Figure 3.5** EDS maps of Metal 1 (A) and Metal 4 (B). EDS maps for Cl (left). EDS map for Cl overlaid on a BSE image (right). Images demonstrate that the Cl-rich material is confined to the disordered material away from the metal grain boundary.

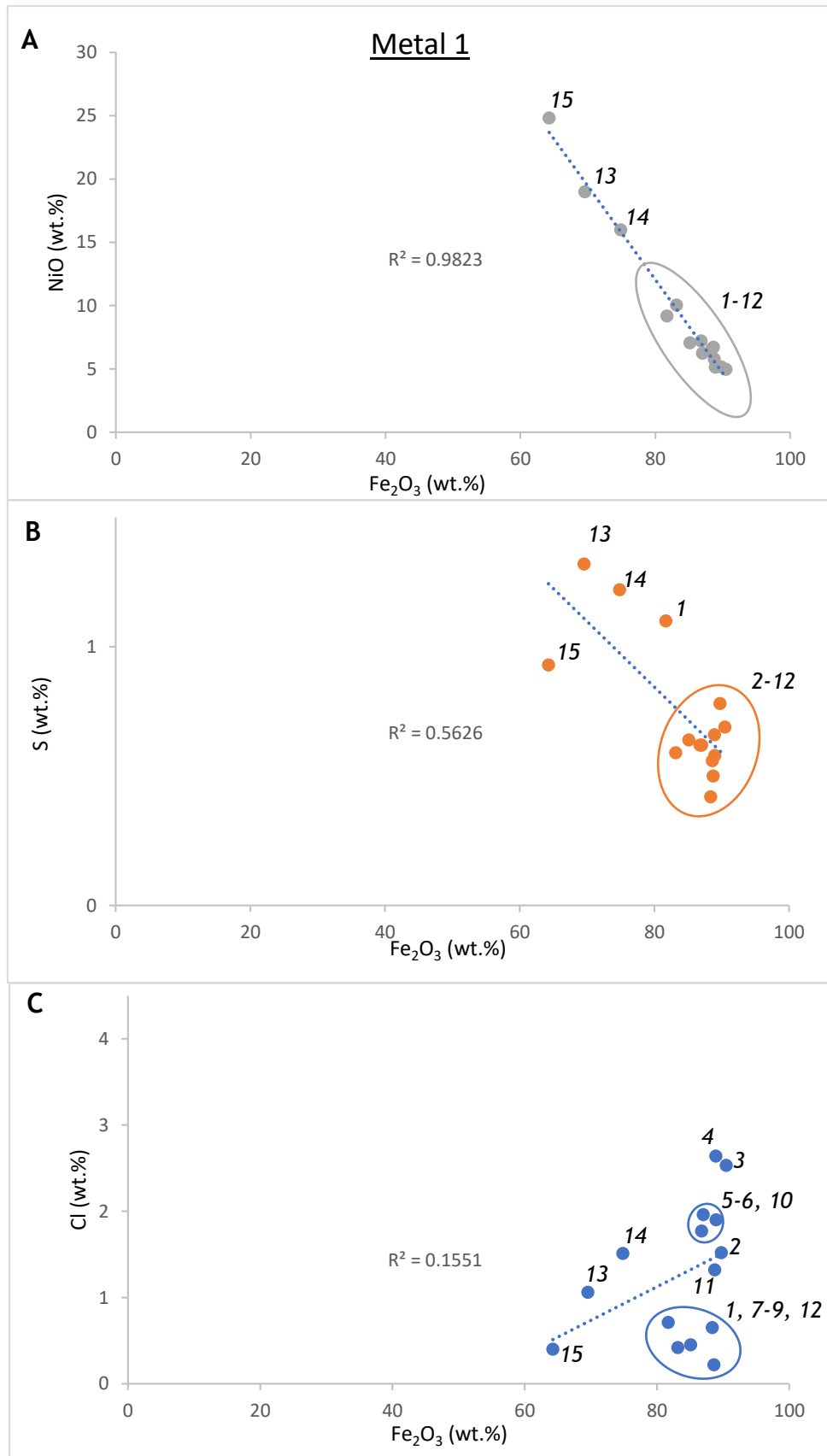


**Figure 3.6** Graphs illustrating the relationship between Fe<sub>2</sub>O<sub>3</sub> (wt.%) and the key elements investigated in metal 1 (a taenite metal grain). Data taken from Appendix: ‘Quantitative analysis of metal 1’ and values given in wt.%. Labels correspond to position numbers in data table. A) Graph of Fe<sub>2</sub>O<sub>3</sub> – NiO. B) Graph of Fe<sub>2</sub>O<sub>3</sub> – S, C) Graph of Fe<sub>2</sub>O<sub>3</sub> – Cl.

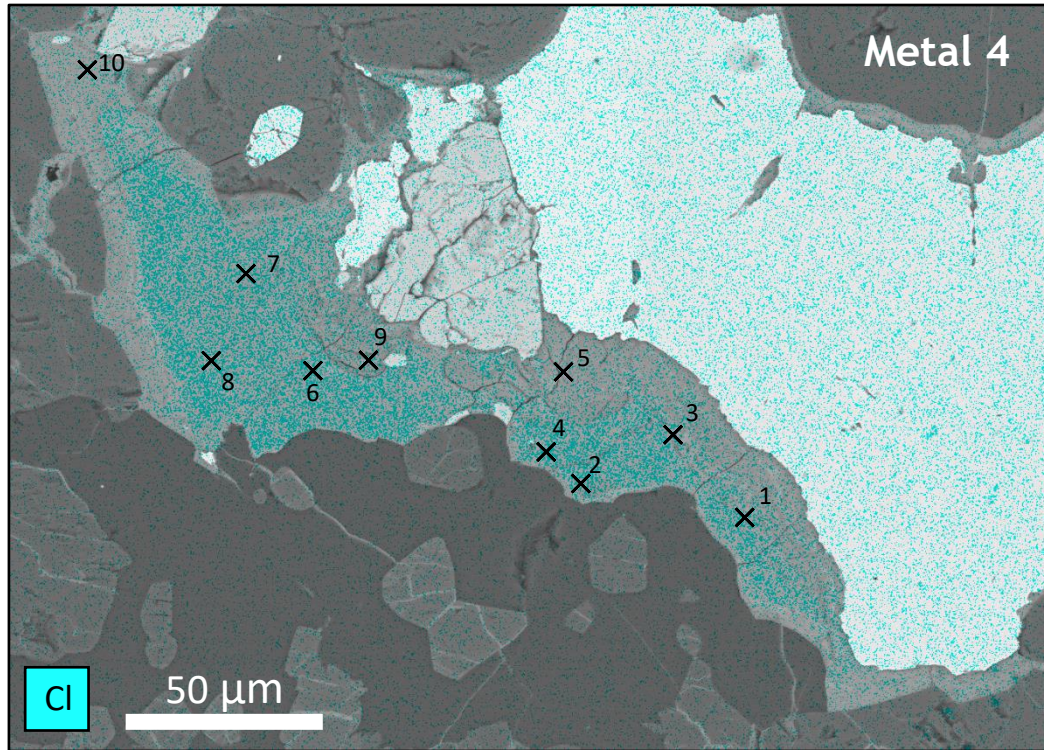


**Figure 3.7** EDS map of Cl overlain on a BSE image of metal 4. Labelled are the points of analysis shown in Table 3.2.

**Table 3.2** Results of EDS analysis in metal 4 with positions numbers corresponding to those shown in figure 3.7. Values shown in wt.%. Minimum detection limits are stated below.

Position Number	$SiO_2$	$Al_2O_3$	$Fe_2O_3$	$MgO$	$CaO$	$NiO$	S	Cl	$Fe_{(m)}$	Ni	Total
1	0.62	0.30	82.53	0.50	0.50	5.23	0.38	0.83	-	-	90.89
2	0.88	0.21	74.19	0.32	0.14	12.55	0.25	2.16	-	-	90.69
3	0.68	-	82.07	0.35	0.55	4.90	0.45	0.98	-	-	89.98
4	0.19	0.21	84.74	0.20	0.17	6.77	0.22	3.50	-	-	96.00
5	0.53	-	58.21	0.48	0.28	24.83	0.81	0.34	-	-	85.48
6	0.62	0.15	87.39	0.20	0.13	4.53	0.25	2.80	-	-	96.07
7	0.32	0.28	85.70	0.20	0.28	4.61	0.32	2.52	-	-	94.23
8	0.21	0.15	87.19	0.30	0.22	3.95	0.22	3.06	-	-	95.30
9	0.53	-	56.29	0.22	0.24	24.85	0.48	0.97	-	-	83.58
10	1.16	0.25	85.76	0.48	0.18	4.15	0.38	0.13	-	-	92.49
Minimum Detection Limit		0.06	0.07	0.17	0.04	0.08	0.25	0.08	0.07	0.17	0.25

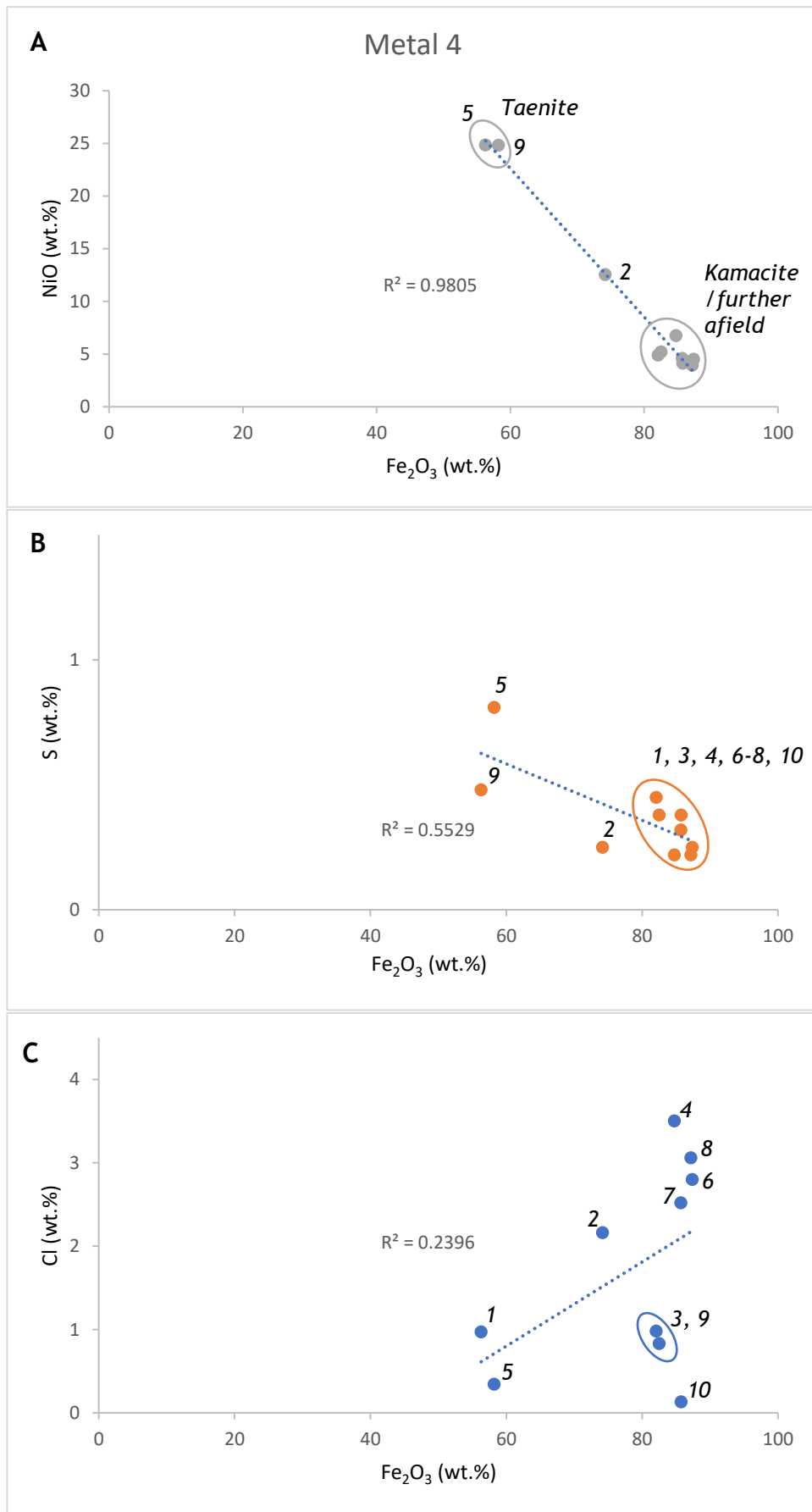


**Figure 3.8** Graphs illustrating the relationships between  $\text{Fe}_2\text{O}_3$  (wt.%) and the key elements investigated in metal 4 (a mixed kamacite, taenite metal grain). Data taken from table 3.2 and values given in wt.%. Labels correspond to position numbers in Figure 3.7 and Table 3.2. A) Graph of  $\text{Fe}_2\text{O}_3 - \text{NiO}$ . B) Graph of  $\text{Fe}_2\text{O}_3 - \text{S}$ . C) Graph of  $\text{Fe}_2\text{O}_3 - \text{Cl}$ .

## Mineralogy

Point analysis Raman spectroscopy was used to identify the iron-oxide minerals making up the alteration rims in metals 1 and 4. EDS maps of Cl guided the Raman spectroscopy measurements.

Raman spectroscopy of Metals 1 and 4 revealed the Cl-rich regions highlighted by chemical analysis correspond to the mineral akaganeite. Figure 3.9 spectra A, D and E are from these Cl-rich regions and all demonstrated the characteristic peak positions for akaganeite. Figure 3.9 spectra B and C are from areas shown to not be rich in Cl. Spectrum B has only two prominent peaks at  $390\text{ cm}^{-1}$  and  $690\text{ cm}^{-1}$ , making identification difficult. The final peak position at  $690\text{ cm}^{-1}$  is earlier than those seen in spectra A, D and E and is more characteristic of the final peak position of goethite ( $\sim 685\text{ cm}^{-1}$ ). Spectrum B may therefore represent a mineral transitioning from akaganeite to goethite. Spectrum C also has two peaks but, here they occur at  $390\text{ cm}^{-1}$  and  $715\text{ cm}^{-1}$ . These peak positions are more characteristic of akaganeite and so this spectrum may have sampled a poorly crystalline phase of akaganeite.

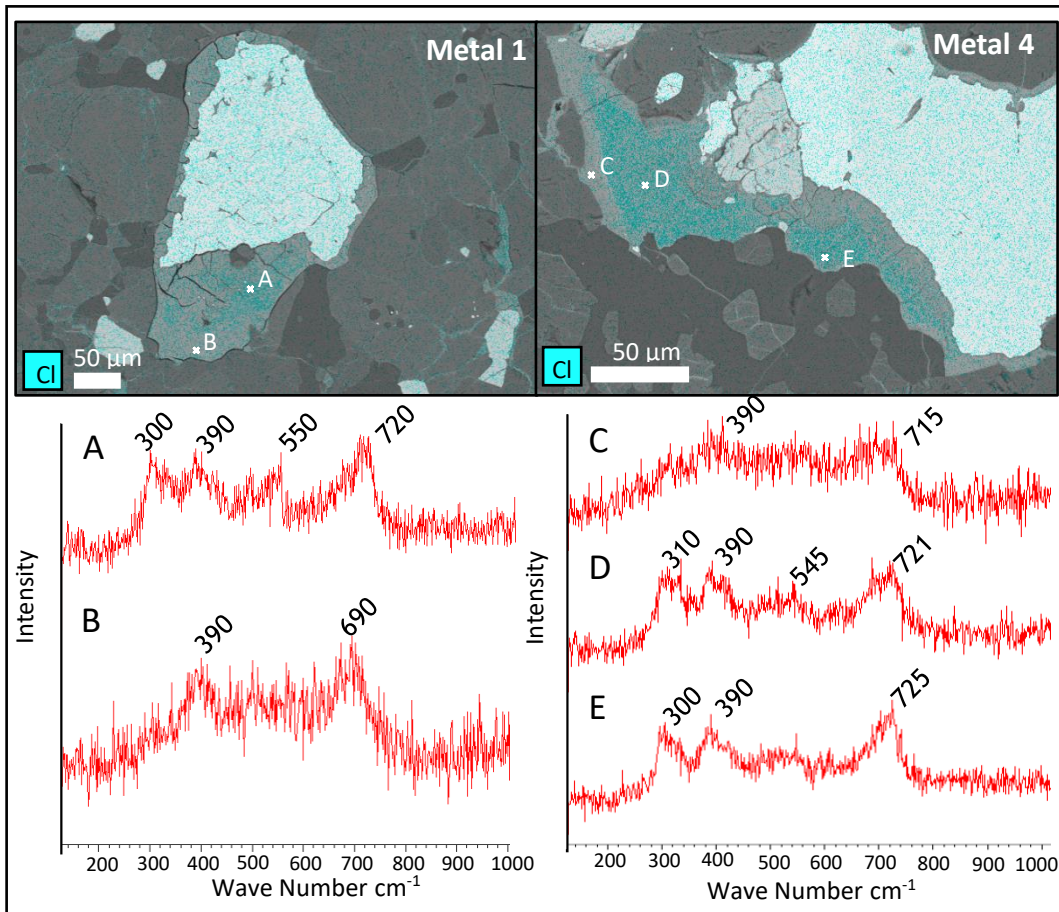


**Figure 3.9** EDS maps and accompanying Raman spectra for selected locations in metals 1 and 4. Spectrum A) Akaganeite, B) Inconclusive, C) Inconclusive, D) Akaganeite, E) Akaganeite.

### 3.1.3.2 ALHA 77180

ALHA 77180 is an L6 chondrite with a weathering category of C- severely rusted. AsB imaging of the alteration rims surrounding Fe,Ni metal grains shows fewer textural changes like those in DOM 14010, with only metal 6 (Figure 3.11) showing a distinct change in texture. Within metal 6 a small portion of ordered material exists along the thin edge of the alteration rim, the remaining material appears disordered. Within metals 5 and 7 (Figure 3.10 and 3.12) alteration rims contain features of the ordered and disordered texture, containing turbulent laminations and fractures.

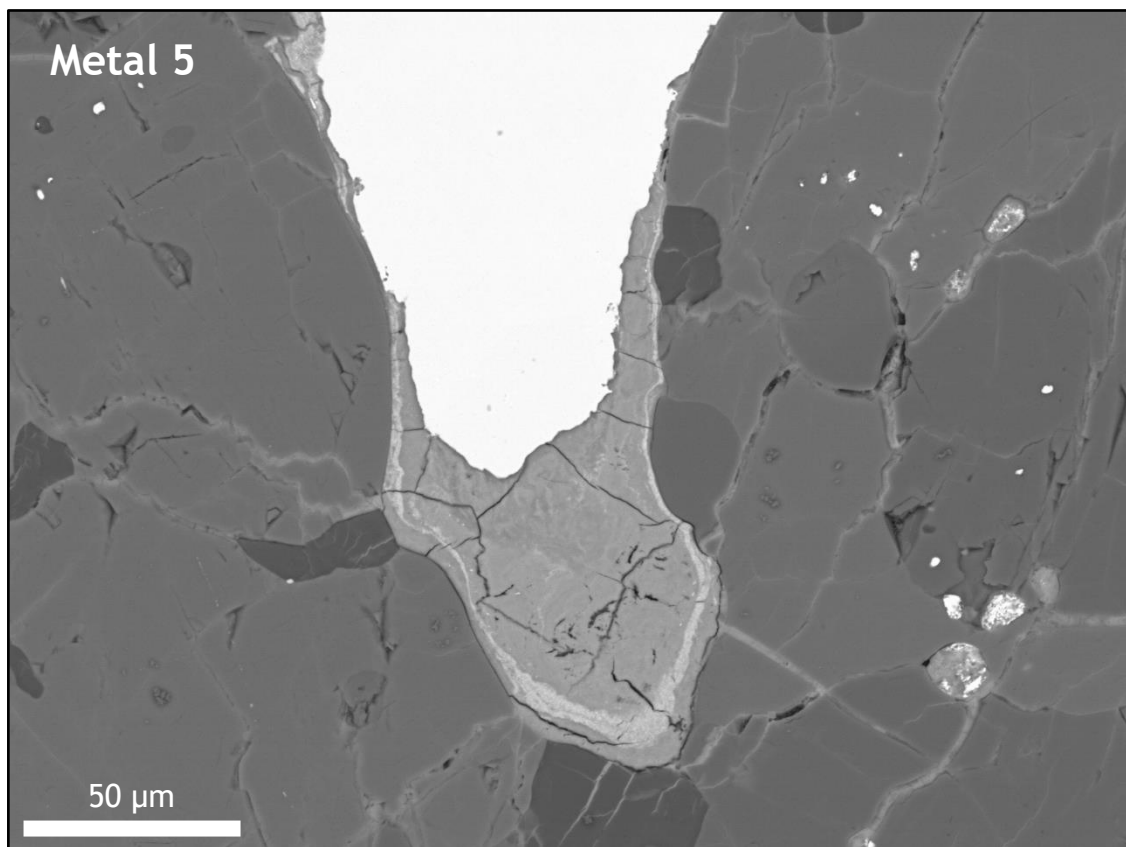


**Figure 3.10** BSE image of metal 5, Fe,Ni metal grain (white) with a large lobe of alteration products. The alteration material appears to have shared characteristics of the ordered and disordered material with crosscutting fractures and coarse, chaotic laminations.

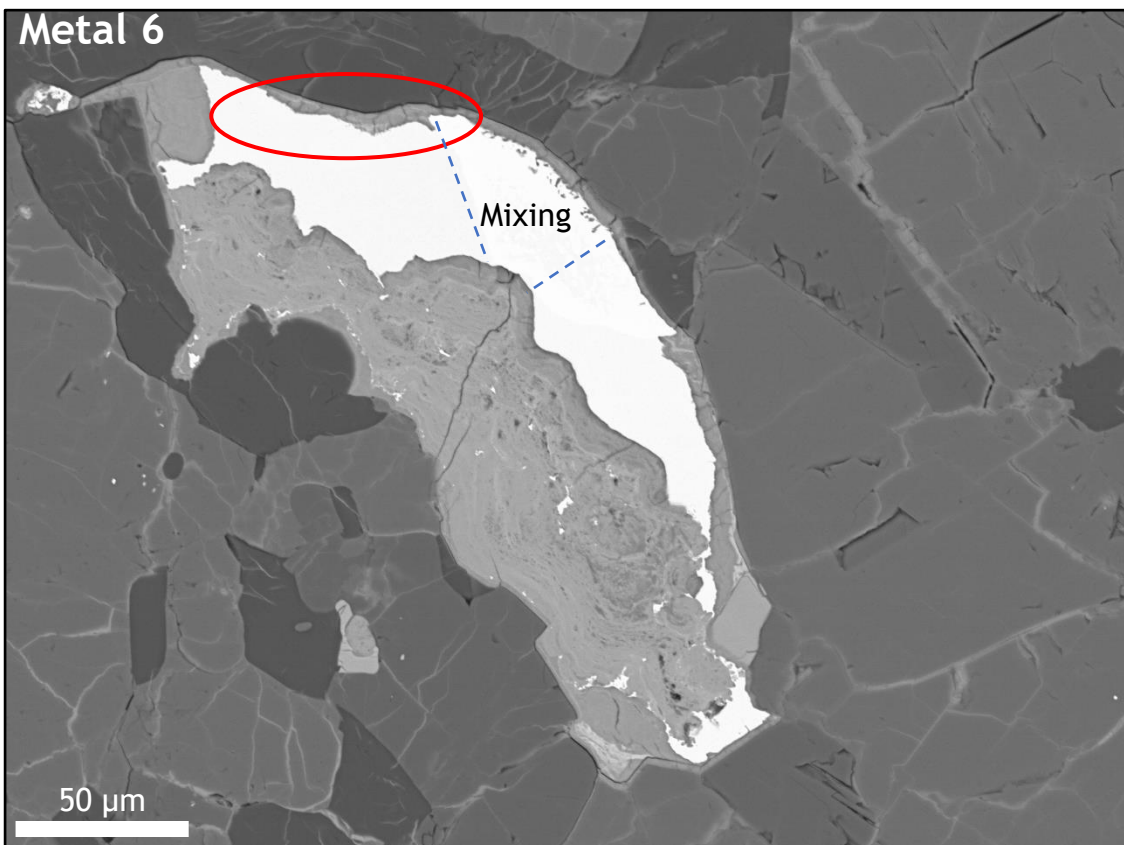


**Figure 3.11** BSE image of metal 6, Fe,Ni metal grain (white) with a zone of mixing between two materials. Most of the material is disordered with a small region of ordered material highlighted.

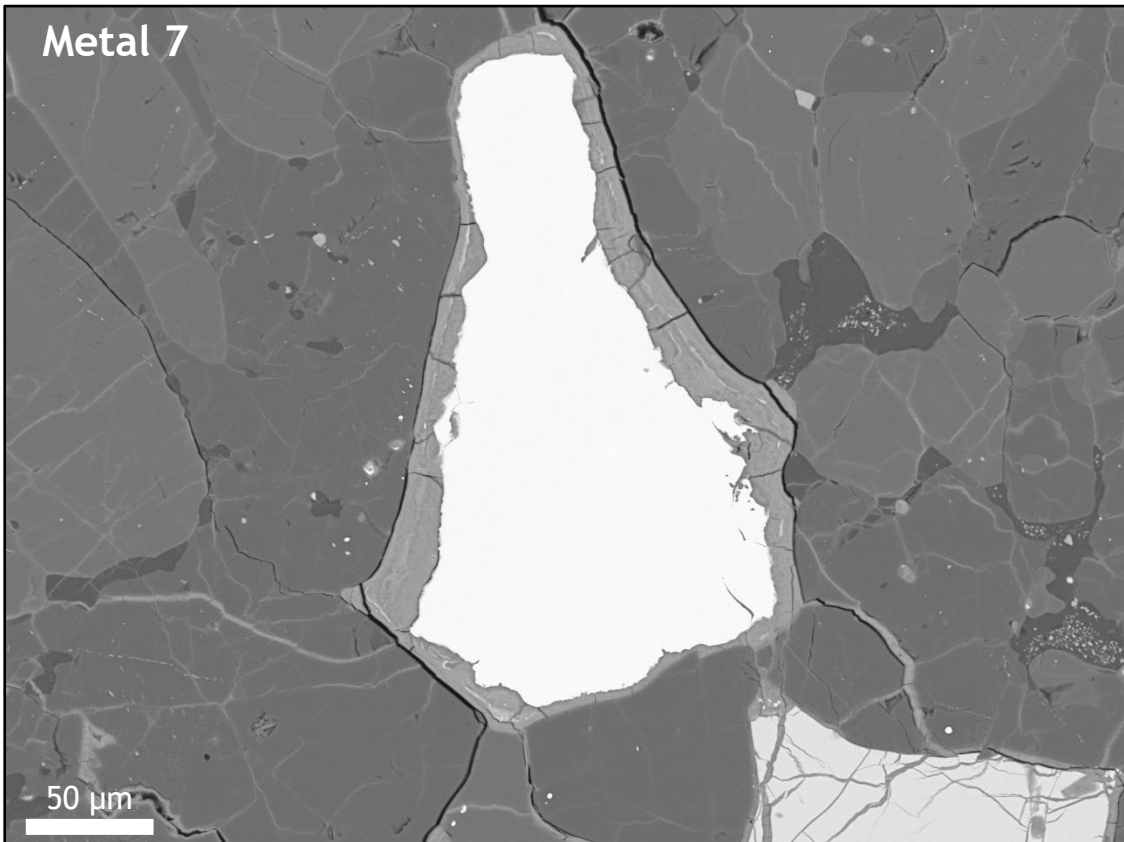


**Figure 3.12** BSE image of Metal 7, Fe,Ni metal grain (white) surrounded by an alteration rim of uniform thickness consisting of fractured and disordered material.

### Chemical Composition:

Chemical analysis shows metals 5 and 7 are kamacite with concentrations of 6.90 wt.% Ni and 6.12 wt.% Ni respectively (see appendix). Metal 6 was composed of both kamacite (5.92 wt.% Ni) and taenite (28.26 wt.% Ni) with a complex zone of mixing at their boundary (see appendix).

Figure 3.13A and C show EDS maps for Cl in metals 5 and 7 respectively. EDS maps and analysis of these metals demonstrates negligible Cl concentrations (0.73 wt.% or less) throughout their alteration rims. Figure 3.11B shows that metal 6 has similarly low Cl concentrations within the disordered material (<0.37 wt.%). However, within the ordered material (highlighted in figure 3.11), a Cl concentration of ~1 wt.% was observed representing a slight increase in Cl amongst the ordered material.

### Mineralogy

Point analysis Raman spectroscopy of metal 5 revealed one weak spectrum for goethite (Figure 3.14, spectrum A) and one inconclusive spectrum (Spectrum B) which was too weak to accurately determine the positions of more than two peaks ( $390\text{ cm}^{-1}$  and  $680\text{ cm}^{-1}$ ). Analysis of metal 6 revealed another inconclusive spectrum from the ordered material (Spectrum C). From the disordered material a very clear and well-defined spectrum for goethite characterised by a distinctive peak at  $390\text{ cm}^{-1}$  was produced (Spectrum D). Goethite is a secondary alteration product believed to form over time from akaganeite (Buchwald and Clarke, 1989).

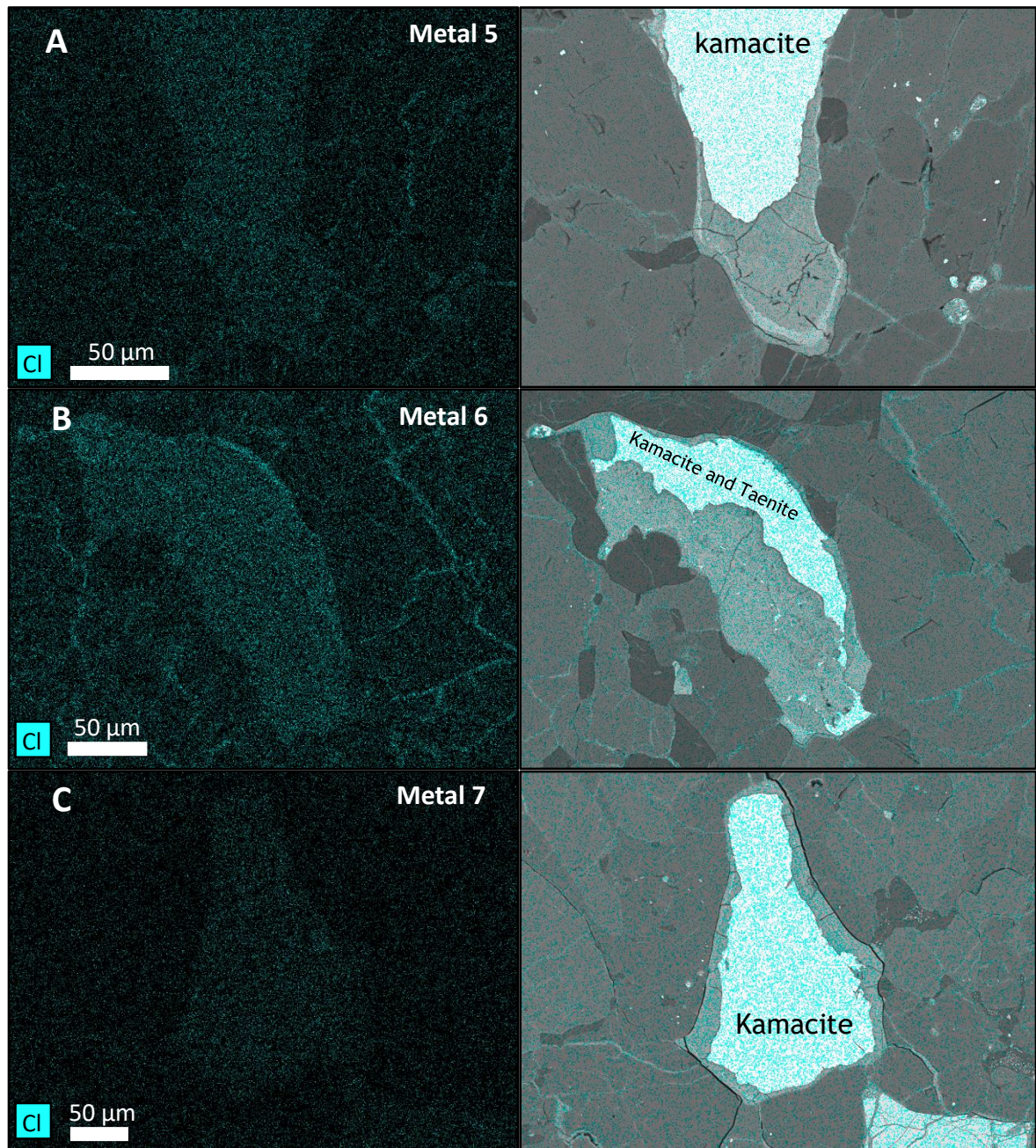


**Figure 3.13** EDS maps of metal 5 (A), metal 6 (B) and metal 7 (C). EDS maps for Cl (left). EDS maps for Cl overlaid on BSE images (right). Maps show consistently low Cl concentrations throughout all the alteration rims with only a slight increase seen in metal 6 (B), within the thin band of ordered material. The increase in Cl is indicated by the brighter blue colouration.

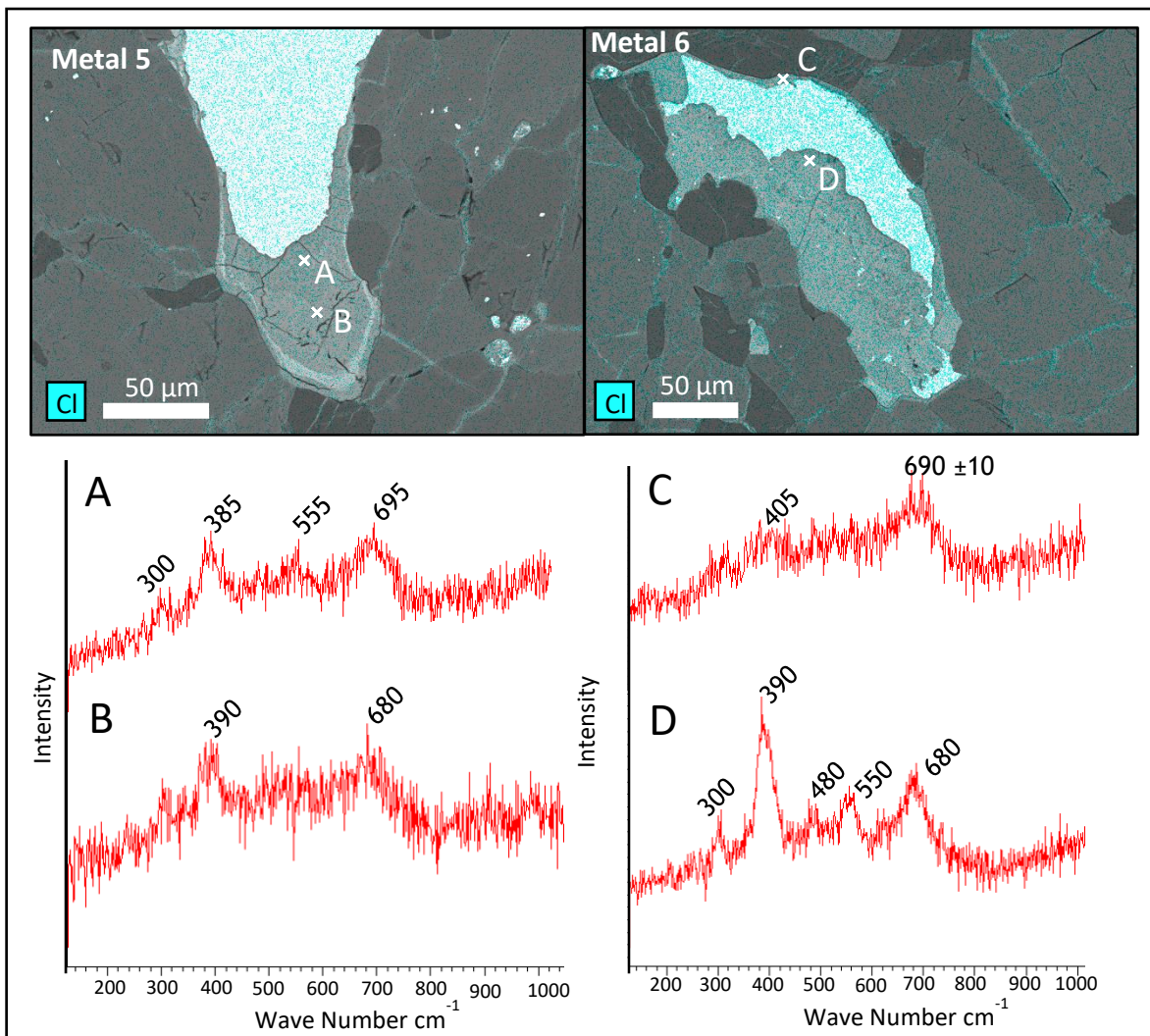


**Figure 3.14** EDS maps and accompanying Raman spectra for selected locations in metals 5 and 6. Spectrum A) Goethite, B) Inconclusive, C) Inconclusive, D) Goethite.

### 3.1.4 Summary of Antarctic Ordinary Chondrite Alteration

The Antarctic ordinary chondrites examined here contained kamacite and taenite. These metal grains were almost always surrounded by significant alteration rims with complex and varied internal structures. These alteration rims are composed of two textures, an ordered and disordered texture. No correlation between the texture, position within alteration rim, composition of Fe,Ni metal or alteration product could be drawn. EDS analysis and Raman spectroscopy showed that regions showing a significant increase in Cl likely corresponded to the mineral akaganeite. Within the Cl-poor areas Raman spectroscopy occasionally proved inconclusive but, generally revealed goethite. The inconclusive spectrum may represent either a sampling error or potentially a transition phase between

akaganeite and goethite. Further investigation would be required to determine this.

## 3.2 Australian Ordinary Chondrites

### 3.2.1 Environment

The Western Australian environment is semi-arid and represents approximately intermediate conditions between the hot and cold desert environments also analysed in this work. The Western Australian samples were collected close to the town of Forrest where the average summer maximum temperature is 33.2°C and average winter maximum temperature is 18.8°C (“Website 3.3”). The average annual rainfall in Forrest was 227.5 mm (“Website 3.3”).

### 3.2.2 Fe,Ni Metal

There was a significant variation in the amount of metal present within samples from this group (Table 3.3). Within Forrest 016 and Gunnadorah 004 the majority of the detected metal is troilite which is not a metal but a sulphide and so the percentages are not representative of Fe,Ni content. Forrest 016 and Gunnadorah are also H-chondrites and so would have naturally higher metal concentrations in their unaltered state than Forrest 028.

**Table 3.3** ImageJ calculated, percentage of kamacite, taenite and troilite in each of the Antarctic samples calculated from reflected light microscopy. Troilite is included despite being a sulphide as it could not be distinguished from Fe,Ni metal in ImageJ.

<i>Sample</i>	<i>Abundance (volume %)</i>
Forrest 016	6.85
Forrest 028	6.61
Gunnadorah 004	0.89

### 3.2.3 Alteration Products

Reflected light microscopy of these samples shows the intensity of alteration varies significantly between samples. Compared to the Antarctic samples there are far fewer large alteration rims surrounding Fe,Ni metal grains and many more veins of alteration material and largely or completely replaced metal grains.

#### 3.2.3.1 Forrest 016

Forrest 016 is an H5-6 chondrite with a weathering category of B-C, moderate to severe rustiness. AsB imaging confirms that the sample contains a significant amount of Fe-rich minerals (unsurprising for an H-chondrite) alongside a significant amount of alteration. The majority of the grains observed are heavily fractured troilite with very few Fe,Ni metal grains or alteration rims observed. Alteration is instead dominated by complete metal grain replacement and vein formation (Figure 3.15). Any alteration rims which are observed (Figure 3.16 and Figure 3.17) are significantly smaller than those seen previously in the Antarctic samples, with a maximum extent of ~50 µm and lacking internal structures and textural differences.

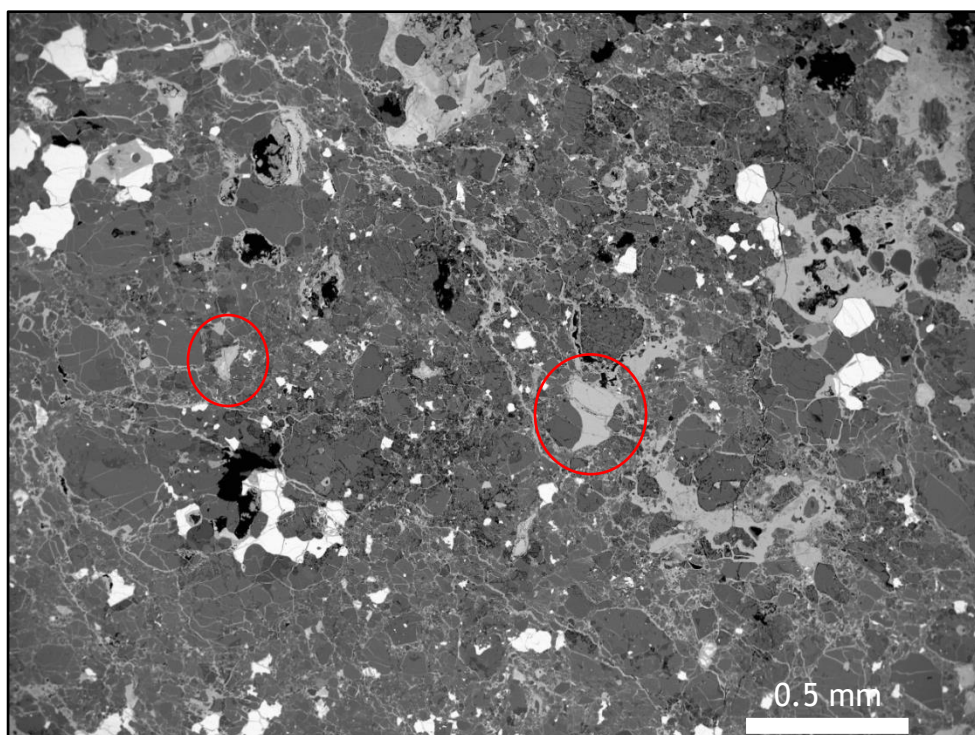


**Figure 3.15** BSE image of Forrest 016 showing the high proportion of Fe-rich minerals (white) and alteration products (grey) within the sample. Alteration products are found in veins and replacing entire metal gains. The highlighted regions are examples of complete metal grain replacement.

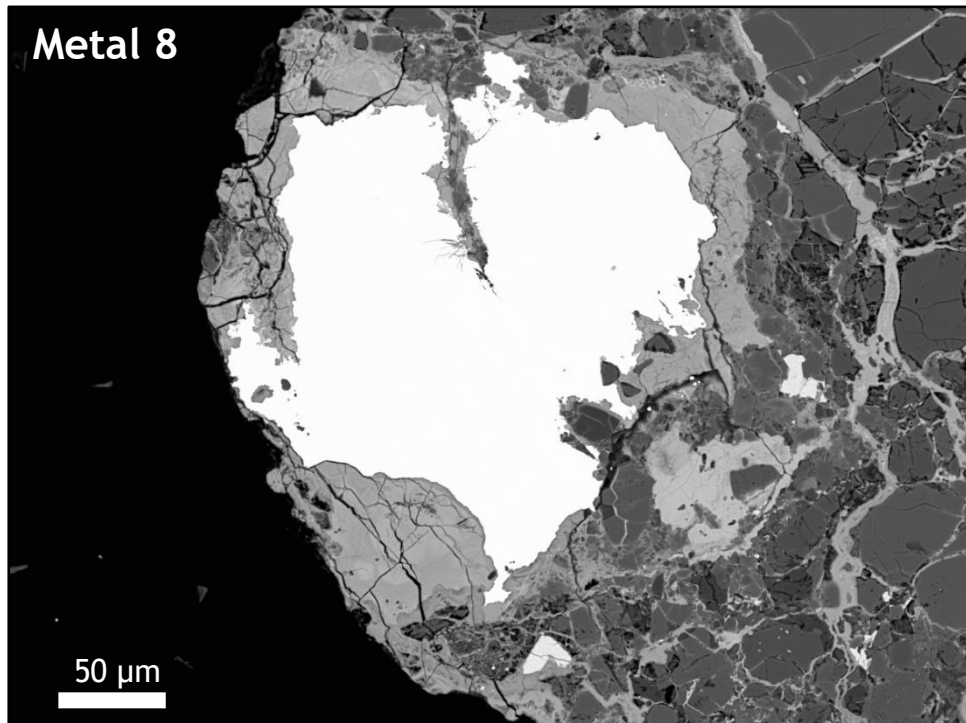


**Figure 3.16** BSE image of metal 8, a rare Fe,Ni metal grain (white) with an irregular and fractured alteration rim. This is the only Fe,Ni metal grain with an alteration rim observed in this sample.

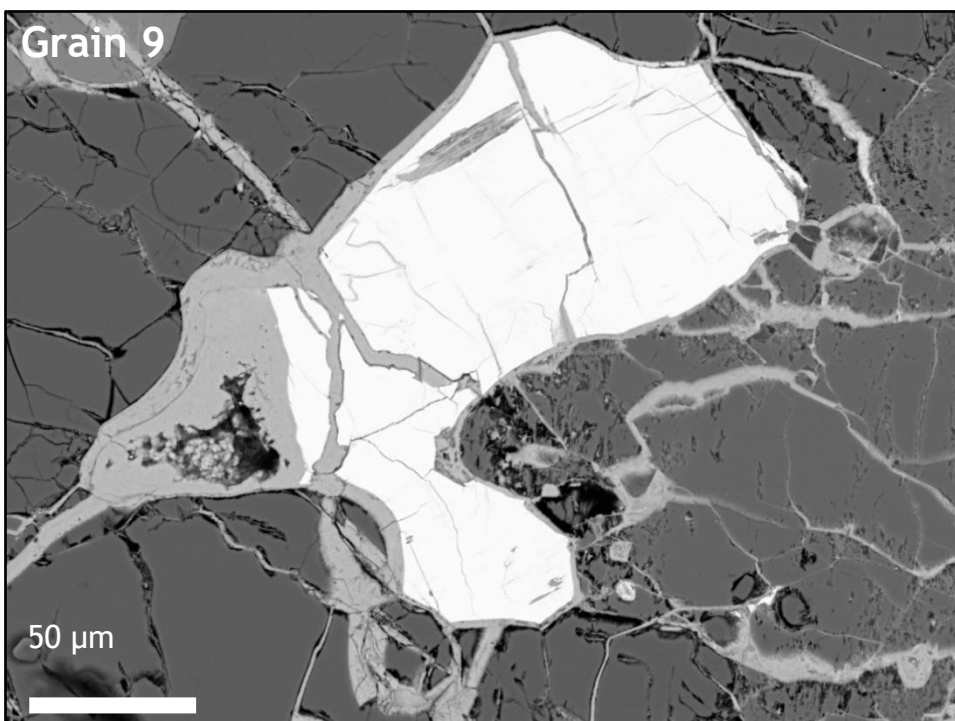


**Figure 3.17** BSE image of grain 9, a troilite grain (white) surrounded by an alteration rim and occluded veins. The material in the alteration rim and veins does not have any of the textural differences seen in the Antarctic samples.

#### Chemical Composition:

EDS mapping and analysis revealed that the majority of the Fe-rich grains in figure 3.15 are troilite (FeS) and that there is almost no Fe,Ni metal. Metal 8

(Figure 3.18A) was the only Fe,Ni identified; it is a kamacite grain with 6.78 wt.% Ni. EDS maps illustrate that the alteration rim surrounding metal 8 is not Cl-rich with EDS analysis detecting a maximum Cl concentration of 0.73 wt.%. The lack of Cl suggests that the alteration rim is not composed of akaganeite and is instead composed of goethite and hydrated iron III oxide or oxyhydroxide. Figure 3.18B shows one of many troilite grains within this sample. Analysis of this grain reveals a 36.17 wt.% S concentration (Table 3.4) in the sulphide grain and a negligible Cl concentration in the alteration rim (Table 3.4), again suggesting the presence of secondary alteration products. Figure 3.20A illustrates the relationship between  $\text{Fe}_2\text{O}_3$  and NiO. Used alongside figure 3.19 and table 3.4 it demonstrates that there is a weak relationship between NiO and  $\text{Fe}_2\text{O}_3$ . Those areas of the alteration rim with a higher  $\text{Fe}_2\text{O}_3$  abundance have a lower NiO abundance. Figure 3.20B shows a low S concentration throughout the alteration products and no relationship between  $\text{Fe}_2\text{O}_3$  and S. The abundant S within the original troilite (Table 3.4) is therefore not being incorporated into the alteration material, thus as the troilite grain is eroded any S released is being re-distributed.

Due to the lack of Fe,Ni metal grains, the abundance of troilite, alongside the negligible Cl concentrations measured within the alteration materials, it is reasonable to assume that this is a very heavily altered sample. Gooding (1986) found troilite was less susceptible than any Fe,Ni metal to weathering and alteration. It is therefore likely that significant alteration has led to the complete replacement of most Fe,Ni metals and only remnant grains, such as metal 8, and troilite grains (which are now beginning to alter) survive. This theory supports the earlier observation of extensive replacement in figure 3.15.

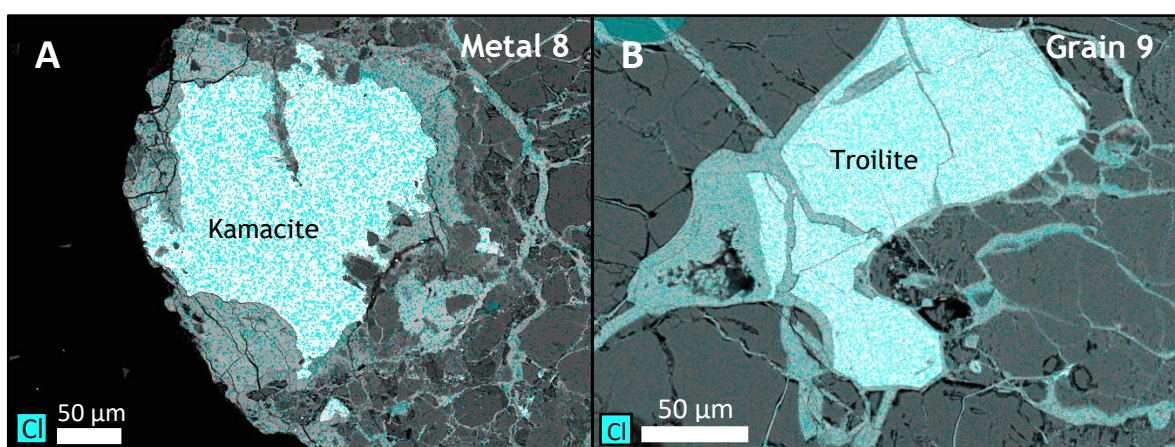


**Figure 3.18** EDS maps of Cl overlaid on BSE images for; Metal 8 (A) and, Grain 9 (B). Maps show negligible increase in Cl between metal, alteration rim and surrounding material.

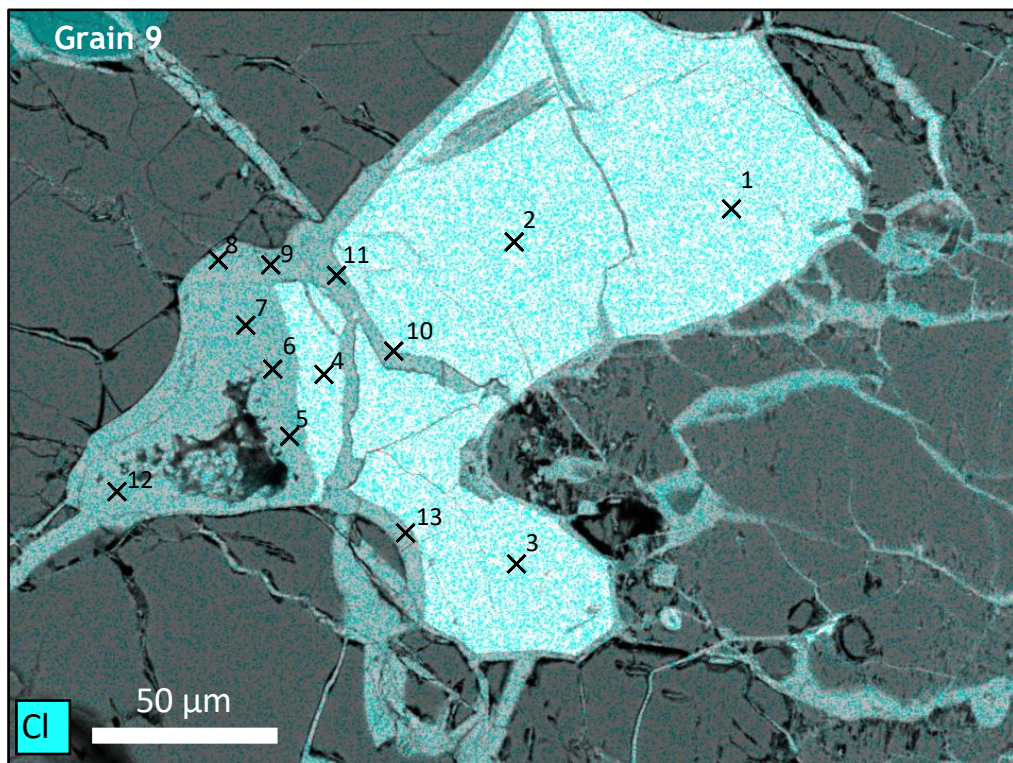


**Figure 3.19** EDS map of Cl overlain on BSE image of grain 9. Labelled are the points of analysis shown in Table 3.4

**Table 3.4** Results of EDS analysis in grain 9 with position numbers corresponding to those shown in figure 3.19. Values shown in wt.%. Minimum detection limits are stated below.

Position Number	SiO <sub>2</sub>	Al <sub>2</sub> O <sub>3</sub>	Fe <sub>2</sub> O <sub>3</sub>	MgO	CaO	NiO	S	Cl	Fe <sub>(m)</sub>	Total
1	0.47	-	-	-	-	-	35.82	-	64.24	100.53
2	-	-	-	-	-	-	35.97	-	65.57	101.54
3	-	-	-	-	-	-	36.17	-	64.66	100.83
4	-	-	-	-	-	-	35.60	-	64.26	99.86
5	3.62	1.28	73.35	-	-	2.64	-	-	-	80.89
6	3.77	0.47	74.88	-	-	2.48	-	-	-	81.59
7	3.38	-	74.58	-	-	2.34	-	0.22	-	80.51
8	4.79	0.68	71.83	0.67	0.21	2.54	-	-	-	80.72
9	5.20	0.89	68.49	0.52	0.27	2.71	-	-	-	78.06
10	4.32	0.51	74.58	-	0.24	2.31	0.97	-	-	82.93
11	3.81	0.81	72.06	-	0.25	2.50	0.23	-	-	79.66
12	3.62	-	74.02	-	0.20	2.45	-	-	-	80.28
13	5.71	1.36	72.33	0.67	0.29	2.65	0.22	-	-	83.24
Minimum detection limit	0.07	0.01	0.20	0.05	0.05	0.28	0.08	0.08	0.20	

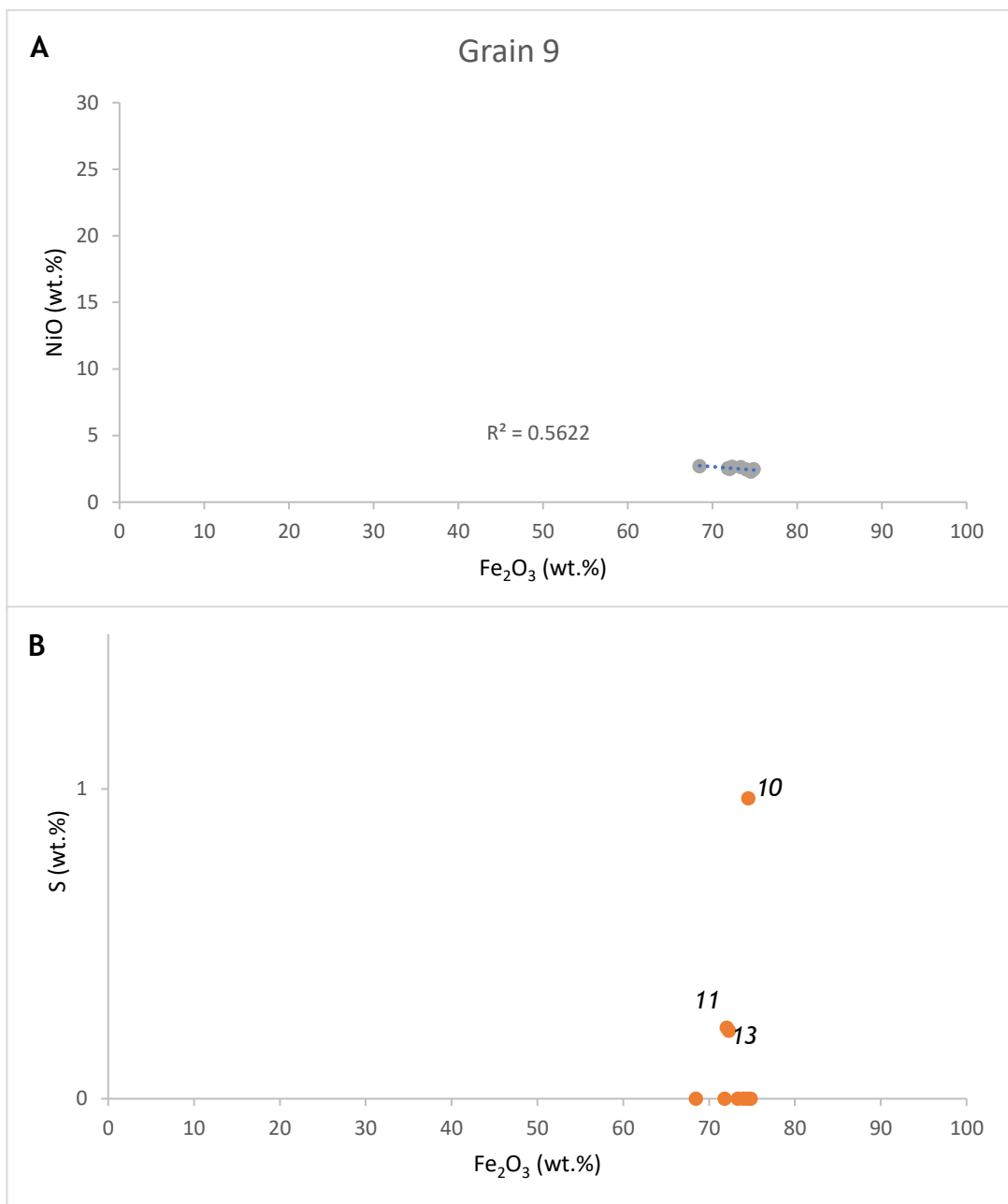


**Figure 3.20** Graphs illustrating the relationships between  $Fe_2O_3$  (wt.%) and the key elements investigated in grain 9 (a troilite). Data taken from Table 3.4 and values given in wt.%. Labels correspond to position numbers in Figure 3.19 and Table 3.4 A) Graph of  $Fe_2O_3 - NiO$ , B) Graph of  $Fe_eO_3 - S$ .

## Mineralogy:

Point analysis Raman spectroscopy was carried out on the alteration products observed around metal 8 and grain 9 (Figure 3.21). The results confirm the findings of the EDS mapping and analysis with no Cl-bearing akaganeite detected. Within metal 8, two different spectra were detected. Spectrum A was not identified previously, in Antarctic meteorites, it is defined by three peaks at  $380\text{ cm}^{-1}$ ,  $495\text{ cm}^{-1}$  and  $700\text{ cm}^{-1}$ . It does not match any spectrum listed on the Wire 4.4 library or the Ruff database. Returning to the literature Neff et al. (2006) and Bellot-Gurlet et al. (2009) find similar spectra and identify it as a hydrated iron III oxide or oxyhydroxide, which is a less crystallised  $\text{Fe}^{3+}$  phase. Hydrated iron III oxide or oxyhydroxide is a generic term which is applied to the poorly crystallised phases of Maghemite, Ferrihydrite 6-line, Ferrihydrite 2-line and feroxyhite ( $\delta$ - $\text{FeOOH}$ ) which all produce very similar Raman Spectra (Bellot-Gurlet et al., 2009).

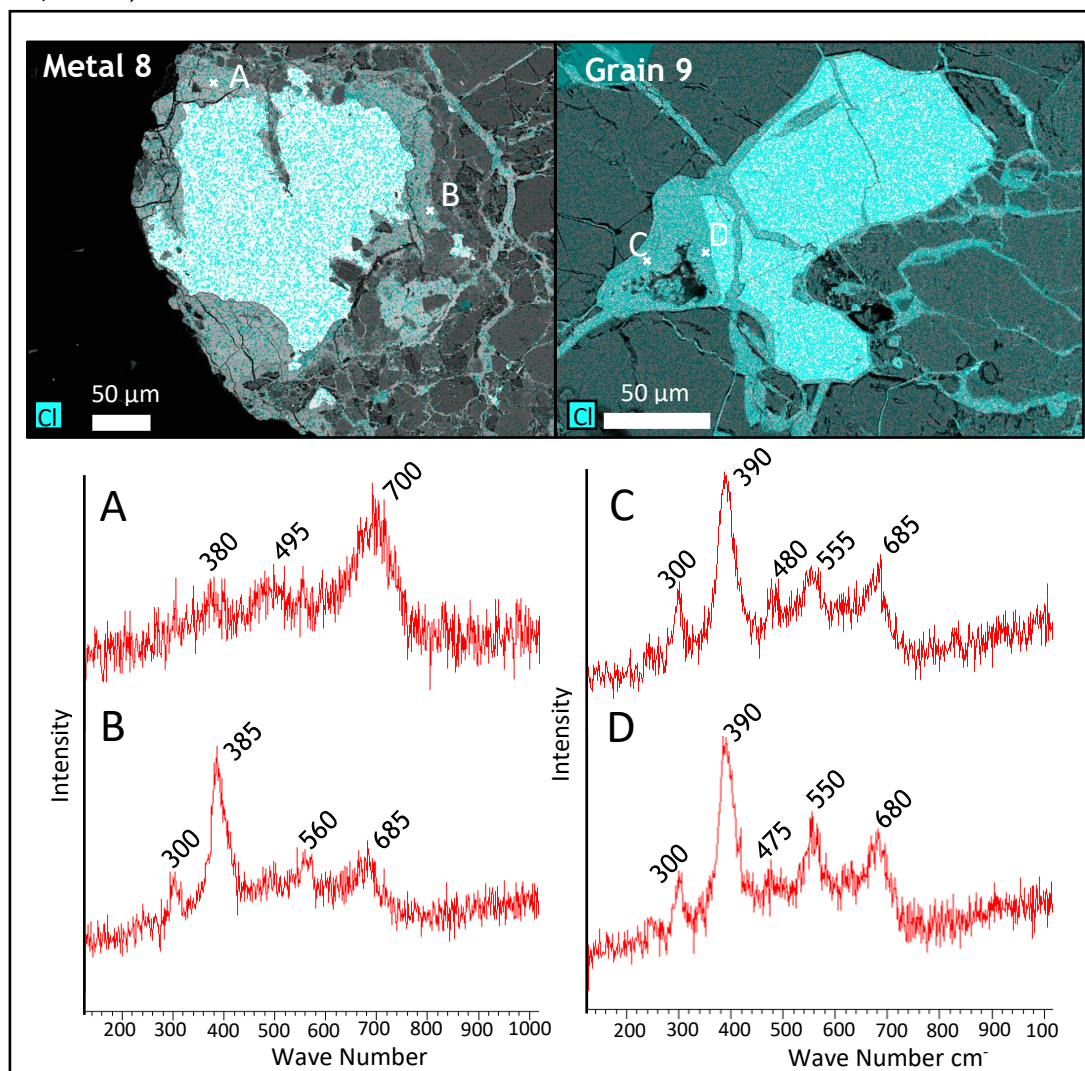


**Figure 3.21** EDS maps and accompanying Raman spectra for selected points in metals 8 and 9. Spectrum A) Hydrated iron III oxide or oxyhydroxide, B) Goethite, C) Goethite, D) Goethite.

Spectrum B from metal 8 returned a spectrum for goethite confirming the presence of more developed alteration products. The alteration rim surrounding grain 9 also returned clear well defined spectra for goethite, suggesting that even within the more resistant troilite, alteration has been significant (Gooding, 1986).

### 3.2.3.2 Forrest 028

Forrest 028 is an L7 chondrite and is of weathering category C - severe rusting. The L7 classification is not used consistently or widely accepted within the literature but represents samples which have been heated to the point of almost melting (The Meteoritical Society, 2017). AsB imaging shows that unlike Forrest 016 this sample has large and abundant Fe,Ni metals with significant alteration rims, in excess of 50 µm thick around the majority of metal grains (Figures 3.22, 3.23, 3.24 and 3.25). Textural variations within the alteration rims, as seen in the Antarctic samples, were absent here. Alteration material was instead characterised by chaotic laminations and variations from pale to dark grey in BSE images of the alteration rim. Changes in the greyscale result from a changing atomic number in the material present and was observed in metals 11, 12 and 13 (Figures 3.23, 3.24 and 3.25) typically forming bands throughout the alteration rims.

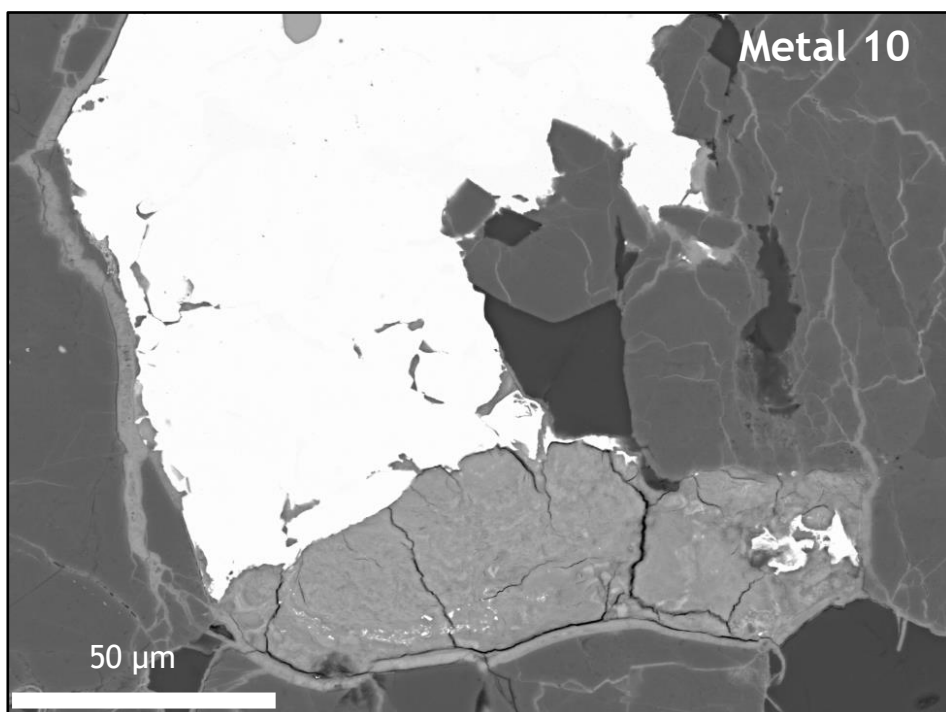


**Figure 3.22** BSE image of metal 10, an Fe,Ni metal grain (white) with a lobe of alteration. This alteration rim has chaotic laminations and fractures throughout and does not show any changes in material colour.

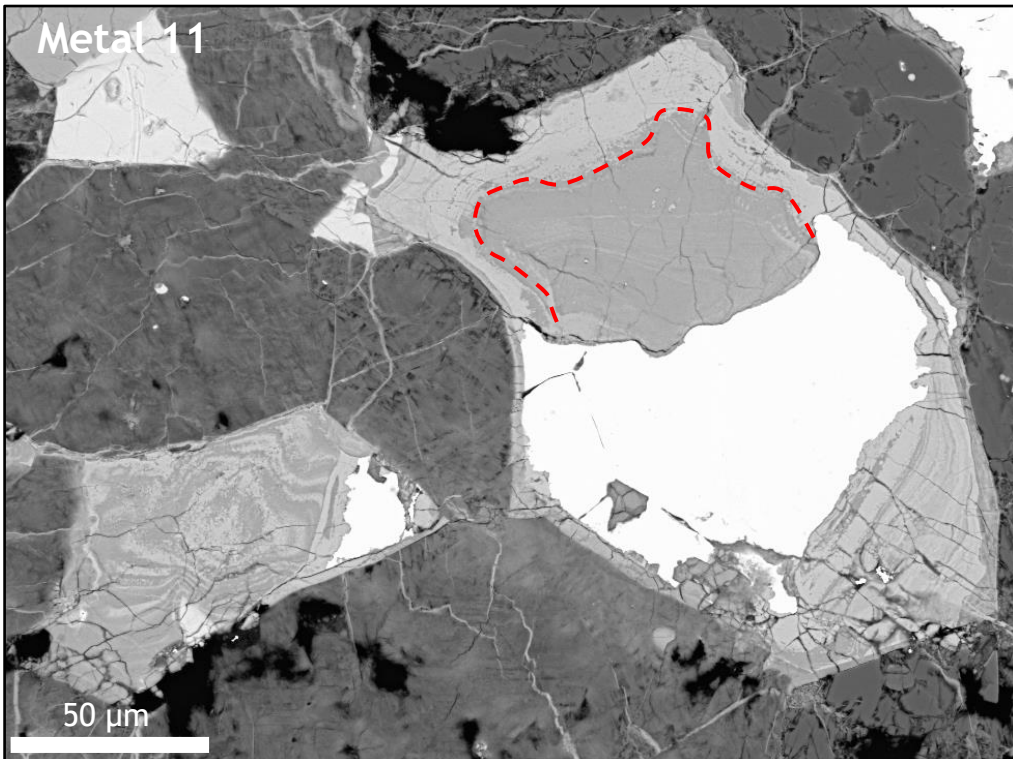


**Figure 3.23** BSE image of metal 11, an Fe,Ni metal grain (white) with a significant alteration rim demonstrating two bands of material (pale and dark grey). The boundary between the bands is highlighted.

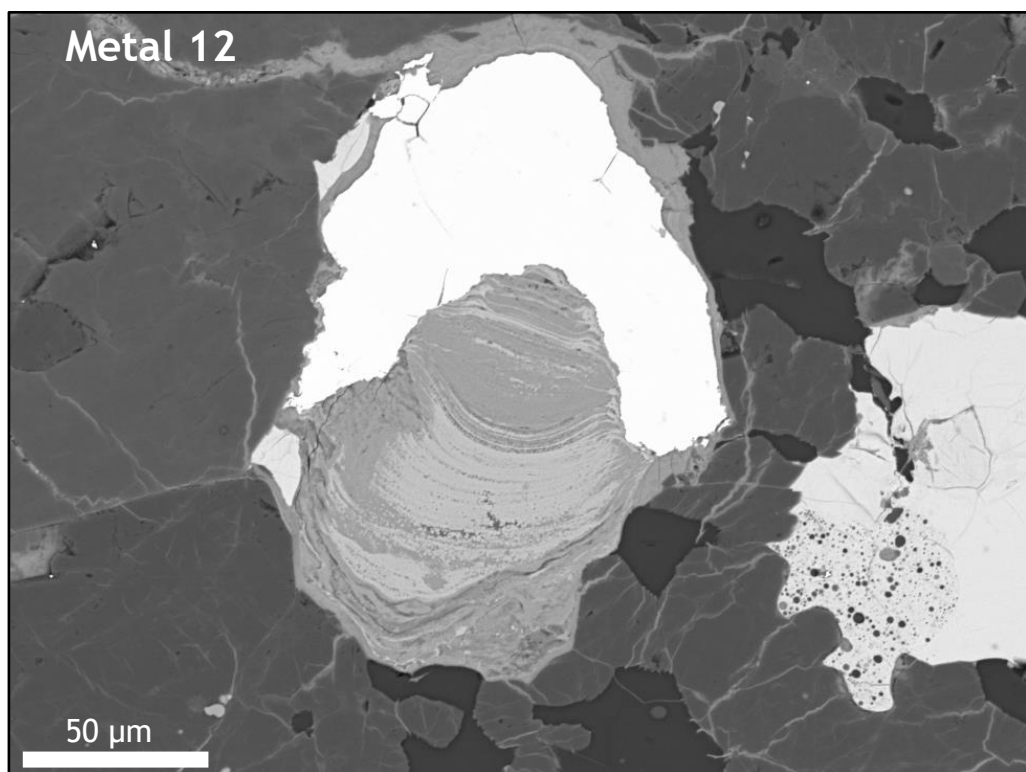


**Figure 3.24** BSE image of metal 12, an Fe,Ni metal grain (white) with a large alteration rim demonstrating alternating bands of material with different greyscales (and thus atomic numbers) throughout the alteration rim.

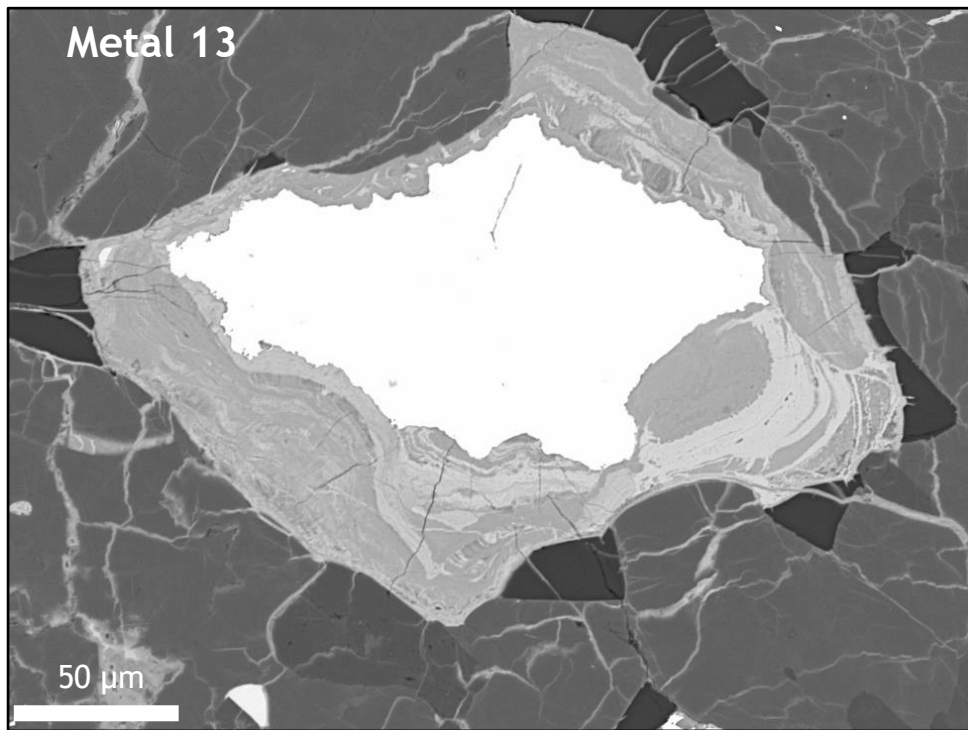


**Figure 3.25** BSE image of metal 13, an Fe,Ni metal grain completely surrounded by a significant alteration rim and demonstrating bands of material running through the alteration rim.

#### Chemical Composition:

Qualitative analysis of metals 10, 11, 12 and 13 revealed a mixture of kamacite and taenite metal grains. Metal 10 was shown to be a taenite grain with a higher concentration of Ni, whilst metals 11, 12 and 13 were all shown to be kamacite grains.

EDS mapping of Cl within metals 10 and 11 (Figures 3.26A and B respectively) revealed the largest and most significant areas of Cl-enrichment seen in any alteration rim so far in this chapter. Metal 10 was shown by EDS analysis to have a Cl content, within the enriched zone, of 1.26 wt.% compared to 0.70 wt.% in the adjoining non-enriched zone. A similar contrast exists in metal 11 where enriched material has a maximum Cl concentration of 5.48 wt.%, compared to just 0.25 wt.% in the non-enriched zone (Table 3.5). Examining the location of this enrichment in metal 11 also reveals that it is confined to the darker coloured material seen by BSE, with the colour boundary and enrichment boundaries matching. Metal 12 (Figure 3.26C) shows the least distinct Cl

enrichment with only a small increase in the Cl concentration towards the alteration rim boundary where darker material is more dominant. In this region Cl concentrations reach ~0.90 wt.%. Towards the middle of the alteration rim, where paler material is dominant Cl is below the detection limits.

Analysis also showed that the Ni concentration within the alteration products also varied between metal 10, taenite and metal 11, kamacite. Alteration products surrounding the taenite had a NiO contents of up to 34.11 wt.%, whereas material surrounding kamacite had a Ni content of up to 7.51 wt.%. This supports the findings of from the Antarctic samples where original parent metal grain Ni is being incorporated into the alteration products at similar concentrations.

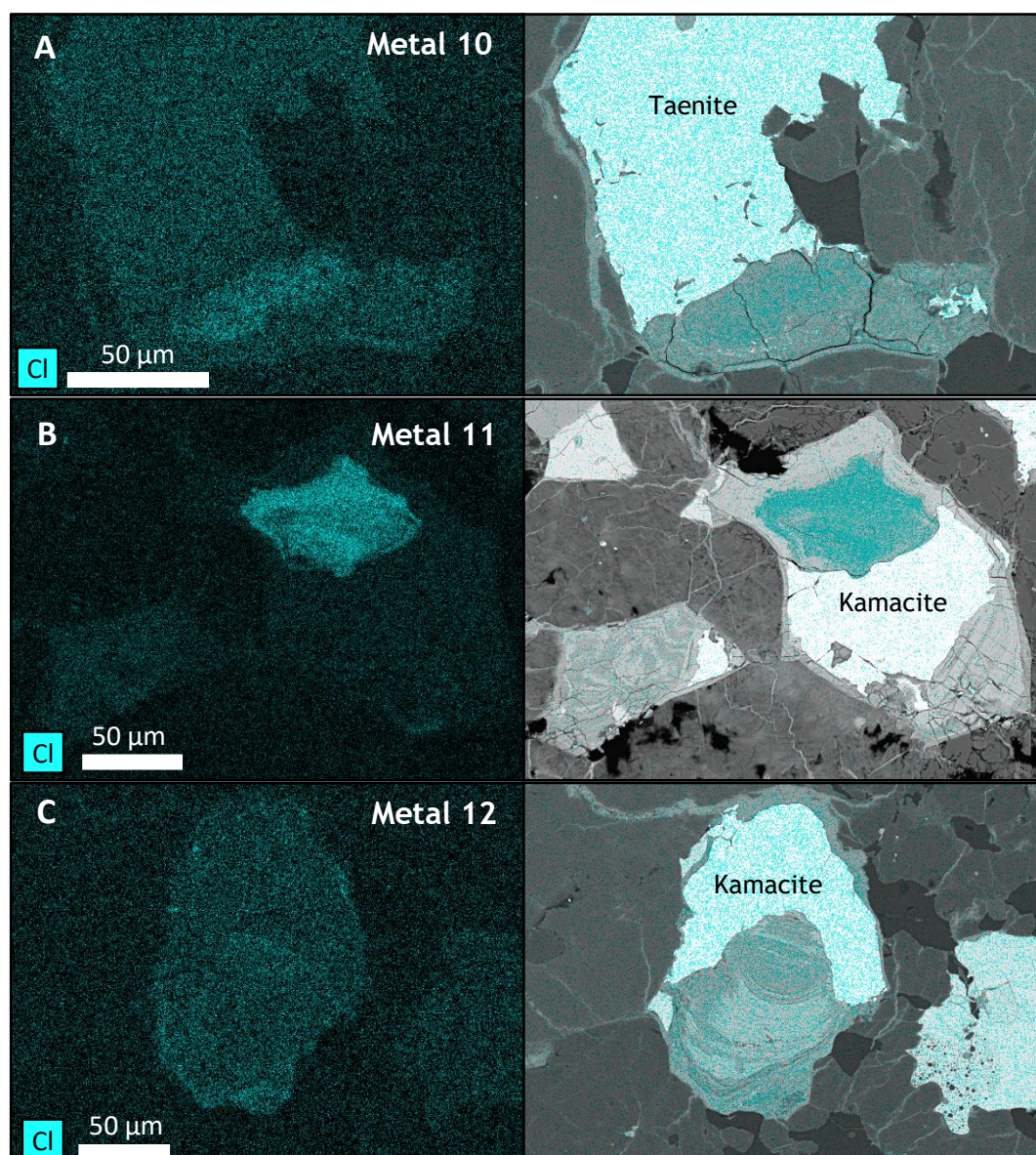


**Figure 3.26** EDS maps of metal 10 (A), metal 11 (B) and metal 12 (C). EDS maps for Cl (left). EDS maps for Cl overlain on BSE images (right). Figures B and C demonstrate the Cl enrichment confined to the darker coloured material.

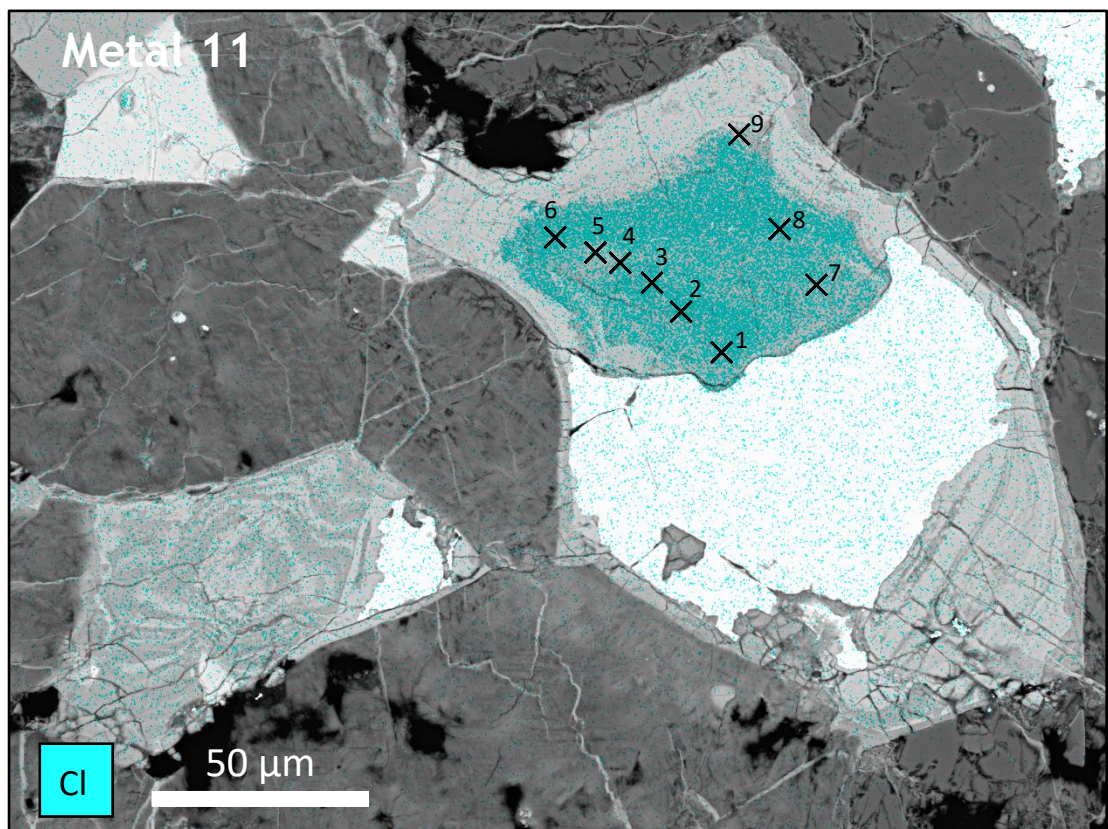


**Figure 3.27** EDS map of Cl overlain on a BSE image of metal 11. Labelled are the points of analysis shown in Table 3.5

**Table 3.5** Results of EDS analysis in metal 11 with positions numbers corresponding to those shown in figure 3.27. Values shown in wt.%. Minimum detection limits are stated below.

Position number	SiO <sub>2</sub>	Al <sub>2</sub> O <sub>3</sub>	Fe <sub>2</sub> O <sub>3</sub>	MgO	CaO	NiO	S	Cl	Fe <sub>(m)</sub>	Ni	Total
1	0.94	0.15	91.00	0.13	-	6.30	-	4.88	-	-	103.41
2	0.64	0.15	89.26	0.12	-	5.87	-	5.18	-	-	101.22
3	1.01	0.17	88.10	0.20	0.11	7.16	-	4.65	-	-	101.40
4	1.56	0.26	89.77	-	0.22	7.39	-	4.04	-	-	103.26
5	1.52	0.13	92.76	-	0.18	6.96	-	3.56	-	-	105.12
6	0.79	0.15	88.84	0.08	-	6.63	-	5.48	-	-	101.98
7	1.56	-	92.63	0.17	0.17	5.32	-	3.60	-	-	103.45
8	0.73	0.25	89.12	-	-	5.78	-	5.05	-	-	100.92
9	0.71	0.25	90.32	0.15	-	7.05	-	3.72	-	-	102.19
<b>Minimum detection limit</b>		0.06	0.07	0.17	0.04	0.08	0.25	0.08	0.07	0.17	0.25

## Mineralogy:

Point analysis Raman spectroscopy was carried on the alteration rims of metals 11 and 12 (Figure 3.28). The results show that the pale, Cl-poor material in metal 11 (figure 3.28 spectrum A) is likely hydrated iron III oxide or oxyhydroxide and the Cl-rich, darker coloured material was akaganeite (figure 3.28 spectrum B). Raman analysis of metal 12 showed a similar pattern with the paler material closest to the metal grain returning spectra for goethite and the Cl-enriched material towards the edge of the metal grain returning spectra for akaganeite. The Raman analysis confirms that the darker coloured, Cl-rich material seen in this sample is the more primitive alteration product and that the paler material is likely represents more developed alteration products.

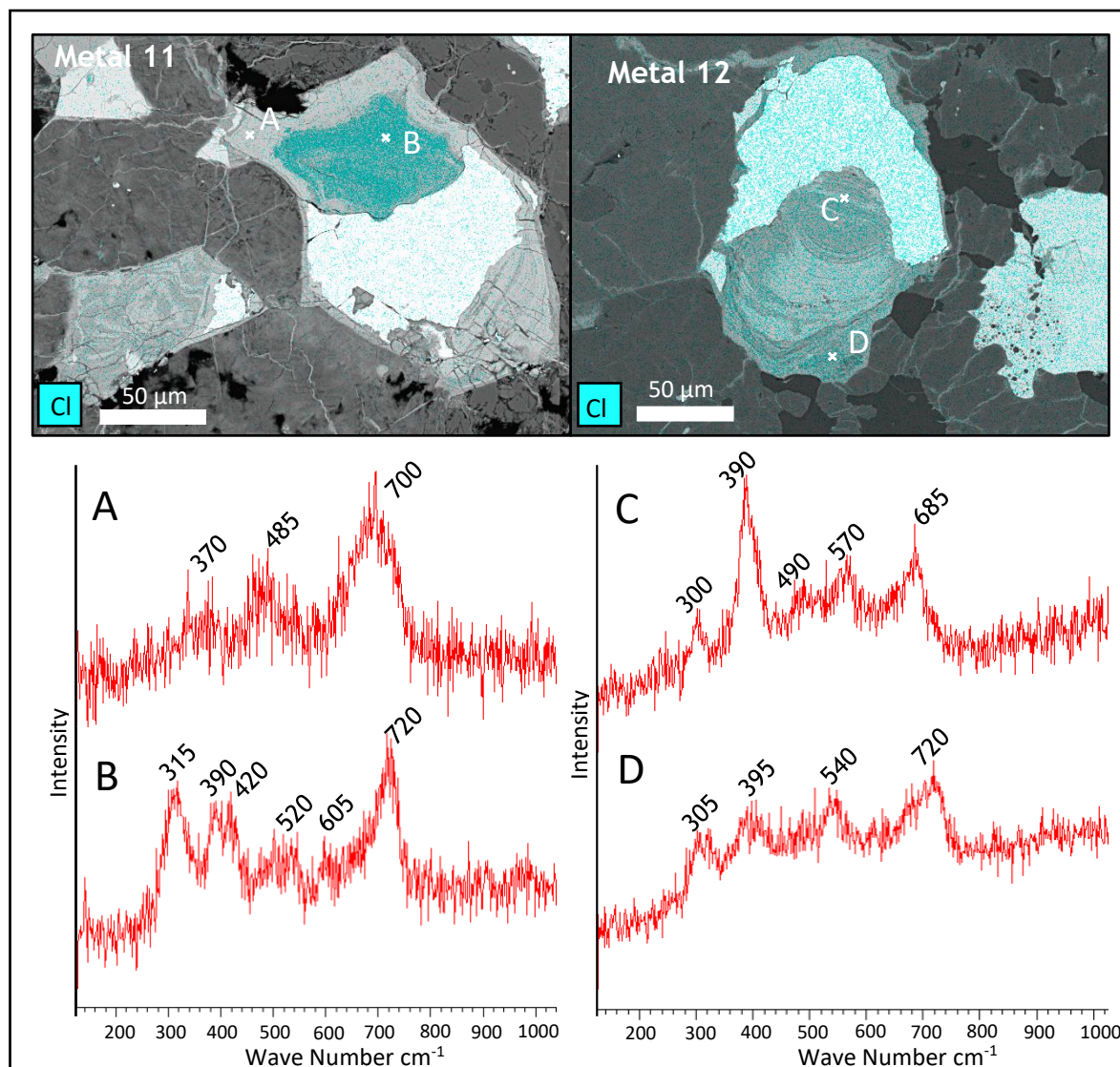


**Figure 3.28** EDS maps and accompanying Raman spectra for selected points within metals 11 and 12. Spectrum A) Hydrated iron III oxide or oxyhydroxide, B) Akaganeite, C) Goethite, D) Akaganeite.

### 3.2.3.3 Gunnadorah 004

Gunnadorah 004 is an H5 chondrite with a weathering classification of W2. AsB imaging shows that similar to Forrest 016 there are very few metal grains within the sample and a significant amount of alteration material forming veins and completely replacing metal grains (Figure 3.29). The few grains which remain only partially altered are troilite (Figure 3.30), suggesting that this sample is heavily weathered and has experienced very significant alteration.

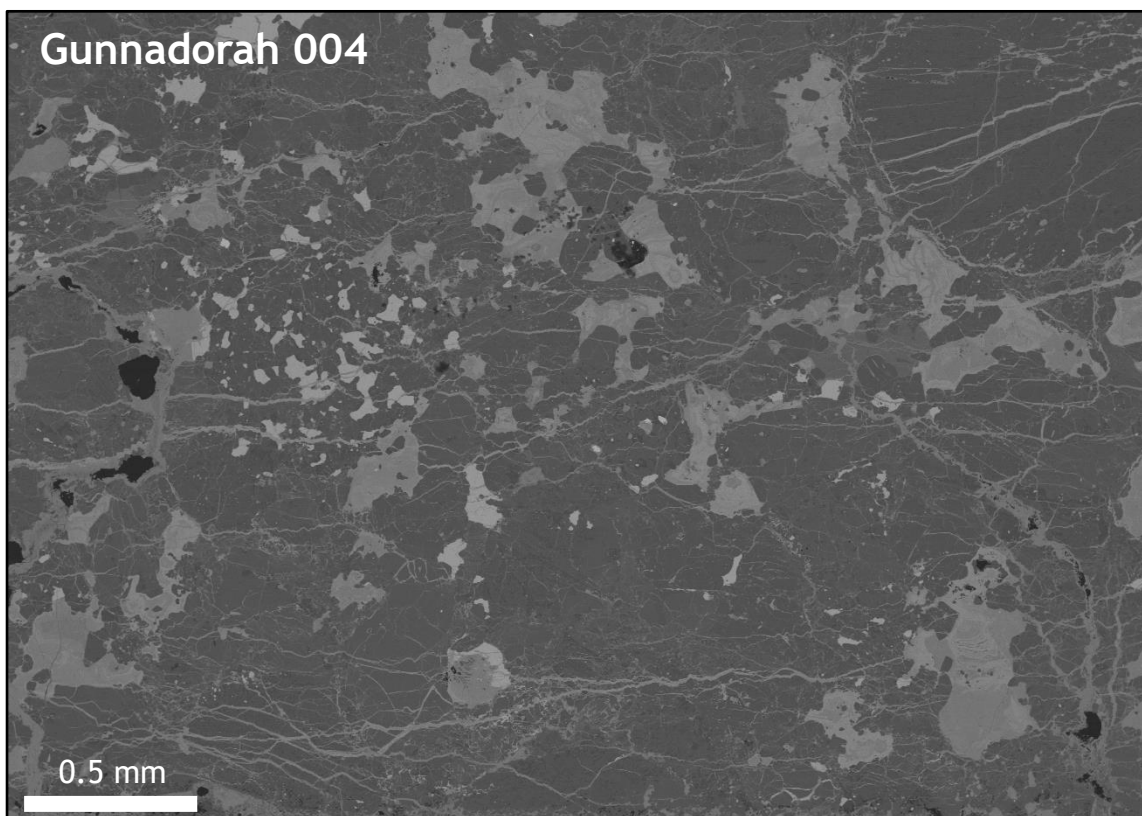


**Figure 3.29** BSE image of Gunnadorah 004 showing no metal grains but significant amounts of alteration material (grey). The alteration material is replacing most of the original metal grains and occluding fractures throughout the sample.

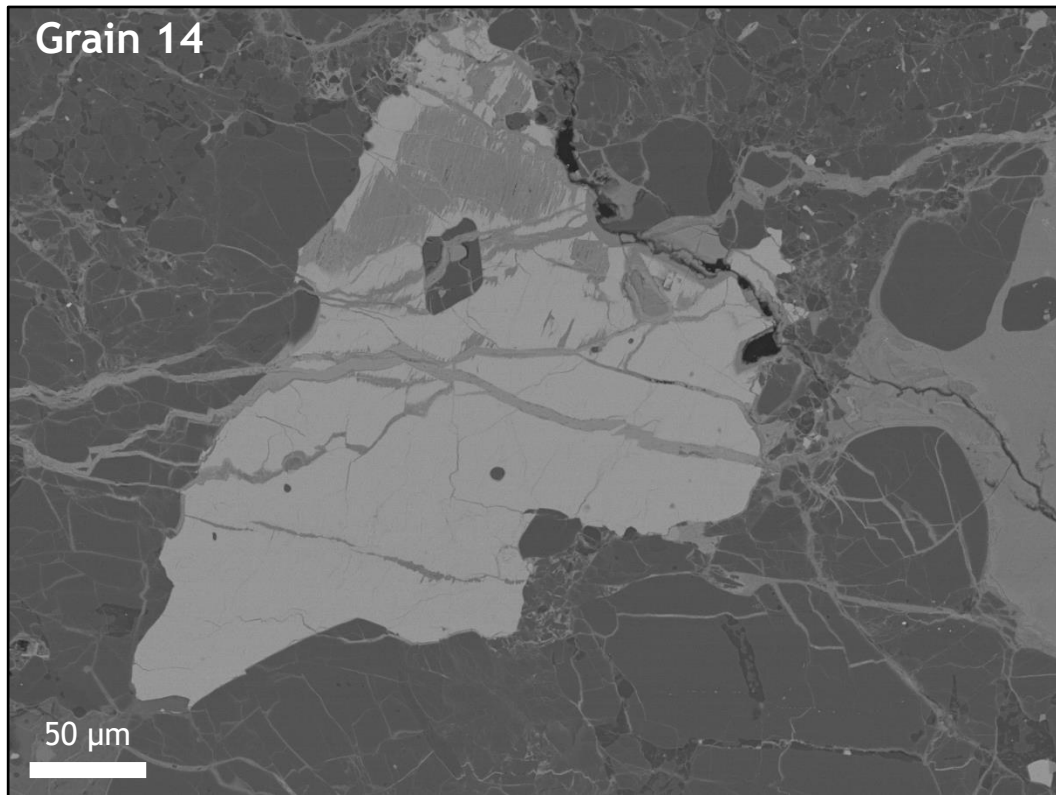


**Figure 3.30** BSE image of grain 14, troilite grain (palest grey), one of only a handful of Fe-rich grains present within Gunnadorah 004. It shows a heavily fractured nature and is surrounded by veins of alteration product.

### Chemical Composition:

EDS Mapping of this sample confirmed the few Fe-rich grains in the sample are troilite and that no Fe,Ni metal remains. EDS analysis of grain 14 revealed a S concentration of 36.29 wt.% within the grain and no Cl detected with the alteration rim (see appendix). EDS mapping of Cl was carried out over a large area in Figure 3.31 to search for any ‘primitive’ alteration products. The results of this mapping revealed negligible amounts of Cl throughout the sample suggesting that the alteration material which has replaced the Fe,Ni metal grains is a secondary alteration product such as goethite. There are two small areas of marginally higher Cl concentration, which are indicated in figure 3.31 however, these regions still have a negligible Cl concentration according to EDS measurements.

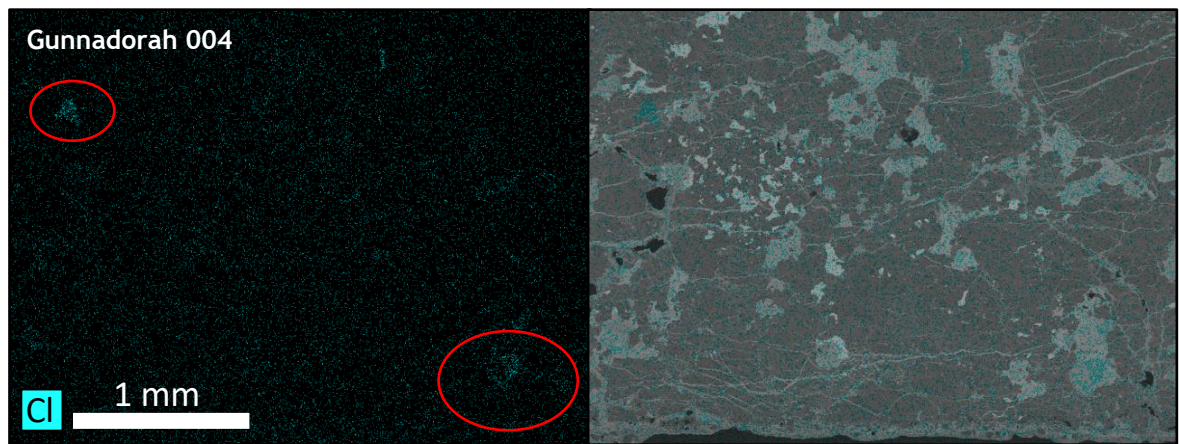


**Figure 3.31** EDS maps of Gunnadorah 004. EDS map of Cl (left). EDS map of Cl overlain on a BSE image (right). Highlighted are areas appearing to be slightly Cl enriched but still have a negligible measured concentration.

### Mineralogy:

Point analysis Raman spectroscopy was carried out on regions of suspected complete metal grain replacement in figure 3.31 and on grain 14. The spectra returned from completely replaced Fe,Ni metal grains confirmed the results of the EDS analysis with no Cl-bearing akaganeite and both points of analysis returning spectra for goethite (Figure 3.32, spectra A and B). The presence of goethite confirms more developed alteration. Spectrum B was sampled from one of the supposedly Cl-rich areas highlighted by the initial EDS mapping. The Raman spectrum for goethite confirms that this Cl increase was not significant and that the more than a visual inspection of the EDS maps of Cl is required for the accurate determination of the alteration product present.

Raman analysis carried out on the troilite grain, grain 14 shows that in areas where there looked to be the beginnings of metal grain replacements there was, with spectrum C returning a result for goethite. Additional analysis was also carried out on a vein cross-cutting the troilite, this returned a spectrum for hydrated iron III oxide or oxy-hydroxide.

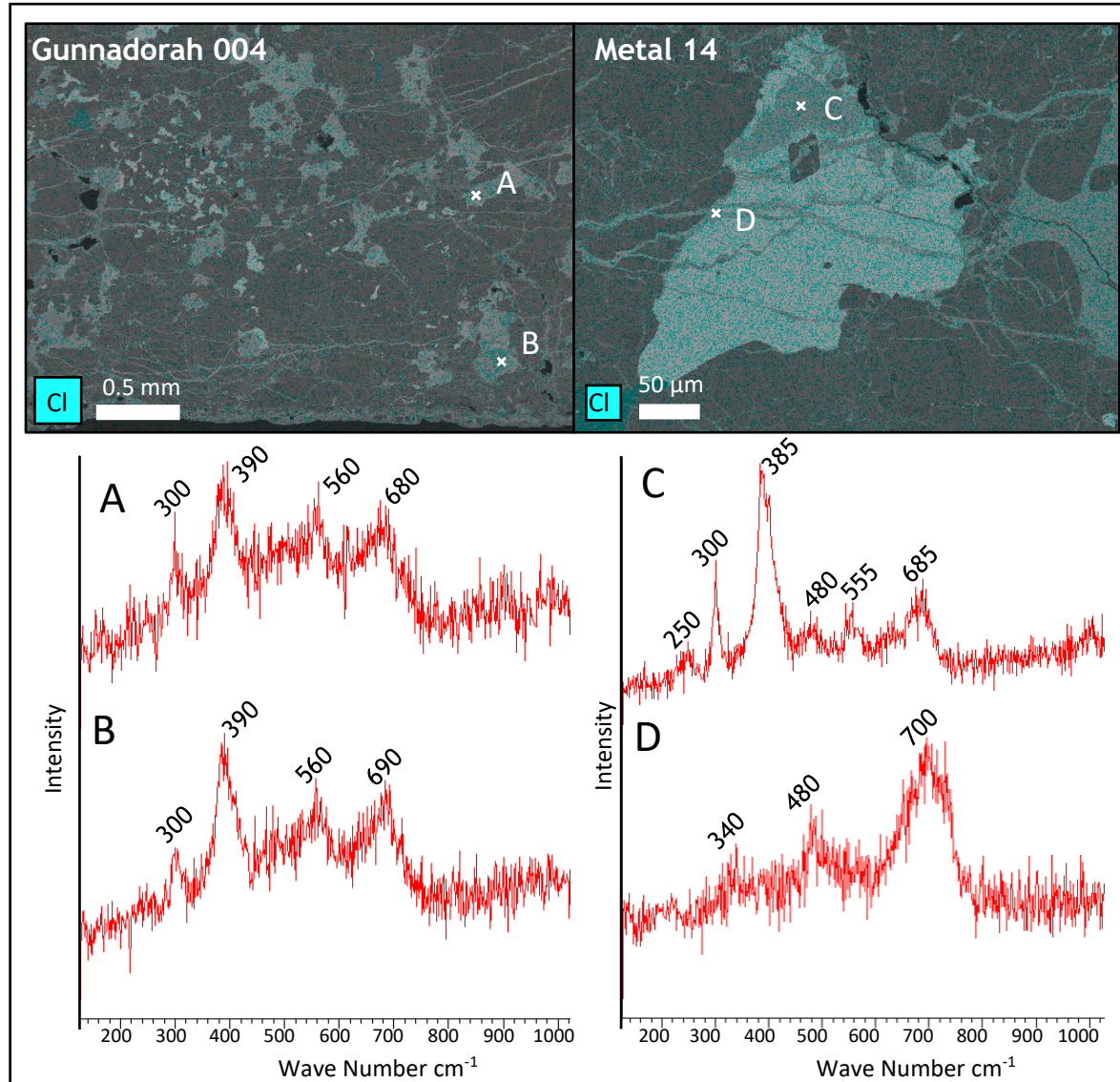


**Figure 3.32** EDS maps and accompanying Raman spectra for selected areas within Gunnadorah 004 and metal 14. Spectrum A) Goethite, B) Goethite, C) Goethite, D) Hydrated iron III oxide or oxyhydroxide.

### 3.2.4 Summary of Australian Ordinary Chondrite Alteration

The samples analysed from the Australian environment showed a range of alteration states. However, they have all experienced far more alteration than the Fe,Ni metal in Antarctic ordinary chondrites. Forrest 016 and Gunnadorah 004 demonstrated the most significant alteration seen with very few surviving Fe,Ni metal grains, the majority of which had been entirely replaced by alteration products such as goethite. Alteration in these samples was so advanced that even troilite grains have begun to alter. The survival of remnant troilite grains when no Fe,Ni metal remains supports Goodings, (1986) findings that troilite is far more resistant to weathering and alteration than both kamacite and taenite. In addition, analysis of the troilite grains has shown that the indigenous S content of 80

troilite is not passed on to the alteration products and so S released from troilite erosion is re-distributed elsewhere.

However, whilst Forrest 016 and Gunnadorah 004 showed almost total metal alteration and replacement, Forrest 028 showed many Fe,Ni metal grains with extensive alteration rims. These alteration rims were shown to have light and dark bands of material running through them and EDS analysis revealed areas of increased Cl were found generally, in these darker bands. Raman spectroscopy confirmed this Cl-rich material as akaganeite and the non-Cl bearing material as goethite or a less crystallised phase. This confirms the findings of from the Antarctic samples that Cl-rich regions are associated with akaganeite and Cl-poor regions are generally associated with goethite.

It remains unclear why Forrest 016 and Gunnadorah 004 are more altered than Forrest 028. All were collected between 1992 and 1994 and so have similar curation ages, thus this change is unlikely to have resulted from an extended time under curated conditions, unless the curation environments differed significantly. Terrestrial aging of the Forrest samples using  $^{14}\text{C}$  was conducted by Jull et al. (2010) and found Forrest 028 to have a terrestrial age of 47 ka and Forrest 016 to have an age of  $41.4 \pm 4.5$  ka. These findings suggest that the less weathered Australian sample has been exposed to terrestrial conditions for the greatest period of time. No terrestrial age data is published for Gunnadorah 004. The more developed weathering stages seen in Forrest 016 are therefore likely the result of localised conditions and support the findings of Buchwald and Clarke (1989) who determined that terrestrial age cannot be used as a proxy for the extent of terrestrial weathering.

### 3.3 Saharan Ordinary Chondrites

#### 3.3.1 Environment

The Saharan environment is a hot desert. Acfer 019 was collected from the Algerian Sahara close to the town of Foggaret ez Zoua. Here the summer average high temperature is 44°C and the winter average high temperature is 21°C (“Website 3.4”). Average annual precipitation in this region is also extremely low, just 11 mm (“Website 3.4”). Daraj 014 was collected from the Libyan Sahara close to the town of Ghadames. Climatic conditions here consist of summer average high temperatures of 42°C and winter average high temperatures of 19°C (“Website 3.5”). Average annual precipitation here is 35 mm (“Website 3.5”).

#### 3.3.2 Fe,Ni Metal

On first inspection of these samples there are numerous metal grains, more than the Australian samples but less than the Antarctic samples.

**Table 3.6** ImageJ calculated, percentage of kamacite, taenite and troilite in each of the Antarctic samples calculated from reflected light microscopy images. Troilite is included despite being as sulphide as it could not be distinguished from Fe,Ni metal in ImageJ.

Sample	Abundance (volume %)
Acfer 019	3.50
Daraj 014	3.97

#### 3.3.3 Alteration Products

Optical and reflected light microscopy of these samples reveals significant alteration rims (some exceeding 100 µm) around the majority of the Fe,Ni metals, making them the largest observed yet. Observations also suggest that alteration material is present as alteration rims and as partial to completely replaced metal grains.

### 3.3.3.1 Daraj 014

Daraj 014 is an L6 chondrite which has not been classified a weathering grade. AsB imaging of Daraj 014 shows that there are numerous Fe,Ni metal grains, each with significant alteration rims. Metals 15 and 16 (Figures 3.33 and 3.34) have alteration rims no thicker than 50 µm. Metal 17 (Figure 3.35) however, has a much thicker rim in excess of 200 µm. The alteration material within these rims also demonstrates the same colour banding (light and dark) which was observed in Forrest 028 (W. Australian). These coloured bands of material are seen in metals 15 and 17 forming almost concentric rings within the alteration rim of metal 17.

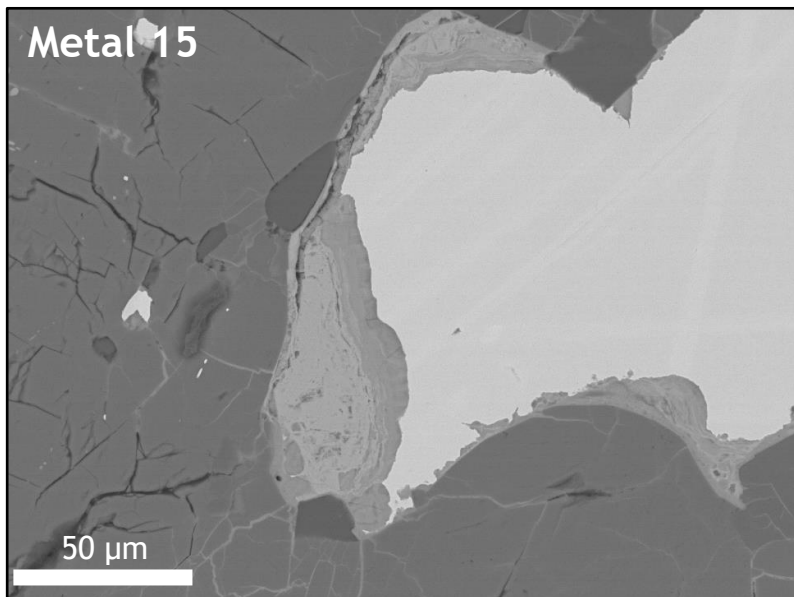


**Figure 3.33** BSE image of metal 15, an Fe,Ni metal grain (white) with alteration rim demonstrating greyscale bands, like those seen in the Western Australian samples.

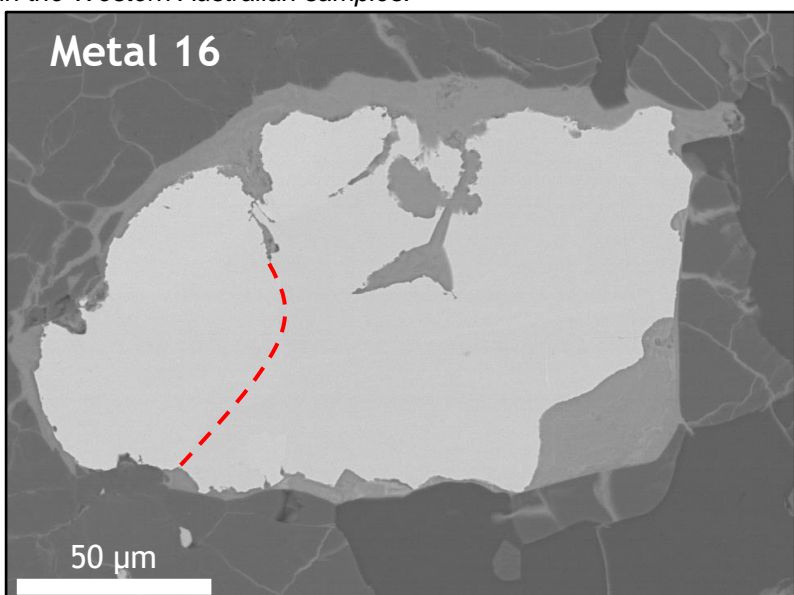


**Figure 3.34** BSE image of metal 16, an Fe,Ni metal grain (white) made up of two materials (boundary highlighted). The alteration rim around this grain does not exhibit colour banding.

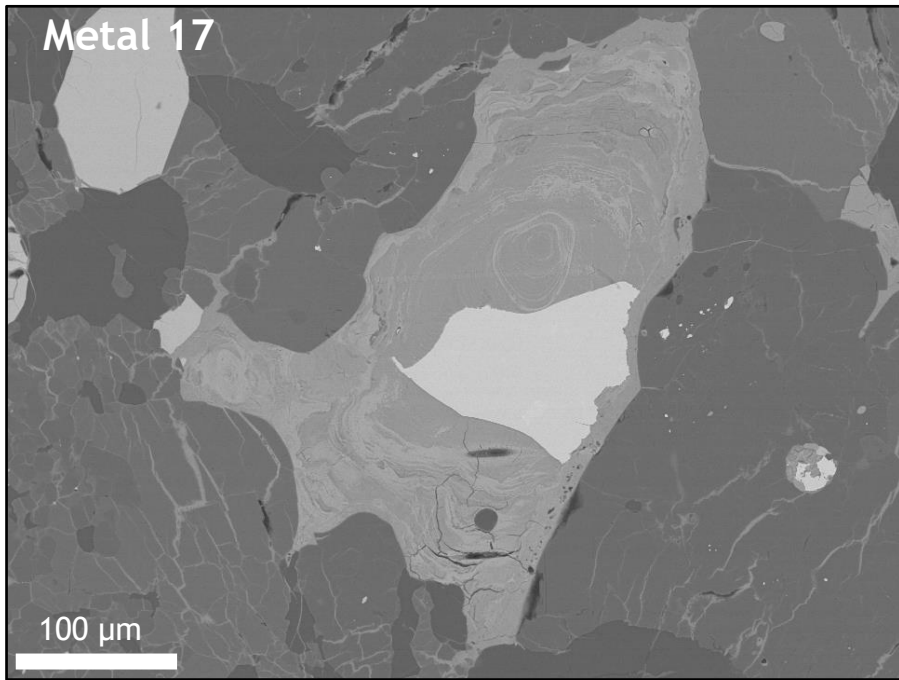


**Figure 3.35** BSE image of metal 17, an Fe,Ni metal grain surrounded by a very large alteration rim demonstrating bands of material forming almost concentric rings within the alteration rim.

#### Chemical Composition:

Qualitative analysis of Daraj 014 revealed that metal 15 and 17 were composed of kamacite and that Metal 16 was composed of a combination of both kamacite and taenite.

EDS maps of Cl showed significant concentrations within the alteration rims of metals 15 and 16. Figure 3.36A and B show the regions enriched in Cl are closest to the metal grain and in metal 15, Cl enrichment is confined to the band of darker coloured material. EDS analysis of Cl concentrations within these enriched regions revealed 3.26 wt.% Cl in metal 15 (see appendix) and 6.38 wt.% Cl in metal 16 (Figure 3.38 and Table 3.7). These values contrast with negligible Cl concentrations in the Cl-poor areas adjacent. Figure 3.38 shows the relationship between  $\text{Fe}_2\text{O}_3$  and NiO, S and Cl within the alteration rim of metal 15. The relationship with NiO (Figure 3.37A) reveals two distinct clusters, alteration material with a higher  $\text{Fe}_2\text{O}_3$  abundance yielding a greater NiO abundance. Comparing this pattern to Cl (Figure 3.37C) shows the alteration material high in NiO has the lowest Cl abundances. This demonstrates that as distance from the metal grain boundary increases the NiO increases and Cl decreases. Figure 3.37B

reveals S to be roughly constant throughout the alteration material. Figure 3.36C (metal 17) shows a more complex area of Cl enrichment.

Within metal 17 most of the Cl enrichment is located in the alteration rim above the metal grain where Cl appears to be loosely confined to arcs mimicking the colour banding. Slightly elevated Cl concentrations (~1.7 wt.%) are detected within the darker coloured material.

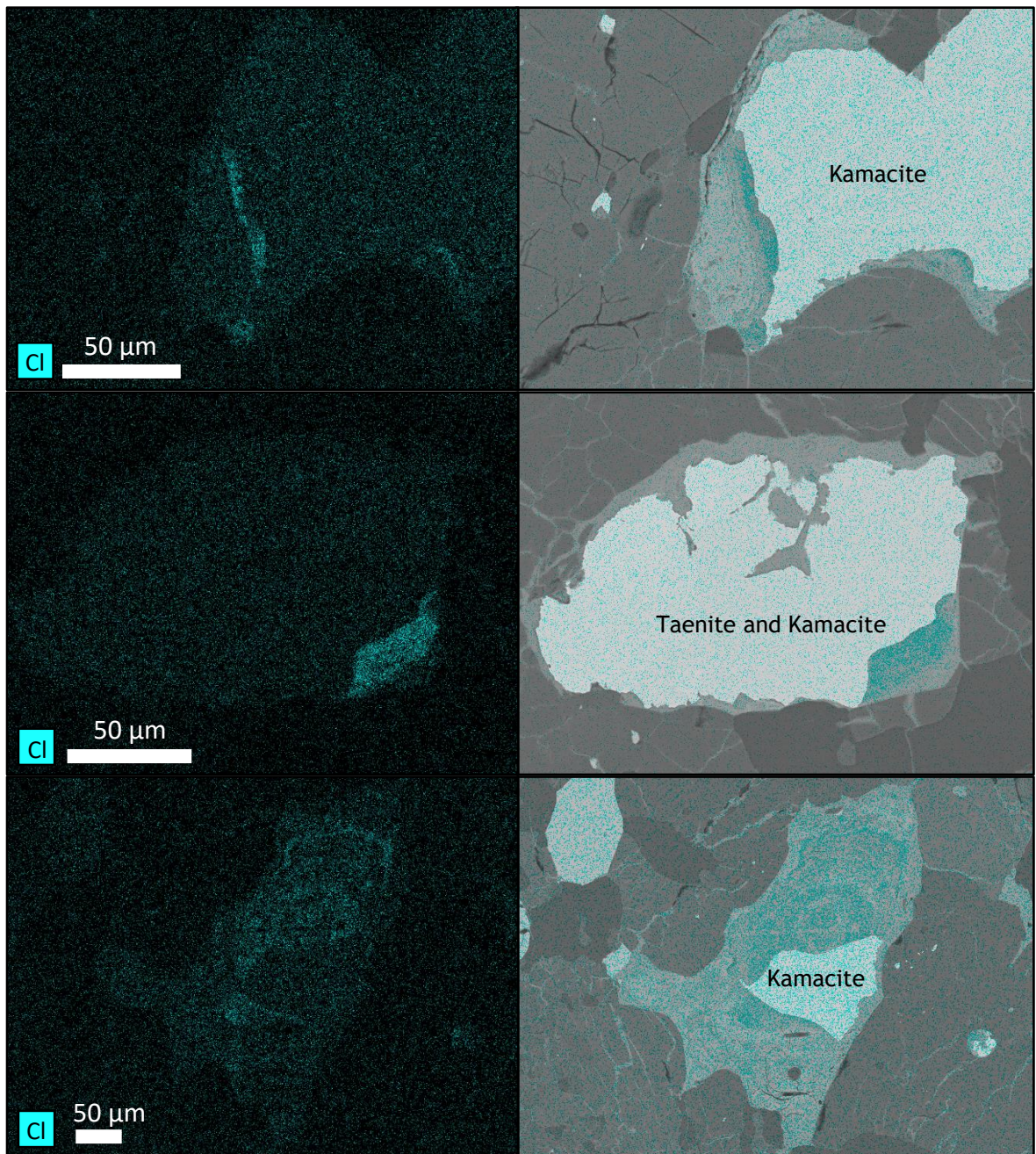


**Figure 3.36** EDS maps of metal 15 (A), metal 16 (B) and metal 17 (C). EDS maps of Cl (left). EDS maps of Cl overlain on BSE images (right). With A and B Cl enrichment is concentrated closest to the metal grain. Within A and C, Cl enrichment is broadly confined to zones or darker coloured alteration material.

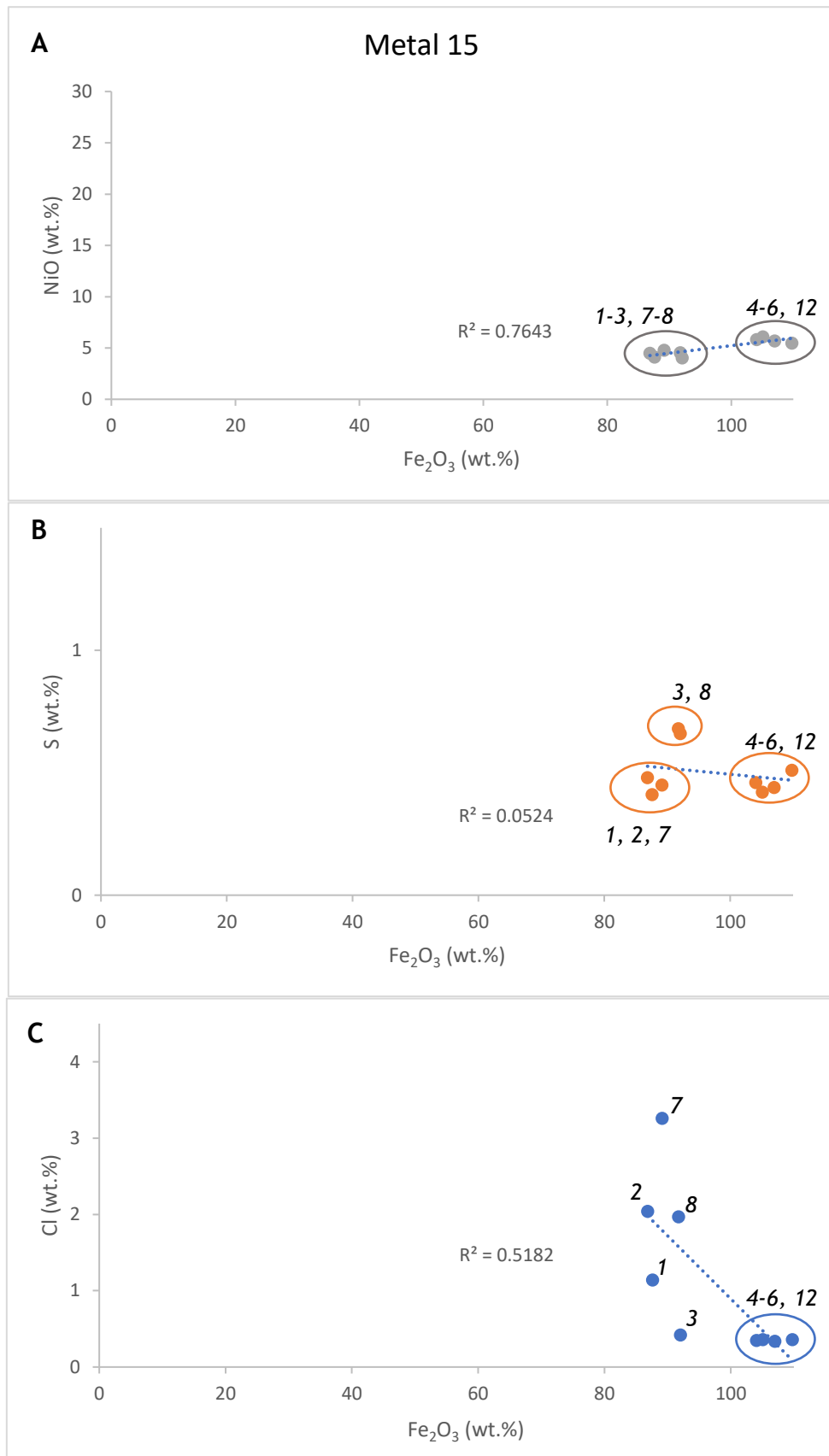


**Figure 3.37** Graphs illustrating the relationships between  $\text{Fe}_2\text{O}_3$  (wt.%) and the key elements investigated in metal 15 (a kamacite grain). Data taken from Appendix: ‘Quantitative analysis of metal 15’ and values given in wt.%. Arrows indicate increasing distance from the metal grain boundary A) Graph of  $\text{Fe}_2\text{O}_3$  - NiO, B) Graph of  $\text{Fe}_2\text{O}_3$  - S, C) Graph of  $\text{Fe}_2\text{O}_3$  - Cl.

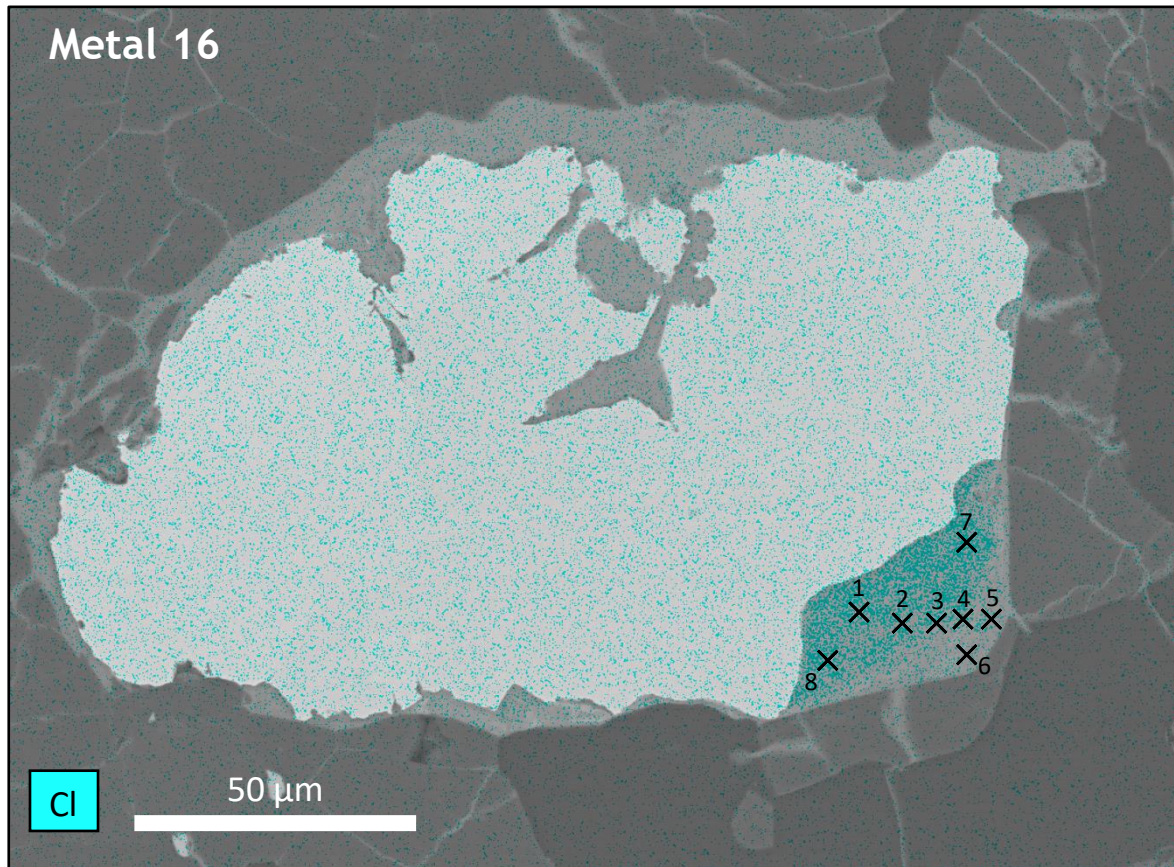


**Figure 3.38** EDS map of Cl overlain on a BSE image of metal 16. Labelled are the points of analysis shown in Table 3.7

**Table 3.7** Results of EDS analysis in metal 16 with positions numbers corresponding to those shown in figure 3.34. Values shown in wt.%. Minimum detection limits are stated below.

Position Number	SiO <sub>2</sub>	Al <sub>2</sub> O <sub>3</sub>	Fe <sub>2</sub> O <sub>3</sub>	MgO	CaO	NiO	S	Cl	Fe <sub>(m)</sub>	Ni	Total
1	0.56	0.13	89.86	0.15	-	5.50	0.26	6.27	-	-	102.73
2	0.73	0.25	89.37	-	-	4.78	0.62	4.67	-	-	100.41
3	0.75	0.32	90.07	0.15	0.14	4.56	0.39	4.98	-	-	101.36
4	0.98	0.19	89.69	0.17	-	5.63	0.66	2.63	-	-	99.94
5	4.15	0.49	88.14	0.52	-	5.93	0.73	0.53	-	-	100.49
6	6.33	0.40	87.84	0.80	0.15	5.36	0.59	0.4	-	-	101.88
7	0.56	0.30	89.02	-	-	5.33	0.19	6.38	-	-	101.78
8	0.41	0.23	89.26	0.18	-	5.85	0.26	5.92	-	-	102.11
<hr/>											
Minimum detection limit	0.06	0.07	0.17	0.04	0.08	0.25	0.08	0.07	0.17	0.25	

## Mineralogy:

Point analysis, Raman spectroscopy was carried out on the alteration rims surrounding metals 15 and 16 (Figure 3.39). The spectra show that in all cases the areas which were shown by EDS mapping to be enriched in Cl were akaganeite (Figure 3.39 spectra B,C and D). Within metal 15 the region not enriched in Cl returned a spectrum for hydrated iron III oxide or oxyhydroxide similar to metal 11 (W. Australian), which also demonstrated two very distinct regions of colour and was also composed of hydrated iron III oxide or oxy-hydroxide and akaganeite. The Cl-poor region in Metal 16 (Figure 3.39, spectrum E) returned a spectrum for goethite.

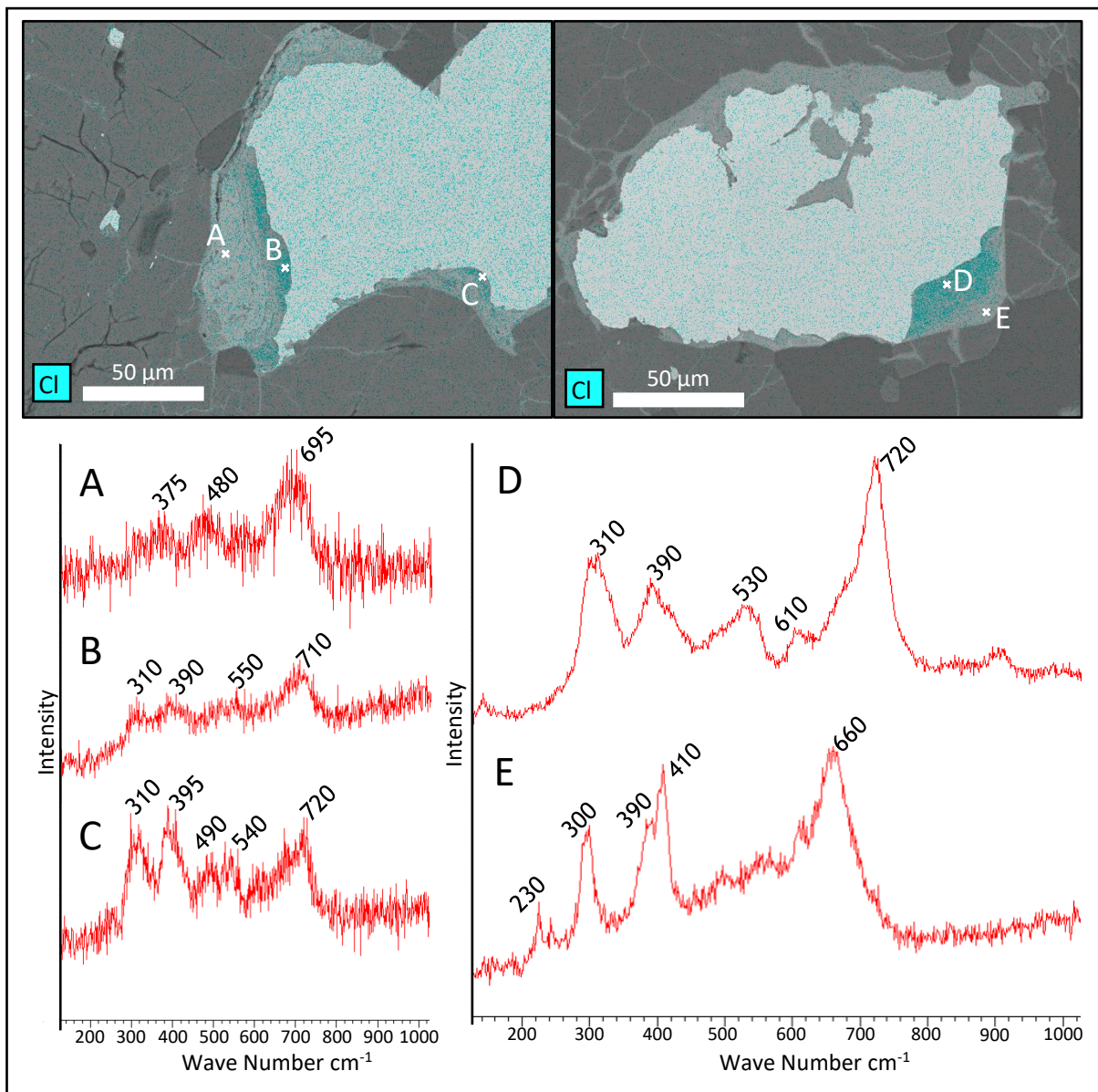


**Figure 3.39** EDS maps with accompanying Raman spectra for selected areas. Spectrum A) Hydrated iron III oxide or oxyhydroxide, B) Akaganeite, C) Akaganeite, D) Akaganeite, E) Goethite.

### 3.3.3.2 Acfer 019

Acfer 019 is another L6 chondrite which has also not been classified a weathering grade. AsB imaging shows that the Fe,Ni metal grains within this sample have also undergone significant alteration, with substantial alteration rims and evidence of entire metal grain replacement (Figures 3.40, 3.41 and 3.42). The alteration rims are a similar size to those in Daraj 014, frequently in excess of 100 µm. The rims in Metals 19 and 20 (Figures 3.41 and 3.42) also show the colour banding within the alteration rim which has been a trademark of the alteration found in warmer environments.

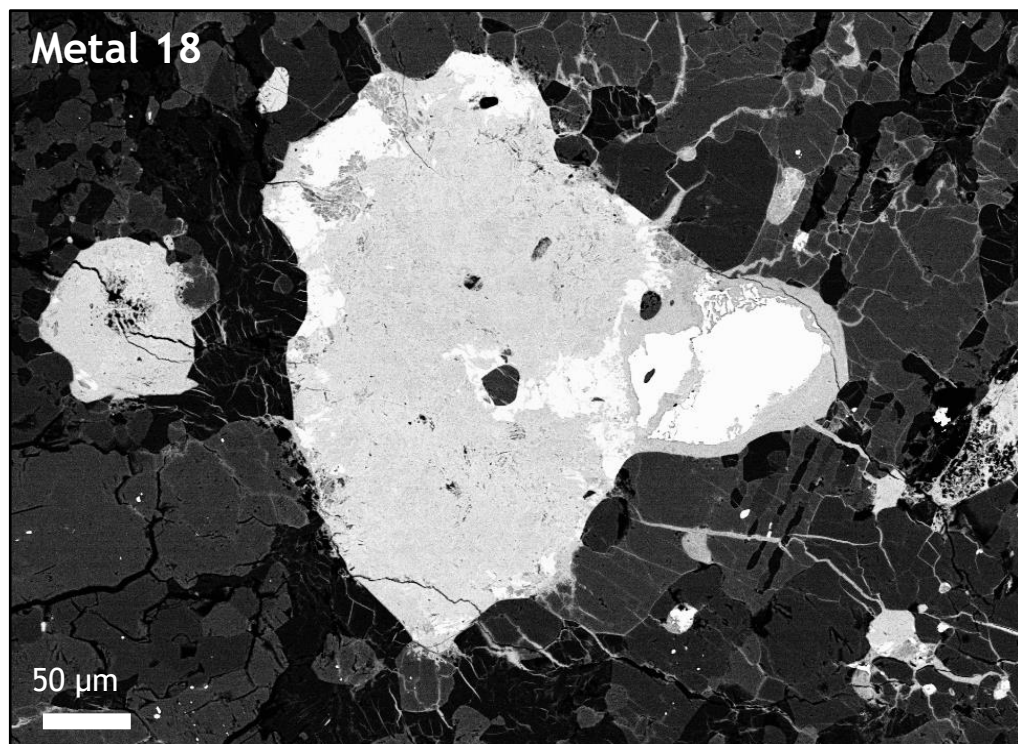


**Figure 3.40** BSE image of metal 18, a group of Fe,Ni metal grains (white) with alteration material between. Previously, this may have been one large metal grain however, alteration has now replaced much of the original gain.

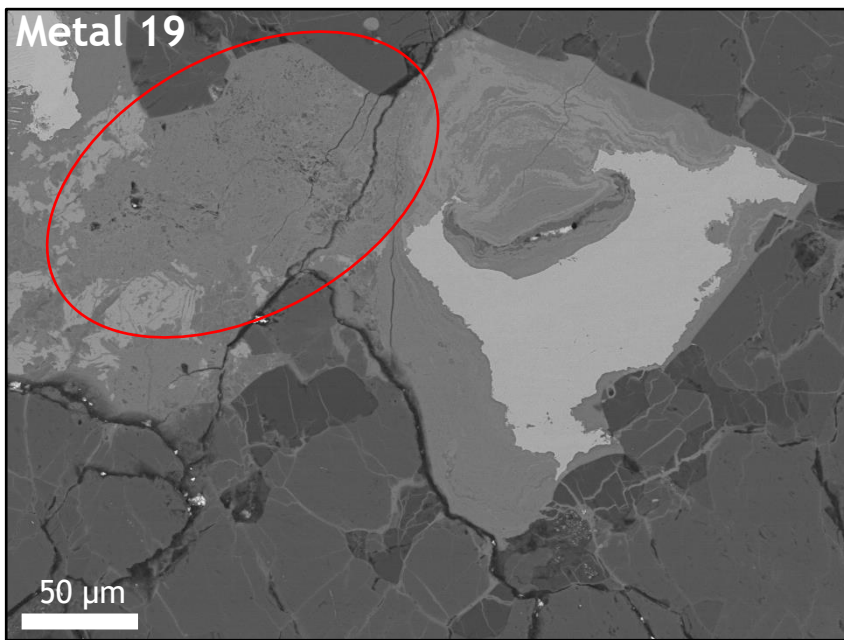


**Figure 3.41** BSE image of metal 19, an Fe,Ni metal grain (white) with extensive alteration rim demonstrating colour banding. The highlighted region is an area of complete metal grain replacement.

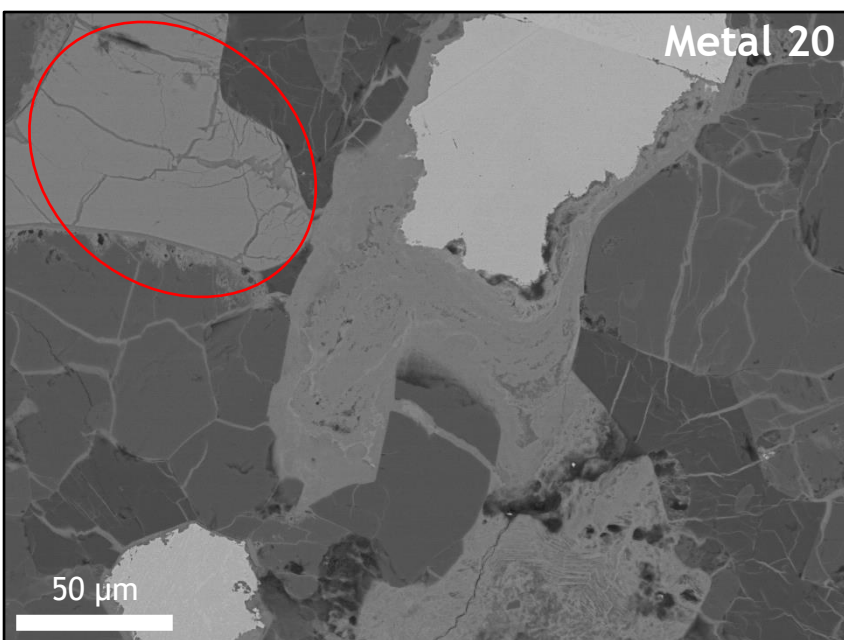


**Figure 3.42** BSE image of metal 20, an Fe,Ni metal grain (white) with extensive alteration rim demonstrating more subtle colour banding. The highlighted area shows another entirely replaced metal grain.

#### Chemical Composition:

EDS mapping of Acfer 019 revealed the complex kamacite, taenite and troilite composite metal grain seen in Metal 18 (Figure 3.40). EDS analysis also showed metal 19 to be a kamacite grain with a Ni concentration of 5.76 wt.% and

metal 20 to be a mixture of kamacite and taenite with 15.92 wt.% Ni in the kamacite and 35.07 wt.% Ni in the taenite (see appendix).

Metals 19 and 20 were also mapped for Cl (Figure 3.43). Metal 19 (Figure 3.43) showed the only area of Cl enrichment, concentrated within a hollowed-out region of the kamacite grain and separated from the surrounding alteration product by a fracture. Here a Cl concentration of 2.49 wt.% was detected (see appendix). The remaining alteration rim and area of replaced metal grain (highlighted in figure 3.41) demonstrated no detectable Cl concentration. Metal 20 (Figure 3.43B) also showed little to no detectable Cl throughout all its alteration rim and throughout the replaced metal (< 0.32 wt.% Cl) (see appendix). The isolated nature of the Cl-rich region in metal 19 suggests that the majority of the alteration product may be secondary alteration, and that this region has only survived due to its separation.

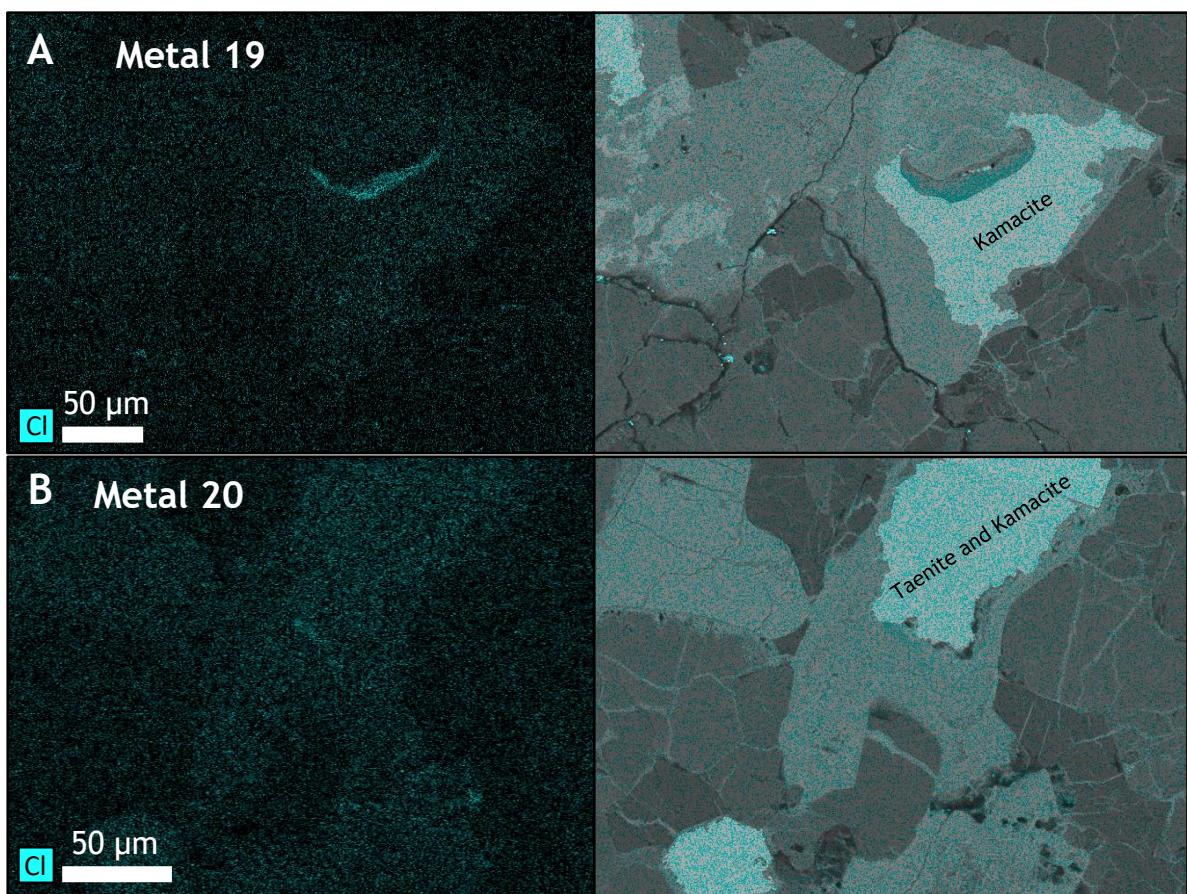


**Figure 3.43** EDS maps of metal 19 (A) and metal 20 (B). EDS maps of Cl (left). EDS maps of Cl overlaid on BSE images (right).

## Mineralogy:

Raman spectroscopy of metals 19 and 20 (Figure 3.44) revealed what was expected from the EDS mapping and from all previous results. Most points of analysis returned spectra for goethite suggesting developed, secondary alteration within most of the alteration rims and replaced metal grains. Metal 19 had some exceptions with spectrum A returning a result for hydrated iron III oxide or oxyhydroxide and the segregated Cl enriched region returning a weak spectrum for akaganeite.

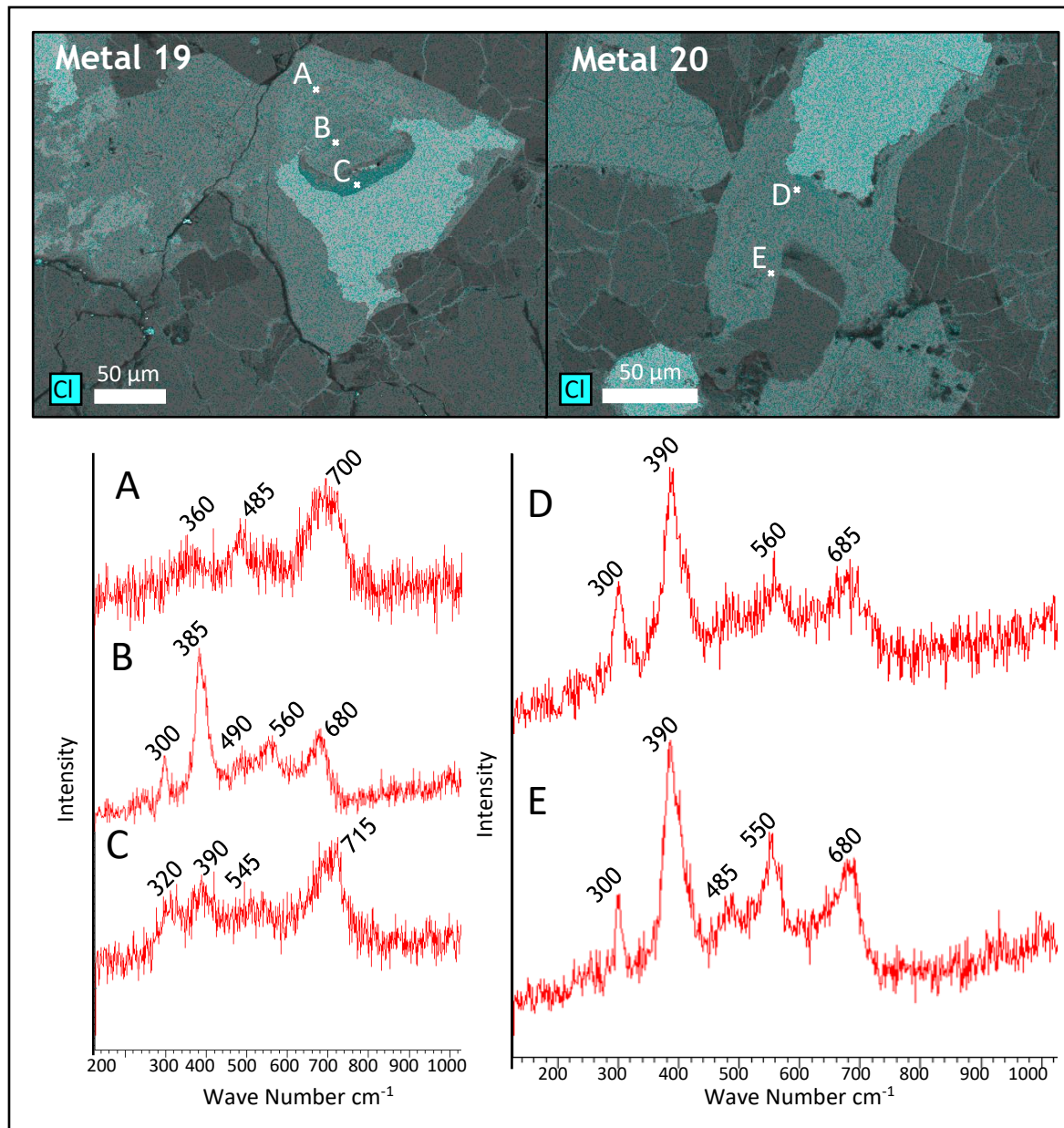


**Figure 3.44** EDS maps with accompanying Raman spectra for selected areas in metals 19 and 20. Spectrum A) Hydrated iron III oxide or oxyhydroxide, B) Goethite, C) Akaganeite, D) Goethite, E) Goethite.

### **3.3.4 Summary of Saharan Ordinary Chondrite Alteration**

Analysis of the Saharan ordinary chondrites has shown that the typical alteration experienced in this environment is extensive, with significant alteration rims existing around the majority of Fe,Ni metal grains. The alteration rims demonstrate the colour banding initially seen in some Western Australian samples and taken together with the Australian results suggest there may be a relationship between this colour banding and the alteration product, with darker areas representing Cl enriched akaganeite. The Saharan samples also have evidence of some complete metal grain replacement, although not on the same scale as the Western Australian samples it is nonetheless a marker of more significant terrestrial weathering.

## **3.4 Summary of Ordinary Chondrite Characterisation**

The analysis of the ordinary chondrites above has shown that the terrestrial environment has a significant impact on the Fe-rich minerals within ordinary chondrites, particularly the Fe,Ni metal. Fe,Ni metal reacts with the terrestrial environment to produce iron-oxide alteration products which, can either replace metals entirely or lead to the development of alteration rim/halos in excess of 200 µm thick. EDS mapping and EDS point analysis used alongside Raman spectroscopy have revealed that three iron oxides dominate these alteration products; akaganeite, goethite and hydrated iron III oxide or oxy-hydroxide.

Akaganeite, is a Cl-rich mineral and can broadly be distinguished from other material in alteration rims by EDS mapping and Raman spectroscopy. AsB imaging of samples from warmer climates could also potentially be used for weathering product characterisation but, further investigation is required regarding any link between the darker material observed and its identification as akaganeite. Generally, akaganeite occurs close to metal grains and is absent in heavily altered samples.

Goethite makes up the majority of alteration products which are not Cl-rich akaganeite. EDS mapping can therefore guide where goethite is likely to exist, but Raman spectroscopy is still needed to differentiate between goethite and other Cl-poor alteration products. Goethite is seen extensively in samples which

have been heavily altered and have, experienced complete metal grain replacement supporting Buchwald and Clarkes (1989) conclusion that as akaganeite ages it transforms into goethite.

Hydrated iron III oxide or oxy-hydroxide was the third alteration product observed in these samples and the least abundant. It was present in samples from warm environments, but this analysis has been unable to distinguish what determines the formation of this poorly crystallised phase over goethite.

It has also been revealed that there is a relationship between NiO content of the alteration product and the Ni content of the metal grain. Alteration products surrounding taenite have significantly higher NiO concentrations than those surrounding kamacite. S has been shown to have a similar, albeit weaker, relationship with Fe<sub>2</sub>O<sub>3</sub> to NiO. Within all the samples analysed Cl does not appear related to Fe<sub>2</sub>O<sub>3</sub> abundance. Finally, analysis of troilite has shown that the indigenous S content of troilite is not passed on to the alteration material.

Regarding the terrestrial environment, the cold desert samples, which were dominated by narrower (~50 µm) alteration rims composed of akaganeite experienced the least weathering and alteration. The hot desert environment contained thicker alteration rims and some evidence of complete grain replacement. Alteration was comprised of some akaganeite but mostly the secondary alteration product goethite. The semi-arid environment of Western Australia demonstrated the most intense alteration, with two samples having experienced almost complete Fe,Ni replacement and beginning to show alteration of troilite grains. The majority of alteration product was goethite. Figures 3.45 and 3.46 show how Cl and S (wt.%) vary in the alteration rims between the three environments. Cl content within alteration rims is shown to be generally less than 0.50 wt.%, regardless of environment (Figure 3.45). Figure 3.45 also illustrates that within the Antarctic environment there is far less high Cl alteration product. S is present in much lower quantities within the alteration rims and is shown to be much lower in Western Australian samples, with alteration rims typically having <0.50 wt.% (Figure 3.46). Within Antarctic and Saharan samples, the S content of the alteration rims is shown to be marginally higher, typically 0.51 - 1.00 wt.% S (Figure 3.46).

From this analysis It can therefore be concluded that warmer, wetter conditions such as those found in Western Australia generally produce the most significant alteration and the colder, drier conditions such as those found in Antarctica produce the least alteration. Whilst the age of meteorites may have an influence on the alteration experienced, this research found that local climatic conditions have a far greater influence, as demonstrated by Forrest 016 and Forrest 028, where the older sample had experienced far less intense alteration.

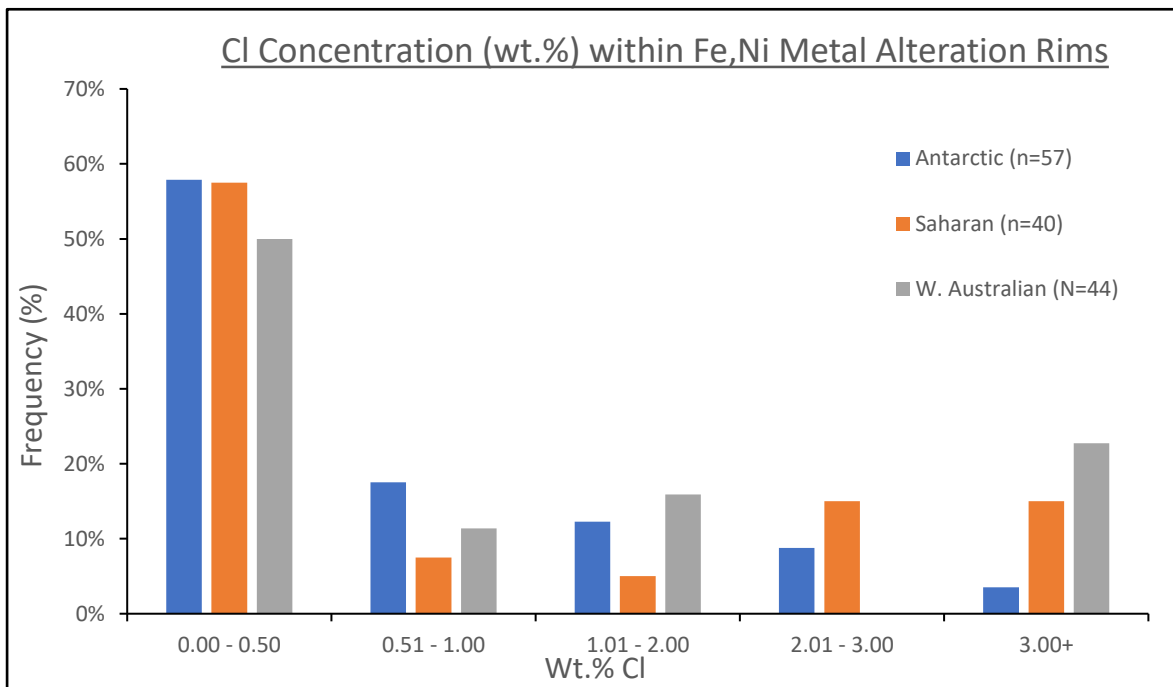


**Figure 3.45** Graph showing how CI (wt.%) within the alteration rims of Fe,Ni metal changes between environments. Data taken from quantitative analysis tables presented in Chapter 3 and in appendix.

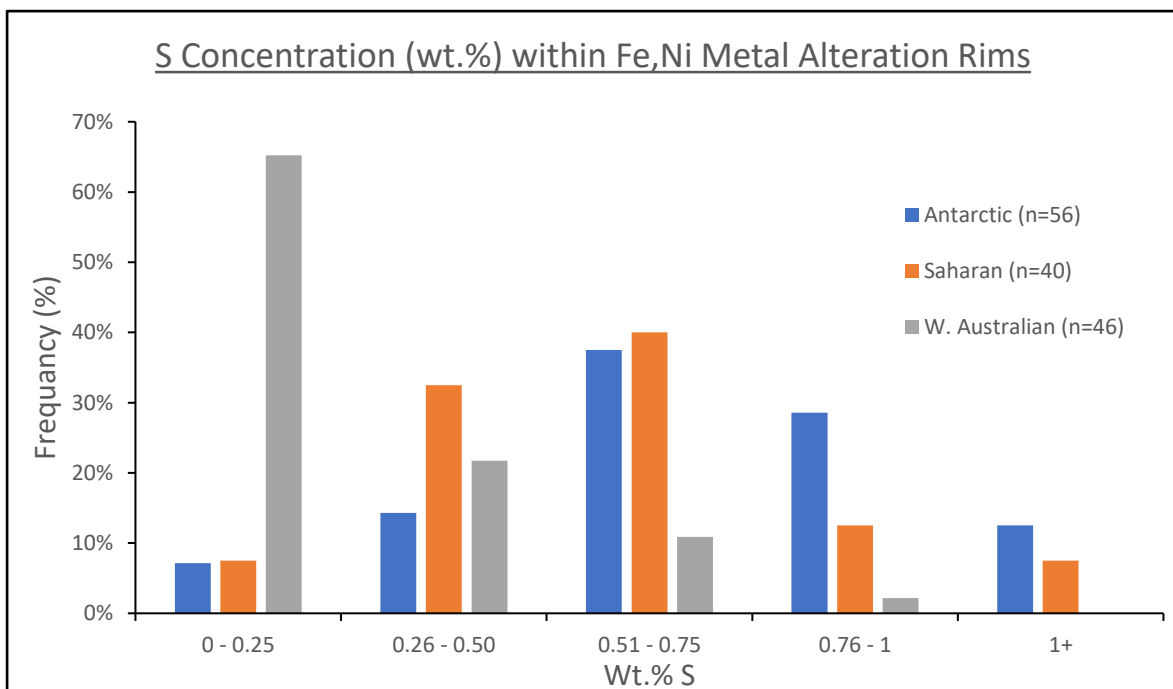


**Figure 3.46** Graph showing how S (wt.%) within the alteration rims of Fe,Ni metal changes between environments. Data taken from quantitative analysis tables presented in Chapter 3 and in appendix.

## 3.5 Discussion

### 3.5.1 Antarctica

The Antarctic environment produces the least weathering of ordinary chondrites compared to other regions. Why is this?

Both oxygen and moisture must be present simultaneously for metal grains to experience rusting and produce the iron oxide alteration products observed around Fe,Ni metal grains (Buddhue, 1957). On the Antarctic continent moisture is limited by the cold, low humidity conditions which prevail (especially deep in the continental interior). Burying samples under the ice (Morcillo et al., 2004) limits the availability of oxygen and moisture, and slows the rate of corrosion significantly. Table 3.8 demonstrates the decreasing steel corrosion rate with increasing distance inland where conditions are colder and drier.

Distance from the coast and the effect this has on temperature and humidity may however, not be the only reason for corrosion rates to decrease with increasing distance inshore. Cl, which is a key component in initiating the corrosion of Fe,Ni metal (Buchwald and Clarke, 1989), and which has been shown to be synonymous with akaganeite in these samples, is thought to be delivered to the Antarctic continent via sea spray (Buchwald and Clarke, 1989). The Cl is carried inland as an aerosol or gas where it is incorporated into newly forming snow and ice (Buchwald and Clarke, 1989). Moving further inland you would therefore expect the amount of Cl available to decrease. Cl decreasing inland may therefore add to the effect of reduced temperature and humidity to produce a decreased corrosive effect inland. ALHA 77180 was collected ~100 km from the coast (The

Meteoritical Society, 2017) and DOM 14010 was collected ~780 km from the coast. No coordinates are listed for DOM 14010 collection, so the distance is approximated from Davis-Ward Nunataks, which was the area sampled during that collection season (Roberts, 2015). Given the change in distance from the coast between these samples one would therefore expect a difference in corrosion rates and thus the alteration products observed. However, no such change is observed. Although, no such variation is visible in this study it is something that should be considered when discussing terrestrial weathering.

**Table 3.8** Table showing the decreasing steel corrosion rate with increasing distance inland from the nearest Antarctic coastline. Also shown are the approximate locations of the Antarctic samples analysed in this research. Edited from Morcillo et al., (2004) with data from Hughes et al., (1996).

Exposure Site	Distance from Sea (km)	Steel Corrosion Rate ( $\mu\text{m/year}$ )
Vanda	80	0.87
ALHA 77180	~100	N/A
Robertsollen	120	0.70
LGB00	186	0.18
LGB010	390	0.10
LGB35	780	0.13
DOM 14010	~780	N/A
Vostok	1200	0.05

### 3.5.2 Sahara and Western Australian

The weathering of meteorites in hot desert and semi-arid environments has been shown by Bland et al. (1998) and Bland (2006) to occur at a much faster rate than in cold desert environments. The results in this chapter support this conclusion. In both these environments oxygen is not limited like in Antarctic ice and moisture in semi-arid environments is far more plentiful. The increase in the extent of alteration products seen in the samples from these environments is therefore unsurprising.

Bland (2006) showed that the first 20 ky are the most significant for metal oxidation within meteorites especially for those in hot environments where there are fewer limitations on oxygen and moisture (Figure 3.47). The results above show Western Australian samples to have more significant alteration than those Saharan samples. This is also the case in Bland's findings. Figure 3.47 shows Australian sample have a faster oxidation rate than Sharan samples. After an initial 20 ky the rate of oxidation begins to slow. It is suggested by Bland (2006) that this slowdown is in fact a consequence of the rapid oxidation. During oxidation there is a significant volumetric expansion of the alteration products which significantly reduces the porosity of a meteorite sample. This process in turn reduces the available surface area for reaction and limits the ability of weathering agents such as; rain water, oxygen, aerosols and Cl to penetrate the rock (Saunier et al., 2010).

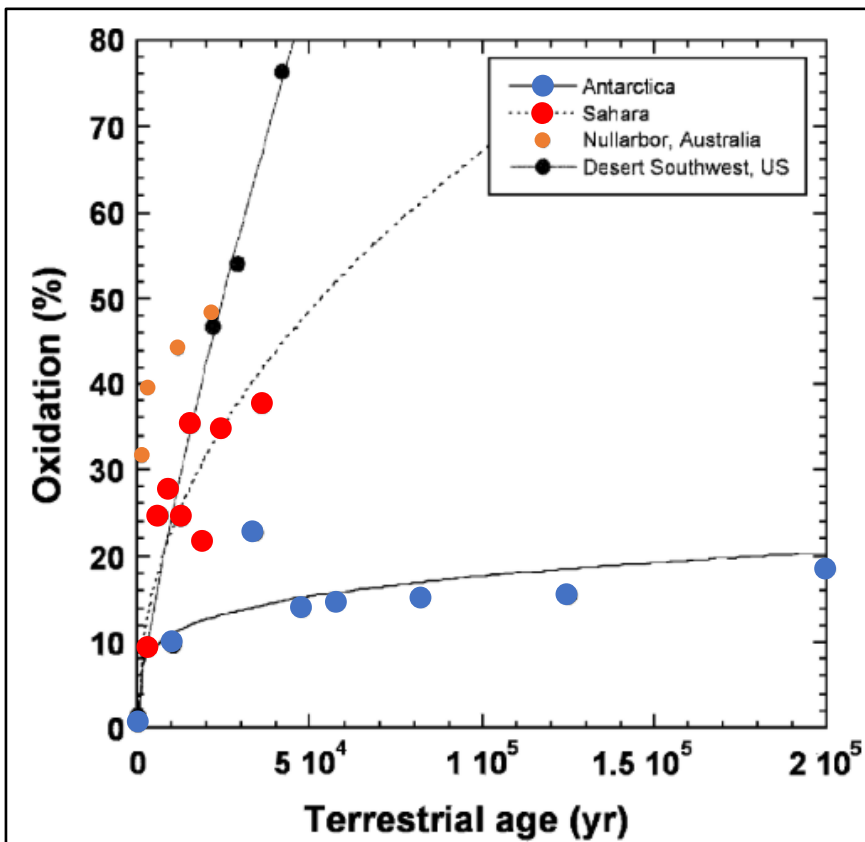


**Figure 3.47** Graph showing how oxidation increases with terrestrial age in different environments. It shows that Australia has the fastest rate of oxidation when compared to the Sahara and Antarctica. Edited from Bland. (2006).

### 3.6 Conclusions

As ordinary chondrites are not believed to have experienced significant aqueous alteration on their parent bodies the alteration products discussed in this chapter can be assumed to be a result of terrestrial weathering.

This chapter has revealed the alteration products produced by the terrestrial environment are akaganeite, goethite and hydrated iron III oxide or oxy-hydroxide. Akaganeite, a Cl-rich iron oxide, is the primary alteration product which over time and as Cl becomes limited, either by the environment or as a result of a reduction in penetration, begins to alter to goethite. Goethite is a secondary alteration product and according to this research a terminal alteration product that does not appear to be converted over time to another product. Hydrated iron III oxide or oxy-hydroxide is detected in the smallest quantities mixed within areas of goethite. Its name is used to describe a number of poorly crystallised Fe<sup>3+</sup> oxides and oxyhydroxide who have exceptionally similar Raman spectra. From this research it is not clear what controls the formation of hydrated

iron III oxide or oxyhydroxide over goethite. Figure 3.48 summarises the processes affecting Fe,Ni metal in ordinary chondrites after they fall. A method of corrosion not involving Cl was not observed during this research. The blue arrows in Figure 3.48 therefore suggest a potential non-Cl pathway for the corrosion of Fe,Ni metal. To date there is little published work on distinguishing between these phases in ordinary chondrites at such high spatial resolution, particularly using Raman spectroscopy. This chapter has shown that significant micron-scale variations exist in the alteration products produced by terrestrial weathering and that Raman spectroscopy is a powerful tool in their characterisation. This chapter has also reinforced previous work by Gooding (1986) showing that troilite is far less susceptible to the influence of terrestrial weathering than kamacite and taenite. From this work the difference in susceptibility between kamacite and taenite cannot be gauged.

In addition to identifying the alteration products this chapter has also shown that the terrestrial alteration an ordinary chondrite experiences is most significantly affected by the prevailing climate of the impact site. Warm, wet climates producing more intense alteration than cold, dry climates.

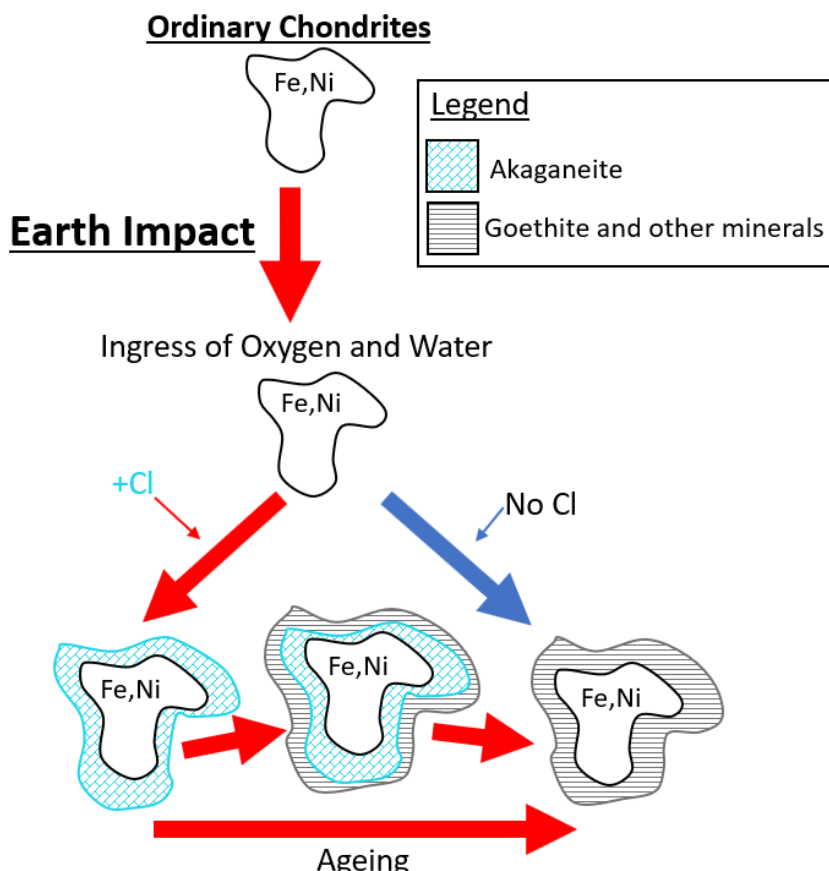


**Figure 3.48** Flow diagram of the processes effecting Fe,Ni metal within ordinary chondrites when they fall and the resulting alteration products. The blue arrow indicates a proposed pathway should Cl not be present in the environment.

# Chapter 4 Carbonaceous Chondrites

Chapter 3 examined the effects of terrestrial weathering on ordinary chondrites, establishing what characterises terrestrial alteration around Fe,Ni metal and Fe-sulphide. This chapter uses those findings to help investigate the alteration observed around Fe,Ni metal in carbonaceous CM chondrite finds.

This class of meteorite shows evidence of aqueous alteration on the parent body (Tomeoka et al., 1989) and therefore carries valuable evidence for asteroidal conditions. The extent of aqueous alteration on carbonaceous chondrites is defined by Rubin et al. (2007) and Howard et al., (2015). The greater the aqueous alteration experienced the greater the proportion of phyllosilicate and the lower the proportion of metal (Rubin et al., 2007). In addition to aqueous parent body alteration these samples have also been exposed to the terrestrial environment.

This chapter aims to investigate evidence of both alteration types and the interaction between them to determine the extent to which terrestrial alteration effects the scientifically important parent body alteration. In Chapter 3 it was demonstrated that the prevailing climate of the find environment had a significant effect on the terrestrial alteration that meteorites experienced. Therefore, in this chapter carbonaceous CM chondrites from the Antarctic (cold desert) and the Sahara (hot desert) will be investigated for evidence of parent-body and terrestrial alteration.

## 4.1 Antarctic CM Chondrites

The Antarctic CM chondrites investigated in this chapter are LEW 85311 and LAP 02239. Both have been classified as having evidence of parent body aqueous alteration. LEW 85311 is classified as a CM 2.6-2.7 indicating it has been mildly altered (Choe et al., 2010; Lee et al., 2018). LAP 022333 is paired with LAP 02239 (examined here) and has a classification as CM 1.5 according to Howard et al.

(2015) or CM 2.4 once converted to the Rubin et al. (2007) classification scale indicating that it has been more severely altered.

#### 4.1.1 Environment

The Lewis Cliff (from which LEW 85311 was sourced) is a 12 mile long cliff extending south from Mount Achernar in Antarctica (Website 4.1). Here LEW 85311 would have been subjected to a mean summer maximum temperature of -16 °C and a mean winter maximum temperature of -42 °C (Website 4.2). Annual precipitation in this region is on average 0 mm (Website 4.2). The LaPaz Icefield (from which LAP 02239 was sourced) is an icefield towards the south of the Trans-Antarctic mountains which experiences similarly low summer maxima of -12 °C and winter maxima of -38 °C. In this region however annual precipitation is higher, 32 mm annually (Website 4.3).

#### 4.1.2 Fe,Ni Metal

The Antarctic CM chondrites analysed here have low metal contents detailed in table 4.1. In both the samples analysed the metal was mostly concentrated in one large grain. LEW 85311 however, did also have a number of much smaller outlying grains.

**Table 4.1** *ImageJ calculated percentage volume of kamacite, taenite and troilite in each of the Antarctic samples calculated from reflected light microscopy images. Troilite is included despite being a sulphide as it could not be distinguished from Fe,Ni metal in ImageJ.*

Sample	Abundance (Volume %)
LEW 85311	1.36
LAP 02239	0.55

#### 4.1.3 Alteration Products

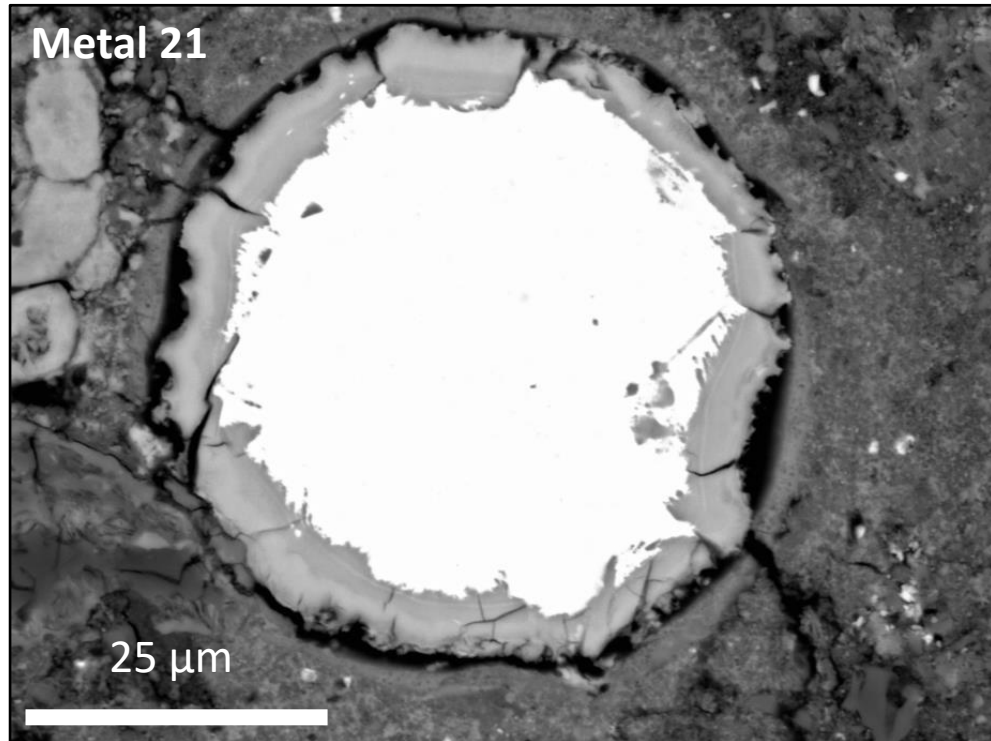
Initial reflected light microscopy of these samples revealed that surrounding each of the large metal grains is an alteration rim 25-100 µm thick with a complex internal structure. Alteration rims surrounding the smaller metal grains observed in LEW 85311 were uncommon and had much thinner alteration rims (10 µm thick) and no obvious internal structures or textures.

#### 4.1.3.1 LEW 85311

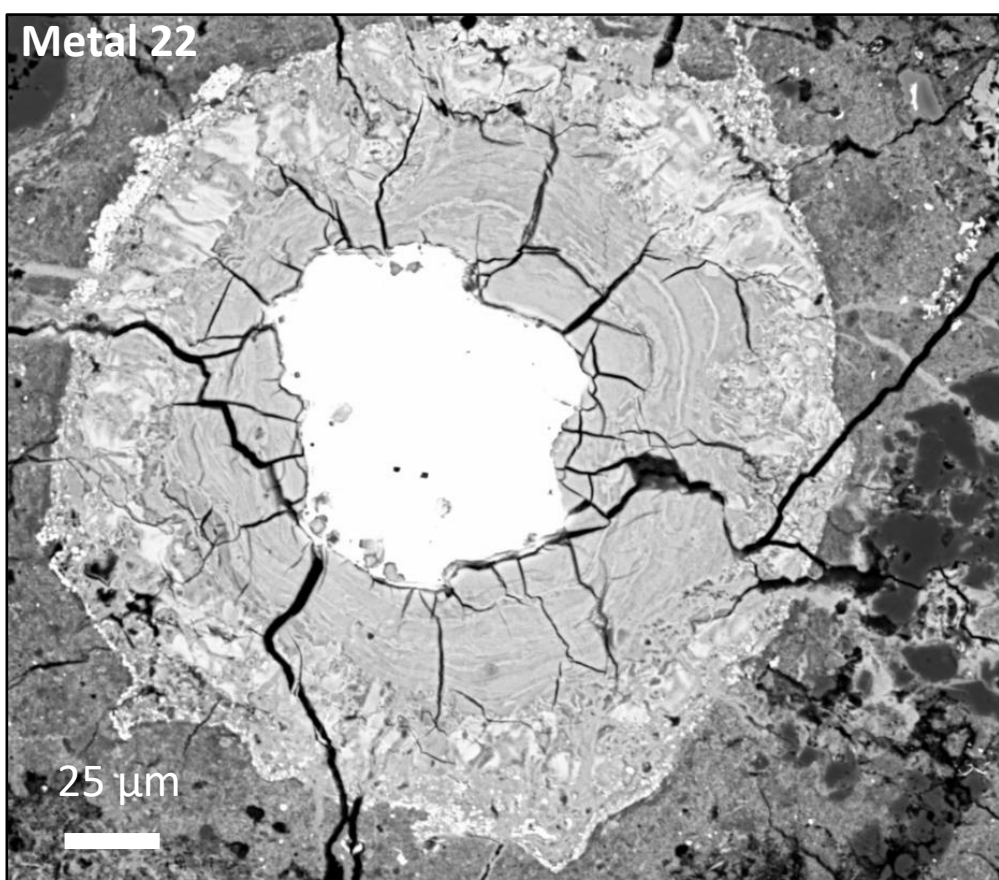
LEW 85311 is a CM2-an carbonaceous chondrite with a weathering category of Be- moderately rusty with evaporites. AsB imaging showed that there was a very distinct difference between the alteration rim observed around the small metal grain and that which was observed around the large metal grain.

Figure 4.1 shows a typical small Fe,Ni metal grain from this sample. It illustrates a thin alteration rim and lack of almost all internal features except a few narrow fractures.

The large Fe,Ni metal grain, shown in figure 4.2, has a much thicker alteration rim ~100 µm thick and an intricate internal structure which consists of three distinct textures as illustrated in figures 4.3 and 4.4. The first texture (T1) is located closest to the metal grain and is the thinnest of the bands, only ~10 µm thick. T1 is characterised by no obvious laminations and a heavily fractured nature. It is similar in appearance to the ordered material observed in the Antarctic ordinary chondrites (Chapter 3). Moving outward, T2 is significantly thicker than T1 (between 25-30 µm thick). T2 is characterised by coarse, chaotic laminations and far fewer fractures. T2 has a broadly similar appearance to the dis-ordered material seen in the Antarctic ordinary chondrites (Chapter 3). The outermost texture is T3 and is roughly the same thickness as T2 (25-30 µm thick). T3 is characterised by seemingly dis-organised blocks of material with no laminations and very few fractures. T3 is also bounded, in places, by a thin and very fine-grained rind of material labelled R (Figure 4.3 and 4.4).



**Figure 4.1** Backscattered electron (BSE) image of Fe,Ni metal grain (white) typical of the smaller-type Fe,Ni metal grains in LEW 85311. The surrounding alteration rim is thin and almost featureless.



**Figure 4.2** BSE image of metal 22, Fe,Ni metal grain. This is the large Fe,Ni metal grain (white) in LEW 85311 and it demonstrates the thick alteration rim.

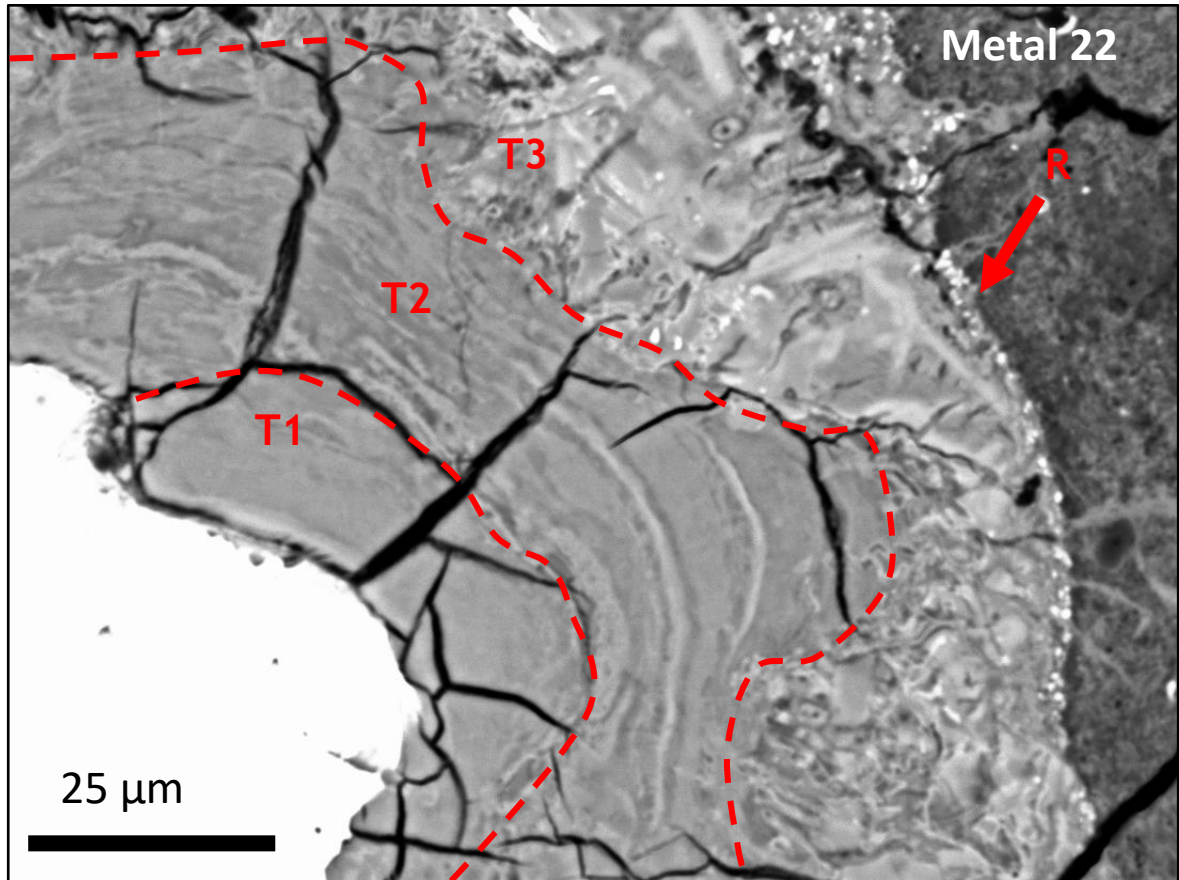


**Figure 4.3** BSE image of metal 22, magnified view of a section around the large Fe,Ni metal (white) and the alteration rim. Annotations show the three different textures observed. T1) finely laminated, heavily fractured 'ordered' material. T2) coarse, chaotic laminations with some fractures 'disordered' material. T3) extremely disordered material surrounded by a thin, fine grain rind of material (R).

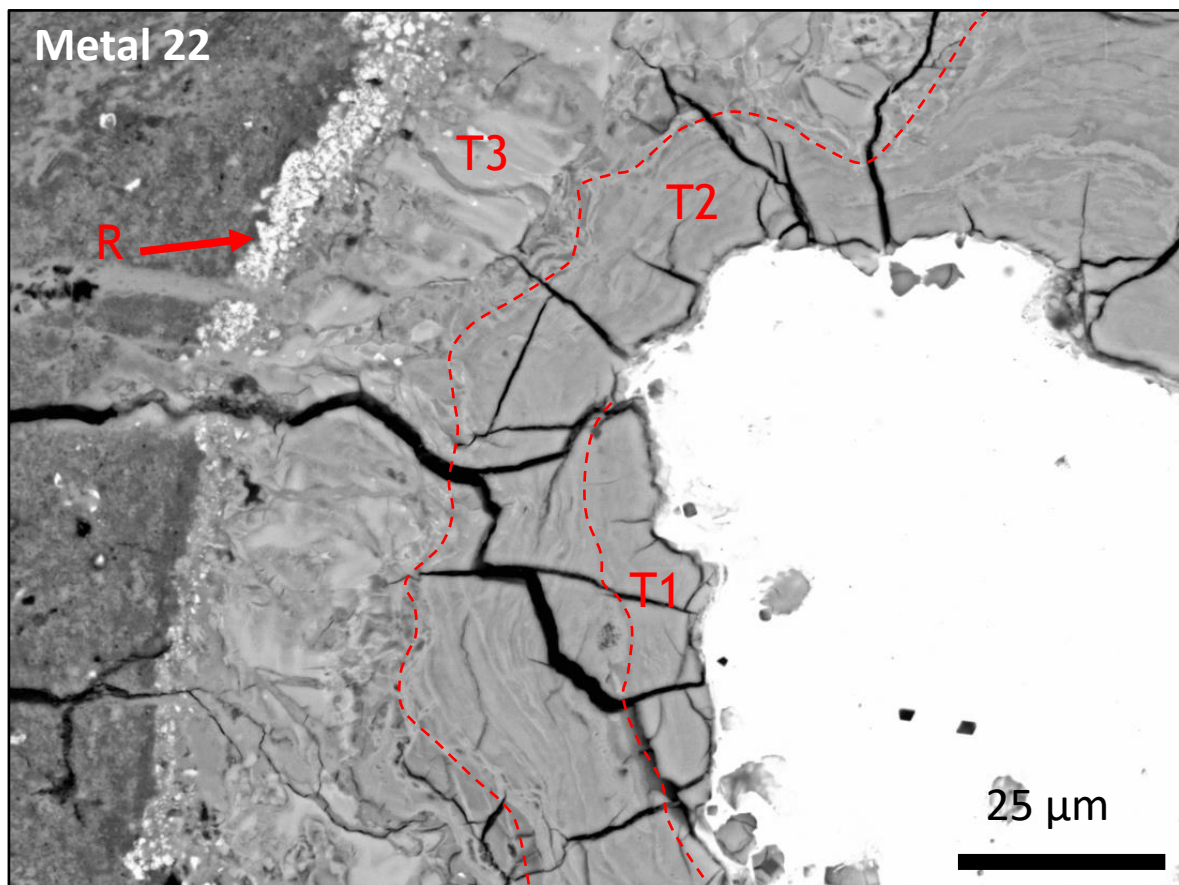


**Figure 4.4** BSE image of Metal 22, a magnified view of a section around the large Fe,Ni metal grain (white) and the alteration rim surrounding it. Textures T1, T2 and T3 (including rind) are labelled.

## Chemical Composition

EDS mapping and EDS analysis was conducted to investigate the Fe,Ni metal present and investigate the composition of the alteration rims. EDS analysis revealed that metals 21 and 22 were both kamacite with ~4.7 wt.% and 5.27 wt.% Ni, respectively (Table 4.2).

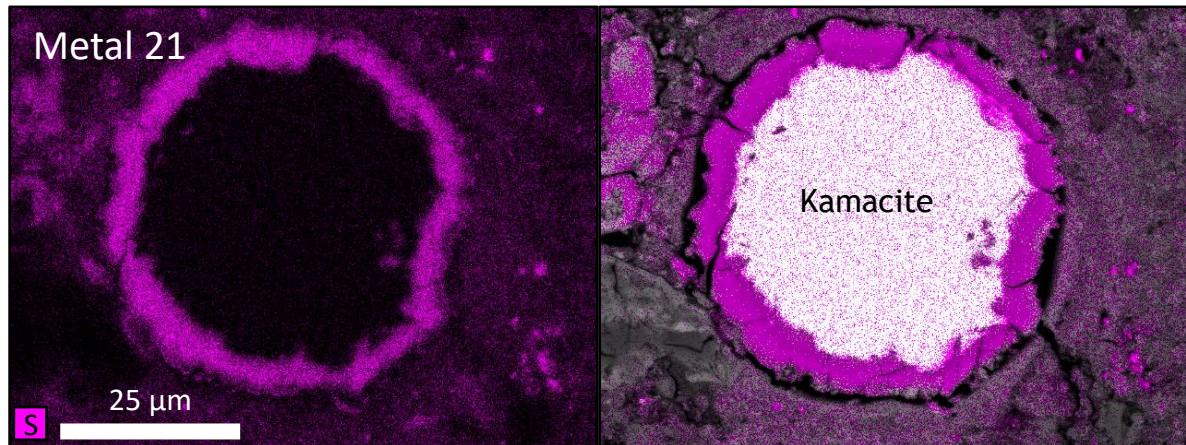
Investigation of the alteration rims included mapping chlorine (Cl) and sulphur (S) concentrations. Cl and S were examined because these samples are expected to show evidence of parent body and terrestrial alteration. Cl was shown in chapter 3 to be synonymous with terrestrial alteration product akaganeite and S is a major element in the mineral tochilinite, which is widely accepted to be a product of parent body alteration (Browning and Bourcier, 1996).

Figure 4.5 shows the results of EDS mapping on a smaller kamacite grain, demonstrating that no Cl is present within the alteration rim. It does however show that there is a significant enrichment in S, with a concentration of ~12.4 wt.%. The abundance of S and lack of Cl suggests that this kamacite grain may have been subjected to only parent body alteration.

Figure 4.6A, B and C show the results of EDS mapping on the larger kamacite grain. The maps reveal zoned enrichment within the textured bands. T1 does not appear significantly enriched in Cl and has a small increase in S (typically <1.00 wt.% Cl and typically <4 wt.% S, table 4.2). Within T2, the disordered material, there is a significant Cl enrichment with concentrations of between 2.15 and 2.56 wt.% (table 4.2). Within T3, EDS mapping reveals an enrichment in S which extended into the rind material. S concentrations in this material are 6-10 wt.% (table 4.2). Also observed in figure 4.6C are veins of Cl-rich material which cross-cut T3, extending from T2 to the meteorite matrix.

Chemical analysis of metal 22 (the large kamacite grain) suggests that this metal may have experienced significant terrestrial and pre-terrestrial (parent body) alteration. If this is the case then the ribbons of Cl rich material cutting through T3, in figure 4.6C could represent veins responsible for bringing Cl to the reaction front and facilitating terrestrial corrosion of the kamacite grain.

Using figure 4.7 and table 4.2 it can be shown that the abundance of  $\text{Fe}_2\text{O}_3$  decreases with increasing distance from the metal grain. Figures 4.8A, B and C are scatter plots comparing the relationships between  $\text{Fe}_2\text{O}_3$  and the key elements investigated (Ni, Cl and S) in metal 22. Figure 4.8A shows that NiO abundance decreases with increasing  $\text{Fe}_2\text{O}_3$  meaning that NiO increases away from the metal grain. The abundance of NiO is also similar to the Ni content within the metal grain, except when furthest from the metal grain when it exceeds this abundance. Figure 4.8B shows the S abundance follows a very similar pattern with S increasing away from the metal grain (highest in S-rich band of material). The material within the alteration rim not significantly enriched in S had broadly similar S-concentrations regardless of rim position. Figure 4.8C shows a much weaker correlation in Cl, demonstrating that Cl is only enriched in areas adjacent to the corrosion fronts.



**Figure 4.5** EDS map of metal 21. EDS map for S (left). EDS map for S overlain on a BSE image (right). Image demonstrates the S rich alteration rim surrounding the kamacite.

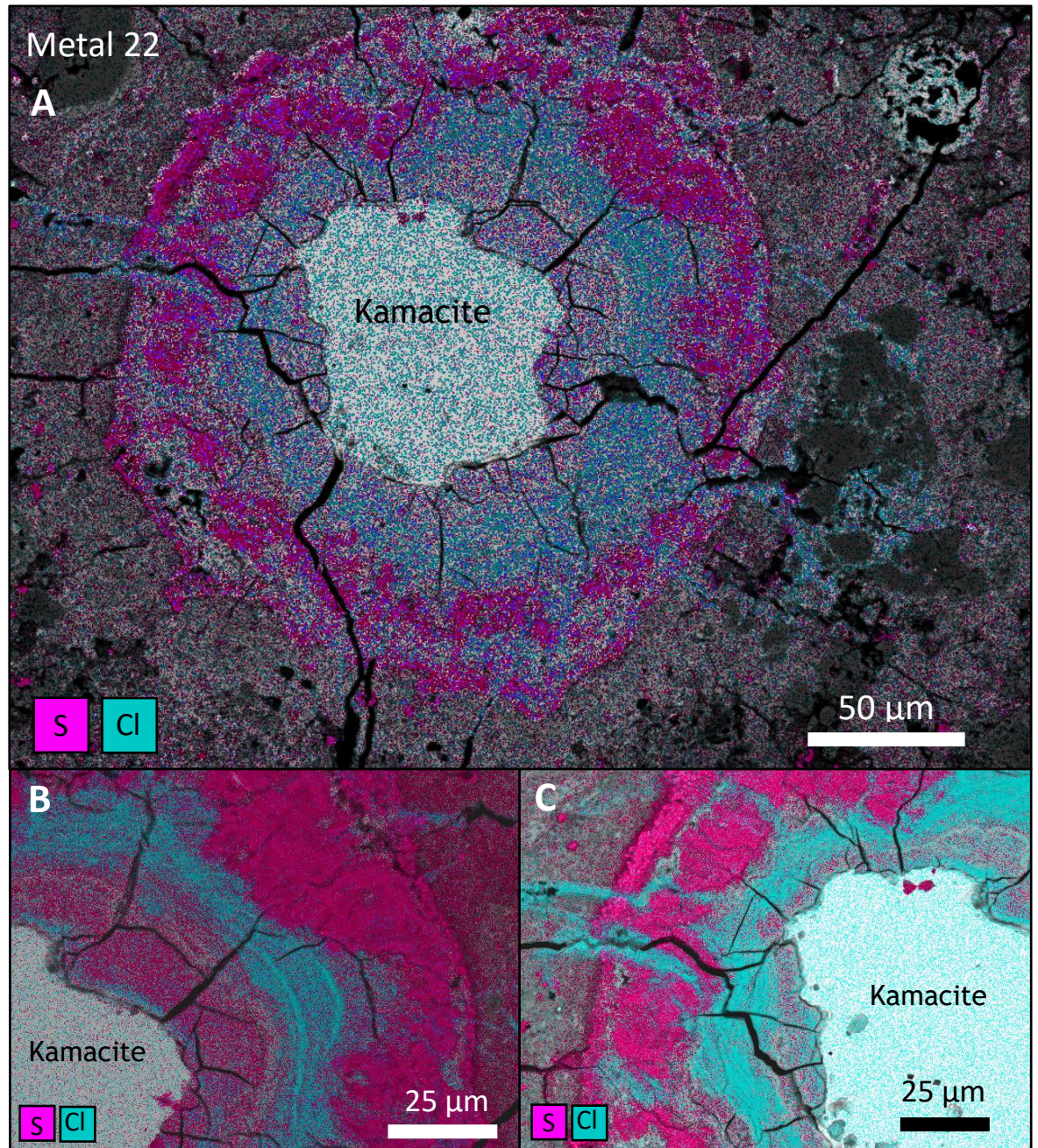


**Figure 4.6** Metal 22, showing S and Cl EDS maps overlaid on BSE images. A) EDS maps of the entire large kamacite grain as shown in figure 4.2. B) EDS map of the magnified region shown in figure 4.3. C) EDS map of the magnified region shown in figure 4.4.

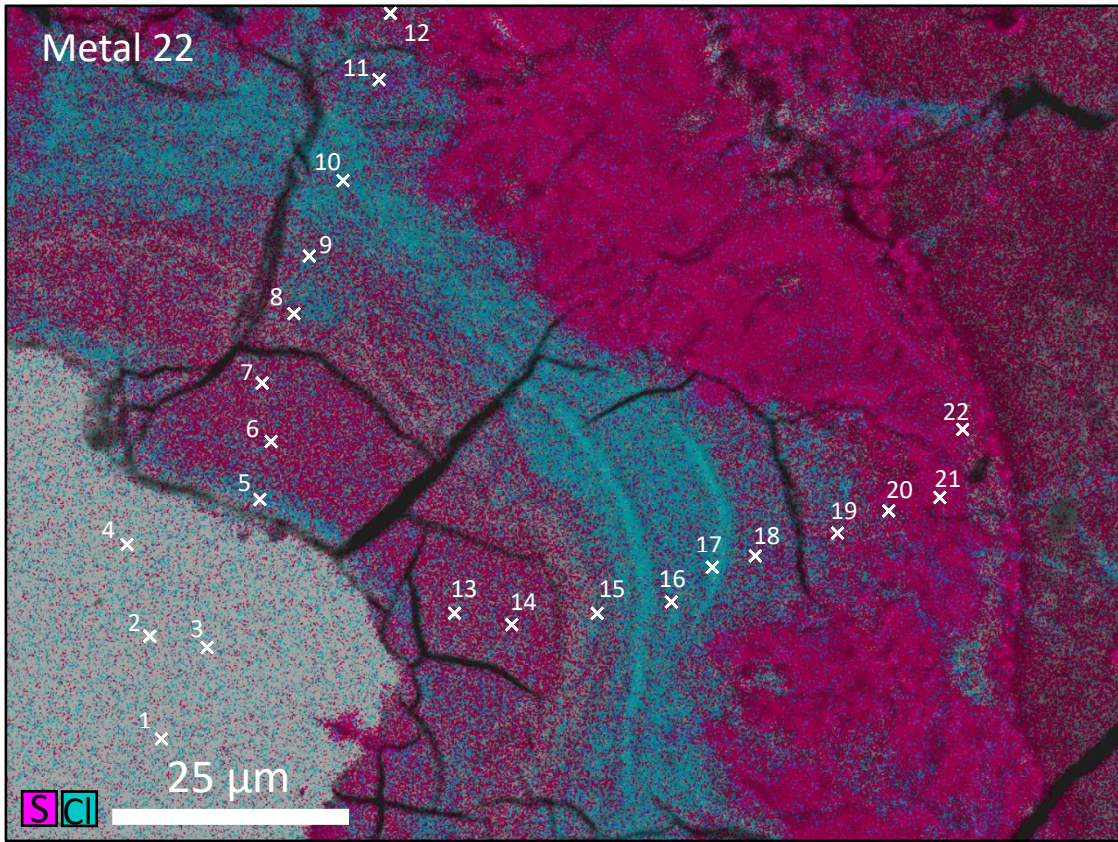


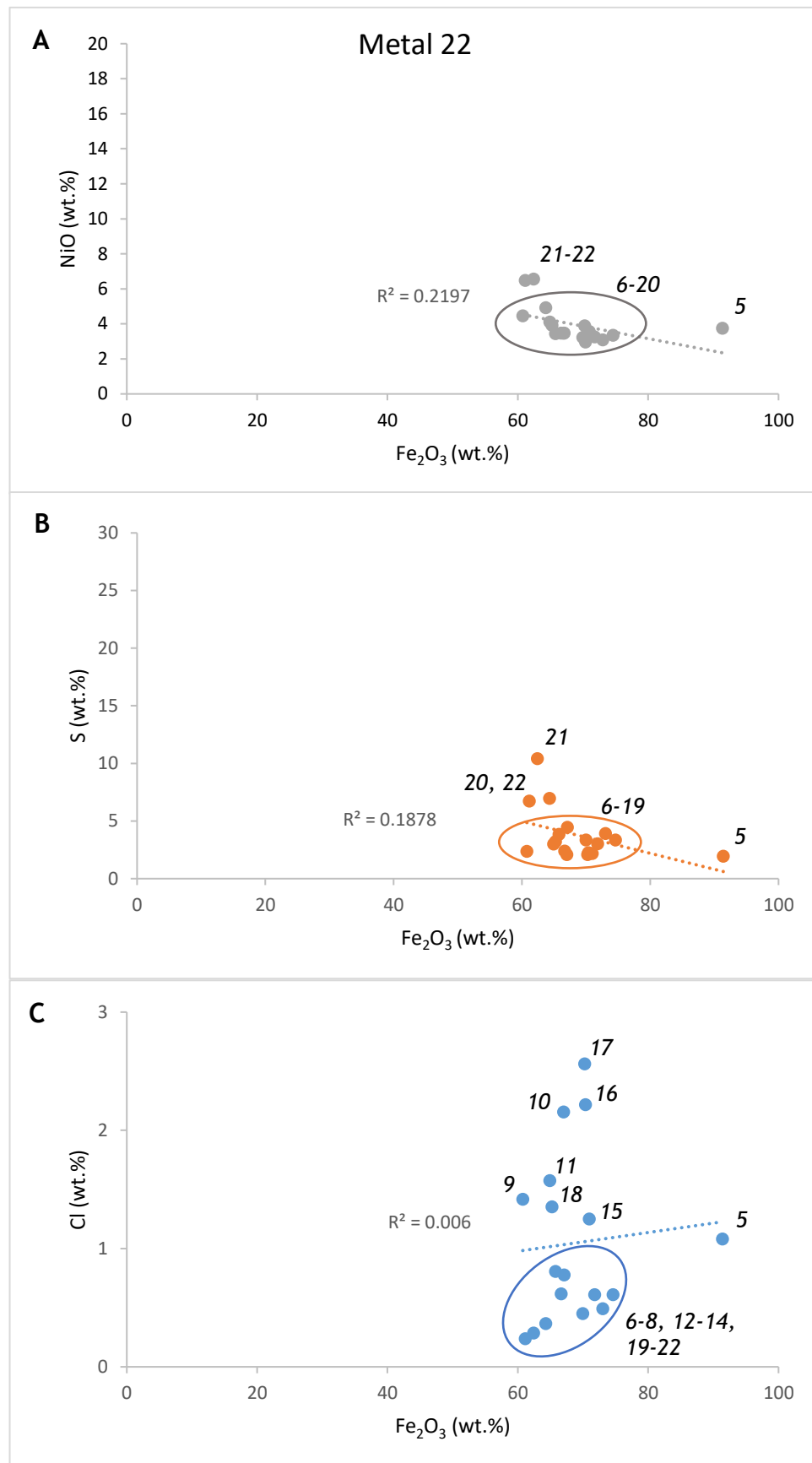
**Figure 4.7** Metal 22, EDS maps of Cl and S overlain on a BSE image of magnified alteration rim around the large kamacite grain. Labelled are the points of quantitative analysis, listed in table 4.2.

**Table 4.2** Results of quantitative analysis around the large kamacite grain and as labelled in figure 4.7. Values shown are in wt. %. Minimum detection limits are stated below.

Position Number	$\text{SiO}_2$	$\text{Al}_2\text{O}_3$	$\text{Cr}_2\text{O}_3$	$\text{Fe}_2\text{O}_3$	$\text{MgO}$	$\text{CaO}$	$\text{P}_2\text{O}_5$	$\text{NiO}$	S	Cl	$\text{Fe}_{(m)}$	Ni	Total
1	0.12	-	1.04	-	0.07	-	0.26	-	-	-	93.53	5.22	101.40
2	0.26	-	0.95	-	0.08	-	0.28	-	-	-	93.88	4.93	101.97
3	0.13	-	1.11	-	-	-	0.31	-	-	-	93.05	5.27	101.22
4	0.15	-	0.96	-	-	-	0.36	-	-	-	93.62	5.21	101.51
5	0.28	-	1.11	91.39	-	-	0.57	3.75	1.95	1.08	-	-	100.13
6	0.28	-	0.93	73.01	0.12	-	1.04	3.08	3.91	0.49	-	-	82.86
7	0.30	-	1.75	69.97	0.00	0.17	1.39	3.22	3.35	0.45	-	-	80.61
8	0.41	-	1.72	66.65	0.18	-	1.17	3.47	2.40	0.62	-	-	76.61
9	0.44	-	2.58	60.75	0.14	-	2.29	4.45	2.36	1.42	-	-	74.42
10	0.34	-	1.65	66.99	0.12	-	0.89	3.46	2.10	2.15	-	-	77.71
11	0.54	-	2.61	64.91	-	0.29	1.92	4.09	3.00	1.57	-	-	78.93
12	0.78	0.15	2.30	67.09	0.42	0.37	1.18	3.46	4.46	0.78	-	-	80.99
13	0.23	-	1.12	74.58	0.10	-	0.68	3.34	3.36	0.61	-	-	84.02
14	0.15	-	1.10	71.78	0.10	-	0.85	3.25	3.03	0.61	-	-	80.87
15	0.18	-	1.59	70.95	-	-	1.03	3.55	2.18	1.25	-	-	80.73
16	0.33	-	1.50	70.35	0.08	-	0.86	2.96	2.25	2.21	-	-	80.54
17	0.23	0.12	1.39	70.23	0.23	-	0.85	3.88	2.08	2.56	-	-	81.57
18	0.62	-	3.10	65.23	0.44	0.22	2.06	3.92	3.21	1.35	-	-	80.14
19	1.04	0.14	3.77	65.79	0.49	0.41	2.36	3.43	3.86	0.81	-	-	82.09
20	1.43	0.27	3.64	64.29	0.92	0.88	1.93	4.92	6.96	0.36	-	-	85.60
21	3.11	0.55	3.17	62.39	1.55	1.63	1.93	6.55	10.42	0.29	-	-	91.60
22	4.87	0.59	3.03	61.14	2.49	0.62	2.76	6.48	6.74	0.24	-	-	88.95

Minimum detection limit	0.05	0.04	0.17	0.22	0.04	0.10	0.08	0.23	0.07	0.08	0.22	0.23	
-------------------------	------	------	------	------	------	------	------	------	------	------	------	------	--



**Figure 4.8** Graphs illustrating the relationships between Fe<sub>2</sub>O<sub>3</sub> (wt.%) and the key elements investigated in metal 22. Data taken from table 4.2 and values given in wt.%. Labels correspond to position numbers in table 4.2. A) Graph of Fe<sub>2</sub>O<sub>3</sub> – NiO, B) Graph of Fe<sub>2</sub>O<sub>3</sub> – S, C) Graph of Fe<sub>2</sub>O<sub>3</sub> – Cl.

## Mineralogy:

Point analysis Raman spectroscopy was undertaken to identify the mineralogy of the Cl- and S-rich bands identified in T2 and T3. The S-rich alteration rim in metal 21 produced two spectra with four distinct peaks (Figure 4.9A and B). Three of the peak positions seen in both spectra (those around  $250\text{ cm}^{-1}$ ,  $300\text{ cm}^{-1}$  and  $350\text{ cm}^{-1}$ ) correspond to the mineral tochilinite (Chapter 2 - Raman Spectrum Identification). The two outlying peaks at  $470\text{ cm}^{-1}$  (Spectrum A) and  $450\text{ cm}^{-1}$  (spectrum B) do not fit the pattern for tochilinite and may represent impurities.

Raman spectroscopy of this metal grain confirms the mineralogy of the S-rich alteration product as tochilinite which is suggestive of parent body aqueous alteration.

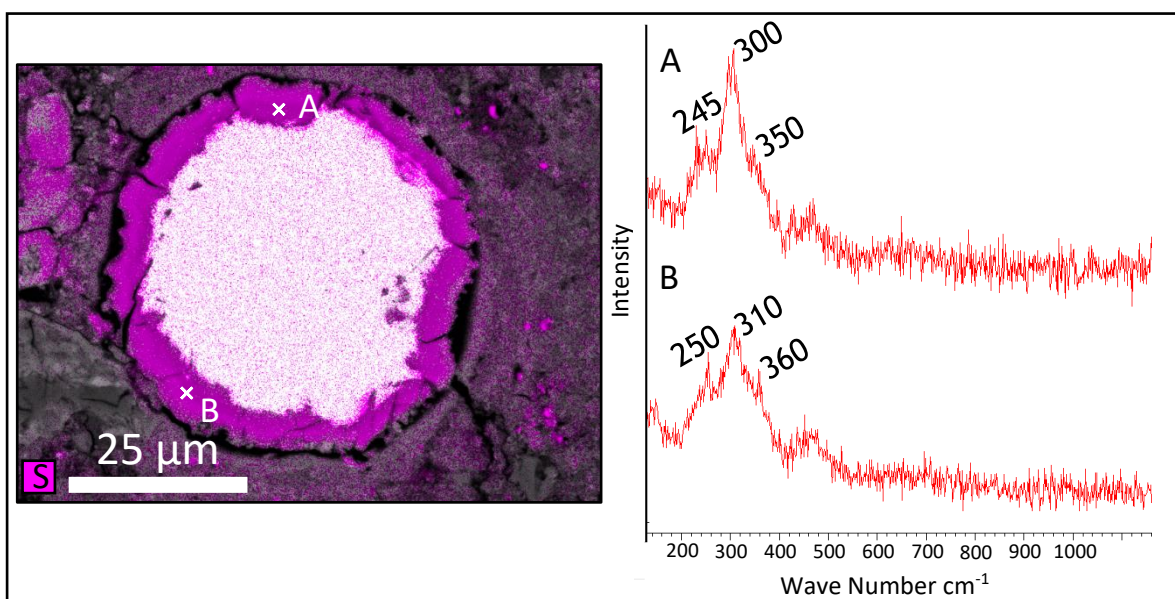


**Figure 4.9** EDS maps of Cl and S in metal 21 overlaid on BSE images and accompanying Raman spectra. Spectrum A) Tochilinite, B) Tochilinite.

Point analysis Raman spectroscopy was then repeated on metal 22 (Figure 4.10). Spectra collected from the Cl-rich, T2 region return peak positions for akaganeite (Figure 4.10, spectrum C). Spectra collected from the S-rich, T3 regions returned peak positions for tochilinite (Figure 4.10, spectrums D and F). T1 which, was not significantly enriched in either Cl or S returned an inconclusive spectrum (Figure 4.10, spectrum A). A measurement collected between T1 and T2 returned a spectrum for goethite (Figure 4.10, spectrum B). Goethite was also

detected by Raman spectroscopy adjacent to the Cl-rich vein cutting the alteration rim in figure 4.6C (Figure 4.10, spectrum E).

Following point analysis on the alteration rim surrounding metal 22, Principle Component Mapping (PCM) was undertaken through the area highlighted in figure 4.10 to investigate if changes in mineralogy could be accurately detected by PCM. If so PCM could be widely applied to more samples to gather accurate information on alteration mineralogy. The area mapped was chosen because the terrestrial products akaganeite and goethite and the pre-terrestrial product tochilinite had been identified. The map is shown in figure 4.11 and was unable to distinguish between akaganeite and goethite. These minerals have far more similar peak positions than tochilinite and given the low-resolution of each spectrum collected to produce the PCM (see Chapter 2, Principle Component mapping), goethite could not be distinguished from akaganeite. Despite this factor when compared to the EDS map of the same area the PCM produces a reasonably accurate result for the location for tochilinite and akaganeite/goethite. However, the inability to distinguish between akaganeite and goethite alongside the 4-hour acquisition time for the data limits the usefulness of PCM. With different equipment capable of producing maps using the multiple exposure method described in Chapter 2, this technique could still prove to be extremely useful.

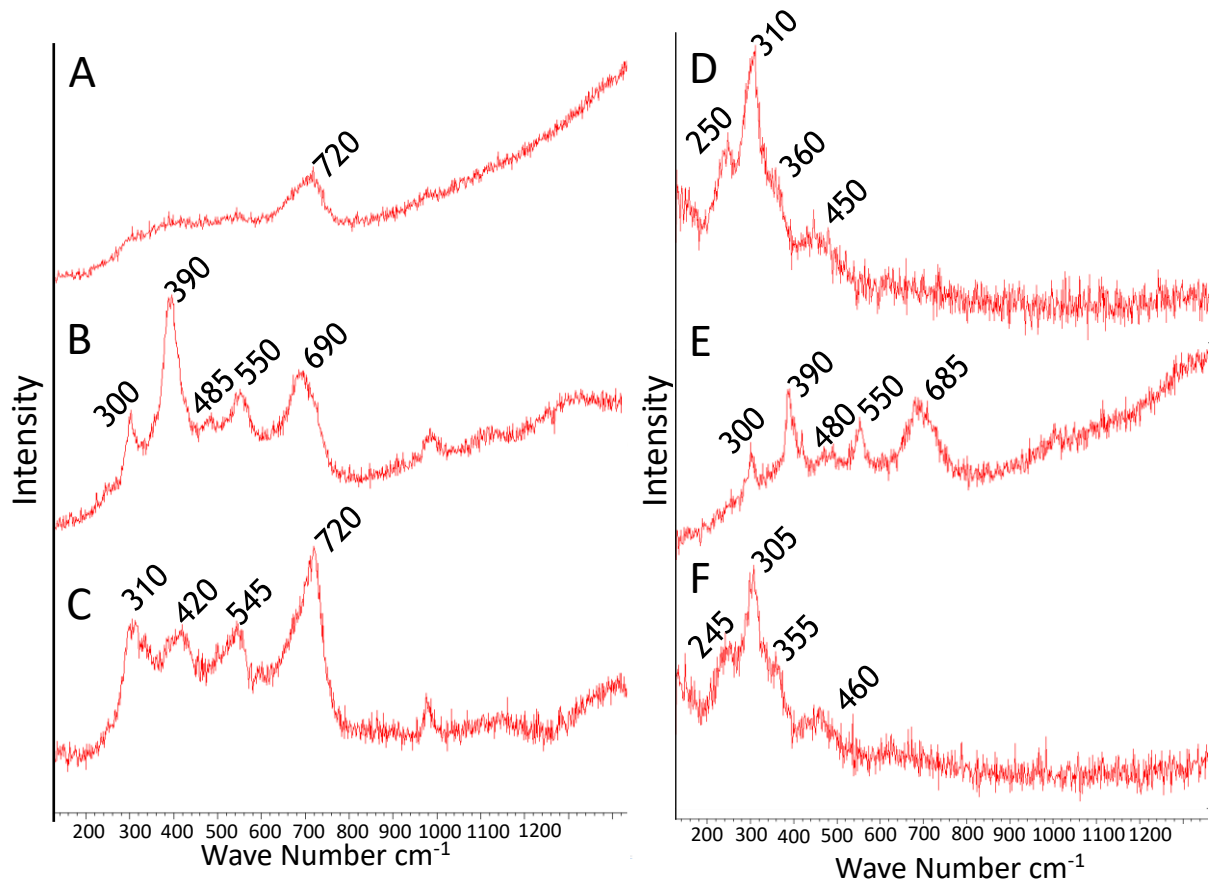
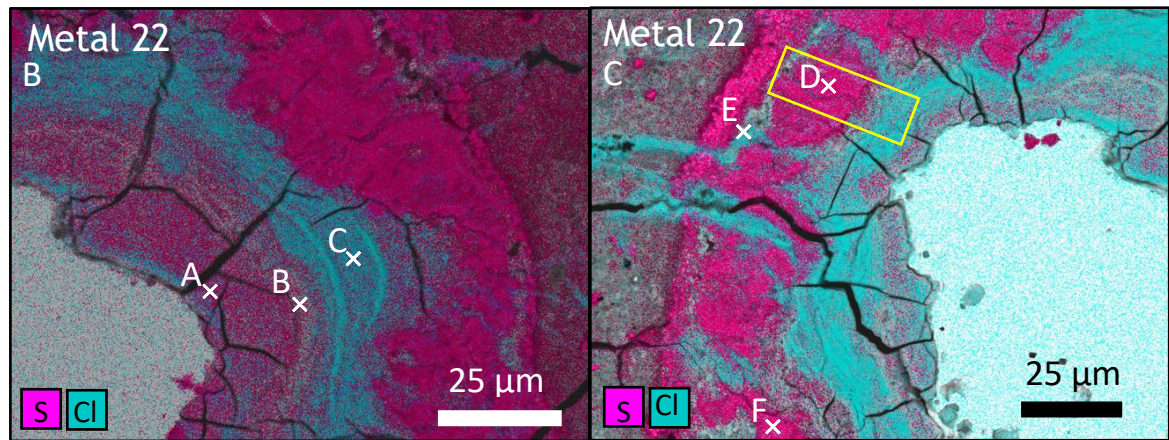


**Figure 4. 10** EDS maps of Cl and S in metal 22 overlain on BSE images and accompanying Raman spectra. The yellow highlighted region represents the region in which Principle Component Mapping was undertaken. Spectrum A) Inconclusive, B) Goethite, C) Akaganeite, D) Tochilinite, E) Goethite, F) Tochilinite.

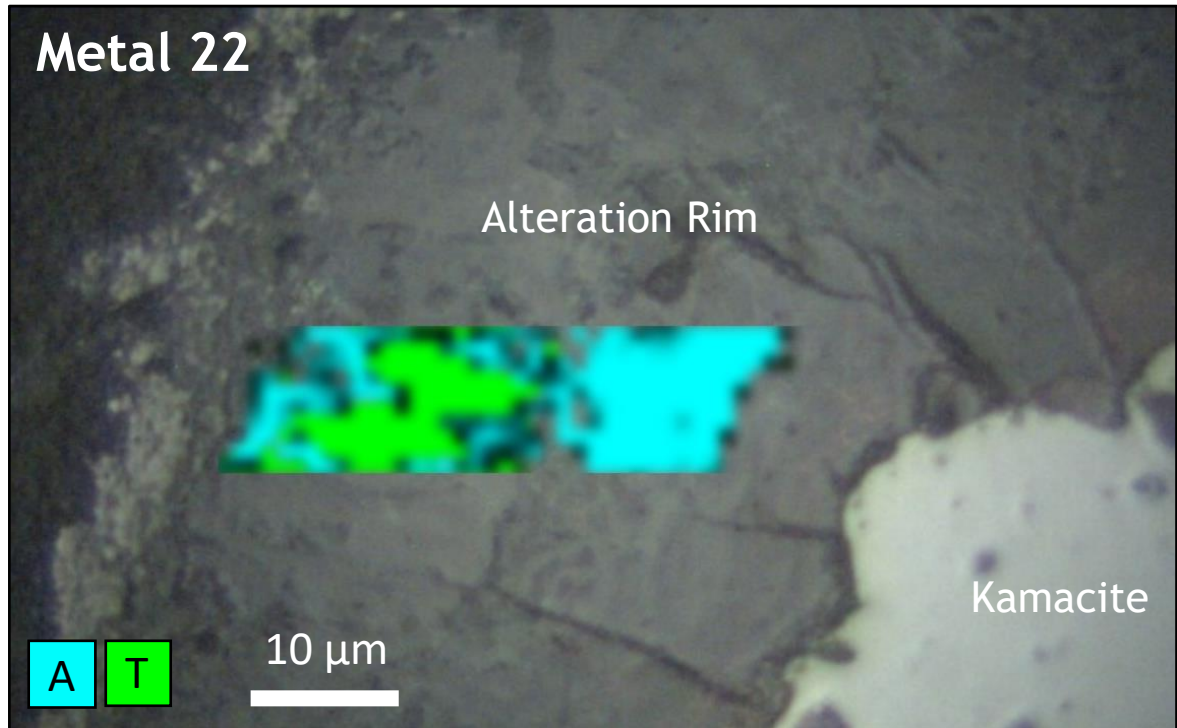


**Figure 4.11** Reflected light image of kamacite grain (metal 22) and the alteration rim with the results of a Principle Component Map (PCM) from the yellow highlighted region in figure 4.9 overlain. A = akaganeite. T = tochilinite.

#### 4.1.3.2 LAP 02239

Lap 02239 is a CM2 chondrite with a weathering grade of B- moderately rusted. AsB imaging revealed just two Fe,Ni metal grains in very close proximity to one another, one significantly larger than the other. These metal grains are connected by substantial alteration rims between ~20-75  $\mu\text{m}$  thick (Figure 4.12A). Figure 4.12A is annotated to show the likely boundary between these alteration rims.

The alteration rims surrounding these Fe,Ni metal grains contain two textures as illustrated in figures 4.12B and C. These textures mimic textures T1 and T3 in LEW 85311. T1, closest to the metal grain, is finely laminated and heavily fractured. T3, furthest from the metal grain, is composed of very disorganized

material. However, in this sample T3 also demonstrates some fracturing which was not observed in LEW 85311.

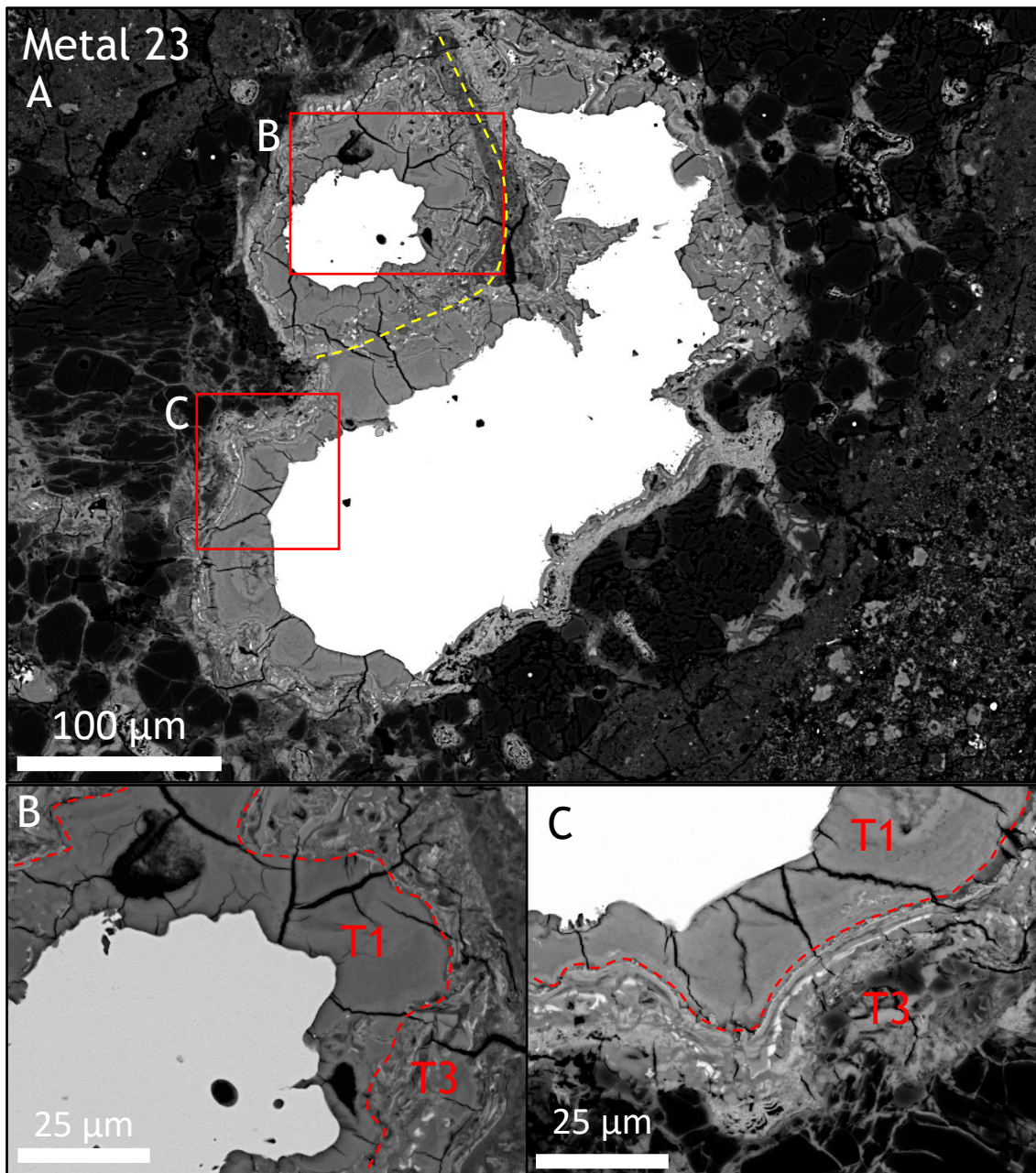


**Figure 4.12** BSE image of metal 23 in LAP 02239. A) Overview of both Fe,Ni metal grains (white) and the conjoined alteration rims, B) Magnified image of the smaller metal grain (white) showing the two textures observed, C) Magnified image of the larger metal grain (white) showing the two textures observed. Textures T1 and T3 mimic those found in LEW 85311.

### Chemical Composition:

EDS mapping and analysis of these metal grains reveals that both are kamacite with nickel concentrations of ~4.3 wt.% in the smaller grain and ~5.6 wt.% in the larger grain.

EDS mapping of Cl and S in the alteration rim reveals the boundary observed in BSE imaging between T1 and T3 also represents a compositional boundary (Figures 4.13 and 4.14). The alteration rim observed surrounding the smaller kamacite grain shows Cl-rich material occupying the T1 region (Figure 4.13B) with a Cl concentration of ~3.2 wt.%. EDS mapping of S (Figure 4.13C) shows that the S-rich material is confined to T3 with a concentration of ~11.8 wt.% S. EDS mapping of the larger metal (Figure 4.14) showed a similar pattern, with T1 dominated by Cl-rich material (~2.7 wt.% Cl) (Figure 4.13B) and T3 again dominated by S-rich material (~13.8 wt.% S) (Figure 4.13C).

Comparing EDS maps collected from LAP 02239 and LEW 85311 both compositional bands (Cl and S) observed in LAP 02239 appear less distinct than in LEW 85311. This difference is especially noticeable among the S-rich material, which shows far more fracturing (Figures 4.13C and 4.14C).

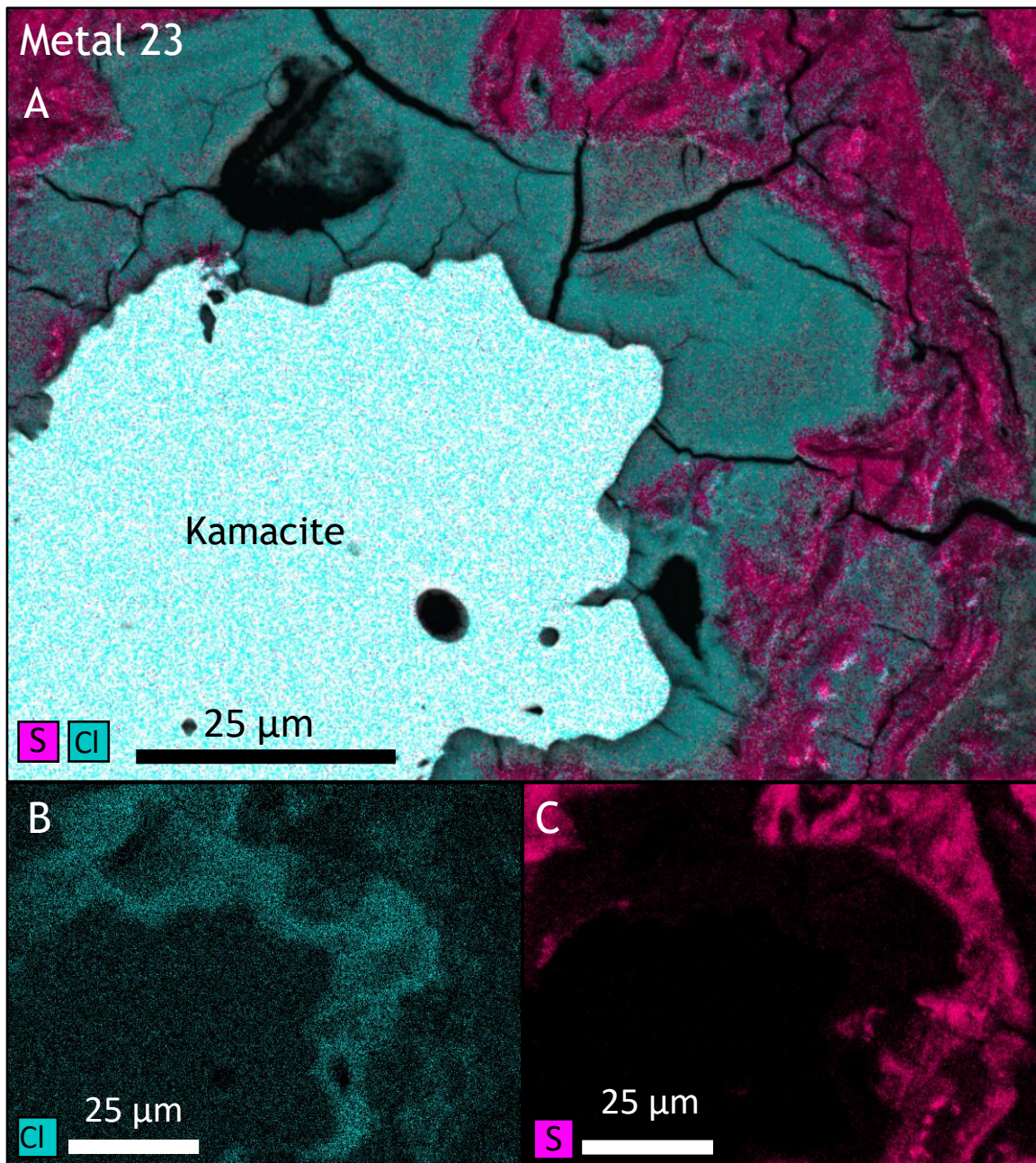


**Figure 4.13** EDS maps of the alteration rim surrounding the smaller kamacite grain. A) EDS maps of Cl and S overlain on a BSE image of the area. B) EDS map of Cl. C) EDS map of S.

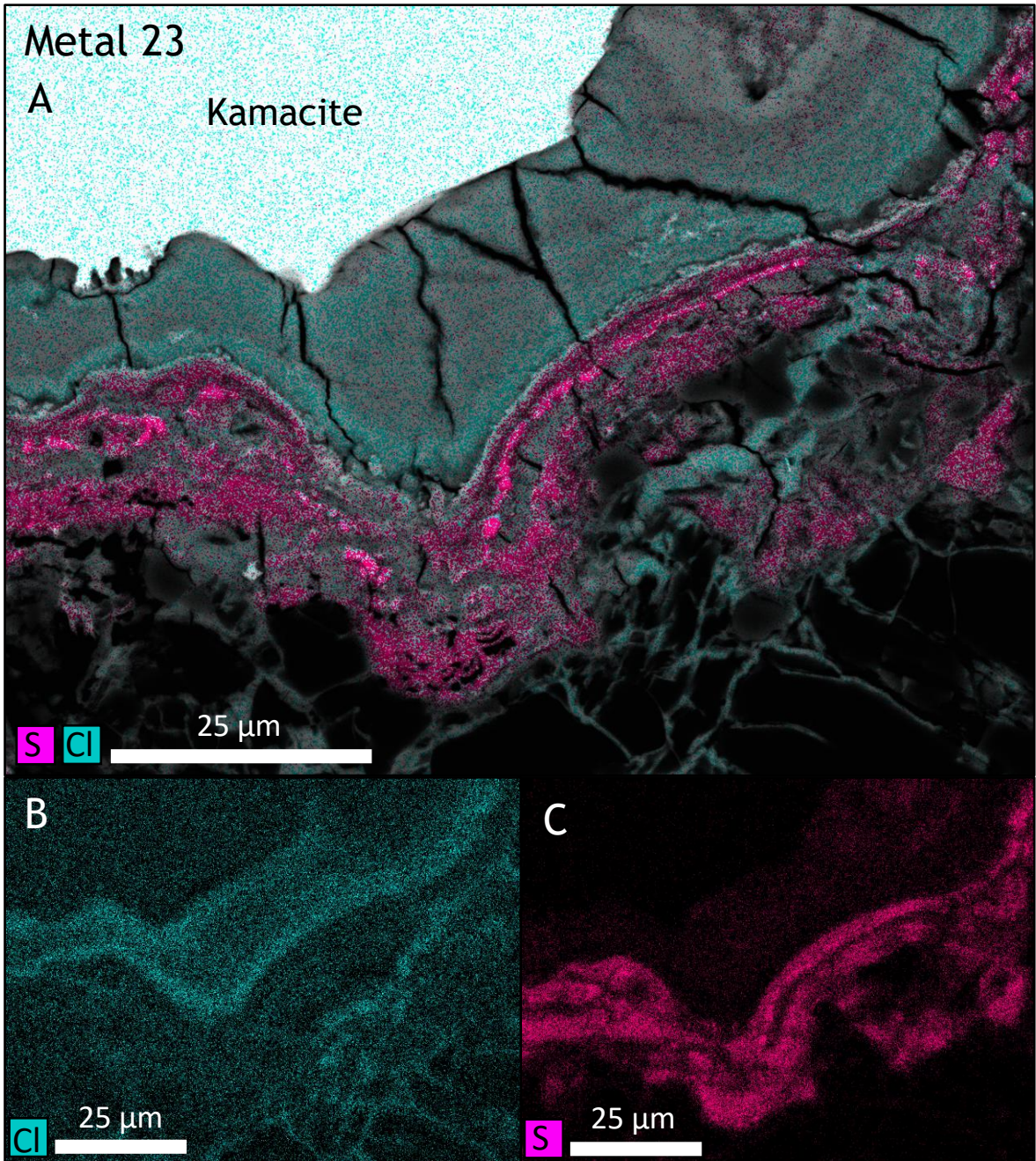


**Figure 4.14** EDS maps of the alteration rim surrounding the larger kamacite grain. A) EDS maps of Cl and S overlaid on a BSE image of the area. B) EDS map of Cl. C) EDS map of S.

### Mineralogy:

Point analysis Raman spectroscopy was carried out on both compositional bands within the alteration rims. The results of are shown in figure 4.15. Around both kamacite grains the Cl-rich, T1 region produced spectra for akaganeite (Figure 4.15, spectra A, C and D). Raman analysis, within the S-rich, T3 region produced less-clear results. Given the elevated S content found during chemical analysis and the findings from the Raman analysis in LEW 85311, this region is

expected to return obvious spectra for tochilinite, but this is not the case. Figure 4.15, spectrum B returns a weak spectrum with two broad peaks at  $300\text{ cm}^{-1}$  and  $470\text{ cm}^{-1}$ , both peaks are characteristic of the peak positions for tochilinite observed in LEW 85311. However, the lack of other identifiable peaks at  $\sim 250\text{ cm}^{-1}$  and  $\sim 350\text{ cm}^{-1}$  makes a positive identification using Raman spectroscopy difficult. Spectrum E was also collected from the S-rich material. In this instance a weak spectrum for akaganeite was obtained. The presence of akaganeite within this S-rich region suggests the breakdown of tochilinite by terrestrial weathering has already begun and the S-rich composition detected by EDS mapping may be misleading as to the mineralogy.

Following difficulties in obtaining clear Raman spectra it should be noted that good quality Raman spectra are obtained from well-crystallised materials. All the spectra collected from the S-rich, T3 region were poor quality spectra with broad peaks. The collection of poor-quality spectra therefore suggests that the material being sampled is poorly crystallised (Hanesch, 2009). Referring to AsB imaging in figure 4.12 shows that much of the S-rich material is heavily broken up with evidence of fracturing throughout. It may therefore be the case that the T3 material in this sample is in the process of alteration from tochilinite to an area of terrestrial alteration with spectrum E indicating this terrestrial alteration product may be akaganeite.

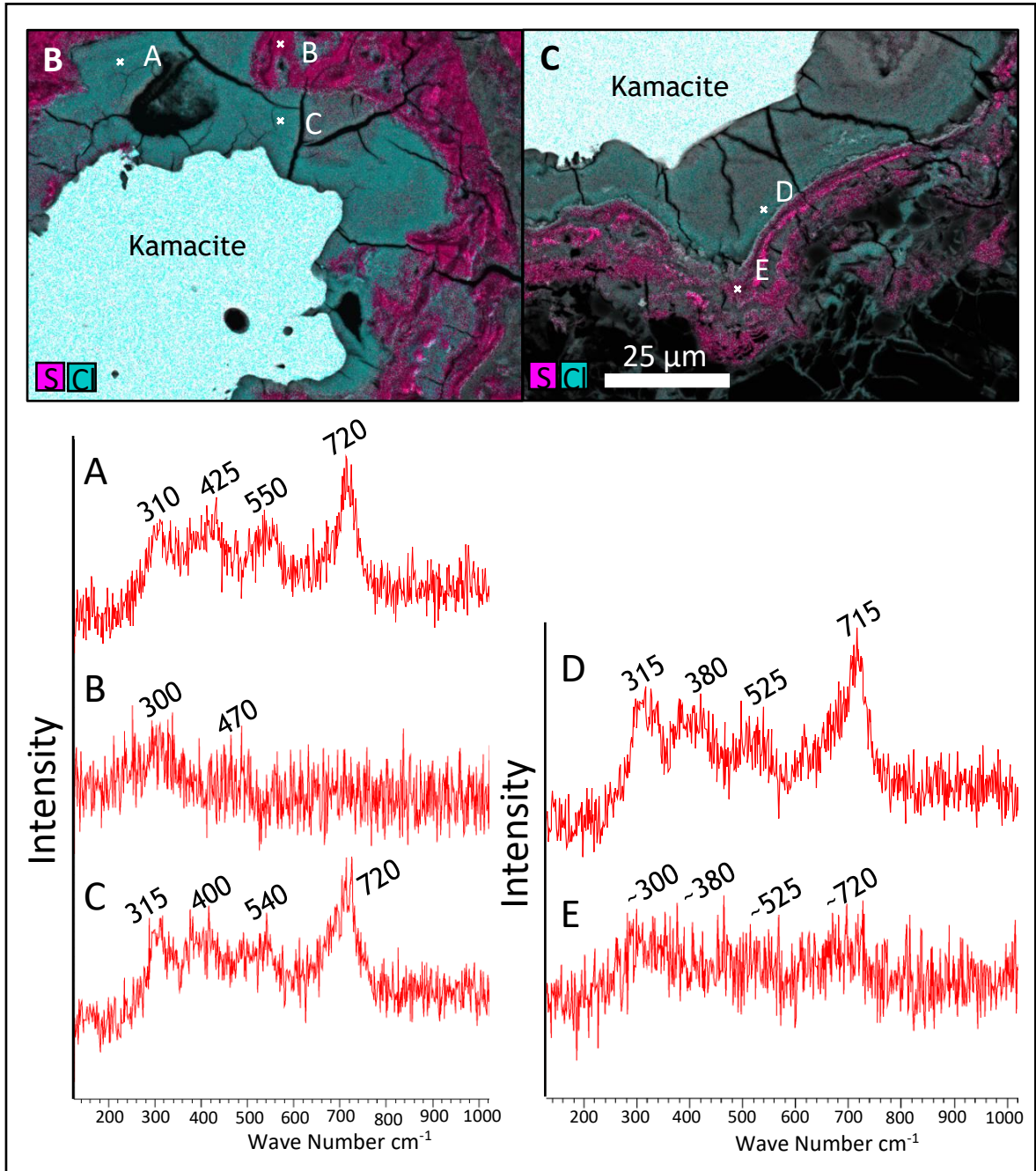


**Figure 4.15** EDS maps of metal 23 overlain on BSE images and accompanying Raman spectra for selected areas (Highlighted). Spectrum A) Akaganeite, B) Inconclusive but potentially tochilinite, C) Akaganeite, D) Akaganeite, E) Akaganeite (weak spectrum).

#### 4.1.4 Summary of Antarctic Carbonaceous Alteration

This analysis of Antarctic CM chondrites reveals that there are very few Fe,Ni metal grains present within these samples and that the alteration rims surrounding them contain evidence for alteration both terrestrially and within the parent body.

The alteration products observed around the Fe,Ni metal grains differ markedly in texture, with each texture corresponding to a difference in chemical composition. T1, is found closest to the metal grain boundary within LEW 85311 is not enriched in Cl, however within LAP 02239, T1 is Cl-rich. Progressively more disordered material with fewer fractures is then encountered moving outward (T2). T3, very disorganised material, is encountered furthest from the metal grain surrounding the alteration rim and is S-rich.

LEW 85311 provides a good example of the interaction between terrestrial and parent body alteration. Small metal grains with S-rich alteration rims return Raman spectra for tochilinite. Meanwhile, within the alteration rim of a larger kamacite grain Cl enriched regions return spectra for akaganeite and S enriched region return spectra for tochilinite. Veins of Cl can also be seen connecting Cl to the reaction front. Scatter plots of the chemical data also revealed that whilst NiO and S increased in abundance away from the metal grain, Cl had a more random correlation and was not related to the distance from the metal grain.

LAP 02239 is a less clear example of the interaction between terrestrial and parent body alteration. EDS mapping reveals distinct compositional variations between the different textures. However, Raman spectroscopy suggests this may be misleading. Raman spectroscopy identified akaganeite in the Cl-rich layers but, within the S-rich layers it struggled to provide a clear spectrum for S-rich tochilinite as expected. This is likely a result of terrestrial alteration beginning to erode the S-rich parent body material resulting in a poorly crystallised phase which does not produce clear Raman spectra.

Analysis of these samples, especially of LAP 02239, highlights the need for both mineralogical and compositional analysis of alteration products to fully understand the processes at work. Using only one approach risks the misinterpretation of alteration product origin.

## 4.2 Saharan CM Chondrites

The Saharan CM chondrite investigated in this chapter is Jbilet Winselwan. It has been classified as CM 1.5 on the Howard et al. (2015) scale and as a CM 2.4 on the Rubin et al. (2007) scale (King et al., 2018).

### 4.2.1 Environment

The Saharan samples analysed here were collected close to the town of Samara in Western Sahara. In this region hot desert conditions prevail with summer average maximum temperatures of 37.5 °C and the winter average maximum temperatures of 25.25 °C (Website 4.4). This area also receives an average of 28 mm of precipitation annually (Website 4.4).

### 4.2.2 Metal Content

The samples studied are two sections from the same meteorite (Jbilet Winselwan) and so the metal content was roughly equal in each, with numerous small metal grains.

**Table 4.3** ImageJ calculated, percentage volume of kamacite, taenite and troilite in each of the Saharan samples calculated from reflected light microscopy images. Troilite is included despite being a sulphide as it could not be distinguished from Fe,Ni metal in ImageJ.

Sample	Abundance (volume %)
Jbilet Winselwan P19398	1.79
Jbilet Winselwan P19399	1.44

### 4.2.3 Alteration Products

Initial reflected light microscopy confirmed the absence of any large metal grains within these samples. The metal grains which were observed were exceptionally small, less than 25 µm across with thin alteration rims observed around some of them.

#### 4.2.3.1 Jbilet Winselwan

Jbilet Winselwan is a CM2 chondrite and has a weathering category of W1. Two sections of Jbilet Winselwan are analysed here, P19398 and P19399. AsB imaging of the section P19398 revealed thin, 5-25 µm, alteration rims surrounding some of the metal grains. Figure 4.16 (metal 24) illustrates the typical small grain size and thin alteration rim. Similar to other samples investigated in this research the alteration rim had two textures. Closest to the metal grain is material with a pitted texture, surrounding this is material with a non-pitted texture (Figure 4.16).

AsB imaging of section P19399 shows similar results. Figures 4.17 and 4.18 show the alteration rims surrounding metals 25 and 26. These alteration rims are also thin with maximum thickness of 20 µm and are dominated by alteration material with a pitted texture. In metal 25 all alteration, except a small, darker region of material above the metal grain, appeared to have a pitted texture (Figure 4.17). Within metal 26 an inner zone of pitted material surrounded by a region of non-pitted material was observed, similar to metal 24.

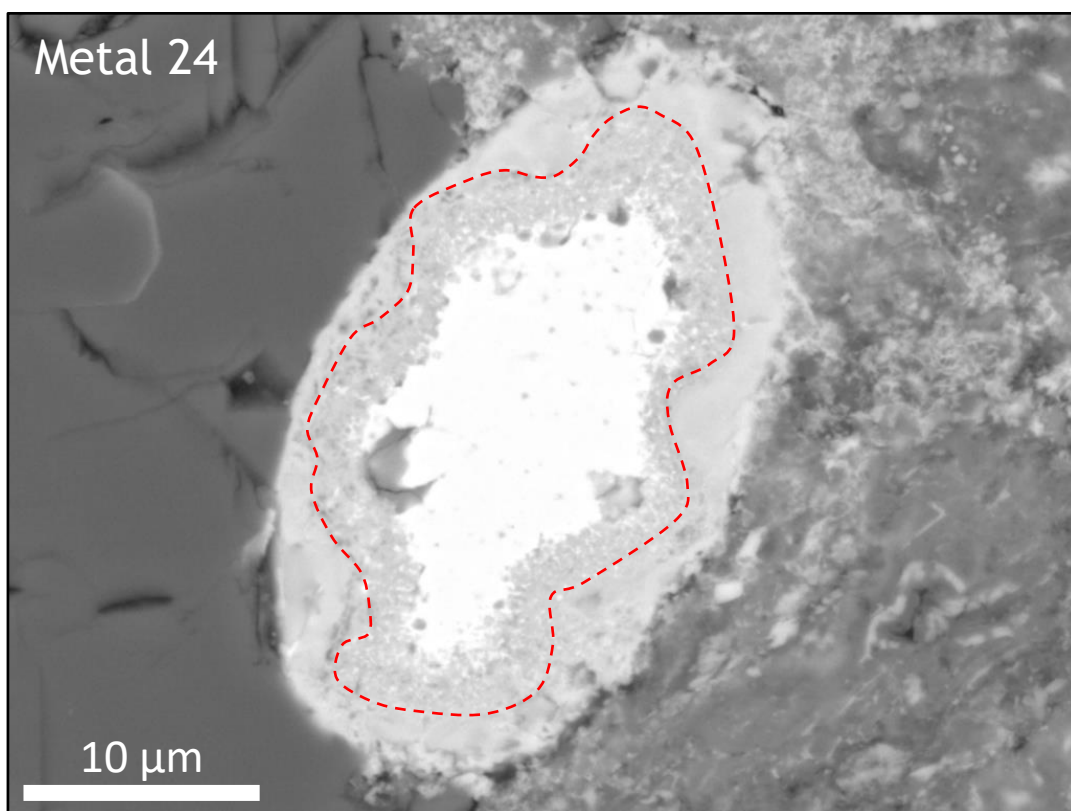


**Figure 4.16** BSE image of metal 24, an Fe,Ni metal grain (white). The alteration rim in this sample displays a pitted region and a non-pitted region. The boundary between these textures is highlighted.

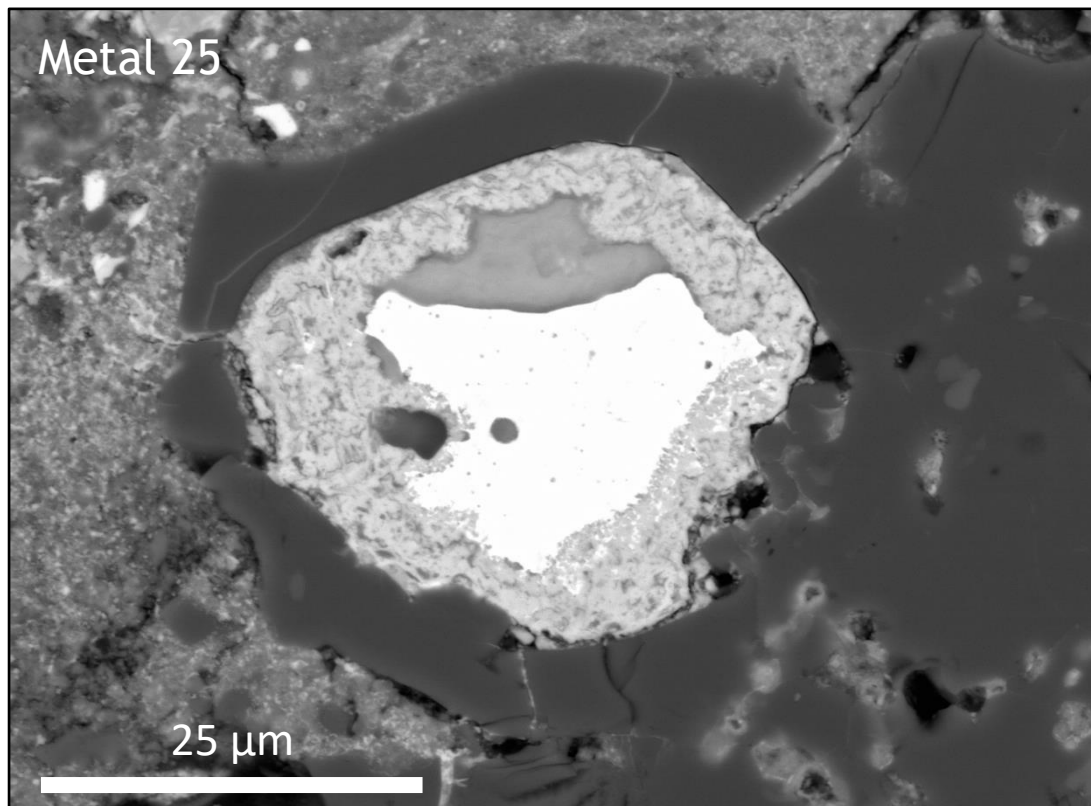


**Figure 4.17** BSE image of metal 25, an Fe,Ni metal grain (white). The alteration rim also appears pitted with the exception of a region of darker coloured material along the top edge.

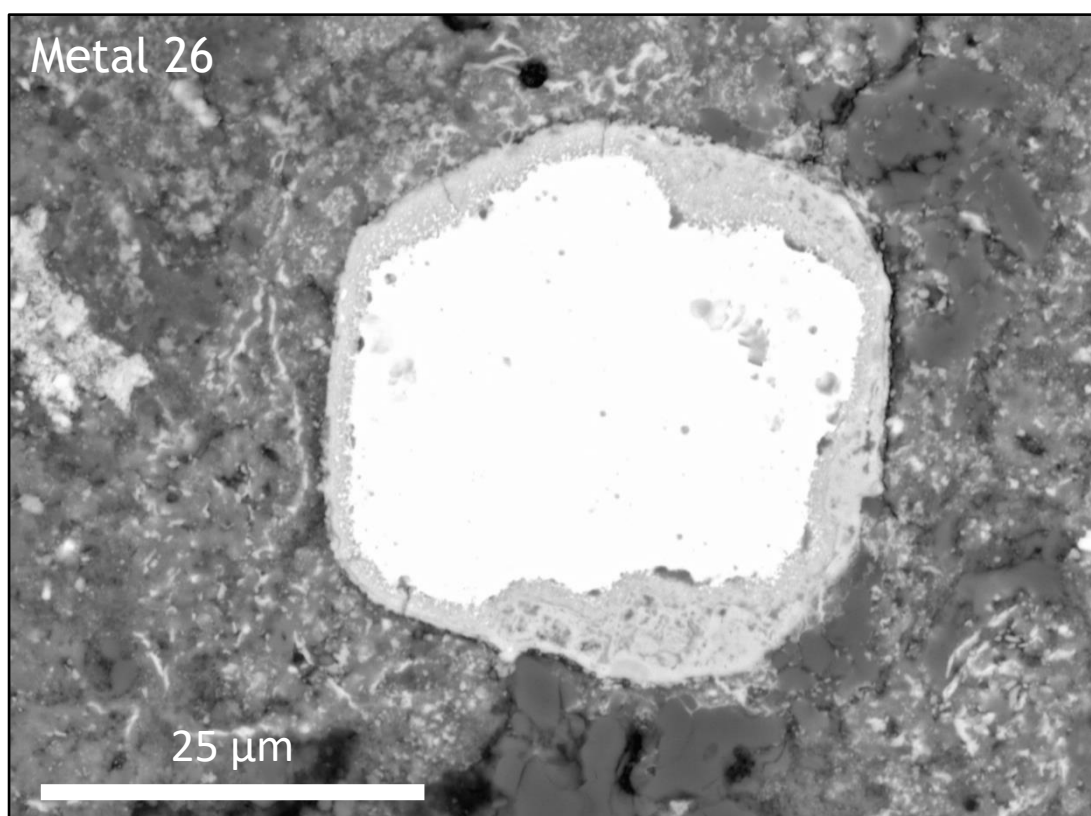


**Figure 4.18** BSE image of metal 26, an Fe,Ni metal grain (white). The alteration rim demonstrates a pitted texture in the inner region and a non-pitted texture in the outer region.

## Chemical Composition:

EDS mapping and EDS analysis was carried out on metals 24, 25 and 26. Results reveal all three metal grains to be kamacite with nickel concentrations of 6.9 wt.%, ~7.0 wt.% and ~4.7 wt.% in metals 24, 25 and 26, respectively (Table 4.4).

EDS mapping of Cl and S was conducted on each alteration rim. In all three metal grains S was detected around the edges of the alteration rim. Within the alteration rim of Metal 24 (Figure 4.19) S occurs extensively in the outer-most, non-pitted material where the S concentration reached up to 26 wt.% (Table 4.4). Metals 25 and 26 (Figures 4.20 and 4.21) had much thinner bands of S-rich material which appeared on the periphery of the alteration rim. In these cases concentrations were ~7 wt.% S in metal 25 and ~6.6 wt.% S in metal 26.

EDS mapping also suggested some Cl enrichment in these alteration rims. The largest area of Cl enrichment is in metal 25 where the darker area of material has a concentration of ~2.4 wt.% Cl compared to a negligible concentration in the surrounding material. Within the alteration rims of metals 24 and 26 Cl appears to be elevated within EDS maps of the alteration rim (Figures 4.19B and 4.21B) however, only negligible concentrations of Cl are detected, only 0.5 wt.% Cl, in metal 24 (Table 4.4).

Using figure 4.22 and table 4.4 it can be seen that the abundance of  $\text{Fe}_2\text{O}_3$  decreases away from the metal grain. Figures 4.23A, B and C are scatter plots comparing the relationships between  $\text{Fe}_2\text{O}_3$  and the key elements investigated (Ni, Cl and S). Figure 4.23A illustrates that NiO decreases with decreasing  $\text{Fe}_2\text{O}_3$ , and is therefore decreasing away from the metal grain. The NiO abundance is also shown to exceed the Ni abundance within the metal grain. Figure 4.23B, shows sulphur decreasing with increasing  $\text{Fe}_2\text{O}_3$  and S is therefore highest away from the metal grain. Sulphur values close to the metal grain boundary are broadly similar. Finally, figure 4.23C illustrates a much weaker relationship between  $\text{Fe}_2\text{O}_3$  and Cl and therefore distance from the metal grain. This is suggestive of chlorine abundance not being related to the abundance of  $\text{Fe}_2\text{O}_3$ .

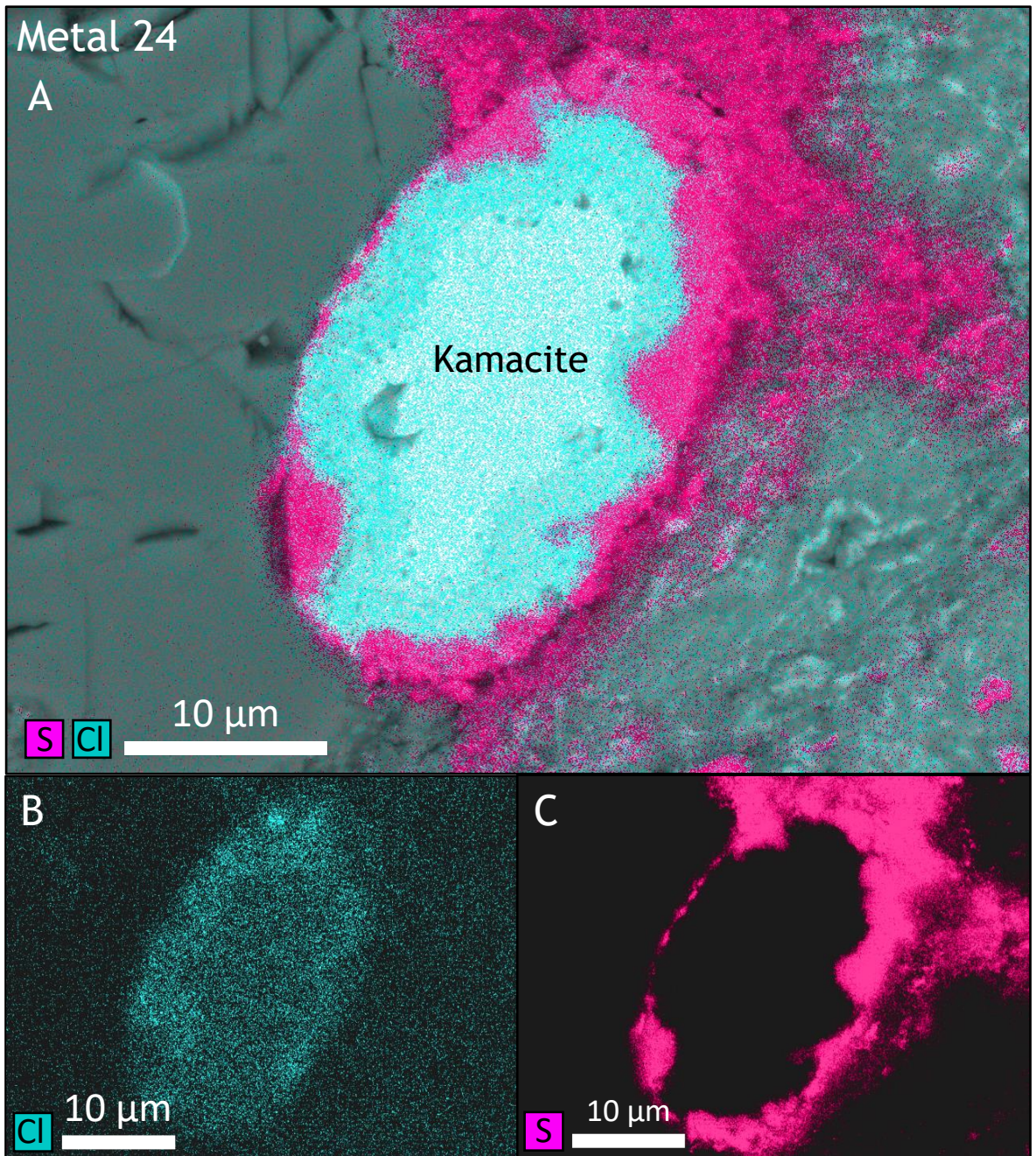


**Figure 4.19** EDS maps of metal 24, showing A) EDS maps of S and Cl overlain on a BSE image. B) EDS map of Cl. C) EDS map of S. These maps show the slight elevation in the Cl concentration within the inner, pitted region of the alteration rim and the S-rich region within the outer, non-pitted area of the alteration rim.

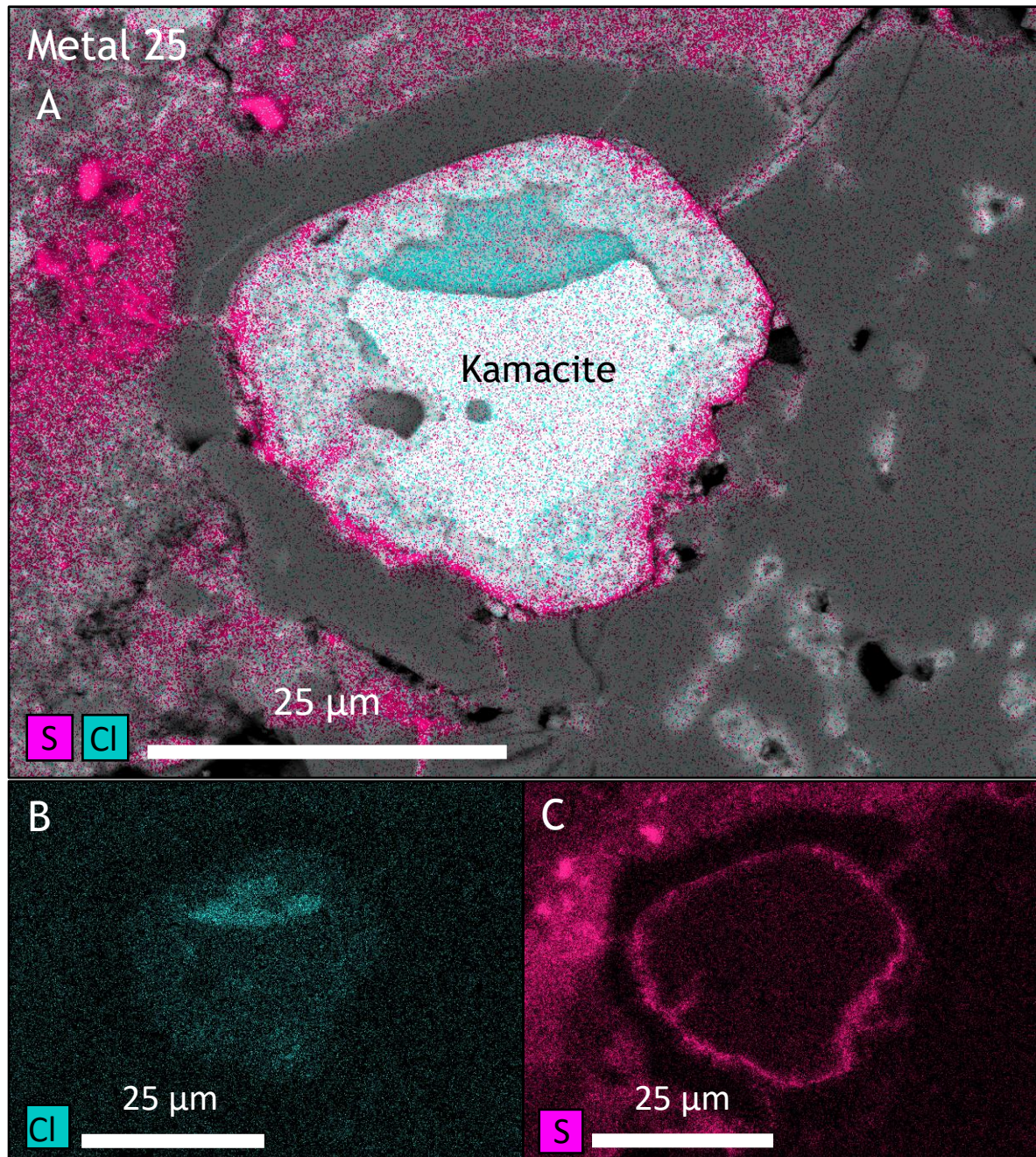


**Figure 4.20** EDS maps of metal 25, showing A) EDS maps of S and Cl overlain on a BSE image. B) EDS map of Cl. C) EDS map of S. These maps show the enrichment in Cl within the dark region of material along the top edge of the alteration rim and the elevated S concentration around the very edge of the alteration rim.

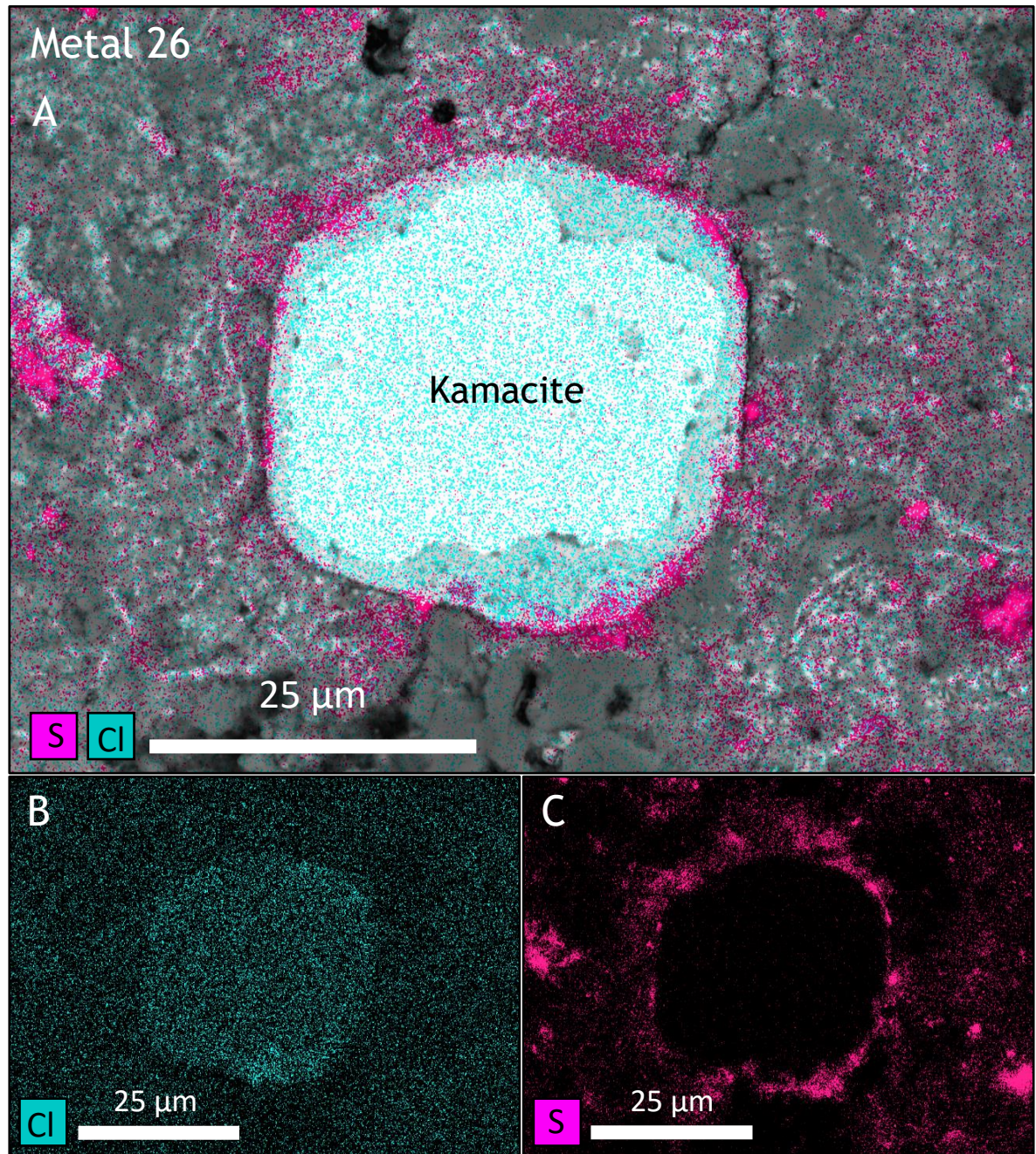


**Figure 4.21** EDS maps of metal 26, showing A) EDS maps of S and Cl overlain on a BSE image. B) EDS map of Cl. C) EDS map of S. These maps show a slight increase in Cl within the bulk of the alteration rim and the patchy areas of elevated S around the periphery of the alteration rim.

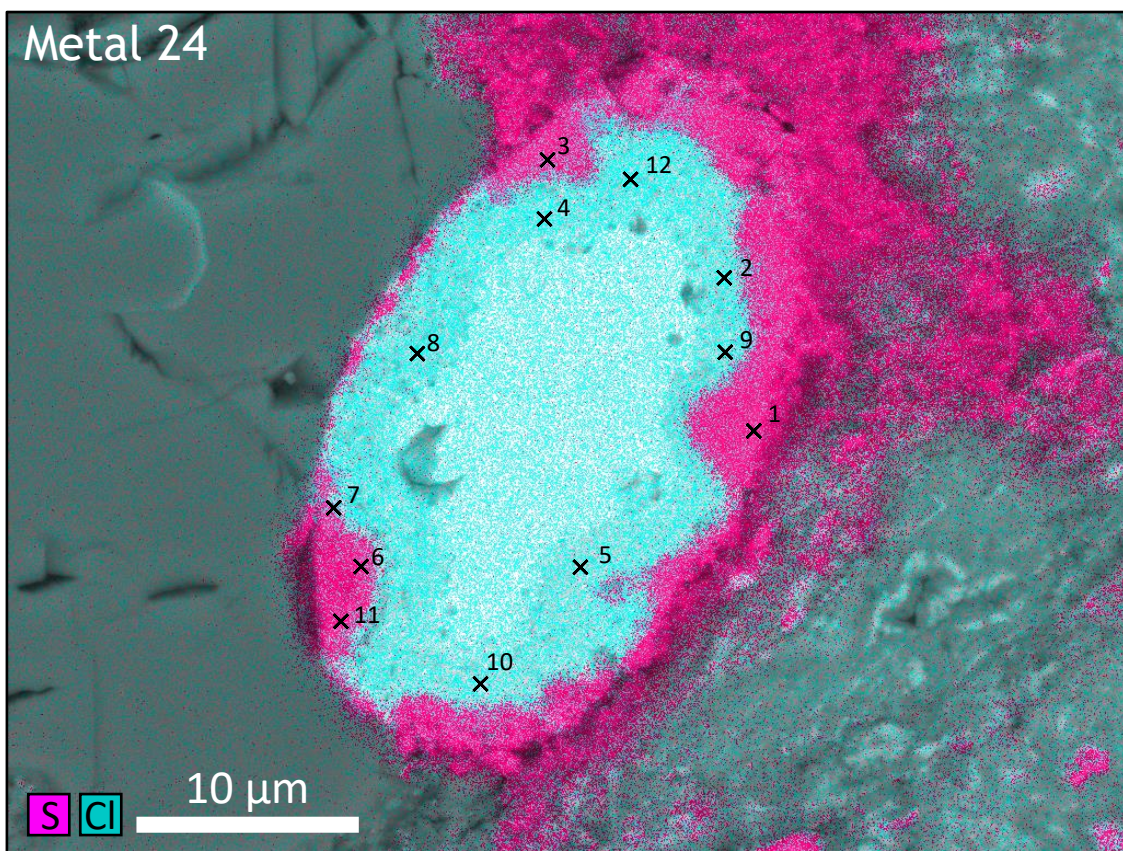


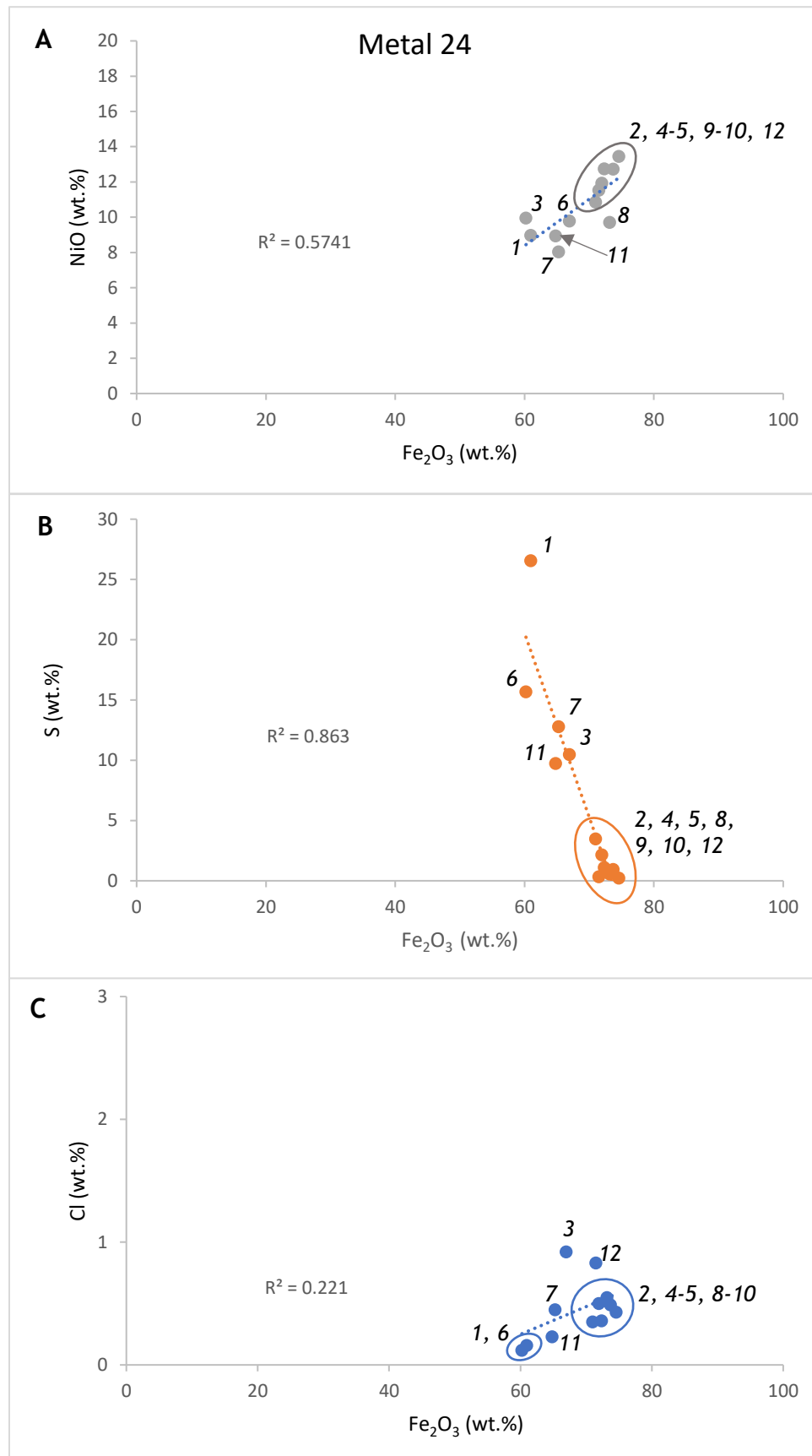
**Figure 4.22** EDS maps of Cl and S overlain on BSE image of metal 24. Labelled are the points of quantitative analysis shown in table 4.4.

**Table 4.4** Results of quantitative analysis around Metal 24 and as labelled in figure 4.21. Values shown are in weight %. Minimum detection limits are stated below.

Position Number	SiO <sub>2</sub>	Al <sub>2</sub> O <sub>3</sub>	Fe <sub>2</sub> O <sub>3</sub>	MgO	CaO	NiO	S	Cl	Fe <sub>(m)</sub>	Ni	Total
1	4.99	1.08	60.97	3.02	-	8.98	26.55	0.16	-	-	105.74
2	0.24	0.40	73.71	-	-	12.74	0.94	0.49	-	-	88.51
3	1.60	0.94	66.95	0.90	0.73	9.79	10.47	0.92	-	-	92.31
4	0.41	0.25	74.59	-	-	13.46	0.22	0.43	-	-	89.36
5	0.26	0.49	72.35	-	-	12.75	1.09	0.36	-	-	87.30
6	8.39	1.51	60.21	2.85	1.54	9.96	15.66	0.12	-	-	100.23
7	5.76	1.30	65.29	3.41	1.11	8.04	12.78	0.45	-	-	98.14
8	0.34	0.36	73.16	-	-	9.72	0.55	0.55	-	-	84.68
9	0.47	0.45	71.95	0.22	0.18	11.94	2.14	0.50	-	-	87.85
10	0.94	0.45	70.99	0.35	0.27	10.86	3.48	0.35	-	-	87.69
11	4.88	0.89	64.81	4.28	0.60	8.95	9.72	0.23	-	-	94.37
12	0.17	0.21	71.48	0.38	-	11.53	0.33	0.83	-	-	84.93

Minimum Detection Limit	0.06	0.06	0.17	0.04	0.07	0.25	0.07	0.07	0.17	0.25	
-------------------------	------	------	------	------	------	------	------	------	------	------	--



**Figure 4.23** Graphs illustrating the relationships between  $\text{Fe}_2\text{O}_3$  (wt.%) and the key elements investigated in metal 24. Data taken from table 4.4 and values given in wt.%. Labels represent position numbers stated in Table 4.4. A) Graph of  $\text{Fe}_2\text{O}_3 - \text{NiO}$ . B) Graph of  $\text{Fe}_2\text{O}_3 - \text{S}$ . Position numbers correspond to Figure 4.22 and Table 4.4. C) Graph of  $\text{Fe}_2\text{O}_3 - \text{Cl}$ .

## Mineralogy:

Point analysis Raman spectroscopy was carried out in the alteration rims of metals 24 and 25 to investigate whether the compositional changes observed correspond to mineralogical changes.

Spectra collected from metal 24 (Figure 4.24) were not of good quality. Spectra A and C show that the pitted texture, which appeared slightly elevated in Cl, produced Raman spectra with three peaks. The first two peaks are broad, low intensity peaks around  $340\text{ cm}^{-1}$  and  $510\text{ cm}^{-1}$  and the third was a much more prominent peak at  $\sim 670\text{ cm}^{-1}$ . These peak positions correspond to magnetite which, has characteristic peak positions at  $310\text{ cm}^{-1}$ ,  $536\text{ cm}^{-1}$ , and  $667\text{ cm}^{-1}$  (Hanesch, 2009). Spectrum B shows the result of measurement within the S-rich material. Measurement here which produces an inconclusive spectrum with significant noise, (Figure 4.24B). Close inspection of spectrum B suggests a slight, broad peak around  $320 \pm 10\text{ cm}^{-1}$  which is broadly characteristic of tochilinite. However, without distinguishable peaks at  $250\text{ cm}^{-1}$  and  $350\text{ cm}^{-1}$  it is not possible to characterise accurately. As discussed previously in section 4.1.3.2 (LAP 02239) these broad peaks are likely the result of sampling poorly crystallised material, suggesting the S-rich area is especially poorly crystalline (Hanesch, 2009).

Within metal 25 the Raman spectra measured were slightly clearer revealing the Cl-rich, darker material to be akaganeite (Figure 4.25, spectrum A). Within the pitted material sampled in metal 25 peak positions at  $310\text{ cm}^{-1}$ ,  $540\text{ cm}^{-1}$  and  $665\text{ cm}^{-1}$  were returned, indicating a mineralogy of magnetite. The peak at  $540\text{ cm}^{-1}$  in spectrum C adds further evidence to the finding of magnetite.

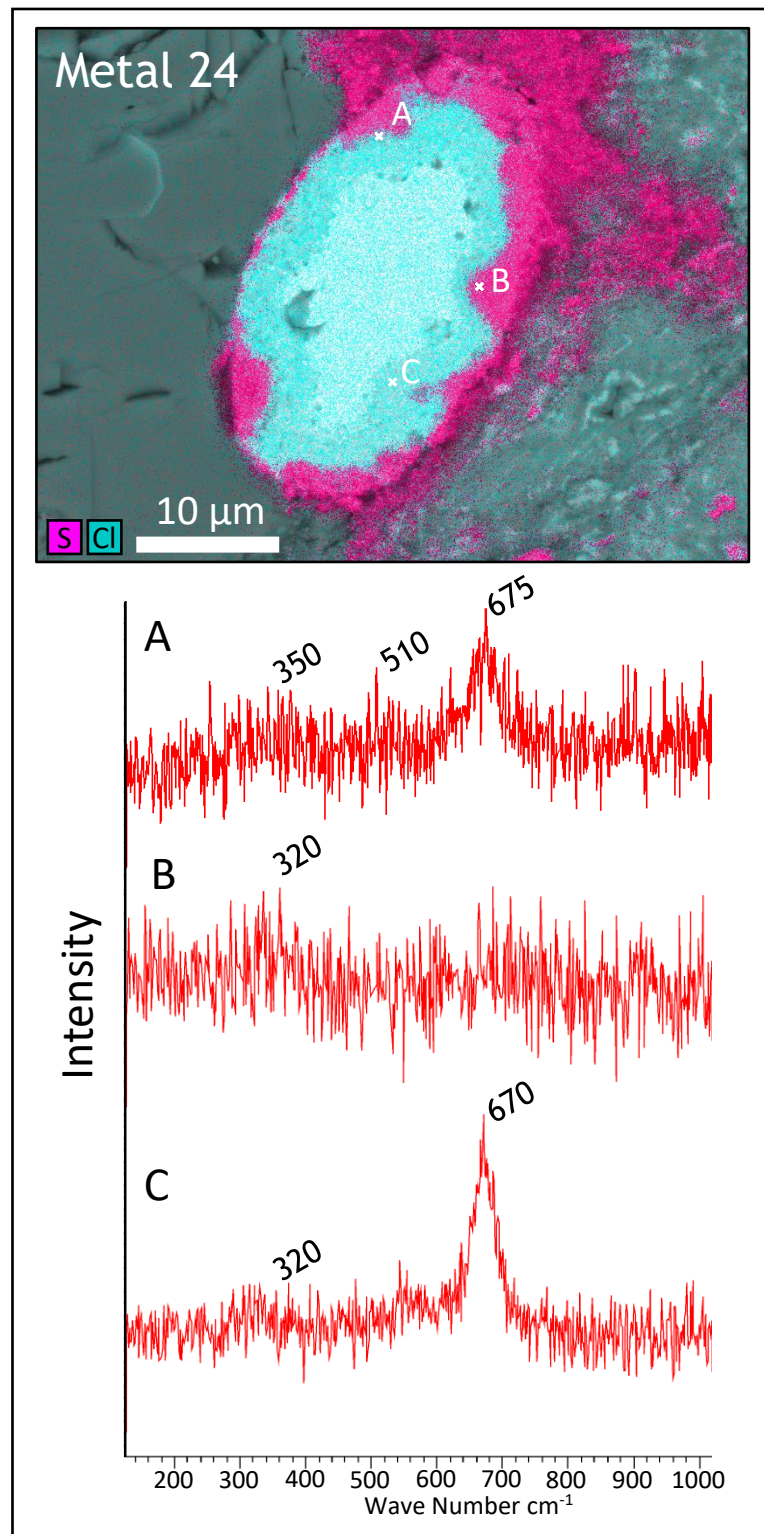


**Figure 4.24** EDS maps of metal 24 overlain on BSE image and accompanying Raman spectra for selected locations (highlighted). Spectrum A) Magnetite, B) Inconclusive, C) Magnetite.

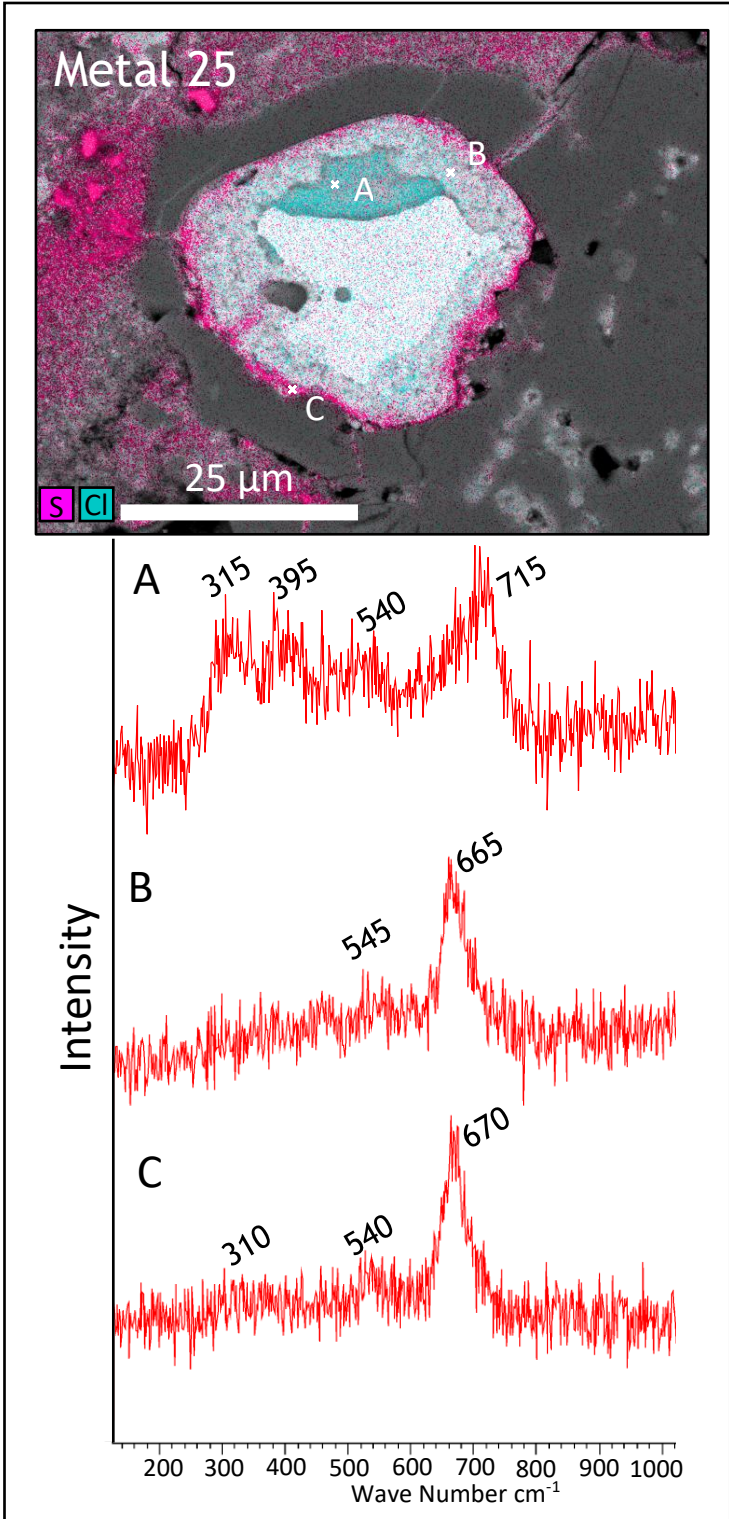


**Figure 4.25** EDS maps of metal 25 overlain on a BSE image and accompanying Raman spectra for selected locations (highlighted). Spectrum A) Akaganeite, B Magnetite, C) Magnetite.

#### **4.2.4 Summary of Saharan Carbonaceous Alteration**

Analysis of this Saharan CM2 chondrite sample has shown that this meteorite is characterised by only a few small kamacite grains, accompanied by narrow alteration rims.

AsB imaging and chemical analysis of these samples reveal the alteration rims are mostly composed of heavily pitted material with some small, confined areas of Cl enrichment which graphical analysis suggests has no relationship to the abundance of  $\text{Fe}_2\text{O}_3$  or position in the alteration rim. Chemical analysis also reveals S-rich material around the outside edge of all the alteration rims analysed suggesting the presence of tochilinite and therefore corresponding to parent-body alteration. However, the S-rich alteration products around these kamacite grains are far more difficult to characterise mineralogically, than in any carbonaceous or ordinary chondrite so far investigated in this research. The S-rich region appears to be composed of a very poorly crystalline phase whose mineralogy is difficult to determine using Raman spectroscopy. Whilst using a higher laser power may improve the quality of the spectra produced and yield a greater insight, this would likely result in sample burning which limits the long-term usefulness of the samples and thus prohibits its application (Hanesch, 2009).

Mineralogical identification of the non-S rich regions proved more fruitful with the pitted material returning spectra for magnetite and the dark coloured region in metal 25 returning a spectrum for akaganeite.

### **4.3 Summary of Analytical Results**

From the analysis here it is clear that carbonaceous chondrite samples have been altered both terrestrially, in their find environment and pre-terrestrially whilst part of their parent bodies. Evidence for both stages of this alteration remain in CM chondrite samples today.

The Antarctic samples have experienced significant terrestrial alteration with akaganeite, and goethite identified alongside pre-terrestrial tochilinite. In the case of LEW 85311 a clear chronology can be seen with the oldest alteration material (parent body material) towards the edge of the alteration rim and the

younger, terrestrial alteration towards the centre, this is the opposite to what was observed in the ordinary chondrites. Over time it is likely that the terrestrial material will continue to develop eventually eroding any evidence of parent-body alteration. Smaller metal grains can also be seen in LEW 85311 solely showing the parent body alteration product tochilinite and thus awaiting terrestrial influence.

The obvious chronology is not repeated as clearly in LAP 02239, but there is chemical and mineralogical evidence that the process is still occurring. In this sample a poorly crystalline S-rich alteration material does not allow for accurate or widespread mineralogical interpretation using Raman spectroscopy and the spectra measured suggest it is beginning to alter to akaganeite. A clear compositional boundary is, however seen between S-rich and Cl-rich products. Analysis of this sample has demonstrated that only by using both mineralogical and chemical analysis techniques can a complete understanding of the alteration be gained.

Within the Saharan sample, evidence is much less forthcoming with narrower alteration rims of poorly crystallised mineral phases within the S-rich regions. Chemical analysis suggests a similar pattern to the Antarctic samples should exist, with Cl enriched inner regions and S-rich outer regions. However, unlike the Antarctic samples Raman spectroscopy reveals the slightly Cl enriched inner regions to be dominated by magnetite and the S-rich, outer region to be very poorly crystallized material which cannot be interpreted using Raman. Only one small area of akaganeite was detected.

## 4.4 Discussion

Carbonaceous chondrites have a far a larger proportion of fine-grained matrix than ordinary chondrites and are enriched in volatile elements and organic compounds. They therefore have a larger and more reactive surface area than ordinary chondrites and should respond differently to terrestrial weathering (Bland et al., 2006). As a result of these differences it would be expected that carbonaceous chondrites are more quickly altered by terrestrial weathering agents. This research can neither support nor refute this hypothesis as only a very limited selection of carbonaceous chondrites was examined.

This research has however revealed for the first time that the products of parent-body alteration and terrestrial alteration co-exist within CM chondrites. During this chapter, tochilinite has proven to be the most difficult mineral to identify mineralogically, especially within LAP 02239 and Jbilet Winselwan. Difficulties in tochilinite identification are perhaps unsurprising given that historically within the literature tochilinite was termed the ‘poorly characterised phase’ (PCP) due to difficulties in interpretation and identification. Today more is known about tochilinite ( $\text{FeS}(\text{Mg}, \text{Fe}^{2+})(\text{OH})_2$ ) and it is widely accepted to be evidence of parent body aqueous processing by circulating S-bearing fluids initiating the first stages of alteration around Fe,Ni metal (Mackinnon and Zolensky, 1984; Browning and Bourcier, 1996; Rubin et al., 2007; Palmer and Lauretta, 2011).

Within the literature, tochilinite occurring within carbonaceous chondrites has been widely investigated but remains relatively poorly understood. Palmer and Lauretta (2011) found tochilinite would occupy either regions that would ordinarily be occupied by kamacite grains (suggesting complete metal grain replacement) or, less often, small areas within the matrix. Palmer and Lauretta (2011) also described how tochilinite and kamacite are not usually co-located. The findings of this research suggest that tochilinite can be and often is co-located with kamacite typically within an alteration rim, supporting Kimura et al. (2011), who found Fe,Ni grains within the matrix to be frequently surrounded by tochilinite assemblages. This contradiction within the literature and the findings presented here highlight the further work needed in this area of carbonaceous chondrite alteration.

With regards to the relationship between parent-body and terrestrial alteration, there is no published work examining this interaction. Only interactions between what is believed to be parent body Fe-oxide (magnetite) and tochilinite have been discussed (Rubin et al., 2007; Palmer and Lauretta, 2011). This work suggests that terrestrial weathering and alteration can have a significant impact on the extent of pre-terrestrial alteration products (tochilinite and magnetite). Within the alteration rims of the CM chondrites examined here the direction of alteration appears reversed in comparison to the ordinary chondrites observed in Chapter 3. Within the CM chondrites the primary alteration product akaganeite was seen in the greatest abundance in the outer region of the alteration rim with

the goethite closer to the metal grain. A proposed explanation for this reversal of weathering directions is that once Cl has reached the Fe,Ni metal interface the weathering products preferentially weather outwards into the Fe-rich and S-rich tochilinite. This has the effect of reversing the direction of corrosion front advancement compared to the ordinary chondrites. As tochilinite is not present in ordinary chondrites the corrosion front is dominant at the Fe,Ni metal boundary and advances inwards.

During their work Palmer and Lauretta (2011) employed Raman spectroscopy, alongside other techniques, to confirm the presence of mineral phases within the Fe-oxides. They too experienced difficulties in obtaining spectra. Using a 532 nm laser at 100 % power for 15 seconds and 8 accumulations Palmer and Lauretta (2011) identified abundant magnetite within the Fe-oxide grains. This magnetite was interpreted as being a product of parent body aqueous alteration likely precipitating out of solution (Palmer and Lauretta, 2011). Line scans by Palmer and Lauretta (2011) showed that this material was being altered from the outside inwards to form tochilinite. What is described by Palmer and Lauretta (2011) mimics the patterns observed around the majority of the Jbilet Winselwan grains examined in this research (section 4.2.3.1) especially within metal 24. In this instance the lack of significant akaganeite in the Jbilet Winselwan samples (only present in metal 25) suggests very limited terrestrial alteration has taken place, surprising for a hot desert sample. As the magnetite detected in this research is likely pre-terrestrial, the simultaneous presence of pre-terrestrially and terrestrially derived Fe-oxide emphasises the requirement for more precise chemical and mineralogical analysis of CM chondrite alteration.

Raman spectroscopy could fulfil the role of providing more accurate mineralogical data however, more detailed investigation of the techniques is required. The use of Raman spectroscopy by Palmer and Lauretta (2011) illustrates why further technique development is required. The laser power used in their study was much higher than could be used during this research, potentially how they were able to gather more definitive spectra. However, using a high laser power risks compromising sample usefulness, if not through sample burning than by the transformation of some iron-rich minerals which are easily transformed when exposed to this high laser powers greater than 1 mW (Hanesch, 2009). This

is something which should be considered when analysing delicate samples such as CM chondrites.

## 4.5 Conclusions

This chapter has revealed that the alteration experienced by CM chondrites is more complex than in ordinary chondrites. Alteration products from the parent body and terrestrial environment co-exist around the majority of Fe,Ni metal grains.

Within the Antarctic samples parent body alteration products are characterised by tochilinite, present as remnant material around the edges of Fe,Ni alteration rims that are otherwise dominated by terrestrial oxidation products: akaganeite, goethite and hydrated iron III oxide or oxyhydroxide. These terrestrial alteration products initiate corrosion at the metal grain boundary and slowly erode much of the original parent body alteration.

Within the Saharan samples the picture is more complex with evidence of two stages of parent body alteration alongside evidence of terrestrial alteration. The parent body alteration is dominated by magnetite which is believed to have precipitated out of solution (Palmer and Lauretta, 2011). Surrounding the magnetite is tochilinite which is believed to have begun altering the magnetite as S-rich fluids circulated through the parent body (Palmer and Lauretta, 2011). In small regions there is then evidence of terrestrial alteration (akaganeite), which is overprinting the earlier (parent body) alteration. The lack of more developed terrestrial alteration in this sample is surprising and suggests either a young terrestrial age, exceptional curation conditions where continued weathering has been prevented or another factor which remains unknown. The alteration of magnetite to tochilinite also appears to have produced a very poorly crystallised phase which is almost uninterpretable using Raman spectroscopy. Using the findings of this work figure 2.26 was produced to illustrate the pathways of alteration, both terrestrial and pre-terrestrial, affecting Fe,Ni metal in CM chondrites. The Blue arrow indicates a proposed pathway should Cl not be present in the environment and therefore not available to produce akaganeite. This pathway is proposed because it was not observed during this research.

Throughout the literature there is no significant work examining the effects of terrestrial oxidation on CM chondrites. This work has shown that there needs to be acknowledgement of this oxidation phase in the alteration of samples as it has significant impacts on the preservation of parent body material. A lack of detailed understanding and by using only one analytical approach (chemical or mineralogical) could lead to severe misinterpretation of the alteration products present and what they represent. It is therefore suggested that more research is urgently needed to better understand the relationship between parent-body and terrestrial alteration products, how best to differentiate between them and how to prevent the irreversible effects of terrestrial alteration eroding scientifically valuable products.

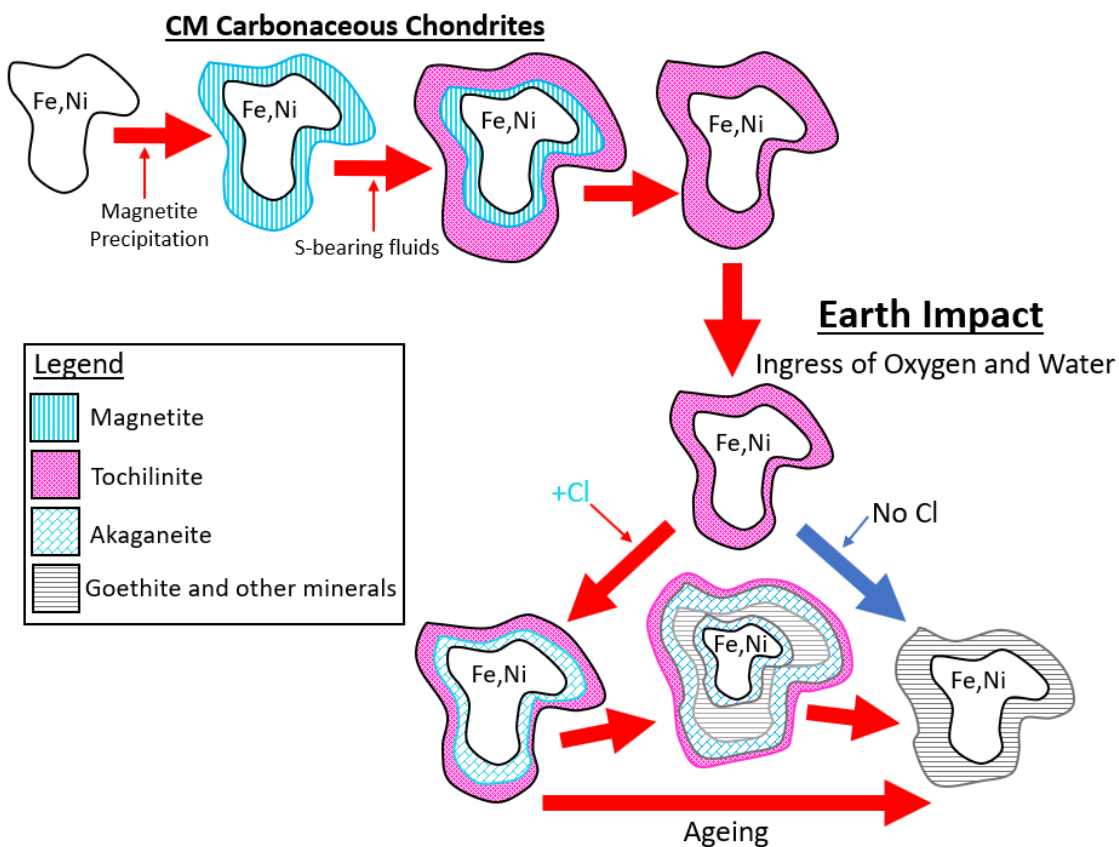


**Figure 4.26** Flow diagram showing the proposed alteration pathways of Fe,Ni metal both terrestrially and pre-terrestrially. The blue arrow indicates what is proposed to occur should Cl not be present in the environment.

# Chapter 5 Summary

This chapter summarises the key findings of this research and the effectiveness of the analytical techniques used. It also discusses potential avenues for future research.

## 5.1 Summary of Analytical Techniques

During this project chemical data was obtained using EDS mapping and point analysis whilst mineralogical information was obtained using Raman spectroscopy. This study is the first to use Raman spectroscopy to investigate terrestrial alteration in ordinary and carbonaceous chondrites. It is also the first study to use both chemical and mineralogical data to investigate terrestrial weathering at a high spatial resolution.

EDS mapping and analysis was used throughout this work to obtain chemical data from Fe,Ni metal grains and their alteration rims. Within ordinary chondrites Cl maps proved effective in highlighting areas composed of akaganeite whilst in carbonaceous chondrites mapping Cl and S proved extremely effective in illustrating the presence, and constraining the boundary between, akaganeite and tochilinite. In some instances (Figure 4.6C) EDS mapping also provided insight into the chemical pathways facilitating the movement of Cl from the environment to the reaction front, by capturing evidence of a Cl-rich vein cross-cutting the alteration rim. EDS analysis collected quantitative chemical data and allowed accurate compositions to be calculated and relationships between  $\text{Fe}_2\text{O}_3$  and the key elements (Ni, S and Cl) to be investigated. Limitations to this chemical data were encountered when sampling regions of significant alteration in Saharan CM chondrites, for example where chemical data suggested regions of S-rich products, mineralogical data suggested non-S rich product magnetite. Chemical data was also not able to distinguish between secondary alteration products goethite and hydrated iron III oxide and oxyhydroxide.

Raman spectroscopy was the approach unique to this work and attempted to obtain detailed, high spatial resolution mineralogical data. Previous work has obtained mineralogical data through Mossbauer spectroscopy (Bland et al., 1998), a bulk technique which lacks spatial resolution. During this work a multiple exposure, averaging technique was used to produce high quality spectra and avoid sample burning resulting from high laser powers. Limitations to this technique came when examining areas of significant alteration (outer most edges of CM chondrites) where alteration has resulted in poorly crystalline material, which Raman spectroscopy, at the power used here, cannot accurately identify.

Raman spectroscopy Principle Component Mapping (PCM) was also attempted during Antarctic CM chondrite analysis. This approach did produce an approximately accurate pattern of the mineralogy, however restrictions in the sampling method by the equipment (single exposure) prevented accurate distinction between akaganeite and goethite. Limitations also arose from the long data collection time (4 hours). However, Bellot-Gurlet et al. (2009) successfully mapped Fe-oxides over a larger area ( $60 \mu\text{m} \times 60 \mu\text{m}$ ) and successfully distinguished between akaganeite, goethite and hydrate iron III oxide or oxyhydroxide. It may therefore be an approach which, with refining and more sophisticated equipment, could prove extremely valuable for precise mineralogical studies in planetary science.

## 5.2 Summary of Alteration Products

### 5.2.1 Ordinary Chondrites

Ordinary chondrites have not experienced significant aqueous alteration on their parent bodies and therefore the three alteration products detected in this research (akaganeite, goethite and hydrated iron III oxide or oxyhydroxide) which are all the result of terrestrial weathering processes.

Akaganeite was detected in samples usually with significant alteration rims. It is a Cl-rich alteration product with a concentration of ~1-6 wt.% Cl which allowed it be loosely constrained by EDS mapping of Cl. Raman spectroscopy confirmed the presence of akaganeite in Cl-rich areas detecting peaks at  $\sim 310 \text{ cm}^{-1}$ ,  $\sim 390 \text{ cm}^{-1}$ ,  $\sim 540 \text{ cm}^{-1}$ ,  $\sim 610 \text{ cm}^{-1}$  and  $\sim 720 \text{ cm}^{-1}$ . It was most frequently detected

in Antarctic samples and is interpreted as the first alteration product to form, providing  $\text{Cl}^-$  ions are present in the environment.

Goethite was the most abundant alteration mineral identified during this work and was identified either surrounding areas of akaganeite making up the majority of alteration material or as a replacement product in regions of complete metal grain replacement. It is not enriched in any element and therefore could not be constrained by EDS mapping. Raman analysis was used to confirm the presence of goethite with peak positions at  $\sim 240 \text{ cm}^{-1}$ ,  $\sim 300 \text{ cm}^{-1}$ ,  $\sim 390 \text{ cm}^{-1}$ ,  $\sim 485 \text{ cm}^{-1}$ ,  $\sim 550 \text{ cm}^{-1}$ ,  $\sim 685 \text{ cm}^{-1}$ . During this research goethite was interpreted as a secondary alteration product forming from the ageing and transformation of akaganeite (Figure 5.1), supporting the findings of Buchwald and Clarke (1989).

Hydrated iron III oxide or oxyhydroxide is described by Bellot-Gurlet et al. (2009) as being a generic term for a group of poorly crystallised minerals with incredibly similar Raman spectra: Maghemite, Ferrihydrite 6-line, Ferrihydrite 2-line and feroxyhite ( $\delta\text{-FeOOH}$ ). In this research it was detected in the smallest quantities by Raman spectroscopy within material otherwise dominated by goethite. Like goethite it is not enriched in any element and Raman spectroscopy is required to distinguish between hydrated iron III oxide or oxyhydroxide and goethite. Hydrated iron III oxide or oxyhydroxide is characterised by Raman peaks at  $\sim 390 \text{ cm}^{-1}$ ,  $\sim 500 \text{ cm}^{-1}$  and  $700 \text{ cm}^{-1}$ . From this research it is not clear how hydrated iron III oxide or oxyhydroxide develops or whether it is a secondary alteration product like goethite as suggested by Buchwald and Clarke (1989) or if it is a tertiary product eventually replacing goethite.

### 5.2.2 Carbonaceous Chondrites

Within carbonaceous chondrites four alteration products were identified: akaganeite, goethite, tochilinite and magnetite. Akaganeite and goethite were shown in ordinary chondrite to be the result of terrestrial weathering. Tochilinite and Magnetite are described as being evidence of parent body alteration (Browning and Bourcier, 1996; Palmer and Lauretta, 2011).

The terrestrial weathering products detected in CM chondrites were akaganeite and goethite. Akaganeite was detected in the inner regions of both

Antarctic and Saharan CM metal grain alteration rims. Goethite was only detected in Antarctic samples and was detected (adjacent to akaganeite) in small quantities. EDS mapping alteration rims also revealed delivery of Cl to the reaction front via Cl-rich veins.

The parent body alteration products detected were tochilinite and magnetite. Tochilinite was detected in both Antarctic and Saharan samples around the outermost edge of alteration rims. EDS analysis showed tochilinite to be a S-rich product with ~6-27 wt.% S. The high S content allowed for accurate constraining using EDS mapping. Raman measurements confirmed the presence of tochilinite with peak positions at  $\sim 250\text{ cm}^{-1}$ ,  $\sim 300\text{ cm}^{-1}$  and  $\sim 350\text{ cm}^{-1}$ . Magnetite was only detected within the inner regions of alteration rims in Saharan CM chondrites. Magnetite was characterised by Raman measurements with peak positions at  $\sim 310\text{ cm}^{-1}$ ,  $356\text{ cm}^{-1}$   $667\text{ cm}^{-1}$ .

Within CM chondrites it was found that the terrestrial alteration products (akaganeite and goethite) were eroding and replacing the pre-terrestrial, parent body products (tochilinite and magnetite). As a consequence of this, detailed mineralogical and chemical analysis is needed to correctly identify the origin of alteration products and prevent misinterpretation. An example of possible misinterpretation within the literature is found in Brearley (2006). In this instance a corrosion rim surrounding an Fe metal grain, within a weakly altered CM chondrite is identified (Figure 5.1). Brearley interpreted the alteration rim as being composed of parent body tochilinite/cronstedtite replacement products. The general appearance of the alteration rim in figure 5.1 is similar to the alteration rims observed in Chapter 4 which were shown to be composed of both terrestrial and parent body alteration products. This study therefore suggests that unless high resolution mineralogical and chemical analysis techniques were used, Brearley's identification may not be accurate.

Following the analysis of the alteration products observed in ordinary and carbonaceous chondrites, figure 5.2 was produced to summarise the results. It illustrates the alteration pathways experienced and proposed (blue arrows) by both ordinary and carbonaceous chondrites.

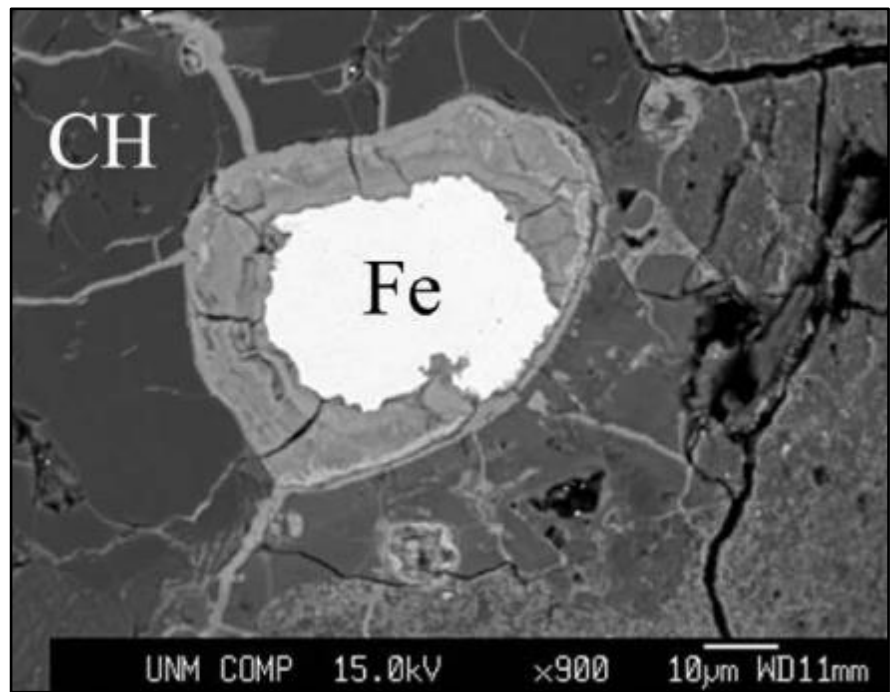


**Figure 5.1** BSE image taken from Brearley (2006), showing a corrosion rim interpreted as being composed of parent body tochilinite/cronstedtite alteration products and which following research here may have been misinterpreted.

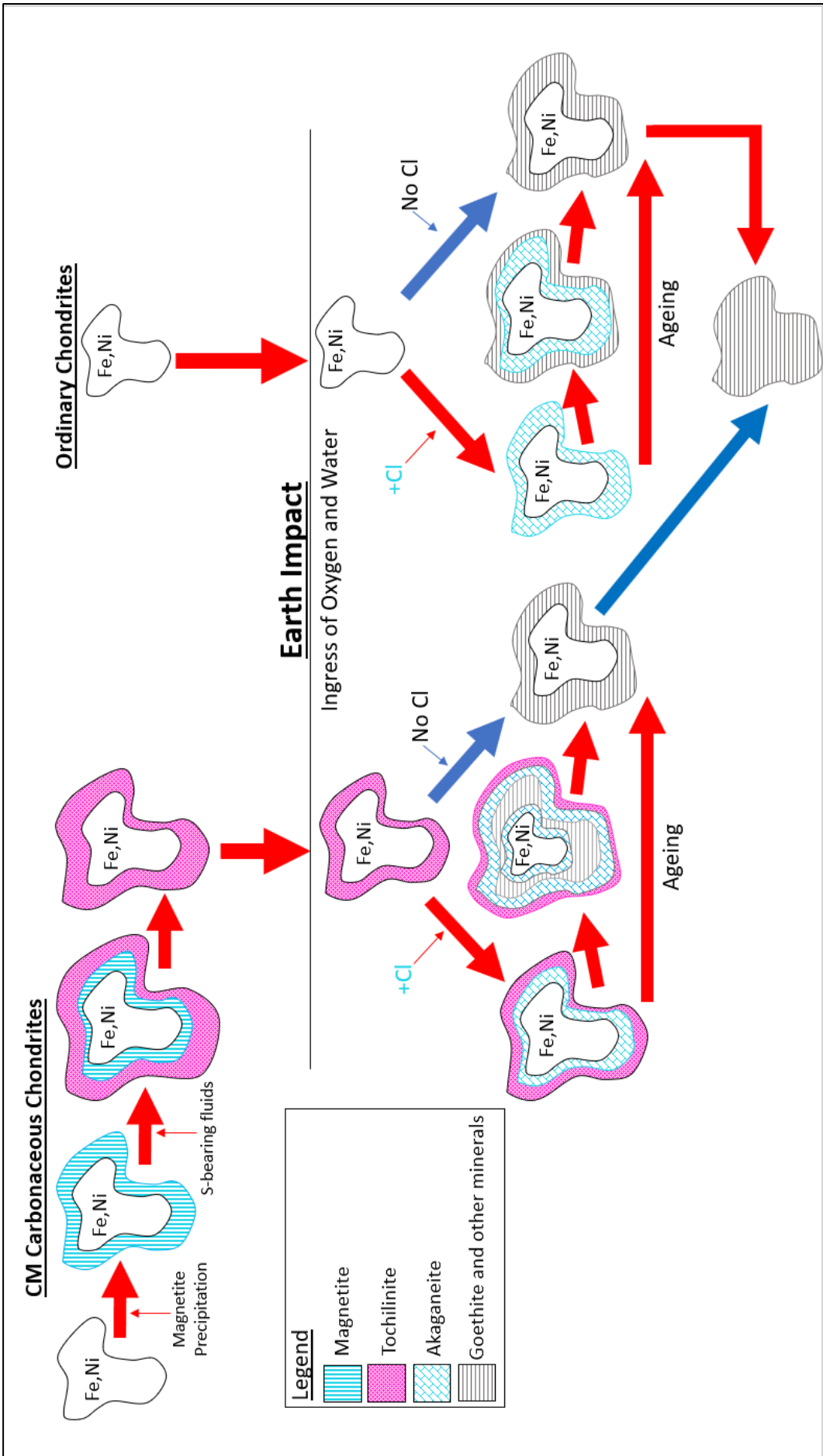


**Figure 5.2** Flow diagram summarising the alteration experienced around Fe,Ni metals in carbonaceous and ordinary chondrites. The blue arrows indicates what is proposed to occur should CM chondrites survive long enough for the reaction to go to completion.

### 5.3 Environmental Differences

Within ordinary chondrites there were distinct differences observed in the alteration products between the three environments investigated. Samples from the Antarctic environment possessed significant quantities of both akaganeite and goethite within thick alteration rims surrounding the majority of metal grains. Within the Saharan environment substantial alteration rims of akaganeite and goethite were also observed. However, this was alongside evidence of complete metal grain replacement. The Western Australian ordinary chondrites showed variation in alteration intensity. The majority of samples showed extensive Fe,Ni metal grain replacement and alteration within the less susceptible troilite grains. The alteration products in these cases were dominated by goethite. However, Forrest 028, a Western Australian sample, showed significant alteration rims surrounding Fe,Ni metal instead of complete metal grain replacement as expected, and had significant quantities of akaganeite. This difference in alteration intensity is likely a result of localised terrestrial conditions producing a less intense weathering effect in Forrest 028 than was experienced in the other samples and highlights the role of localised condition within the broader climatic content. Analysis of the ordinary chondrites is therefore generally suggestive of the warm, wet Western Australian environment having the most detrimental impact on original composition and the cold, dry Antarctic environment having the least impact.

The carbonaceous samples were far more complex with terrestrially derived akaganeite and goethite occurring alongside parent body magnetite and tochilinite. Within the Antarctic samples evidence of extensive terrestrial alteration, composed of akaganeite and goethite, was seen surrounding larger Fe,Ni metals, and replacing parent body tochilinite. Smaller metal grains were also seen but lacked evidence of terrestrial alteration. Following analysis of Saharan and western Australian ordinary chondrites it was expected that Saharan CM samples would have experienced more intense alteration than Antarctic CM samples. This is not the case. Only very small amounts of terrestrial akaganeite were detected and no secondary alteration products such as goethite were recorded. Instead there was extensive tochilinite and magnetite both of which formed on the parent body. However, only one Saharan CM chondrite was analysed during this research and the results may not be representative. It is therefore not possible to say with

certainty which environment produces the greatest terrestrial weathering effect on CM carbonaceous chondrites.

## 5.4 Future Work

This study has highlighted the need for more research on the effects of terrestrial weathering on ordinary, and particularly CM chondrites. In addition to this it has also emphasized the use of Raman spectroscopy as a powerful mineralogical identification tool within planetary sciences. Below are areas which following this work either require further study or could be exciting avenues for further research.

Following the observations in chapter 3 investigating how increasing the distance from the coast and thus increasing the distance from the Cl supply is one such area for further research. This would help aid our understanding of terrestrial weathering when the Cl, essential for akaganeite development is limited.

The effects of terrestrial weathering on hot desert CM chondrites requires more attention. Chapter 4 showed terrestrial akaganeite completely replacing two phases of parent body alteration (magnetite and tochilinite). If such a process is widespread among Saharan CM chondrites, then this could have significant impacts on the scientific usefulness of hot desert CM samples. Unfortunately, only one hot desert CM chondrite was available for study in this research and so more data is needed to develop a thorough understanding of the terrestrial weathering impacts on hot desert CM chondrites.

During this research Raman spectroscopy proved to be a useful and powerful tool for mineralogical identification of Fe-oxides. In 2020 the European Space Agency (ESA) and Russian space agency (Roscosmos) are set to launch a joint rover to Mars as part of the Exo Mars mission. Attached to this rover will be a Raman spectrometer with the aim of establishing precise identification of mineral phases and detecting organic compounds (Rull et al., 2017). Akaganeite has already been detected on Mars via orbital measurements using the Compact Reconnaissance Imaging Spectrometer for Mars (CRISM) instrument on the Mars Reconnaissance Orbiter (MRO) (Carter et al., 2015) and by the Chemistry and Mineralogy (CheMin) and Sample Analysis at Mars (SAM) instruments onboard the

Curiosity rover. The addition of a Raman spectrometer on the Exo Mars 2020 mission facilitates further opportunities to detect akaganeite and other Fe-oxide minerals on the red planet at a greater spatial resolution. Greater understanding of the development of Fe-oxides on Mars can help improve our understanding of the palaeoconditions which may have existed there. In addition to possible Martian applications, Raman spectroscopy could also be utilised on other meteorite classes to investigate how they are affected by the terrestrial environment. This may prove beneficial for investigations of Fe-rich meteorites.

Principle Component Mapping (PCM) is another technique which could be investigated further. It is already extensively used in archaeology for Fe-oxide investigations and if it could be adapted for use on more fragile, extra-terrestrial samples to provide high resolution mineralogical information of weathering Fe-oxide weathering products.

The final area for further research is museum weathering, investigating the effects of curation conditions on the development of terrestrial alteration products. This study has shown the effects of exposed terrestrial environments but what are the optimum curation conditions to prevent or limit the continued alteration of samples after collection? Buchwald and Clarke (1989) suggested flushing Cl from the crust and storage in low oxygen, low humidity environments. This research suggests alteration develops slowest in cold, low humidity environments, but is there a way to prevent development? Understanding alteration in the curated environment is especially important given the upcoming Hayabusa 2 and OSIRIS-REx sample return missions where samples will need to be carefully curated to prevent contamination from the terrestrial environment.

## 5.5 Conclusion

This work has characterised the effects of terrestrial weathering on ordinary and CM carbonaceous chondrites at a high spatial resolution, demonstrating how terrestrial alteration products can corrode and replace evidence for parent-body alteration around Fe,Ni metal. This work has shown that akaganeite, goethite and poorly crystalline hydrated iron III oxide or oxyhydroxide are the products of terrestrial weathering and that warm, wet terrestrial conditions facilitate the most intense alteration. This work has also demonstrated the importance of a dual

approach to alteration product identification. Both chemical and mineralogical information are required for an accurate understanding of the processes involved using only one approach risks misinterpretation of the alteration experienced.

# Appendix

## Quantitative analysis of metal 1

Results of chemical analysis on the alteration rim surrounding metal 1 in DOM 14010 (wt.%)											
Position Number	SiO <sub>2</sub>	Al <sub>2</sub> O <sub>3</sub>	Fe <sub>2</sub> O <sub>3</sub>	MgO	CaO	NiO	S	Cl	Fe <sub>(m)</sub>	Ni	Total
1	0.21	0.13	81.71	0.30	0.14	9.18	1.10	0.71	-	-	93.49
2	0.41	0.19	89.73	0.17	0.14	5.17	0.78	1.52	-	-	98.10
3	0.26	0.21	90.47	0.33	0.18	4.97	0.69	2.53	-	-	99.64
4	-	0.23	88.92	0.17	0.11	5.16	0.66	2.64	-	-	97.88
5	0.39	0.17	87.00	0.00	0.11	6.25	0.62	1.96	-	-	96.50
6	0.36	0.25	86.77	0.08	0.11	7.23	0.62	1.77	-	-	97.19
7	0.73	0.32	88.37	0.10	0.24	6.59	0.42	0.65	-	-	97.42
8	1.22	0.26	88.62	0.20	-	6.72	0.56	0.22	-	-	97.80
9	2.29	0.21	85.11	1.17	-	7.06	0.64	0.45	-	-	96.93
10	0.51	0.30	88.94	0.13	0.11	5.22	0.58	1.90	-	-	97.71
11	0.41	0.42	88.73	-	0.15	5.79	0.50	1.32	-	-	97.32
12	0.77	0.17	83.14	0.32	-	10.05	0.59	0.42	-	-	95.45
13	0.28	0.25	69.57	0.22	0.18	19.00	1.32	1.06	-	-	91.87
14	0.15	0.21	74.85	0.07	-	16.00	1.22	1.51	-	-	94.00
15	0.28	-	64.25	0.35	0.14	24.83	0.93	0.40	-	-	91.18
<b>Minimum Detection Limit</b>	0.06	0.07	0.17	0.04	0.08	0.25	0.08	0.07	0.17	0.25	

## Quantitative analysis of metal 5

Results of chemical analysis on the alteration rim surrounding metal 5 in ALHA 77180 (wt.%)											
Position Number	SiO <sub>2</sub>	Al <sub>2</sub> O <sub>3</sub>	Fe <sub>2</sub> O <sub>3</sub>	MgO	NiO	S	Cl	Fe <sub>(m)</sub>	Ni	Total	
1	-	-	-	-	-	-	-	-	97.22	6.68	103.90
2	-	-	-	-	-	-	-	-	96.01	6.90	102.91
3	-	-	-	-	-	-	-	-	96.29	6.64	102.93
4	3.87	-	66.96	0.52	5.23	1.35	0.46	-	-	-	78.39
5	3.49	0.49	70.24	-	4.32	0.99	0.30	-	-	-	79.83
6	3.29	-	69.39	-	4.47	1.12	0.34	-	-	-	78.61
7	3.17	-	69.44	-	4.36	0.95	0.38	-	-	-	78.30
8	4.32	-	70.03	0.53	4.15	0.96	0.21	-	-	-	80.21
9	4.21	-	69.94	0.72	4.01	0.72	0.20	-	-	-	79.81
10	3.98	-	68.44	0.48	4.39	0.85	-	-	-	-	78.15
11	2.31	-	84.87	-	5.65	0.42	-	-	-	-	93.25
12	6.55	-	63.02	2.32	4.75	0.82	0.29	-	-	-	77.75
13	2.67	-	87.06	-	5.68	0.41	-	-	-	-	95.82
14	3.96	-	68.20	0.48	5.44	1.24	0.37	-	-	-	79.69
15	3.40	-	71.80	0.48	4.47	0.76	0.20	-	-	-	81.12
<b>Minimum Detection Limit</b>	0.07	0.01	0.20	0.05	0.28	0.08	0.08	0.20	0.28		

## Quantitative analysis of metal 6

Results of chemical analysis on the alteration rim surrounding metal 6 in ALHA 77180 (wt.%)								
Position Number	SiO <sub>2</sub>	Fe <sub>2</sub> O <sub>3</sub>	NiO	S	Cl	Fe <sub>(m)</sub>	Ni	Total
1	-	-	-	-	-	97.92	5.28	103.20
2	-	-	-	-	-	98.12	5.72	103.84
3	-	-	-	-	-	80.97	22.63	103.60
4	-	-	-	-	-	74.60	28.26	102.86
5	-	-	-	-	-	97.26	5.92	103.18
6	-	-	-	-	-	97.40	5.46	102.86
7	1.56	73.17	3.38	0.74	-	-	-	78.85
8	0.83	74.58	3.42	0.92	-	-	-	79.75
9	0.66	76.19	3.28	0.75	-	-	-	80.88
10	0.88	76.69	3.51	0.68	-	-	-	81.75
11	1.16	74.35	2.79	0.83	0.32	-	-	79.45
12	0.81	75.68	2.90	0.71	-	-	-	80.10
13	2.40	76.94	4.15	0.59	0.25	-	-	84.32
14	1.45	69.57	4.23	1.01	0.37	-	-	76.64
15	0.83	77.18	3.63	0.62	-	-	-	82.26
<b>Minimum Detection Limit</b>	0.07	0.20	0.28	0.08	0.08	0.20	0.28	

## Quantitative analysis of metal 7

Results of chemical analysis on the alteration rim surrounding metal 7 in ALHA 77180 (wt.%)									
Position Number	SiO <sub>2</sub>	Fe <sub>2</sub> O <sub>3</sub>	MgO	NiO	S	Cl	Fe <sub>(m)</sub>	Ni	Total
1	-	-	-	-	-	-	96.40	5.81	102.21
2	-	-	-	-	-	-	96.03	5.82	101.85
3	-	-	-	-	-	-	96.34	6.12	102.46
4	-	-	-	-	-	-	96.40	6.03	102.43
5	4.56	70.73	-	2.68	0.79	0.27	-	-	79.03
6	3.92	68.90	-	3.01	0.99	0.52	-	-	77.33
7	4.30	68.63	0.70	2.73	0.80	0.56	-	-	77.72
8	4.90	72.96	-	2.83	0.74	0.34	-	-	81.77
9	3.59	71.30	-	2.98	0.96	0.61	-	-	79.45
10	4.62	72.40	-	2.79	0.64	-	-	-	80.46
11	4.86	70.76	0.58	2.93	0.67	-	-	-	79.80
12	3.36	68.44	-	2.97	1.00	0.73	-	-	76.50
13	3.62	74.72	-	3.06	0.71	0.52	-	-	82.63
14	4.64	68.04	-	3.20	0.74	0.32	-	-	76.95
15	4.73	69.09	-	3.18	0.73	0.00	-	-	77.72
<b>Minimum Detection Limit</b>	0.07	0.20	0.05	0.28	0.08	0.08	0.20	0.28	

## Quantitative analysis of metal 8

Results of chemical analysis on the alteration rim surrounding metal 8 in Forrest 016 (wt.%)											
Position Number	SiO <sub>2</sub>	Al <sub>2</sub> O <sub>3</sub>	Fe <sub>2</sub> O <sub>3</sub>	MgO	CaO	NiO	S	Cl	Fe <sub>(m)</sub>	Ni	Total
1	-	-	-	-	-	-	-	-	96.28	6.78	103.06
2	-	-	-	-	-	-	-	-	96.65	6.67	103.32
3	-	-	-	-	-	-	-	-	97.38	6.48	103.86
4	-	-	-	-	-	-	-	-	95.41	6.76	102.17
5	6.25	1.95	72.02	0.53	0.70	4.86	-	-	-	-	86.31
6	5.35	1.74	71.49	-	0.60	3.29	-	0.73	-	-	83.20
7	1.65	0.51	75.42	-	0.21	2.53	-	-	-	-	80.31
8	1.48	-	74.10	-	0.17	2.49	-	-	-	-	78.24
9	4.56	1.04	70.39	-	0.50	4.18	-	0.25	-	-	80.91
10	3.92	0.93	70.16	0.47	0.41	5.03	0.20	0.40	-	-	81.50
11	2.27	0.76	70.47	-	0.29	4.24	0.38	0.35	-	-	78.76
12	5.63	1.47	66.61	0.42	0.43	5.02	-	0.21	-	-	79.79
13	4.11	1.23	74.88	-	0.45	3.78	-	-	-	-	84.44
14	4.99	2.27	68.70	-	0.48	4.08	-	-	-	-	80.50
<b>Minimum Detection Limit</b>	0.07	0.01	0.20	0.05	0.05	0.28	0.08	0.08	0.20	0.28	

## Quantitative analysis of metal 10

Results of chemical analysis on the alteration rim surrounding metal 10 in Forrest 028 (wt.%)											
Position Number	SiO <sub>2</sub>	Al <sub>2</sub> O <sub>3</sub>	Fe <sub>2</sub> O <sub>3</sub>	MgO	CaO	NiO	S	Cl	Fe <sub>(m)</sub>	Ni	Total
1	6.05	0.19	67.84	0.87	0.62	21.70	0.48	0.70	-	-	98.45
2	2.93	0.36	65.50	0.17	0.41	23.72	0.41	1.26	-	-	94.75
3	3.49	0.13	68.96	0.18	0.41	24.92	0.55	1.01	-	-	99.64
4	4.64	0.23	63.17	0.63	0.48	25.18	0.49	1.25	-	-	96.07
5	3.34	0.26	64.25	0.22	0.50	24.69	0.47	1.56	-	-	95.29
6	4.34	0.25	59.72	0.38	0.63	28.13	0.55	1.01	-	-	95.01
7	5.09	0.28	61.35	0.60	0.43	27.64	0.59	0.55	-	-	96.53
8	4.24	0.26	62.81	0.30	0.56	25.64	0.56	1.25	-	-	95.62
9	5.01	0.45	49.50	0.63	1.15	34.11	0.53	0.41	-	-	91.79
<b>Minimum Detection Limit</b>	0.06	0.07	0.17	0.04	0.08	0.25	0.08	0.07	0.17	0.25	

## Quantitative analysis of grain 14

Results of chemical analysis on the alteration rim surrounding grain 14 in Gunnadorah 004 (wt.%)									
Position Number	SiO <sub>2</sub>	Fe <sub>2</sub> O <sub>3</sub>	MgO	CaO	NiO	S	Fe <sub>(m)</sub>	Ni	Total
1	-	-	-	-	-	36.29	66.03	-	102.32
2	-	-	-	-	-	35.94	65.76	-	101.70
3	1.97	84.38	-	0.25	5.44	9.04	-	-	101.08
4	2.52	76.38	0.65	0.48	1.14	0.62	-	-	81.79
5	2.08	80.41	0.88	0.22	0.70	0.50	-	-	84.79
6	2.35	79.11	0.82	0.31	0.62	0.41	-	-	83.62
7	1.65	84.36	-	0.25	5.17	0.21	-	-	91.63
<b>Minimum Detection Limit</b>		0.08	0.20	0.05	0.05	0.28	0.08	0.20	0.28

## Quantitative analysis of metal 15

Results of chemical analysis on the alteration rim surrounding metal 15 in Daraj 014 (wt.%)											
Position Number	SiO <sub>2</sub>	Al <sub>2</sub> O <sub>3</sub>	Fe <sub>2</sub> O <sub>3</sub>	Mg O	Ca O	NiO	S	Cl	Fe <sub>(m)</sub>	Ni	Total
1	7.53	0.21	87.62	0.18	0.36	4.11	0.41	1.14	-	-	101.5
2	3.74	0.21	86.86	0.22	0.20	4.50	0.48	2.04	-	-	98.24
3	0.79	0.00	92.06	0.22	0.15	4.05	0.66	0.42	-	-	98.36
4	0.71	0.38	104.09	0.00	0.18	5.83	0.46	0.35	-	-	111.9
5	0.64	0.43	105.10	0.00	0.00	6.10	0.42	0.36	-	-	113.0
6	0.75	0.21	106.99	0.33	0.00	5.70	0.44	0.34	-	-	114.7
7	2.03	0.17	89.16	0.13	0.14	4.78	0.45	3.26	-	-	100.1
8	1.33	0.25	91.75	0.10	0.13	4.55	0.68	1.97	-	-	100.7
9	0.92	0.43	0.00	0.00	0.10	0.00	0.00	0.00	108.09	6.90	116.4
10	0.77	0.64	0.00	0.00	0.00	0.00	0.00	0.00	108.57	7.03	117.0
11	0.81	0.43	0.00	0.08	0.00	0.00	0.00	0.00	108.30	6.80	116.4
12	0.75	0.34	109.79	0.15	0.08	5.47	0.51	0.36	-	-	117.4
<b>Minimum Detection Limit</b>		0.06	0.07	0.17	0.04	0.08	0.25	0.08	0.07	0.17	0.25

## Quantitative analysis of metal 19

Results of chemical analysis on the alteration rim surrounding metal 19 in Acfer 019 (wt.%)											
Position Number	SiO <sub>2</sub>	Al <sub>2</sub> O <sub>3</sub>	Fe <sub>2</sub> O <sub>3</sub>	MgO	CaO	NiO	S	Cl	Fe <sub>(m)</sub>	Ni	Total
1	-	-	-	-	-	-	-	-	98.07	5.75	103.82
2	-	-	-	-	-	-	-	-	97.74	5.76	103.50
3	1.97	0.60	74.93	-	0.22	2.55	0.47	0.78	-	-	81.53
4	1.54	-	73.58	-	-	3.11	0.60	2.43	-	-	81.26
5	2.87	0.81	70.23	-	0.34	2.01	2.05	0.49	-	-	78.79
6	0.75	-	77.94	-	-	2.17	0.81	0.25	-	-	81.92
7	1.01	-	79.75	-	-	2.92	0.63	-	-	-	84.31
8	0.58	-	82.43	-	-	3.96	0.60	-	-	-	87.57
9	0.53	-	81.98	-	-	5.12	0.62	-	-	-	88.26
10	0.56	-	84.53	-	-	4.15	0.63	-	-	-	89.87
11	3.38	-	71.32	-	0.25	4.31	0.64	-	-	-	79.89
12	2.97	-	70.16	-	0.28	4.31	0.79	-	-	-	78.51
13	2.35	-	73.63	-	0.29	3.18	0.74	-	-	-	80.19
14	2.37	0.51	77.02	-	0.41	0.72	1.60	-	-	-	82.64
15	1.88	-	79.52	-	0.38	-	0.62	-	-	-	82.40
16	3.49	0.83	76.95	0.47	0.45	0.58	0.33	-	-	-	83.10
17	1.28	-	74.15	-	0.22	3.19	0.48	2.44	-	-	81.76
18	1.82	0.49	73.76	-	0.28	2.59	0.85	0.94	-	-	80.73
19	1.58	-	76.52	-	0.18	3.14	0.35	2.38	-	-	84.15
20	1.33	-	74.75	-	0.15	3.35	0.46	2.49	-	-	82.53

Minimum Detection Limit	0.07	0.01	0.20	0.05	0.05	0.28	0.08	0.08	0.20	0.28
-------------------------	------	------	------	------	------	------	------	------	------	------

Quantitative analysis of metal 20

Results of chemical analysis on the alteration rim surrounding metal 20 in Acfer 019 (wt.%)										
Position Number	SiO <sub>2</sub>	Al <sub>2</sub> O <sub>3</sub>	Fe <sub>2</sub> O <sub>3</sub>	CaO	NiO	S	Cl	Fe <sub>(m)</sub>	Ni	Total
<b>1</b>	-	-	-	-	-	-	-	71.68	32.52	104.20
<b>2</b>	-	-	-	-	-	-	-	68.74	35.07	103.81
<b>3</b>	-	-	-	-	-	-	-	97.26	6.28	103.54
<b>4</b>	-	-	-	-	-	-	-	97.04	6.31	103.35
<b>5</b>	-	-	-	-	-	-	-	97.16	6.40	103.56
<b>6</b>	-	-	-	-	-	-	-	87.37	15.92	103.29
<b>7</b>	-	-	-	-	-	-	-	87.93	15.21	103.14
<b>8</b>	2.18	-	83.71	-	-	0.39	-	-	-	86.28
<b>9</b>	0.94	-	78.09	-	2.82	0.66	0.23	-	-	82.74
<b>10</b>	1.35	-	70.70	0.21	1.64	3.35	-	-	-	77.25
<b>11</b>	0.98	-	74.82	-	2.57	0.69	0.32	-	-	79.38
<b>12</b>	1.13	-	75.98	-	2.67	0.77	-	-	-	80.55
<b>13</b>	0.94	-	75.81	-	2.41	0.77	-	-	-	79.93
<b>14</b>	5.20	-	73.35	0.39	3.11	0.22	-	-	-	82.27
<b>15</b>	6.31	-	71.64	0.38	3.81	0.23	-	-	-	82.37
<b>16</b>	6.40	0.64	69.40	0.41	4.06	0.43	-	-	-	81.34
<b>Minimum Detection Limit</b>	0.07	0.01	0.20	0.05	0.28	0.08	0.08	0.20	0.28	

1<sup>st</sup> Quant Analysis Session (LEW 85311) - Pre-calibration, machine values for the standards:

Element in Standard	Wt.% in Standard
Mg	57.90
Al	55.38
Si	24.12
P	16.89
S	52.25
Cl	7.62
Ca	18.28
Cr	68.24
Fe	70.43
Ni	99.78

2<sup>nd</sup> Quant Analysis Session (DOM 14010, ALHA 77180, Forrest 016, Forrest 028, Gunnadorah 004, Daraj 014, Acfer 019, Jbilet Winselwan) - Pre-calibration, machine values for the standards:

Element in Standard	Wt.% in Standard
Mg	63.04
Al	54.78
Si	24.49
S	52.99
Cl	7.49
Ca	17.67
Fe	75.01
Ni	102.98

## Reference List

Al-Kathiri, A., Hofmann, B.A., Jull, A.J.T., and Gnos, E., 2005, Weathering of Meteorites from Oman: Correlation of Chemical and Mineralogical Weathering Proxies with  $^{14}\text{C}$  Terrestrial Ages and the Influence of Soil Chemistry: *Meteoritics & Planetary Science Archives*, v. 40, p. 1215-1239, <https://journals.uair.arizona.edu/index.php/maps/article/view/15162>.

Alexander, C.M.O., Bowden, R., Fogel, M.L., Howard, K.T., Herd, C.D.K., and Nittler, L.R., 2012, The provenances of asteroids, and their contributions to the volatile inventories of the terrestrial planets.: *Science* (New York, N.Y.), v. 337, p. 721-3, doi:10.1126/science.1223474.

Anders, E., 1964, Origin, age, and composition of meteorites: *Space Science Reviews*, v. 3, p. 583-714, doi:10.1007/BF00177954.

Bellot-Gurlet, L., Neff, D., Réguer, S., Monnier, J., Saheb, M., and Dillmann, P., 2009, Raman Studies of Corrosion Layers Formed on Archaeological Irons in Various Media: *Journal of Nano Research*, v. 8, p. 147-156, doi:10.4028/www.scientific.net/JNanoR.8.147.

Bischoff, A., 2001, Meteorite classification and the definition of new chondrite classes as a result of successful meteorite search in hot and cold deserts: *Planetary and Space Science*, v. 49, p. 769-776, doi:10.1016/S0032-0633(01)00026-5.

Bland, P.A., 2006, Terrestrial weathering rates defined by extraterrestrial materials: *Journal of Geochemical Exploration*, v. 88, p. 257-261, doi:10.1016/j.gexplo.2005.08.051.

Bland, P.A., Berry, F.J., Bevan, A.W.R., Astin, T.R., Pillinger, C.T., Jull, A.J.T., Thornley, D.M., Sexton, A.S., and Britt, D.T., 1998, Climate and rock weathering: a study of terrestrial age dated ordinary chondritic meteorites from hot desert regions: *Geochimica et Cosmochimica Acta*, v. 62, p. 3169-3184, doi:10.1016/s0016-7037(98)00199-9.

Bland, P.A., Berry, F.J., Smith, T.B., Skinner, S.J., and Pillinger, C.T., 1996, The flux of meteorites to the earth and weathering in hot desert ordinary chondrite finds: *Geochimica et Cosmochimica Acta*, v. 60, p. 2053-2059, doi:10.1016/0016-7037(96)00125-1.

Bland, P. a, Zolensky, M.E., Benedix, G.K., and Sephton, M. a, 2006, Weathering of chondritic meteorites: *Meteorites and the Early Solar System II*, p. 853-867.

Bouvier, A., and Wadhwa, M., 2010, The age of the Solar System redefined by the oldest Pb-b age of a meteoritic inclusion: *Nature Geoscience*, v. 3, p. 637-641, doi:10.1038/ngeo941.

Brearley, A.J., 2006, The Action of Water: Meteorites and the early solar system II, p. 587-624, doi:10.1039/AN9214600270.

Britt, D.T., Guy Consolmagno, S.J., and Lebofsky, L., 2014, Main-Belt Asteroids, in *Encyclopedia of the Solar System*, Elsevier, p. 583-601, doi:10.1016/B978-0-12-415845-0.00026-8.

Browning, L.B., and Bourcier, W.L., 1996, Tochilinite: A sensitive indicator for alteration conditions on the CM asteroidal parent body, in *Lunar and Planetary Science Conference*, v. 27, p. 171-172, [http://articles.adsabs.harvard.edu/cgi-bin/nph-iarticle\\_query?db\\_key=AST&bibcode=1996LPI....27..171B&letter=0&classic=YES&defaultprint=YES&whole\\_paper=YES&page=171&epage=171&send=Send+PDF&filetype=.pdf](http://articles.adsabs.harvard.edu/cgi-bin/nph-iarticle_query?db_key=AST&bibcode=1996LPI....27..171B&letter=0&classic=YES&defaultprint=YES&whole_paper=YES&page=171&epage=171&send=Send+PDF&filetype=.pdf) (accessed February 2019).

Buchwald, V.F., and Clarke, R.S., 1989, Corrosion of Fe-Ni alloys by Cl-containing akaganeite ( $\beta$ -FeOOH): the Antarctic meteorite case: *American Mineralogist*, v. 74, p. 656-667, [http://www.minsocam.org/ammin/AM74/AM74\\_656.pdf](http://www.minsocam.org/ammin/AM74/AM74_656.pdf) (accessed January 2019).

Buddhue, J.D., 1957, The oxidation and weathering of meteorites.: Albuquerque, <http://hdl.handle.net/2027/mdp.39015065660600> (accessed

November 2018).

Bunch, T.E., and Chang, S., 1980, Carbonaceous chondrites—II. Carbonaceous chondrite phyllosilicates and light element geochemistry as indicators of parent body processes and surface conditions: *Geochimica et Cosmochimica Acta*, v. 44, p. 1543-1577, doi:10.1016/0016-7037(80)90118-0.

Burns, R.G., Burbine, T.H., Fisher, D.S., and Binzel, R.P., 1995, Weathering in Antarctic H and CR chondrites: quantitative analysis through Mossbauer spectroscopy: *Meteoritics*, v. 30, p. 625-633, doi:10.1111/j.1945-5100.1995.tb01159.x.

Cambier, S.M., Verreault, D., and Frankel, G.S., 2014, Raman Investigation of Anodic Undermining of Coated Steel During Environmental Exposure: *CORROSION*, v. 70, p. 1219-1229, doi:10.5006/1358.

Carter, J., Viviano-Beck, C., Loizeau, D., Bishop, J., and Le Deit, L., 2015, Orbital detection and implications of akaganéite on Mars: *Icarus*, v. 253, p. 296-310, doi:10.1016/J.ICARUS.2015.01.020.

Chapman, C.R., 1996, S-type asteroids, ordinary chondrites, and space weathering: The evidence from Galileo's fly-bys of Gaspra and Ida: *Meteoritics and Planetary Science*, v. 31, p. 699-725, doi:10.1111/j.1945-5100.1996.tb02107.x.

Chicot, D., Mendoza, J., Zaoui, A., Louis, G., Lepingle, V., Roudet, F., and Lesage, J., 2011, Mechanical properties of magnetite ( $\text{Fe}_3\text{O}_4$ ), hematite ( $\alpha\text{-Fe}_2\text{O}_3$ ) and goethite ( $\alpha\text{-FeO}\cdot\text{OH}$ ) by instrumented indentation and molecular dynamics analysis: *Materials Chemistry and Physics*, v. 129, p. 862-870, doi:10.1016/J.MATCHEMPHYS.2011.05.056.

Choe, W.H., Huber, H., Rubin, A.E., Kallemeyn, G.W., and Wasson, J.T., 2010, Compositions and taxonomy of 15 unusual carbonaceous chondrites: *Meteoritics and Planetary Science*, v. 45, p. 531-554, doi:10.1111/j.1945-5100.2010.01039.x.

Colomban, P., Cherifi, S., and Despert, G., 2008a, Raman identification of corrosion products on automotive galvanized steel sheets: Journal of Raman Spectroscopy, v. 39, p. 881-886, doi:10.1002/jrs.1927.

Colomban, P., Cherifi, S., and Despert, G., 2008b, Raman identification of corrosion products on automotive galvanized steel sheets: Journal of Raman Spectroscopy, v. 39, p. 881-886, doi:10.1002/jrs.1927.

Eugster, O., 2003, Cosmic-ray Exposure Ages of Meteorites and Lunar Rocks and Their Significance: Geochemistry, v. 63, p. 3-30, doi:10.1078/0009-2819-00021.

F. Buchwald, W., 1975, Handbook of iron meteorites: Their history, distribution, composition, and structure. Volumes 1, 2 & 3: v. 1.

French, B., Macpherson, G., and Clarke, R., 2010, ANTARCTIC METEORITE TEACHING Originally prepared and written by ANTARCTIC METEORITE TEACHING: Chondrites and the Protoplanetary Disk, ASP Conference Series, v. 341,  
[https://curator.jsc.nasa.gov/education/\\_documents/educationmeteorite.pdf](https://curator.jsc.nasa.gov/education/_documents/educationmeteorite.pdf) (accessed October 2018).

Gaffey, M.J., and Gilbert, S.L., 1998, Asteroid 6 Hebe: The probable parent body of the H-type ordinary chondrites and the IIE iron meteorites: Meteoritics and Planetary Science, v. 33, p. 1281-1295, doi:10.1111/j.1945-5100.1998.tb01312.x.

Gattacceca, J. et al., 2011, The densest meteorite collection area in hot deserts: The San Juan meteorite field (Atacama Desert, Chile): Meteoritics and Planetary Science, v. 46, p. 1276-1287, doi:10.1111/j.1945-5100.2011.01229.x.

Geiger, B., 2018, Hot on the trail of Antarctic meteorites:,  
<https://www.sciencenewsforstudents.org/article/hot-trail-antarctic-meteorites> (accessed July 2019).

Goethite R120086 - RRUFF Database: Raman, X-ray, Infrared, and Chemistry,  
<http://rruff.info/goethite/display=default/R120086> (accessed June 2019).

Gooding, J.L., 1982, Mineralogical aspects of terrestrial weathering effects in chondrites from Allan Hills, Antarctica: Lunar and Planetary Science, v. 12B, p. 1105-1122, [http://adsbit.harvard.edu/cgi-bin/nph-iarticle\\_query?1982LPSC...12.1105G&defaultprint=YES&page\\_ind=0&filetype=.pdf](http://adsbit.harvard.edu/cgi-bin/nph-iarticle_query?1982LPSC...12.1105G&defaultprint=YES&page_ind=0&filetype=.pdf) (accessed November 2018).

Gooding, J.L., 1986, Weathering of stony meteorites in Antarctica, *in* International Workshop on Antarctic Meteorites, p. 48-54, <https://ntrs.nasa.gov/archive/nasa/casi.ntrs.nasa.gov/19860019346.pdf> (accessed November 2018).

Hanesch, M., 2009, Raman spectroscopy of iron oxides and (oxy)hydroxides at low laser power and possible applications in environmental magnetic studies: Geophys. J. Int, v. 177, p. 941-948, doi:10.1111/j.1365-246X.2009.04122.x.

Howard, K.T., Alexander, C.M.O., Schrader, D.L., and Dyl, K.A., 2015a, Classification of hydrous meteorites (CR, CM and C2 ungrouped) by phyllosilicate fraction: PSD-XRD modal mineralogy and planetesimal environments: Geochimica et Cosmochimica Acta, v. 149, p. 206-222, doi:10.1016/J.GCA.2014.10.025.

Howard, K.T., Alexander, C.M.O., Schrader, D.L., and Dyl, K.A., 2015b, Classification of hydrous meteorites (CR, CM and C2 ungrouped) by phyllosilicate fraction: PSD-XRD modal mineralogy and planetesimal environments: Geochimica et Cosmochimica Acta, v. 149, p. 206-222, doi:10.1016/J.GCA.2014.10.025.

Hughes, J., King, G.A., and O'Brien, D.J., 1996, Corrosivity in Antarctica—Revelations on the Nature of Corrosion in the World's Coldest, Driest, Highest, and Purest Continent, *in* Proc. 13th International Corrosion Conference, p. 1-10, <https://publications.csiro.au/rpr/pub?list=BRO&pid=procite:5f6ad8a7-1570->

4b6b-adc4-14f3477e9b80 (accessed December 2018).

Jarosewich, E., 1990, Chemical analyses of meteorites: A compilation of stony and iron meteorite analyses: Meteoritics, v. 25, p. 323-337, doi:10.1111/j.1945-5100.1990.tb00717.x.

Jull, A.J.T., 2001, Terrestrial ages of meteorites, in Accretion od extraterrestrial matter throughout Earth's history, p. 241-266, doi:10.1038/293433a0.

Jull, A.J.T., McHargue, L.R., Bland, P.A., Greenwood, R.C., Bevan, A.W.R., Kim, K.J., Lamotta, S.E., and Johnson, J.A., 2010, Terrestrial ages of meteorites from the Nullarbor region, Australia, based on  $^{14}\text{C}$  and  $^{14}\text{C}-\text{Be}$  measurements: Meteoritics and Planetary Science, v. 45, p. 1271-1283, doi:10.1111/j.1945-5100.2010.01289.x.

Jull, A.J.T., Wlotzka, F., and Donahue, D.J., 1991, Terrestrial Ages and Petrologic Description of Roosevelt County Meteorites: Abstracts of the Lunar and Planetary Science Conference, volume 22, page 667, (1991), v. 22, <http://adsabs.harvard.edu/abs/1991LPI....22..667J> (accessed May 2019).

Kimura, M., Grossman, J.N., and Weisberg, M.K., 2011, Fe-Ni metal and sulfide minerals in CM chondrites: An indicator for thermal history: Meteoritics and Planetary Science, v. 46, p. 431-442, doi:10.1111/j.1945-5100.2010.01164.x.

King, A.J., Russell, S.S., Schofield, P.F., Humphreys-Williams, E.R., Strekopytov, S., Abernethy, F.A.J., Verchovsky, A.B., and Grady, M.M., 2018, The alteration history of the Jbilet Winselwan CM carbonaceous chondrite: An analog for C-type asteroid sample return: Meteoritics & Planetary Science, v. 54, p. maps.13224, doi:10.1111/maps.13224.

Krot, A.N., Hutcheon, I.D., Brearley, A.J., Pravdivtseva, O. V, Petaev, M.I., and Hohenberg, C.M., 2006, Timescales and settings for alteration of chondritic meteorites: Meteorites and the early solar system II, p. 525-553, <https://www.lpi.usra.edu/books/MESSII/9006.pdf> (accessed November

2018).

Krot, A.N., Keil, K., Scott, E.R.D., Goodrich, C.A., and Weisberg, M.K., 2007,

Classification of Meteorites: Treatise on Geochemistry, p. 1-52,

doi:10.1016/B0-08-043751-6/01062-8.

Lauretta, D.S. et al., 2017, OSIRIS-REx: Sample Return from Asteroid (101955)

Bennu: Space Science Reviews, v. 212, p. 925-984, doi:10.1007/s11214-017-

0405-1.

Lauretta, D., and Killgore, M., 2005, A color atlas of meteorites in thin section:

Tucson, AZ: Golden Retriever Publications., 301 p.

Lee, M.R., and Bland, P.A., 2004, Mechanisms of weathering of meteorites

recovered from hot and cold deserts and the formation of phyllosilicates:

Geochimica et Cosmochimica Acta, v. 68, p. 893-916, doi:10.1016/S0016-

7037(03)00486-1.

Lee, M.R., Cohen, B.E., Mark, D.F., and Boyce, A., 2018, Ephemeral nebular

components in the mildly aqueous altered cm carbonaceous chondrite lewis

cliff (lew) 85311: Lunar and Planetary Science,

<http://eprints.gla.ac.uk/157627/1/157627.pdf> (accessed September 2019).

Li, S., and Hihara, L.H., 2015, A Micro-Raman Spectroscopic Study of Marine

Atmospheric Corrosion of Carbon Steel: The Effect of Akaganeite: Journal of

The Electrochemical Society, v. 162, p. 495-502, doi:10.1149/2.0881509jes.

Losiak, A., and Velbel, M.A., 2011, Evaporite formation during weathering of

Antarctic meteorites--A weathering census analysis based on the ANSMET

database: Meteoritics and Planetary Science, v. 46, p. 443-458,

doi:10.1111/j.1945-5100.2010.01166.x.

Mackinnon, I.D.R., and Zolensky, M.E., 1984, Proposed structures for poorly

characterized phases in C2M carbonaceous chondrite meteorites: Nature, v.

309, p. 240-242, doi:10.1038/309240a0.

Magnetite R061111 - RRUFF Database: Raman, X-ray, Infrared, and Chemistry,  
<http://rruff.info/magnetite/R061111> (accessed September 2019).

Miyamoto, M., Fujii, N., and Takeda, H., 1981, Ordinary chondrite parent body - An internal heating model: In: Lunar and Planetary Science Conference, v. 12, p. 1145, [http://articles.adsabs.harvard.edu/cgi-bin/nph-iarticle\\_query?1982LPSC...12.1145M&data\\_type=PDF\\_HIGH&whole\\_paper=YES&type=PRINTER&filetype=.pdf](http://articles.adsabs.harvard.edu/cgi-bin/nph-iarticle_query?1982LPSC...12.1145M&data_type=PDF_HIGH&whole_paper=YES&type=PRINTER&filetype=.pdf) (accessed November 2018).

Mohammed, S., Elnoor, M., and Hamad, I., 2018, The Structural Properties of Iron Oxides using Raman Spectroscopy: Available online [www.jsaer.com](http://www.jsaer.com) Journal of Scientific and Engineering Research 183 Journal of Scientific and Engineering Research, v. 5, p. 183-187, [www.jsaer.com](http://www.jsaer.com) (accessed April 2019).

Morcillo, M., Chico, B., de la Fuente, D., Almeida, E., Joseph, G., Rivero, S., and Rosales, B., 2004, Atmospheric corrosion of reference metals in Antarctic sites: Cold Regions Science and Technology, v. 40, p. 165-178, doi:10.1016/j.coldregions.2004.06.009.

Nakamura, T. et al., 2011, Itokawa Dust Particles: A Direct Link Between S-Type Asteroids and Ordinary Chondrites: Science, v. 333, p. 1113-1116, doi:10.1126/science.1207758.

Neff, D., Bellot-Gurlet, L., Dillmann, P., Reguer, S., and Legrand, L., 2006, Raman imaging of ancient rust scales on archaeological iron artefacts for long-term atmospheric corrosion mechanisms study, in *Journal of Raman Spectroscopy*, John Wiley & Sons, Ltd, v. 37, p. 1228-1237, doi:10.1002/jrs.1581.

Nishiizumi, K., Elmore, D., and Kubik, P.W., 1989, Update on terrestrial ages of Antarctic meteorites: Earth and Planetary Science Letters, v. 93, p. 299-313, doi:10.1016/0012-821X(89)90029-0.

Norton, R., and Chitwood, L., 2008, Minerals in Meteorites, in *Field Guide to*

Meteors and Meteorites, p. 239-287,  
[https://cds.cern.ch/record/1339655/files/978-1-84800-157-2\\_BookBackMatter.pdf](https://cds.cern.ch/record/1339655/files/978-1-84800-157-2_BookBackMatter.pdf) (accessed February 2019).

Okada, T. et al., 2017, Thermal Infrared Imaging Experiments of C-Type Asteroid 162173 Ryugu on Hayabusa2: Space Sci Rev, v. 208, p. 255-286, doi:10.1007/s11214-016-0286-8.

Palmer, E.E., and Lauretta, D.S., 2011, Aqueous alteration of kamacite in CM chondrites: Meteoritics and Planetary Science, v. 46, p. 1587-1607, doi:10.1111/j.1945-5100.2011.01251.x.

Potts, P.J., 1992, A Handbook of Silicate Rock Analysis: New York, Springer, 622 p., doi:10.1007/978-1-4615-3270-5 10.

Roberts, J., 2015, Hunting Hidden Treasures: Antarctic Meteorites Arrive at JSC:, <https://www.nasa.gov/content/hunting-hidden-treasures-antarctic-meteorites-arrive-at-jsc> (accessed July 2019).

Rubin, A.E., Trigo-Rodríguez, J.M., Huber, H., and Wasson, J.T., 2007, Progressive aqueous alteration of CM carbonaceous chondrites: Geochimica et Cosmochimica Acta, v. 71, p. 2361-2382, doi:10.1016/J.GCA.2007.02.008.

Rull, F. et al., 2017, The Raman Laser Spectrometer for the ExoMars Rover Mission to Mars: Astrobiology, v. 17, p. 627-654, doi:10.1089/ast.2016.1567.

Saunier, G., Poitrasson, F., Moine, B., Gregoire, M., and Seddiki, A., 2010, Effect of hot desert weathering on the bulk-rock iron isotope composition of L6 and H5 ordinary chondrites: Meteoritics and Planetary Science, v. 45, p. 195-209, doi:10.1111/j.1945-5100.2010.01017.x.

Scherer, P. et al., 1997, Allan Hills 88019: An Antarctic H-chondrite with a very long terrestrial age: Meteoritics and Planetary Science, v. 32, p. 769-773, doi:10.1111/j.1945-5100.1997.tb01567.x.

Van Schmus, W.R., 1969a, The mineralogy and petrology of chondritic

meteorites: Earth-Science Reviews, v. 5, p. 145-184, doi:10.1016/0012-8252(69)90076-2.

Van Schmus, W.R., 1969b, The mineralogy and petrology of chondritic meteorites: Earth Science Reviews, v. 5, p. 145-184, doi:10.1016/0012-8252(69)90076-2.

Scott, E.R.D., and Krot, A.N., 2013, Chondrites and Their Components, *in* Treatise on Geochemistry: Second Edition, Elsevier, v. 1, p. 65-137, doi:10.1016/B978-0-08-095975-7.00104-2.

Shu, F.H., Shang, H., Gounelle, M., Glassgold, A.E., and Lee2, T., 2001, THE ORIGIN OF CHONDRULES AND REFRACtORY INCLUSIONS IN CHONDRTIC METEORITES:, <http://iopscience.iop.org/article/10.1086/319018/pdf> (accessed November 2018).

Tachibana, S. et al., 2014, Hayabusa2: Scientific importance of samples returned from C-type near-Earth asteroid (162173) 1999 JU<inf>3</inf>: Geochemical Journal, v. 48, p. 571-581, doi:10.2343/geochemj.2.0350.

The Meteoritical Society, 2017, Meteoritical Bulletin: Search the Database:, <https://www.lpi.usra.edu/meteor/metbull.php> (accessed November 2018).

Tochilinite - RRUFF Database: Raman, X-ray, Infrared, and Chemistry, <http://rruff.info/Tochilinite> (accessed July 2019).

Tomeoka, K., McSween Jr., H.Y., and Buseck, P.R., 1989, Mineralogical alteration of CM carbonaceous chondrites: a review:, <https://core.ac.uk/download/pdf/51483933.pdf> (accessed February 2019).

Vacher, L.G., Marrocchi, Y., Villeneuve, J., Verdier-Paoletti, M.J., and Gounelle, M., 2017, Petrographic and C & O isotopic characteristics of the earliest stages of aqueous alteration of CM chondrites: Geochimica et Cosmochimica Acta, v. 213, p. 271-290, doi:10.1016/j.gca.2017.06.049.

Velbel, M.A., 2014, Terrestrial weathering of ordinary chondrites in nature and

continuing during laboratory storage and processing: Review and implications for Hayabusa sample integrity: Meteoritics and Planetary Science, v. 49, p. 154-171, doi:10.1111/j.1945-5100.2012.01405.x.

Velbel, M.A., 1988, The distribution and significance of evaporitic weathering products on Antarctic meteorites: Meteoritics, v. 23, p. 151-159, doi:10.1111/j.1945-5100.1988.tb00910.x.

Velbel, M.A., and Gooding, J.L., 1990, Terrestrial weathering of Antarctic stony meteorites-developments 1985-1989., *in* Workshop on Differences between Antarctic and non-Antarctic Meteorites, p. 94-98, <http://adsabs.harvard.edu/full/1990anam.work...94V>.

Velbel, M.A., Long, D.T., and Gooding, J.L., 1991, Terrestrial weathering of Antarctic stone meteorites: Formation of Mg-carbonates on ordinary chondrites: Geochimica et Cosmochimica Acta, v. 55, p. 67-76, doi:10.1016/0016-7037(91)90400-Y.

Vernazza, P., Zanda, B., Nakamura, T., Scott, E., and Russell, S., 2015, The Formation and Evolution of Ordinary Chondrite Parent Bodies, *in* Asteroids IV, doi:10.2458/azu\_uapress\_9780816532131-ch032.

Walsh, K.J., Morbidelli, A., Raymond, S.N., O'Brien, D.P., and Mandell, A.M., 2012, Populating the asteroid belt from two parent source regions due to the migration of giant planets—"The Grand Tack": Meteoritics and Planetary Science, v. 47, p. 1941-1947, doi:10.1111/j.1945-5100.2012.01418.x.

Watanabe, S. et al., 2019, Hayabusa2 arrives at the carbonaceous asteroid 162173 Ryugu-A spinning top-shaped rubble pile.: Science (New York, N.Y.), v. 364, p. 268-272, doi:10.1126/science.aav8032.

Watanabe, S. ichiro, Tsuda, Y., Yoshikawa, M., Tanaka, S., Saiki, T., and Nakazawa, S., 2017, Hayabusa2 Mission Overview: Space Science Reviews, v. 208, p. 3-16, doi:10.1007/s11214-017-0377-1.

Website 1.1, <https://www.asteroidmission.org/objectives/bennu/> (accessed

July 2019).

Website 1.2, <https://www.meteorite-recon.com/home/meteorite-documentaries/meteorites-in-situ> (accessed July 2019).

Website 2.1, <https://www.fine-tools.com/G10019.html> (accessed July 2019).

Website 2.2, <https://www.nanophoton.net/raman-spectroscopy/lessons/lesson-1> (accessed May 2019).

Website 2.3, <http://webmineral.com/data/Akaganeite.shtml#.XYpKJyhKi70> (accessed September 2019).

Website 2.4, <http://webmineral.com/data/Goethite.shtml#.XYpM6yhKi71> (accessed September 2019).

Website 2.5, <http://webmineral.com/data/Tochilinite.shtml#.XYpKSShKi70> (accessed September 2019).

Website 2.6, <http://webmineral.com/data/Magnetite.shtml#.XYpKUihi70> (accessed September 2019).

Website 3.1,

[https://www.meteoblue.com/en/weather/historyclimate/climatemodelled/dominion-range\\_antarctica\\_6632249](https://www.meteoblue.com/en/weather/historyclimate/climatemodelled/dominion-range_antarctica_6632249) (accessed June 2019).

Website 3.2,

[https://www.meteoblue.com/en/weather/historyclimate/climatemodelled/-76.717N159.667E0\\_Antarctica%2FSouth\\_Pole](https://www.meteoblue.com/en/weather/historyclimate/climatemodelled/-76.717N159.667E0_Antarctica%2FSouth_Pole) (accessed June 2019).

Website 3.3,

[http://reg.bom.gov.au/climate/averages/tables/cw\\_011052\\_All.shtml](http://reg.bom.gov.au/climate/averages/tables/cw_011052_All.shtml) (accessed June 2019).

Website 3.4,

[https://www.meteoblue.com/en/weather/historyclimate/climatemodelled/foggaret-ez-zoua\\_algeria\\_2496381](https://www.meteoblue.com/en/weather/historyclimate/climatemodelled/foggaret-ez-zoua_algeria_2496381) (accessed June 2019).

Website 3.5,

[https://www.meteoblue.com/en/weather/historyclimate/climatemodelled/ghadames\\_libya\\_2217440](https://www.meteoblue.com/en/weather/historyclimate/climatemodelled/ghadames_libya_2217440) (accessed June 2019).

Website 4.1,

[https://geonames.usgs.gov/apex/f?p=gnispq:5:::NO::P5\\_ANTAR\\_ID:8773](https://geonames.usgs.gov/apex/f?p=gnispq:5:::NO::P5_ANTAR_ID:8773)  
(accessed August 2019).

Website 4.2,

[https://www.meteoblue.com/en/weather/historyclimate/climatemodelled/-84.283N161.083E0\\_Antarctica%2FSouth\\_Pole](https://www.meteoblue.com/en/weather/historyclimate/climatemodelled/-84.283N161.083E0_Antarctica%2FSouth_Pole) (accessed August 2019).

Website 4.3,

[https://www.meteoblue.com/en/weather/historyclimate/climatemodelled/-86.367N-70E0\\_Antarctica%2FSouth\\_Pole](https://www.meteoblue.com/en/weather/historyclimate/climatemodelled/-86.367N-70E0_Antarctica%2FSouth_Pole) (accessed August 2019).

Website 4.4,

[https://www.meteoblue.com/en/weather/historyclimate/climatemodelled/26.668N-11.677E224\\_Africa%2FEl\\_Aaiun](https://www.meteoblue.com/en/weather/historyclimate/climatemodelled/26.668N-11.677E224_Africa%2FEl_Aaiun) (accessed August 2019).

Weisberg, M.K., McCoy, T.J., and Krot, A.N., 2006, Systematics and Evaluation of Meteorite Classification: Meteorites and the early solar system II, p. 19-52, <https://www.lpi.usra.edu/books/MESSII/9014.pdf> (accessed October 2018).

Wlotzka, F., 1993, A weathering scale for the ordinary chondrites: Meteoritics, v. 28, p. 460.